THE SCATTERING OF 3MEV NEUTRONS FROM HEAVY NUCLEI

Thesis

Submitted by

JOHN R.M. ANNAND

for the degree of

DOCTOR OF PHILOSOPHY

Department of Physics

University of Edinburgh

April 1982

To Janette

DECLARATION

I declare that all of the work produced in this thesis is entirely my own except where indicated otherwise

John R.M. Annand

Contents

Contents Continued

Contents Continued

Abstract

A neutron polarimeter has been developed which can measure fast neutron differential cross sections and analysing power distributions at up to twelve angles simultaneously .The maximum angular range is 13-167 degrees with a minimum interval of 7 degrees. Its object is to collect data of good statistical accuracy and reliability in order to provide a rigorous test of nuclear models currently used to describe these phenomena.

In order to service the maximum of 24 liquid scintillation counters in the polarimeter, a NIM based system of electronics has been built up and new hardware interfacing and software installed for the Camac-PDP11/05 system which controls its operation automatically. This present system has some new features, notably automatic detector efficiency calibration, faster and more versatile pulse height analysis and the provision of on line data analysis.

Care has been taken to ensure that preliminary results obtained agree with previous measurements where these are reasonably well established. ^{56}Fe samples scattering 3.0 MeV neutrons were chosen. Two sample sizes were used in this test so that the reliability of finite sample corrections to the data could be ascertained. Analytical and Monte Carlo methods to this end were devised and compared. Due to the large size of the bigger sample, the test was especially stiff, but the final results showed good agreement for both samples. The large sample size was thought necessary to the achievment of accurate analysing power data within reasonable experimental running time.

After proving , 3.0 Mev data for the heavy elements W,Hg, Tl, Pb, Bi, U was collected. Previous attempts at analysing power measurement have generally been of poor accuracy, covered limited angular ranges,

and often contradicted each other. Two separate sets of data were taken for each sample, one 20-160 degrees and the other 27-167 degrees both at 14 degree intervals. This has helped define the analysing power distributions especially, and accurate meshing together of the two sets lends credence to the results. Improvement in detector efficiency calibration has resulted in much smoother differential cross section distributions, and improved statistical accuracy has reduced wild fluctuations in analysing powers.

Results are compared with the predictions of the Optical Model, taking account of compound nucleus formation. Various spherical potentials are used including best fit ones obtained after parameter search. Where collective effects are suspected, notably for isotopes of W and ^{238}U, Coupled Channels calculations are employed.

Chapter 1

Introduction

1.1 Nuclear Reactions

The interaction between one nucleon and an assembly of nucleons is of central importance in nuclear structure and reaction studies. Making the assumption that it can be described as a two body interaction, it is the shell model potential which generates nuclear single particle states, for structure studies, while for reactions it is the interaction between an incident particle and target nucleus. It may be determined in two ways: deduced from the fundamental nucleon-nucleon interaction, which is known through studies of the deuteron, or inferred from experimental data. Since the former runs into very serious mathematical difficulties if realistic calculations are attempted, and the latter fails to produce uniquely valued results, uncertainties still remain. At present the best results are probably to be found by combination of microscopic calculations and phenomenological analyses of experimental data. This work will concentrate heavily on the experimental approach.

Information about the nature of the nucleon-nucleus interaction is extracted from measurements of differential cross-sections, integrated cross-sections and polarisations. When it impinges on a target nucleus, an incident particle may undergo one of a number of different types of reaction, the relative probabilities of which depend on incident energy amongst other things. They may be divided into two classes, direct which happen approximately within the time that it takes the incident particle to traverse the nuclear diameter , and compound where an intermediate compound nucleus is temporarily formed. Many reactions proceed through both modes (figure 1.1). Often direct or shape elastic scattering is the dominant feature with compound nucleus reactions decreasing and other direct reactions increasing in

NEUTRON REACTION CHANNELS

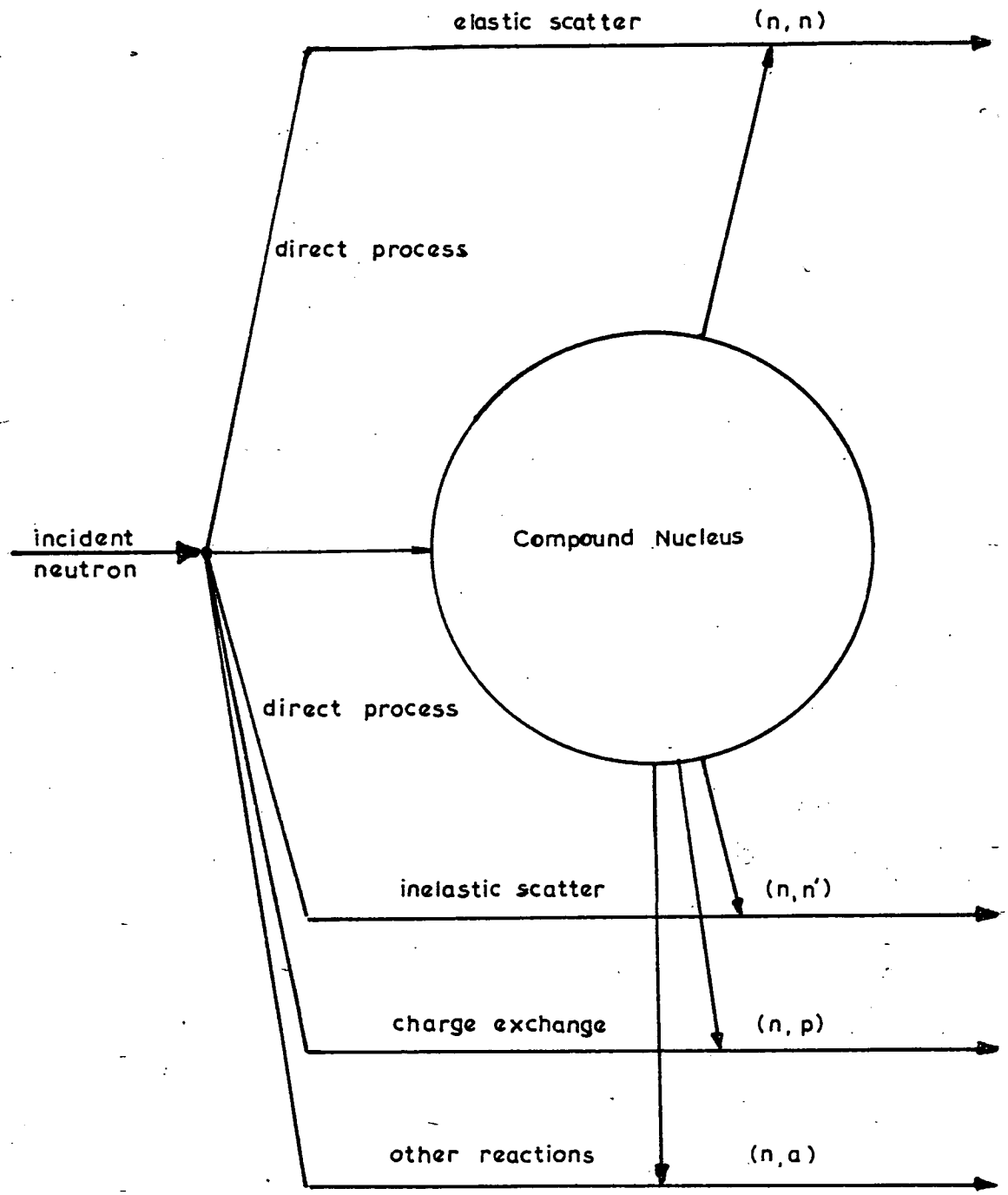

Figure 1.1

importance with increasing energy. Where competing direct and compound modes exist in the same reaction channel, there is no known way of separating them. The lifetime of a compound state, although very long when compared with the transit time across the nuclear diameter , is not remotely approached by the time resolution of existing experimental apparatus. However if one feature is dominant, it may be deduced by inspection of the differential cross-section. Direct processes produce a highly anisotropic distribution, often like a diffraction pattern with a strong forward peak and secondary maxima and minima in intensity. Compound distributions are often close to being isotropic and show symmetry about the 90 degree scattering angle. Direct processes may also induce polarisation, preferential alignment of the exit particle's spin vector, while, at least for medium to heavy nuclei with closely spaced, overlapping energy levels, compound processes do not.

1.2 The Nucleon-Nucleus Potential

The nucleon-nucleon interaction is short range and attractive decaying exponentially at large distances. Therefore it is not unreasonable that the nucleon-nucleus interaction should do likewise. Nucleons within the nucleus experience only their nearest neighbours, the saturation effect, so it is feasible that that the potential will be approximately constant, well within the nuclear surface, varying smoothly with radial distance until radial dependence is exponential at distances substantially greater than the nuclear radius. A convenient and widely used analytical expression for this is the Woods Saxon form

$$f(r) = 1/\{1 + \exp[(r-R)/a]\} \qquad (1.1)$$

R: Nuclear Radius

a: Nuclear Surface Diffuseness

The nucleon-nucleon interaction is also spin dependent. Of the various allowed forms in the nucleon-nucleus interaction, the spin-orbit explains very simply the separation of $J = L \pm 1/2$ states of nuclei and the increase of separation with L. Following atomic theory it is usually given the Thomas-Fermi form

$$V_s(r) = (h/m_{\pi}c)^2 V_s/r.[df(r)/dr]\ \mathbf{L}.\sigma \qquad (1.2)$$

The squared term is the pion wavelength. However these potentials, when substituted into a simple Schrodinger equation, are unable to account for non-elastic cross sections. This can be remedied by using a complex potential, the so called Optical Potential proposed by Le Levier and Saxon [1] and Feshbach et al [2]. It is analagous to the optical situation where the real part of a complex refractive index describes refraction and the complex part absorption.

The Optical Model (OM) treats the nucleus as a lump of matter, ignoring details of structure. It is usually most successful when the energy resolution of the detection aparatus is much poorer than the mean energy level spacing of any intermediate states formed, so that one is effectively averaging over many states. This is often not the case with low incident energies and light nuclei, and Optical Model analyses are usually confined to the medium to heavy nuclei when the energy is less than 5 MeV.

1.3 Neutron Scattering

The type of reaction of interest in this work is Neutron scattering. Neutrons being uncharged, do not suffer any coulomb interaction and hence are not repelled by the target nucleus. This allows them to be used as probes down to the lowest of energies and can also ease calculations as the relatively slowly decaying coulomb interaction requires many partial waves in the analysis. However

compared with proton experiments , scattered neutron count rates are always low. Of primary interest will be elastic scattering, where the only energy loss is through target recoil, notably the measurement of elastic differential cross-sections and the polarisation induced by elastic scattering, or analysing power.

The former can be found directly from count rate at specific scattering angles if the incident flux and detection efficiencies are known.

$$\sigma(\theta) = Sr^2/IN \qquad (1.3)$$

S: scattered neutron flux at angle θ

N: number of nuclei in scatterer

I: neutron flux incident on scatterer

r: average distance between scatterer and detector

Since neutron detectors are insensitive to spin alignment, the latter must be deduced from variation of count rate with asimuthal angle (fig 1.2). This is directly attributable to a spin- orbit component in the nuclear interaction. Analagous to optical polarisation measurement, both a polariser and analyser are required in order to detect any asimuthal asymmetry. This can be done by double elastic scattering of initially unpolarised neutrons or single elastic scattering of partially polarised source neutrons, e.g. from the $^{2}H(d,n)^{3}He$ and $^{3}H(d,n)^{4}He$ reactions. The latter method is used here as the final count rate after double scattering is extremely low. However the polarisation induced by the source reaction has to be known in order to find the analysing power. This must be done in a separate experiment normally using ^{4}He or ^{12}C as the analyser. The analysing power of these light, spin zero nuclei can be calculated with some confidence

BASIC LAYOUT OF POLARISATION EXPERIMENT

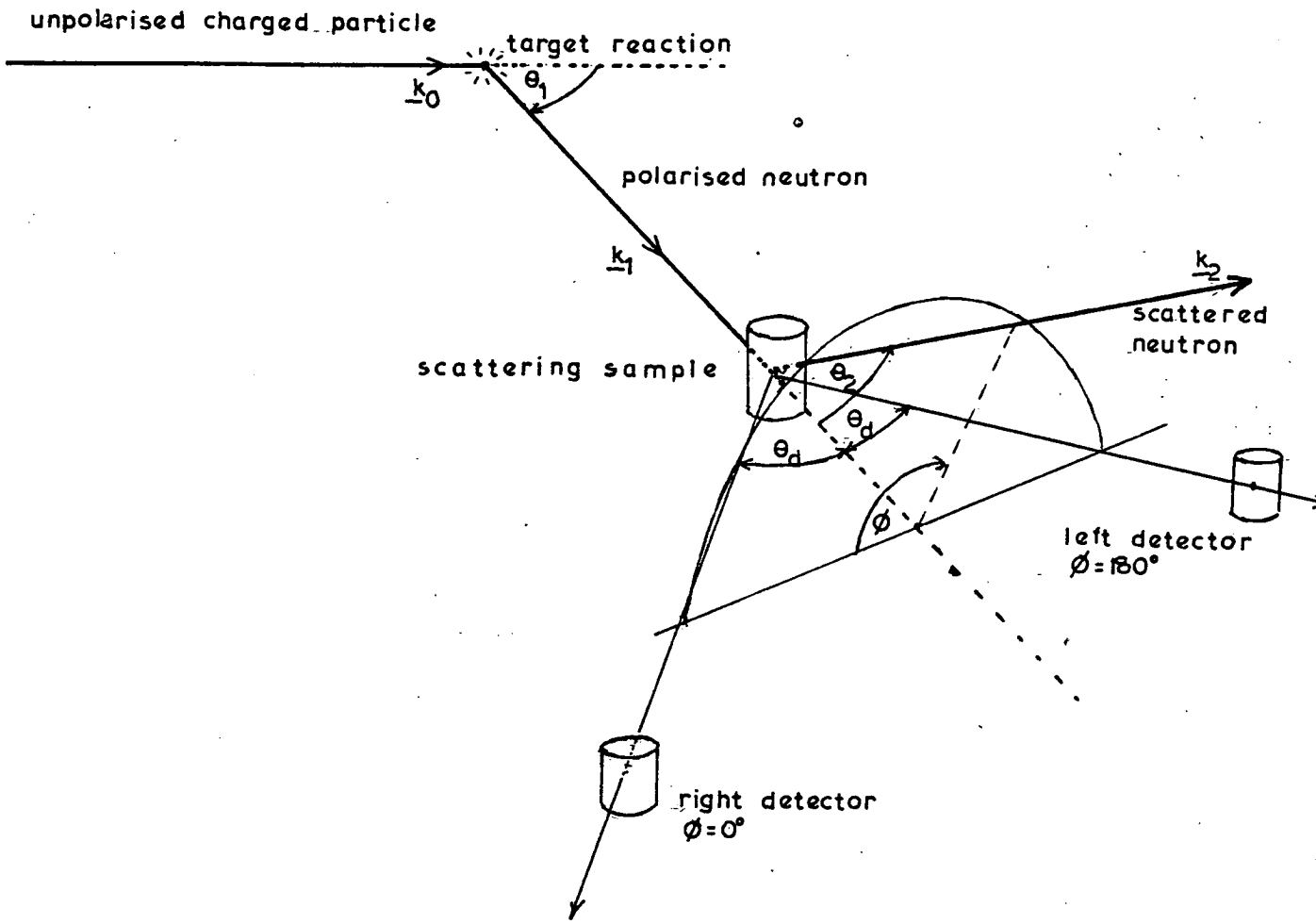

$\underline{k}_0$= charged particle direction

$\underline{k}_1$= reaction neutron direction

$\underline{k}_2$= scattered neutron direction

Figure 1.2

from phase shifts found from differential cross-section data. The basic experimental geometry is shown in figure 1.2. The number of neutrons scattered by the analyser through angles θ and ϕ can be expressed as.

$$\sigma(E_1,\theta_2,\phi)= \sigma(E_1,\theta_2)[1 + P(E_0,\theta_1)A(E_1,\theta_2)\cos\phi] \qquad (1.4)$$

E_0: charged particle energy

E_1: reaction neutron energy

θ_1: reaction angle

θ_2: scattering angle

ϕ: angle between reaction planes= $(\mathbf{k}_0 x \mathbf{k}_1).(\mathbf{k}_1 x \mathbf{k}_2)$

P: polarisation induced in the reaction

A: elastic scattering analysing power

It is usual to situate the neutron detectors in the reaction plane defined by $\mathbf{k}_0 x \mathbf{k}_1$ so that ϕ= 0 degrees(right) and ϕ=180 degrees(left). Therefore the right/left asymmetry in count rate is

$$R= (1 + PA)/(1 - PA) \qquad (1.5)$$

The signs of all polarisation values given in this work will conform with the Basel Convention [3]. Namely neutrons with spin pointing along the direction $\mathbf{k}_0 x \mathbf{k}_1$ are positively polarised.

1.4 Review

In the evaluation of phenomenological nuclear reaction models the goal has usually been to find phenomenological potentials which can reproduce total cross sections, differential cross sections and analysing powers . Successes which have been achieved have usually been over limited mass and energy range with cross sections generally

being more accurately reproduced. Attempts to produce global Optical Potentials have never been totally successful, and are really beyond the scope of a simple spherical OM . Where nuclear deformation or other collective effects are suspected, Coupled Channels calculations are more appropriate, but are rather long and involved, and have been attempted only rarely on neutron data. However the manner in which Optical Potential parameters vary may in itself be instructive. The comparative paucity of polarisation data has precluded large scale simultaneous cross section and polarisation analysis. The first extensive OM analysis on neutron data was carried out on Barschall's cross sections[4] measured in 1952 and the first analysis of analysing power data was produced in 1954 by Adair et al [5]. The following summarises some of the related low energy neutron scattering work which has been performed in the past seventeen years or so. As analysing power measurements are few and far between some work of this nature at slightly higher energy has been included.

1966 Ferguson et al [7]: analysing power at 55 degrees for 14 elements in mass range A=48-210 at energies 0.4, 0.7, 1.0 MeV. They compared their data with calculations using Perey and Buck's non-local potential [8] derived from lead data and obtained reasonable agreement given the large errors, except where nuclei are highly deformed.

1966 Becker et al [9]: differential cross sections over 20-130 degrees for 36 elements in mass range A=26-209 at energy 3.2 MeV. They were unable to find a set of global potential parameters which accurately reproduced cross sections for all nuclei. They also tried Rosen's parameters [11] with similar results

1967 Mahayan [10]: analysing power at 40,60 and 90 degrees for 20

elements in mass range 48-209 at energies 4.4, 5.0, 5.5 MeV. He found agreement with his data using Rosen's potential parameters [11] within the poor statistical accuracy of the data.

1968 Holmquist [14]: differential cross sections over 20-160 degrees for Al, S, Ca, Cr, Mn, Fe, Co, Ni, Cu, In, Bi in energy range 1.46-8.05 MeV. Time of flight neutron spectra. He optimised OM parameters for each element and obtained good agreement with his data even with light elements. He did not attempt a global potential but investigated the dependence of potential parameters on mass and energy.

1969 Ellgehausen et al [12]: analysing power over 30-138 degrees for elements Ti, Cr, Fe, Cu, Zn, Zr at energy 3.25 MeV. These are some of the most accurate analysing power measurements performed, in reasonable agreement with Rosen's parameters [11] for Ti, Cr, Fe and Cu. Poor agreement was found for Zr and there were discrepances at angles less than 60 degrees with Zn. Calculations account for competing compound nuclear scattering. Data by the same team [13] for light elements positively disagrees with the OM

1970 Pasechnik et al [15]: analysing power over 20-145 degrees for Ti and Cr at 3.25 MeV. Differential cross sections in energy range 0.3-4.1 MeV. They optimised potential parameters for the data produced.

1974 Zijp and Jonker [16]: analysing power over a maximum range of 30-150 degrees for 20 elements in mass range 48-209 at energy 3.2 MeV. They found reasonable agreement with the data of Ellgehausen et al. Optimised potential parameters gave good agreement with experimental data except for tungsten. Coupled Channels

calculations were tried.Other published potentials reproduced general trends but failed to give detailed agreement.

1977 Hussein et al [17]: analysing power and differential cross sections over 1.5-65 degrees for elements Pb and Bi at energy 10.4 MeV. The potential parameters of Becchetti and Greenlees [18] gave the best fit to their data. The Mott-Schwinger [19] interaction was also accounted for at small angles.

1977 Ramstrom and Goransson [20]: extreme backward angle differential cross sections over 130-174 degrees for elements Fe,Co,In,Bi at energy 7.5 MeV. This was an attempt to pin down the strength of the spin-orbit interaction.

1979 Galloway and Waheed [21]: analysing power and differential cross sections over 20-160 degrees for elements Fe, Cu, I, Hg, Pb at energy 2.9 MeV. They optimised potential parameters for each element but still had poor agreement with I, Hg and Pb analysing powers. Other published potentials gave general trends of Fe and Cu distributions.

1978/81 Smith,Guenther et al [22-26]: accurate differential cross sections for Fe, Ti, ^{107}Ag and ^{209}Bi over maximum energy range 0.25-4.5 MeV. They optimised parameters for each nucleus but were unable to reproduce strong fluctuations in cross sections of Ti and Fe at low energy. They also measured inelastic cross sections and compared predictions of Optical/Statistical and Coupled Channels calculations where direct inelastic scattering was suspected.

1979 Beghian et al [27]: differential elastic and inelastic cross sections for ^{238}U in the energy range 0.9-3.1 MeV. High resolution

time of flight spectrometry, sufficiently good to separate the ground and 45KeV first excited states. The results were compared with predictions of previous coupled channels calculations.

1981 Begum and Galloway [28]: analysing power and differential cross sections over 20-160 degrees for elements W, Tl, Bi, U at 2.9 MeV. Neither optimised parameters nor those previously published gave convincing fits to their analysing power data.

The single most extensive set of good quality data are probably Holmquists[12] differential cross sections and the most convincing analysing power measurements those of Ellgehausen et al [12] and Zijp and Jonker [16]. Extensive data analyses covering large ranges of mass and energy have been performed by Rosen [11], Becchetti and Greenlees [18] and Holmquist [14] amongst others, but not surprisingly better fits to individual data sets have been obtained with optimised parameters rather than with "semi-global" parameters. Optimised parameters often vary erratically from nucleus to nucleus and energy to energy, indeed sometimes taking on unphysical values. They are thus of limited use.

Determination of the strength of the spin-orbit interaction is especially vague. This is best done by measuring analysing power distributions or backward angle differential cross sections. To date, experiments of this type have been infrequent, particularly with heavy nuclei, and have sometimes produced contradictory results. The chosen samples W,Hg,Tl,Pb,Bi,U form a reasonable set, others being precluded because of non-availability and high cost. This also dictated the use of natural elements although Bi and U are mono-isotopic.

The analysing power data taken on these nuclei has so far not been very convincing, having poor accuracy, except at forward angles.

W:With tungsten the data of refs. 16 and 28 compares resonably for angles less than 50 degrees. Otherwise errors are too large to merit comparison.

Hg: The one known set of mercury data, [21], has poor accuracy, and is totally at variance with model predictions.

Tl:Refs. 16 and 28 broadly agree on thalium analysing powers. However the former only measured up to 75 degrees and both show poor accuracy at angles greater than 60 degrees.

Pb: With lead refs.16 and 21 show marked discepancy . The former only goes up to 75 degrees and the latter again has poor accuracy at larger angles.

Bi:With bismuth the data of ref.16 has relatively good accuracy, but in general the magnitudes of the analysing powers are much smaller than those found in ref.28, which except at forward angles are somewhat less precise.

U: The one known set of uranium data, ref. 28, is insufficiently accurate except at 20 and 34 degrees for quantitative comparison with theory.

As it is relatively easy to achieve good statistical accuracy on a differential cross section measurement, there is usually more of this data available. However for these nuclei it seems quite scarce around 3 MeV incident energy, although other measurements have been made at higher incident energies, noteably with lead [29]. Where more than one set exists, there is generally qualitative agreement, although in some cases points are scattered appreciably instead of lying on a smooth curve.

W: This last point is true of the tungsten data in refs. 9 and 28. Ref.28 suggests an unusually low cross section at backward angles, which could do with confirmation. A time of flight measurement [68] at slightly higher energy (3.4 MeV) on separated isotopes which manages to

separate elastic from inelastic neutrons also shows a comparatively low cross section at backward angles. This data shows very deep minima in the cross section not reproduced in the other two sets [9,28] which can at least in part be attributed to their inability to separate out inelastically scattered neutrons.

Hg: Refs. 9 and 21 broadly agree on mercury cross sections. However the behaviour at angles greater than 100 degrees is not well defined.

Tl: With thalium refs. 9 and 28 are in reasonable agreement, although confirmation of behaviour at angles greater than 130 degrees is required.

Pb: Refs. 9 and 21 agree on lead cross sections except around 130 degrees. Above this the data in ref.21 needs confirmation.

Bi: Up to 130 degrees refs.9 and 30 show reasonable agreement for bismuth. Ref.28 has considerably higher values in the range 50-130 degrees and disagrees with ref.30 above 130 degrees where only these two have data.

U: There is little agreement between refs. 27 and 28 above 50 degrees for uranium cross sections. Ref. 27 has probably the better data, having had sufficiently good energy resolution to separate the 45 KeV 1st excited state, but has not measured at many angles.

The present measurements are intended to provide analysing power and differential cross section data of sufficient accuracy to make quantitative comparison with model predictions for heavy nuclei at 3.0 MeV. This is about the highest energy which may be obtained using the $^{2}H(d,n)^{3}He$ reaction and a 500KV accelerator as a source of partially polarised neutrons. At this energy compound elastic scattering cross sections are considerable and due allowance has to be made using Hauser Feshbach [31] theory or its derivative by Moldauer [32] accounting for level width fluctuation. This type of analysis may however be inadequate for permanently deformed nuclei such as the common isotopes

of tungsten and ^{238}U where coupled channels calculations [33] have been used.

The following chapters present a detailed description of the experimental system built up to perform these measurements, the procedures for collecting and correcting the raw experimental data and finally comparison of results with the predictions of Optical/Statistical and Coupled Channels calculations

Chapter 2

The Neutron Polarimeter

2.1 Introduction

In order to make this series of measurements a completely new neutron polarimeter was constructed as well as associated instrumentation and control systems. The basic experimental geometry has the neutron detectors deployed in a ring about the scattering sample. The detectors are sited in equal angle pairs for left, right scattering asymmetry measurement. Accurate determination of this quantity requires variation in detection efficiency to be cancelled by interchanging left and right detectors. This may be performed by precessing the incident neutron spin through 180 degrees in a magnetic field [16], or by physically interchanging the detector pair [34]. The former has the disadvantage that stray magnetic fields, which can never be totally suppressed, may effect photomultipliers, while movement of the detectors in the latter may also cause disturbance. It has however been used successfully with other neutron polarimeters [34,35] built in this laboratory and thus was used for this project.

2.2 Construction

The polarimeter is constructed almost entirely of aluminium alloy for lightness and to eliminate stray magnetic fields, sometimes encountered with steel components, which can upset photomultipliers. Its front, side and top aspects can be seen in figures 2.1, 2.2, 2.3. Figure 2.11 shows a photograph of the polarimeter in its experimental situation surrounded by shielding. It can mount a maximum of 24 scintillation counters on two scattering tables, which lie parallel to the reaction plane, and which are rotatable about a vertical axis passing through the scattering sample. This enables the scattering

NEUTRON POLARIMETER FRONT VIEW

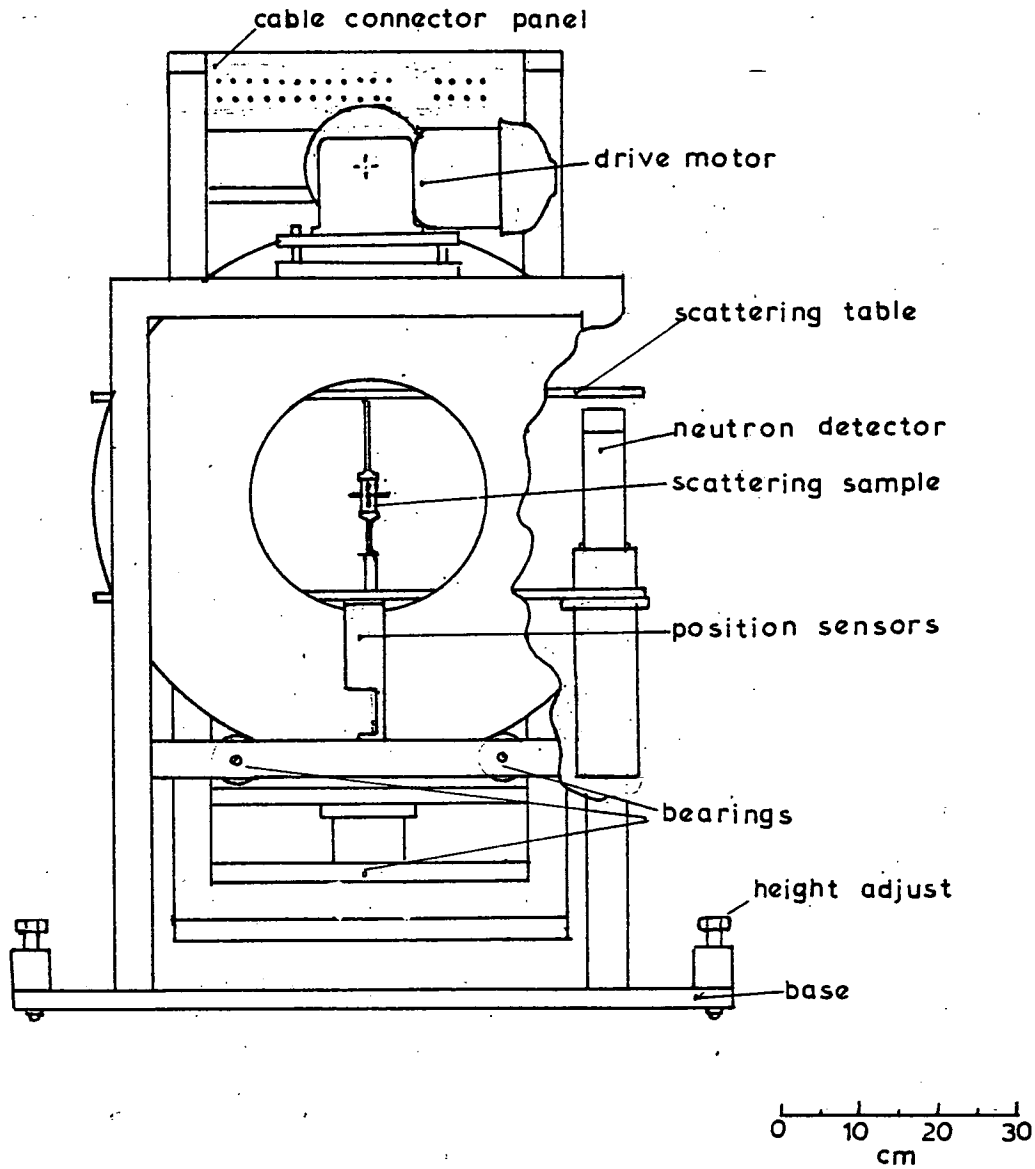

Figure 2.1

NEUTRON POLARIMETER SIDE VIEW

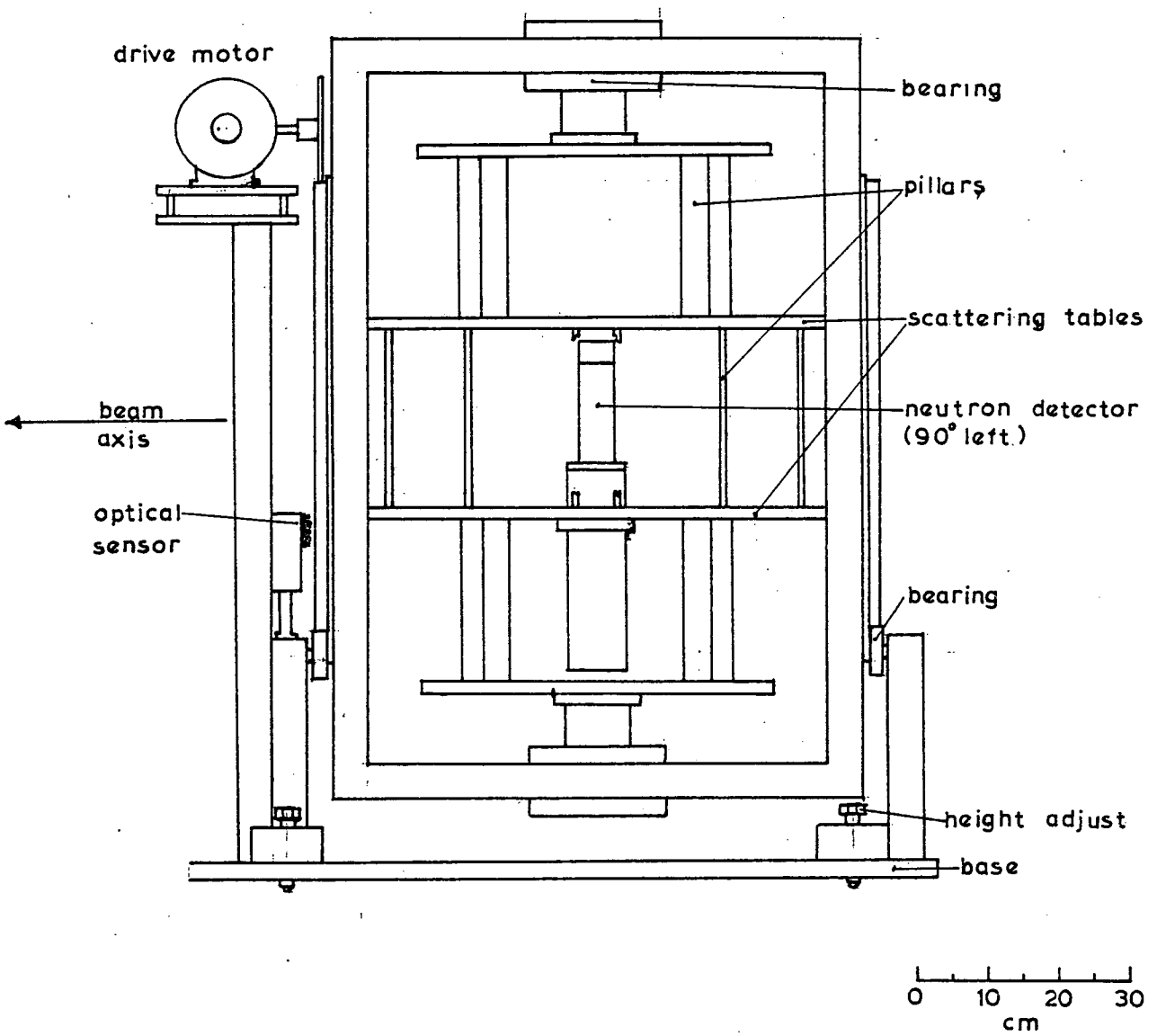

Figure 2.2

NEUTRON POLARIMETER TOP VIEW

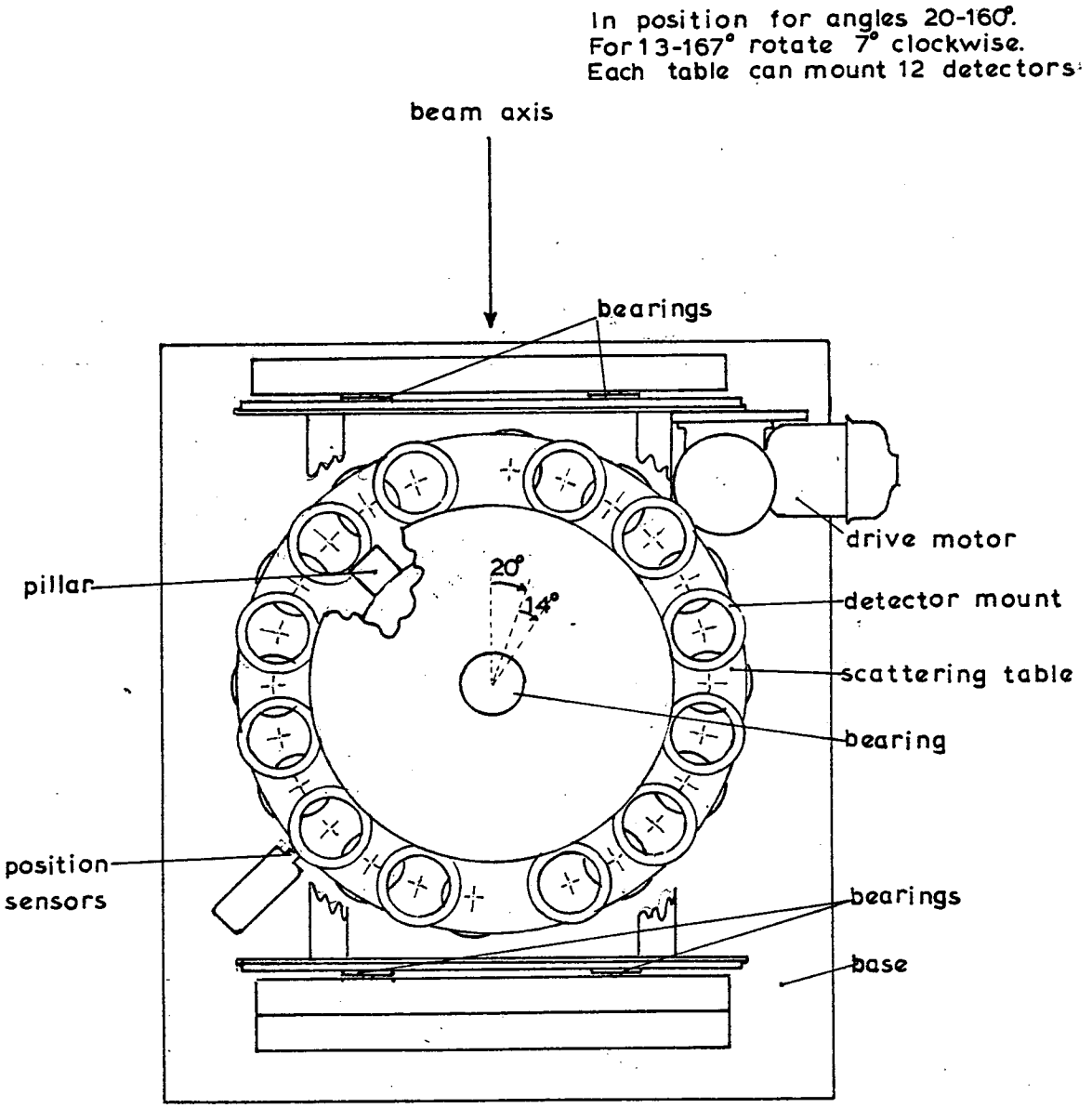

Figure 2.3

angle at which the detectors sit, to be varied, and also allows detectors to be rotated into the neutron beam. This is necessary to the determination of relative detection efficiency which has to be known when finding differential cross sections. The maximum angular range covered is 13-167 degrees in 7 degree intervals. As only 12 angles may be used simultaneously, this is covered by two positions, one spanning 20-160 degrees in 14 degree intervals, the other spanning 13-167 degrees in 14 degree intervals. The sample itself is attached to a pneumatic piston so that it can be retracted remotely from the in-beam position, enabling background counts to be taken. The frame which holds the scattering tables rotates with respect to the polarimeter base plate which is adjusted so that rotation is about the axis defined by the neutron collimator. Alignment is performed optically using pin-hole inserts in the collimator and polarimeter end plates. Rotation through 180 degrees interchanges left and right detectors so as to cancel any differences in efficiency when measuring the left/right asymmetery in scattered neutron intensity. Four ninety degree spaced orientations are provided, the extra two positions setting detectors perpendicular to the reaction plane. In this configuration there should never be any left/right asymmetry , any measured being a systematic fault. The two orientations where the scattering tables lie parallel to the reaction plane are designated orientation A and B. In figure 2.1 the polarimeter is shown in orientation A. Twenty-seven positions are provided for the scattering table rotation, three counting positions and 24 in-beam positions. For all rotations automatic drive is by geared down reversible AC electric motors via a rubber ring clad pulley. This allows some slip should anything become snagged.

2.3 Motor Control Electronics

Position sensing is by slotted optical sensors. These are switched off when the infra red radiation passing from a photo-diode to a photo-transistor is interrupted by a small black plastic tab. Four are used for the beam axis rotation, one for each position, and five for the scattering table rotation giving the 5 bit binary code for each position. To initiate a position change the appropriate bit pattern is selected remotely, the command is given to start (a positive going pulse) and the motors drive until the bit pattern is replicated by the optical sensors. Comparison is made and correct drive direction selected by 74 series TTL logic circuitry (figure 2.4) situated at the polarimeter. In order to stop the motors overrunning a short reverse thrust is provided by the circuitry when the correct position is reached. The position of the scattering tables after rotation was thought to be fairly critical and so this is also defined mechanically by a solenoid activated tab which engages in a slot at the edge of one of the tables. This is AC powered so that no permanent magnets are produced. Fast AC switching for the motors is provided by triac devices interfaced optically to the TTL outputs.

2.4 Pulse Electronics

Pulse shaping, amplification, and neutron/gamma discrimination is performed for each detector by a double width NIM module (figure 2.5) known as a neutron selector. The basic design of the electronics is identical to that developed by H Davie [36], but with the updating of many of the components and use of printed circuit boards, the space occupied has been somewhat decreased. A block diagram of the electronics is shown in figure 2.5. Amplifiers are of conventional op-amp based design with shaping done by RC differentiation and integration. Neutron/gamma discrimination is by the "zero cross over"

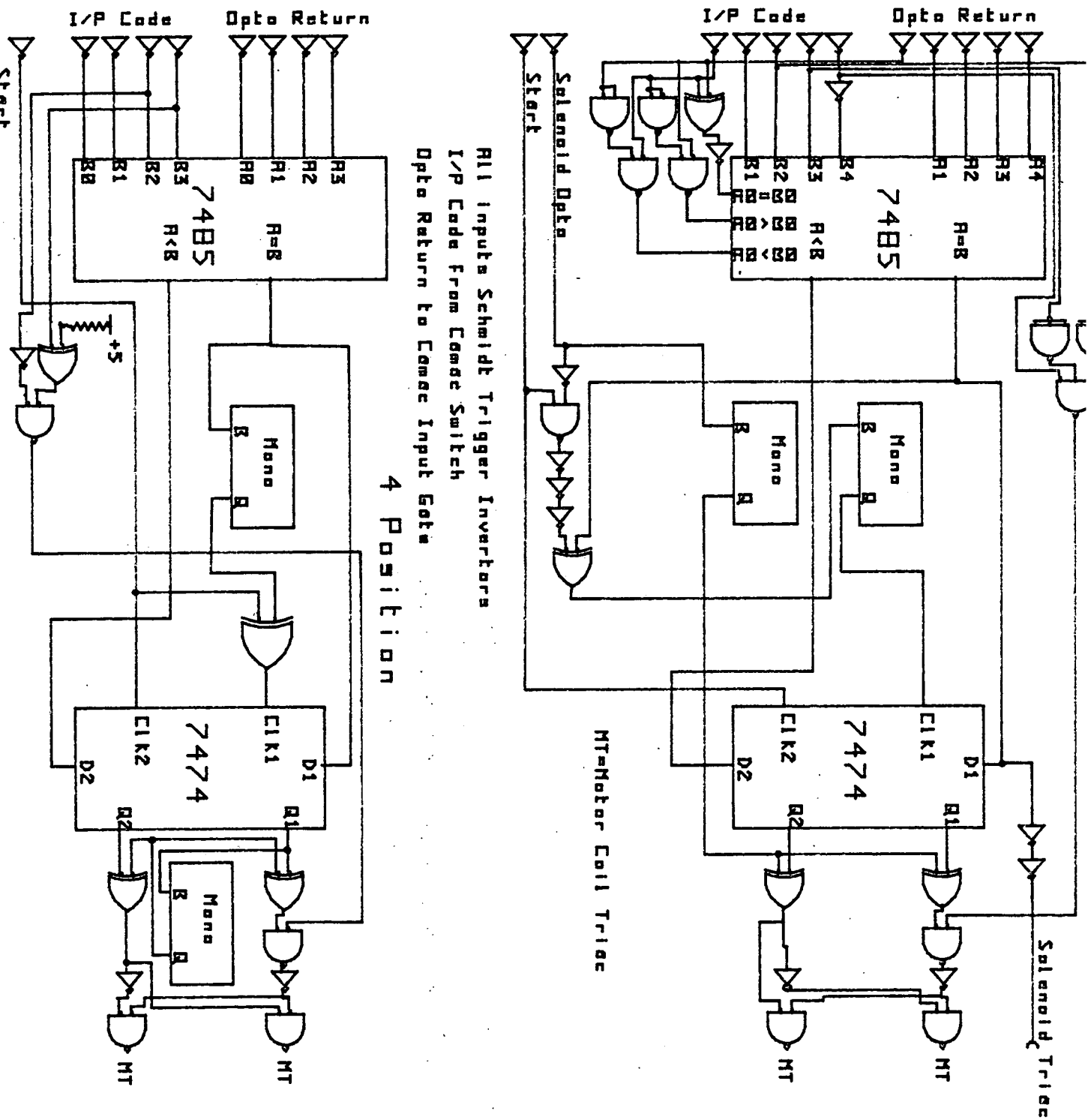
I/P Code
Opto Return
Start
Solenoid Opto
7485
A=B
A<B
Mono
7474
Clk1
Clk2
D1
D2
Q1
Q2
MT
MT=Motor Coil Triac
Solenoid Triac
All Inputs Schmidt Trigger Inverters
I/P Code From Comac Switch
Opto Return to Comac Input Gate
4 Position

Figure 2.4

PULSE ELECTRONICS

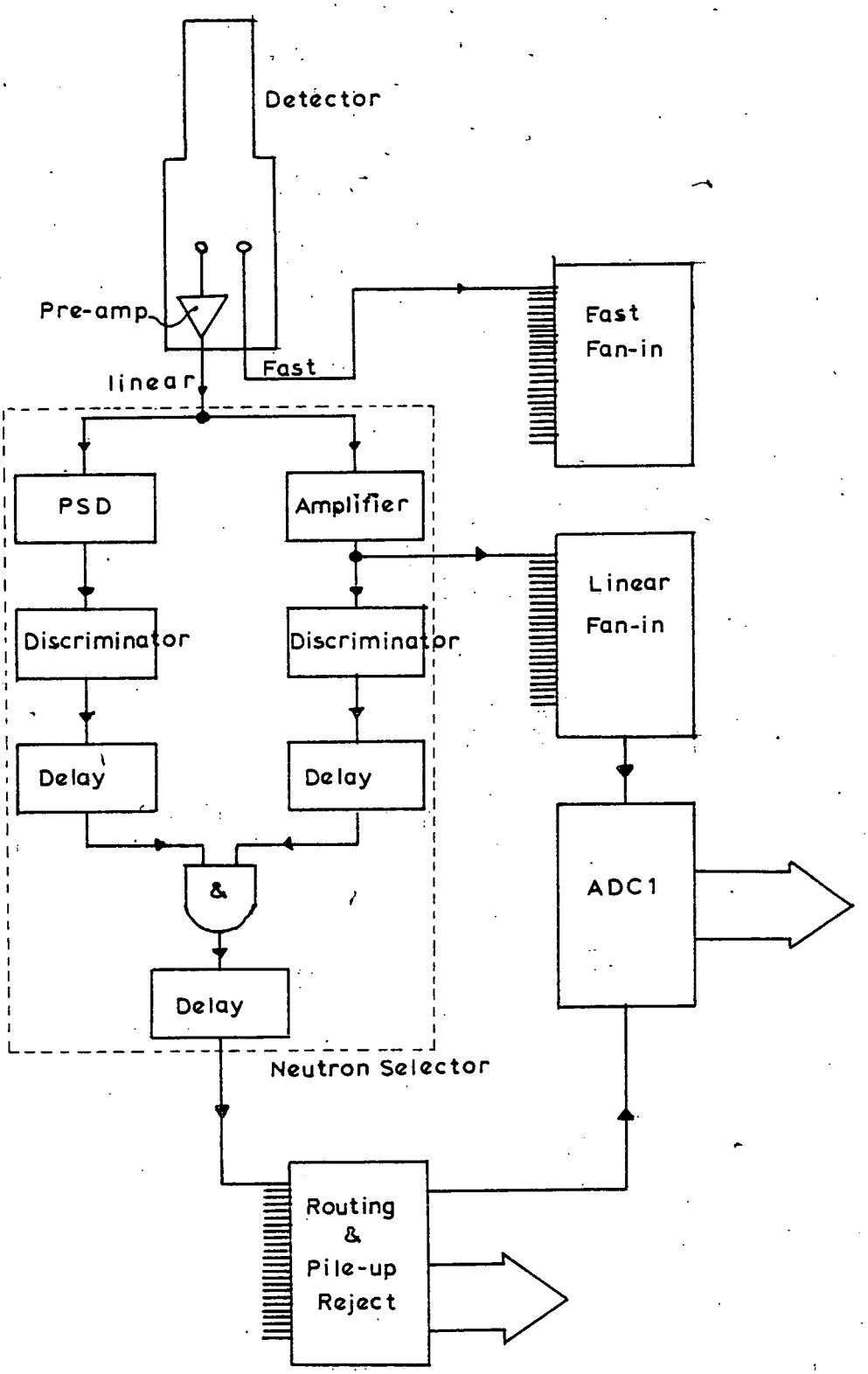

Figure 2.5

method [37] of pulse shape discrimination (PSD) . Ionisation and excitations produced in the scintillator by proton recoil (neutrons) gives rise to pulses with a longer fall time than those produced by electrons (gammas). When double RC differentiated, these pulses take longer to return to the zero voltage axis. After the time differences have been converted to voltage differences by a simple time to height converter, discrimination may be performed. Outputs of amplifier and PSD circuits feed into leading edge discriminators whose outputs can be set so that their logical AND denotes detection of a proton recoil of energy above the preset value. Amplifier outputs are also fed via a linear fan-in unit to a Laben 256 channel ADC for pulse height analysis. The fan-in is a simple resistive network to which has been added an op-amp in order to provide a more convenient pulse height for the ADC. The accumulation of noise and "glitches", caused by logic gates switching, on the amplifier outputs was sometimes enough to trigger the ADC. This did not result in spurious counts being made as the coincident conversion start pulse was not provided by the pulse routing logic circuitry. However using 4μs rise time protection this increased system dead time markedly. A simple chopping circuit was added so that only "real" pulses were allowed through.

2.5 Polarimeter Control Hardware

The polarimeter is controlled remotely by a PDP11/Camac system which includes some custom built pulse routing and interfacing. It is developed from one built up by F.K.McNeil-Watson to control a 12 detector polarimeter [38]. A block diagram of the system is shown in figure 2.6.

Logic pulses from a maximum of 24 neutron selectors feed into a custom built routing and pileup reject network (figure 2.7). Only one ADC is used to service the polarimeter's detectors and so pulses have

POLARIMETER CONTROLL

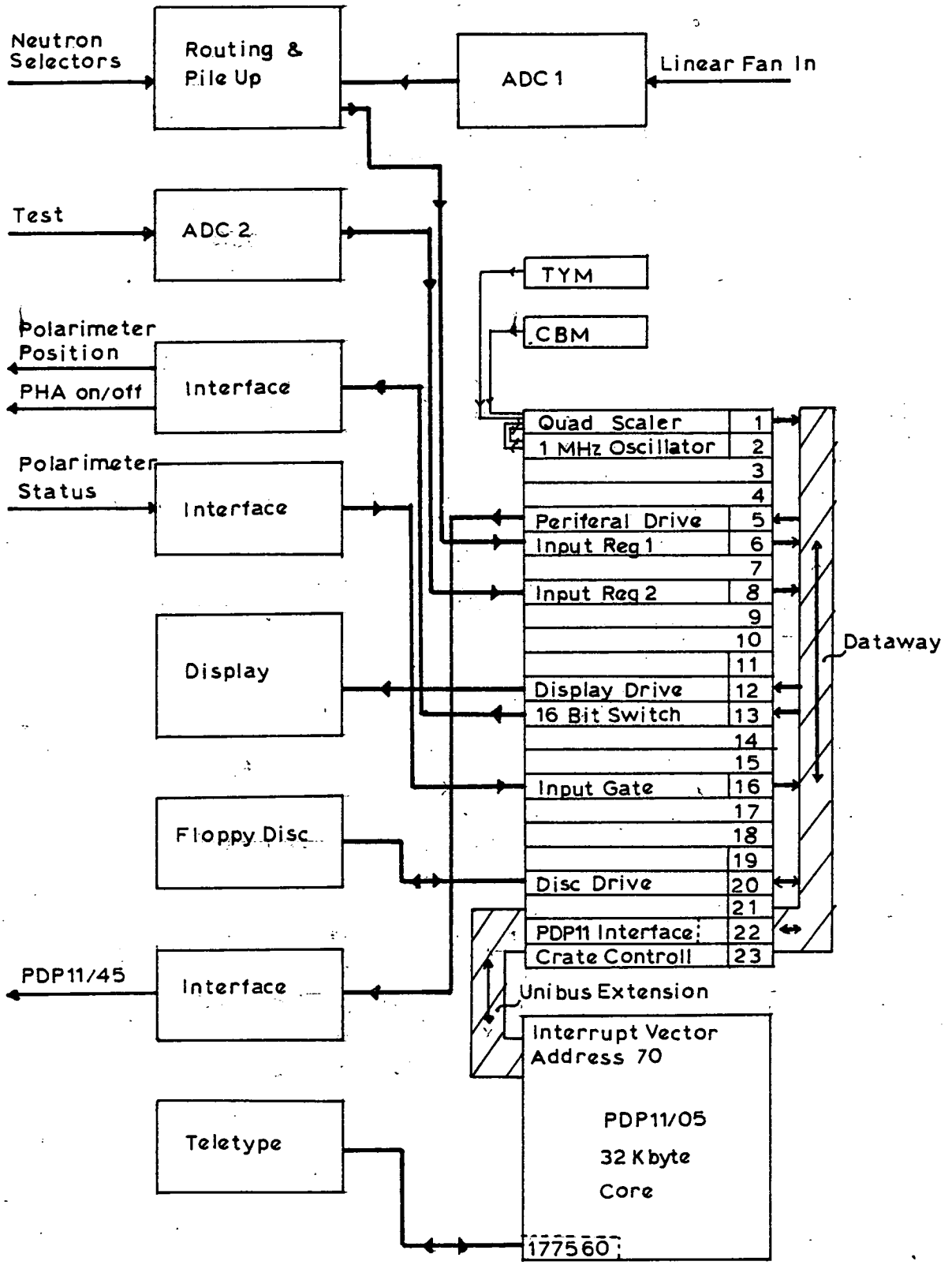

Figure 2.6

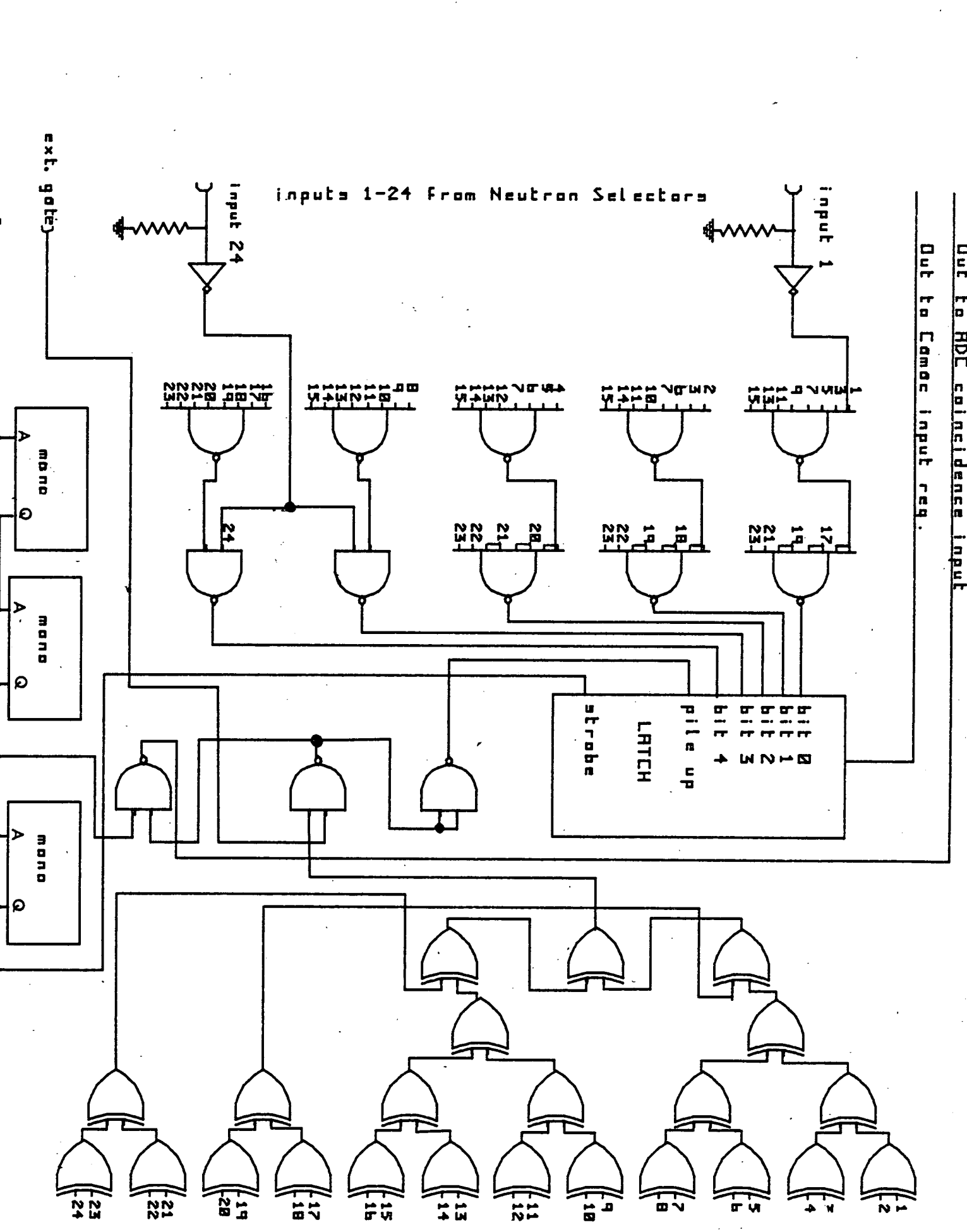
inputs 1-24 From Neutron Selectors
input 1
input 24
ext. gate
Out to Camac input reg.
Out to ADC coincidence input
LATCH
strobe
pile up
bit 4
bit 3
bit 2
bit 1
bit 0
mono
A
Q

Figure 2.7

to be identified. This is achieved by a network of NAND gates which produces the 5 bit code corresponding to the active(high) input 1-24. However if two or more inputs are simultaneously active, misrouting will occur. Pileup is detected by the EXCLUSIVE OR network whose output goes low for all combinations of 2 and some combinations of 3 simultaneous active inputs. This is used to gate the conversion start pulse within the ADC, and so pileup events are not counted, except for those which manage to beat the EXCLUSIVE OR network. As most of the neutron detectors are fairly close to eachother, most of the pileup comes from neutrons scattering out of one detector into another. Doubles events are rare compared with singles, and triples negligible.

The 5 routing bits and one pileup reject bit are latched, as are the 8 bits from conversion of the linear fan-in pulse height. The total dead time output which switches low signaling a pulse for convertion at the ADC is used, after being suitably delayed, to strobe the latch. The bits are then transferred to a Camac Parallel Input Register of type NE7014 which acts as a storage buffer, making a request for servicing to the CPU, while at the same time releasing the ADC and routing systems so that dead time is not prolonged. The 5+8 bits are used to calculate an address in core memory, with the routing bits most significant. Normally the full 8 bit resolution of the ADC is not used, 6 being prefered as core space is limited, conversion is 4 times faster and proton recoil spectra, having no peaks or valleys, do not require more than 64 channels. An identical ADC feeding direct to a NE 7014 register gives a pulse height analysis facility useful in testing and adjustment of detectors and neutron selectors, as for example with the detector light output tests described in Chapter 3.

A DEC PDP11/05 with 16K words of core memory attached to a single Camac crate is dedicated to the 24 detector polarimeter. A block diagram is shown in figure 2.6. It has proved very reliable, sometimes

running continuously for months at a time. Standard input/output is by an ASR 33 teletype which includes a punched tape reader for the input of system programs. Other in/out functions are performed via the Camac crate. Spectra stored in core may be viewed on a 19 in screen controlled by a NE 7011 display driver. An 8in floppy disc drive and controller built by McNeil-Watson [39] provide extra storage space for spectra and programs. Transfer of data to a PDP11/45 and hence large mainframe machines is by a NE 7065 Peripheral Driver and small custom built interface. Control of the polarimeter orientation ADC's and scalers is by a NE 7066 Switch extended from 12 to 16 bits by the inclusion of 4 reed relays. This unit was originally used with a system which had microswitch position sensors. With the present system contact bounce on the switching relays had to be suppressed before command levels were fed to TTL orientated circuitry. Polarimeter status, from optical sensors, is fed in via some interfacing by an NE 7060 Input Gate.

The system clock consists of a 1MHz oscillator feeding into one channel of an NE 9021 Quad Scaler. Neutron target flux monitors feed the other channels. Finally the crate and 11/05 buses are interfaced by a NE 9030/9032 Controller.

2.6 Software

Of the 16K words of core memory, 10K is dedicated to data storage and 6K assigned to system programs. Programs are initially fed in on paper tape and may then be held on disk. The normal system program occupies 5K of space, starting at address 1000 octal. Lower locations are held as trap vectors and storage space for the stack. Under normal circumstances the program sits at command level, waiting for a keyboard command, or interrupt from some other peripheral, whereupon it jumps to the appropriate routine, returning to command level on completion. Keyboard commands consist of two character mnemonics, for example "*C"

means restart pulse height analysis. On receipt of two characters, the table of available commands is scanned, and if a match is found, the program jumps to the address specified in the corresponding table of system routines.

2.6.1 Priority Structure

As several peripherals may request servicing simultaneously, each input/output function is assigned a priority level, which is in the main set by the software. Thus the CPU may arbitrate between competing functions according to which has the greatest need or importance. The structure is as follows.

1:All polarimeter position change movements

1:Transfers to and from disk

1:Transfers to and from PDP11/45

2:Clock scaler overflows

3:Other scaler overflows

4:Input register 1 from polarimeter detector ADC

5:Input register 2 from auxiliary ADC

6:Display

7:Teletype

Functions labeled 1 cannot be interrupted once started, until they have completed or a failure condition causes premature exit. During this time the keyboard is disabled. Functions labeled 2-6 come via the Camac Crate which interrupts at vector address 70 octal. The interrupt initiates a scan of the Camac device "Look At Me" flags, starting with 2 and ending with 6. At the first flag found to be set the program jumps to the appropriate service routine. On completion, return is made to whichever process was running before interrupt. Class 1 functions do not do this but always return to command level.

2.6.2 Polarimeter Movement

The various polarimeter orientations are described in section 2.1, and remote position commands are made via the 16 bit switch. The routine first checks that the polarimeter is in a recognised position. If not it fails and returns to command level. If so it gives the appropriate position change command and then sits in a loop waiting for the correct position response via the Camac Input Gate. It does this up to a preset time when, if the correct position has not been reached, motor drive is cut and an error signaled. This saves the drive burning itself out should anything have become stuck. Provision is made for sequencing position changes, as is performed in an experimental run. The desired sequence of left, right detector interchanges, scattering sample in and out of beam and frequency of detector calibration may be typed in at the start of a run. Thereafter no further manual intervention is required in the data collection process, barring equipment failure.

2.6.3 Data Storage

The 10K 16 bit words of data store is divided into 5 areas of 2K, which in turn may be subdivided into sub-areas of 1K, 512, 256, 128 or 64 words. Thus area and sub-area may be specified for purposes of spectrum input, display, output or numerical analysis. In an experimental run area 5 is reserved for detector efficiency calibration data, while areas 1-4 store data taken in polarimeter orientations A and B, both with scattering sample in and out of beam. For test runs any area may be used with any orientation.

2.6.4 Pulse Height Analysis

Three modes of pulse height analysis are provided. ADC 1 services the polarimeter detectors, ADC 2 services test equipment and both ADC's together provide a bidimensional facility. Mode 1 gives routed spectra of either 64, 128 or 256 channels apiece, set by the

switch on the ADC which specifies 6, 7 or 8 bit resolution. Because of lack of core space, 24 detectors can only be used with 64 channel spectra. Routing, ADC and pileup information is taken from the input register. A check that pileup is not set and that routing bits do not amount to more than 24 is then made. If all is well the information is left shifted, i.e. multiplied by 2, since PDP11's calculate address on the basis of bytes, and added to an offset which specifies the start of a data area. The modified information gives the core address to be incremented. Checks were made on the amount of mis-routing which occurred. Even at high count rates, when the proportion of mis-routed events increases, this was about one in a thousand, and less than one in ten thousand at normal experimental count rates. During detector calibration only counts from the detector directly in beam are accepted, as neutrons transmitted through that detector may be counted by other detectors. A multiscaler option, as used in detector stability tests described in 3.3, is also available. In this case ADC bits are ignored and counts stored to double precision (32 bits) . The offset is incremented after each run so that the number of counts for each run is stored separately.

Mode 2 gives 64, 128 or 256 channel spectra which may be placed anywhere in data store by specifying area and sub-area. This determines the offset which is added to the information from ADC 2.

In bidimensional mode information from both ADC's is combined to produce an address for incrementation. The first 7 bits are taken from each giving a total of 8K channels for the spectrum. A check that both LAM flags are simultaneously set is made and singles events rejected.

All pulse height analysis routines have been made as short and concise as possible in the intrests of speed.

2.6.5 Other Peripheral Input/Output

The 8 inch floppy disk provides an extra 256Kbytes of storage

space. This is divided into 76 tracks, each of which is divided into two sectors. Data may be read or written in blocks of 2K words, i.e. one data area. This is done in two gulps, 1K of data into each sector. Thus the total 10K of data occupies 5 tracks. Data is checked after each 1K gulp, and up to 10 attempts are allowed before the routine fails.

Data transfer to the Edinburgh Physics Department PDP11/45 may be performed in blocks of 64,128,256, 1K, 2K or 10K words. A data checking and receiving program has to be run simultaneously on the PDP11/45. The 11/05 routine terminates unless a handshake signal is received within 2 sec of sending data.

The display shows data blocks of 64,128, 256, 512 or 1K words. As it has low priority its use does not effect pulse height analysis, and the scan is noticeably slowed when count rates are high.

2.6.6 On Line Analysis

In order to provide a measure of progress in data collection so that further amounts of running time necessary could be assessed, a routine to calculate neutron polarisations and polarisation statistical errors was added to the system program. This proved invaluable eliminating the need for tedious manual calculations, or alternatively the need for back-up computing power, frequently not available. The routine makes use of a modified version of the DEC floating point software package [40]. Data for the calculations is taken direct from the scattered neutron spectra, integration limits being set beforehand, and calculations can be made at any time during a run as they operate at keyboard priority.

2.7 Further Developement

An NE 9080 Camac Buffer Memory unit has been aquired, which contains 16K 24 bit words. It is planned to use this as the main data store, freeing the PDP11 core for running system programs. Direct

memory access will be possible with this unit, which should speed up pulse height analysis and allow programs to be run at the same time without any interference. New interfacing, pulse routing and address calculating boards are currently being constructed to enable its use with the system.

2.8 The Neutron Producing Target and Shielding

The target consists of a deuterium impregnated titanium strip on a copper backing . This is soft-soldered to a water-cooled finger [41] and is capable of supporting over 50μA of DC beam current at 500KeV. The active area is approximately 5mm by 3mm so that the incident beam must be well focused for maximum yield. The end of the finger makes an angle of 45 degrees with the beam direction as shown in figure 2.8 . This allows slight movement of the beam in the horizontal plane, which happens if the accelerator voltage varies slightly, without throwing the neutron source off the collimator axis. The whole of the target assembly is flexibly mounted on the end of the beam line so that accurate alignment on the collimator axis may be made. Deuterons are provided by a voltage stabilised 500KV Van de Graaff which is capable of running continuously for periods upwards of one week under good conditions. It incorporates additional automatic shut down circuitry so that it may be run without supervision for periods of several hours. Experimental runs were made at 390KV with maximum beam current available and not less than 25μA on target. Carbon deposits on the target material, from vacuum pump oil, caused some problems and prior to striking the target the beam passes through a liquid nitrogen cooled copper tube.

Taking recent Ti stopping power data [42,43] and hydrogen stopping power data [44], target thickness was calculated as 175 KeV at 390KeV incident energy. Using a Q value of 3.26MeV for the $^{2}H(d,n)^{3}He$

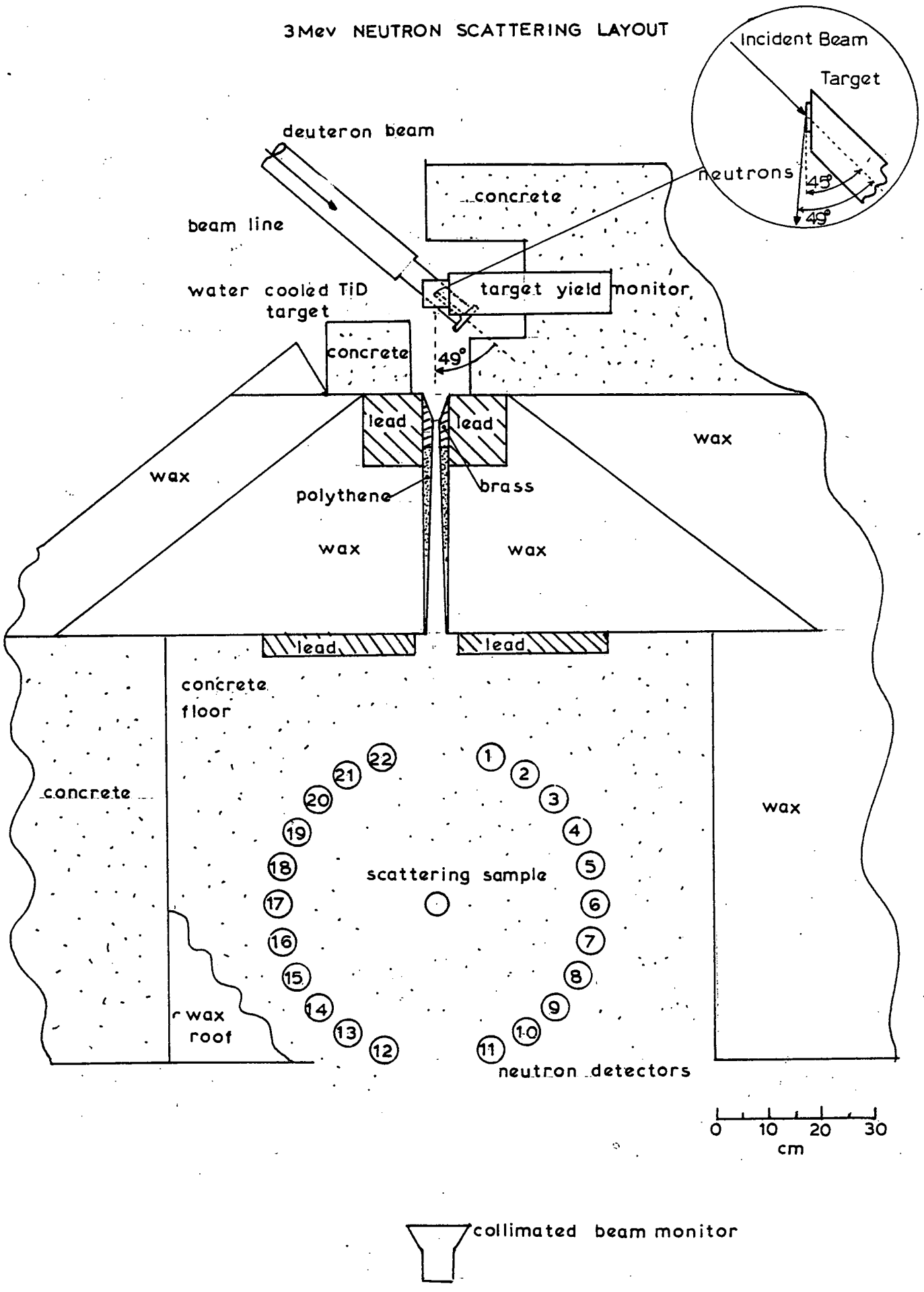
3Mev NEUTRON SCATTERING LAYOUT
Incident Beam
Target
neutrons
45°
45°
deuteron beam
beam line
concrete
water cooled TiD target
target yield monitor
concrete
49°
lead
lead
wax
wax
polythene
brass
wax
wax
lead
lead
concrete floor
concrete
wax
wax roof
scattering sample
1
2
3
4
5
6
7
8
9
10
11
12
13
14
15
16
17
18
19
20
21
22
neutron detectors
0 10 20 30
cm
collimated beam monitor

Figure 2.8

reaction, this produces neutrons with average energy 3.0MeV and a spread of about 0.2MeV. In reality target thickness will probably increase as drive in deuterons accumulate in the copper backing, but as the object was to make energy averaged measurements on heavy nuclei , the precise determination of this was not considered important. Using available Ti and H stopping power data and the energy dependence of the D,D reaction [67], the shape of the neutron energy spectrum was estimated (figure 2.9). The accumulation of drive in deuterons would tend to put a low energy tail on the spectrum, and reduce the average energy marginally.

Massive shielding of paraffin wax and concrete is deployed about the polarimeter as shown in figure 2.8. A circular cross section throated collimator of brass and high density polythene is used which produces quite a well defined beam . A profile was taken using a 3mm thick stilbene crystal mounted on a 56AVP photomultiplier. Stilbene counts were corrected for variations in neutron flux produced in the target. As can be seen from figure 2.10, the beam cut off is quite sharp and there is also a slight anisotropy in flux which can be attributed to variation in the D,D differential cross section around 49 degrees .

Two neutron flux monitors record the target output during a run. One is positioned directly in the collimated beam behind the polarimeter, the Collimated Beam Monitor (CBM), and the other built into the shielding directly above the target, viewing the target through a one inch diameter collimator. The latter is designated the Target Yield Monitor (TYM). It was mounted thus to cut down spurious counts which occur when stray deuteron beam hits part of the beam line. After long periods of running the metal beam line contains a considerable amount of deuterium, and the neutron flux produced can be quite large. The CBM is a 12cm diameter by 5cm long cylinder of NE213

coupled to a EMI 9814B photomultiplier, and the TYM a 5cm diameter by 5cm long cylinder of NE213 coupled to a 56AVP photomultiplier. Both employ similar electronics to those used with the polarimeter detectors described in chapter 3, with PSD against gamma rays.

12/03/82 Energy Spectrum of D,D Neutrons

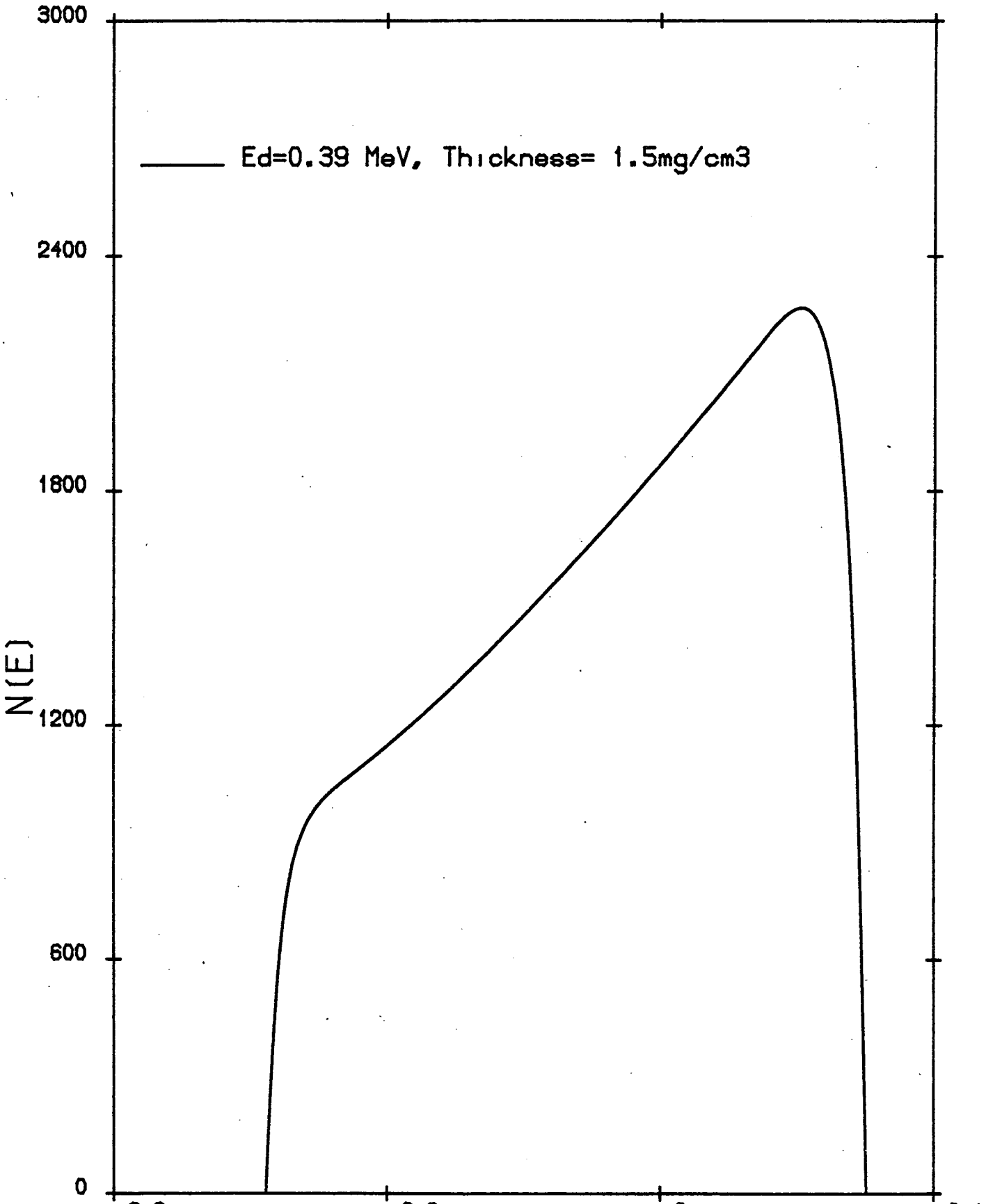

Figure: 2.90

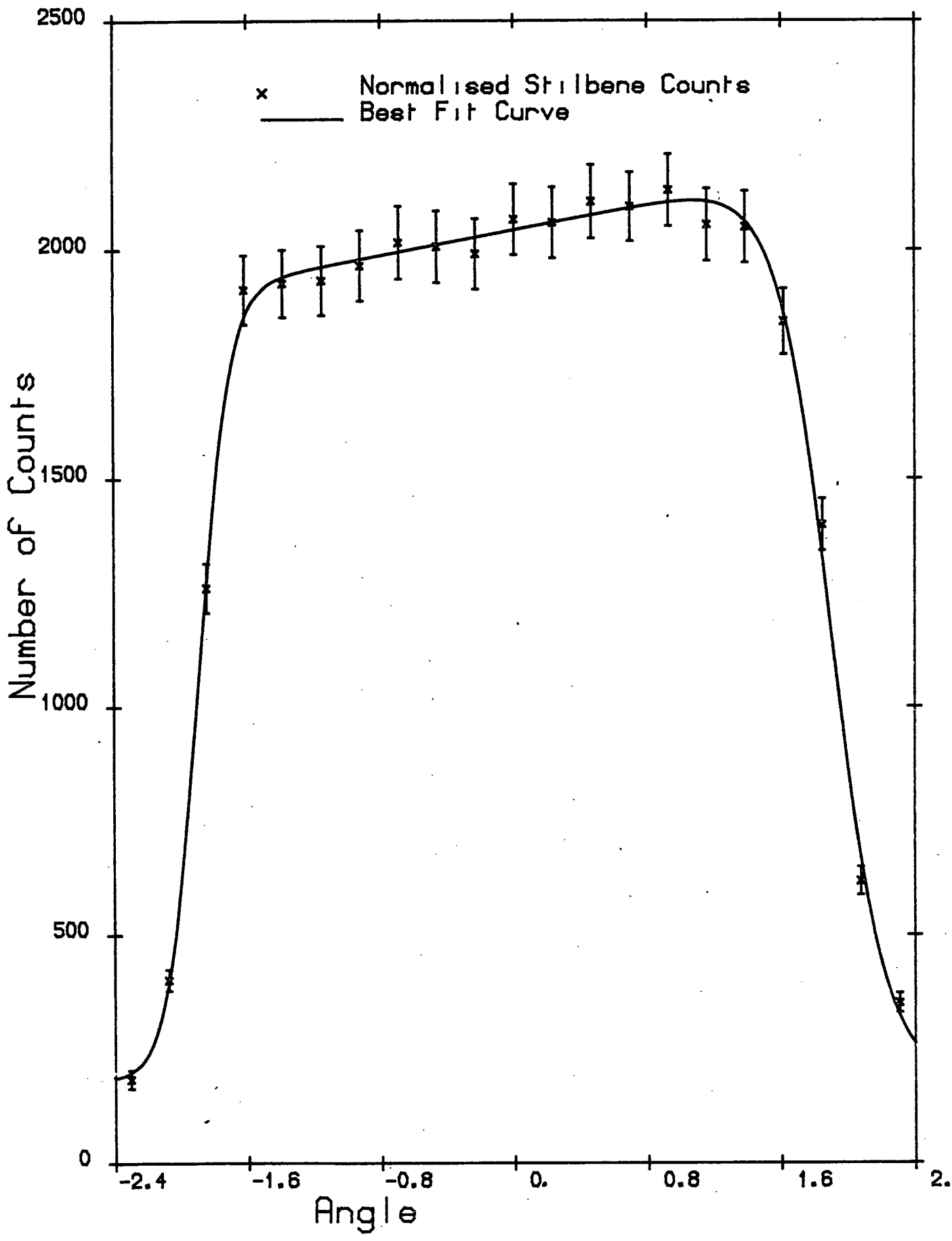
09/09/82 Beam Width=1.89+-0.03 degrees
Normalised Stilbene Counts
Best Fit Curve
Number of Counts
2500
2000
1500
1000
500
0
-2.4
-1.6
-0.8
0.
0.8
1.6
2.4
Angle

Figure: 2.10

THE NEUTRON POLARIMETER

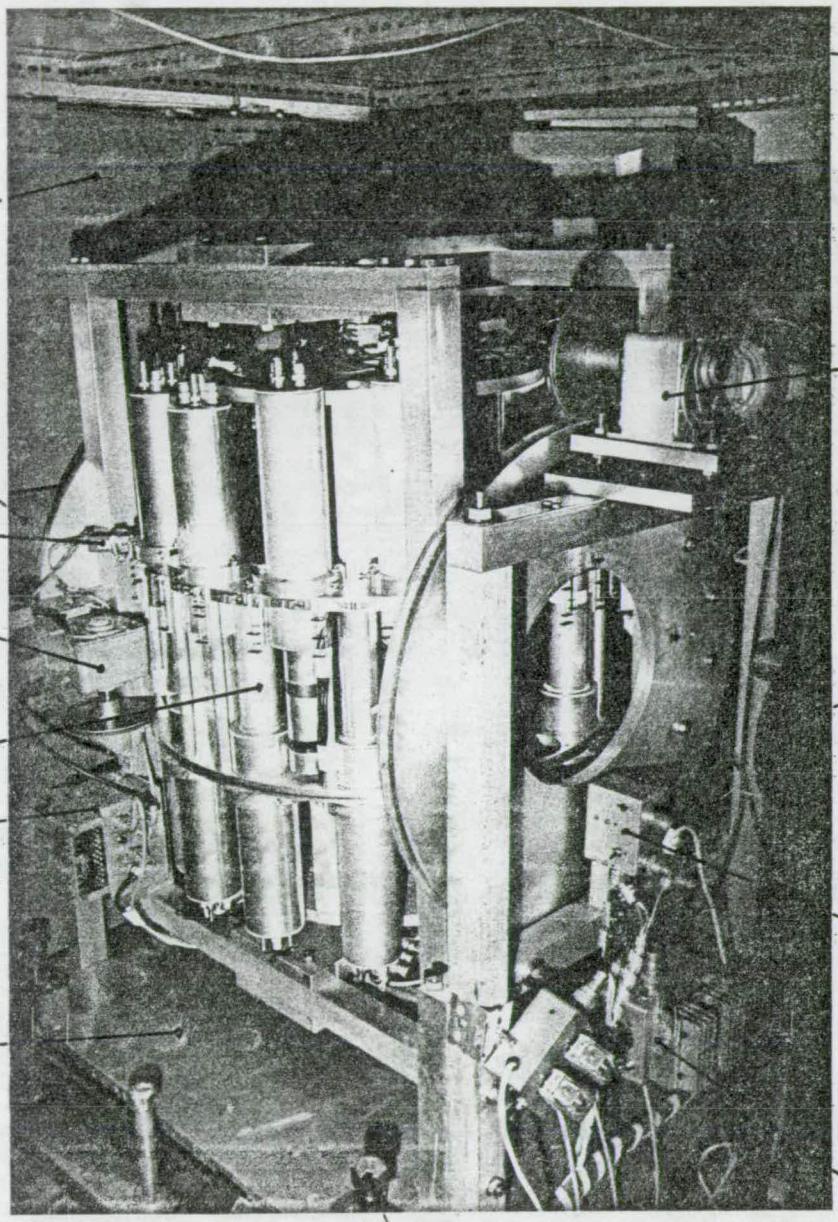

Figure 2.11

Chapter 3

Neutron Detectors

3.1 Description

The neutron detectors are liquid scintillation counters which consist of a 15.4 cm long by 2.5 cm radius aluminium cylinder, containing NE213 liquid scintillator, optically coupled to a fast linear focused type photomultiplier tube. The inside of the cylinder is coated with a highly reflective TiO_2 based paint. Cable driving ability, important when the rig is remote from pulse processing electronics , is provided by a simple compound emitter-follower pre-amplifier. All of this is enclosed in a light-tight aluminium tube as shown in figure 3.1.

The photomultipliers used are of type EMI 9814B and Mullard 56AVP with voltage dividers as shown in figure 3.2. Both have similar spectral response and electron transit time spread. The 14 stage 56AVP delivers more current at the anode, but the 9814B was found to be entirely adequate. Each voltage divider chain draws roughly 1mA at 2KV, which is adequate to ensure pulse height stability under the range of count rates encountered . Scattered neutron count rates are very low, but upwards of 2500 counts per second may be had when detectors are rotated in beam for calibration. HT is provided by a common 30mA Fluke supply. Differences in photomultiplier gain, caused by differences in photo-cathode quantum efficiency, are smoothed out by adding a resistor in series with the divider chain, thus reducing anode potential. A common 24V supply powers the pre-amplifiers. Output voltage pulses are developed across resistors at the anode and 10th (12th 56AVP) dynode, which with the stray capacitance present at these points, effectivly form an RC integration network. Dynode 10(12) gives a highly linear positive pulse for the taking of proton or electron

LIQUID SCINTILLATION COUNTER

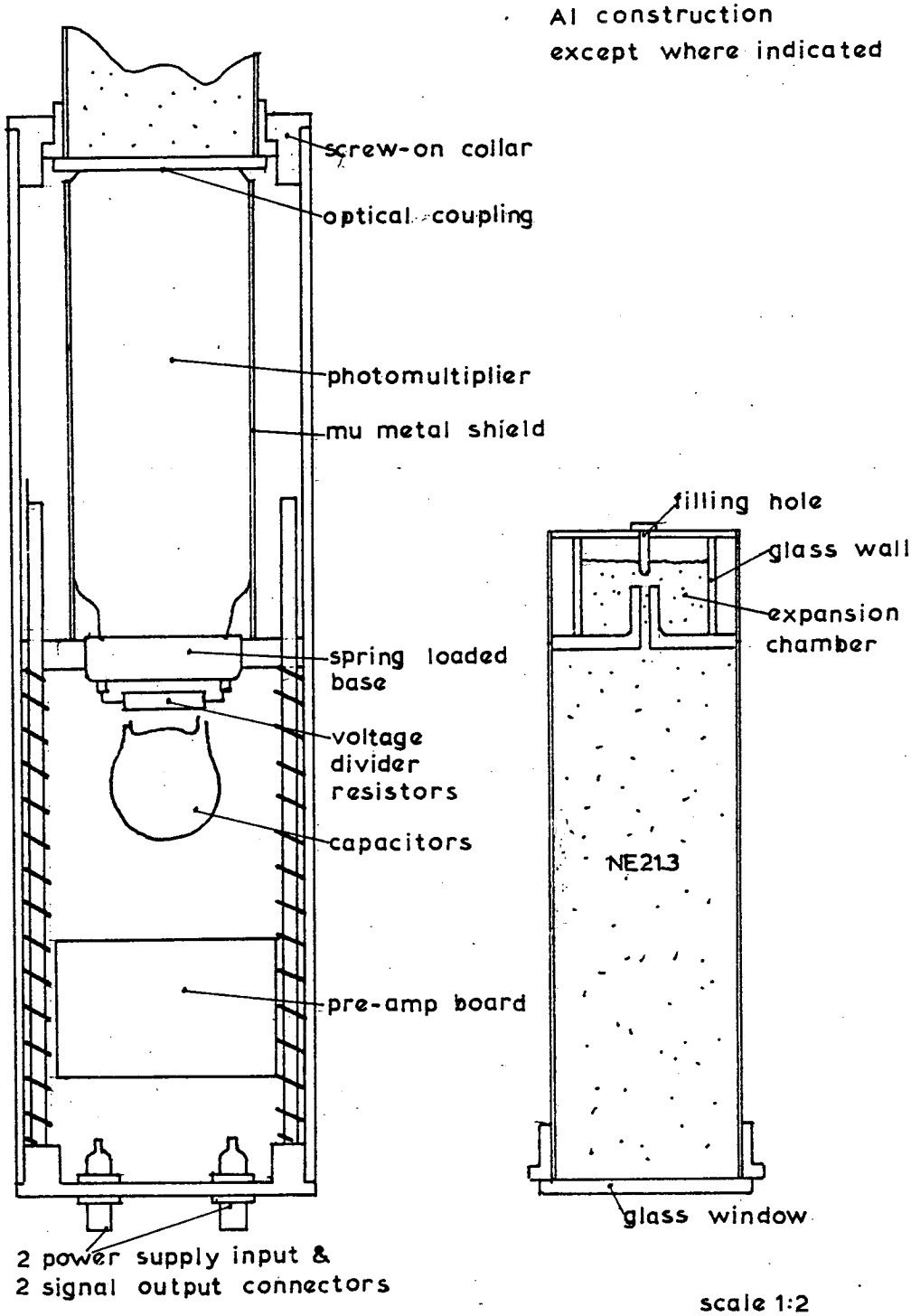

figure 3.1

DYNODE CHAINS

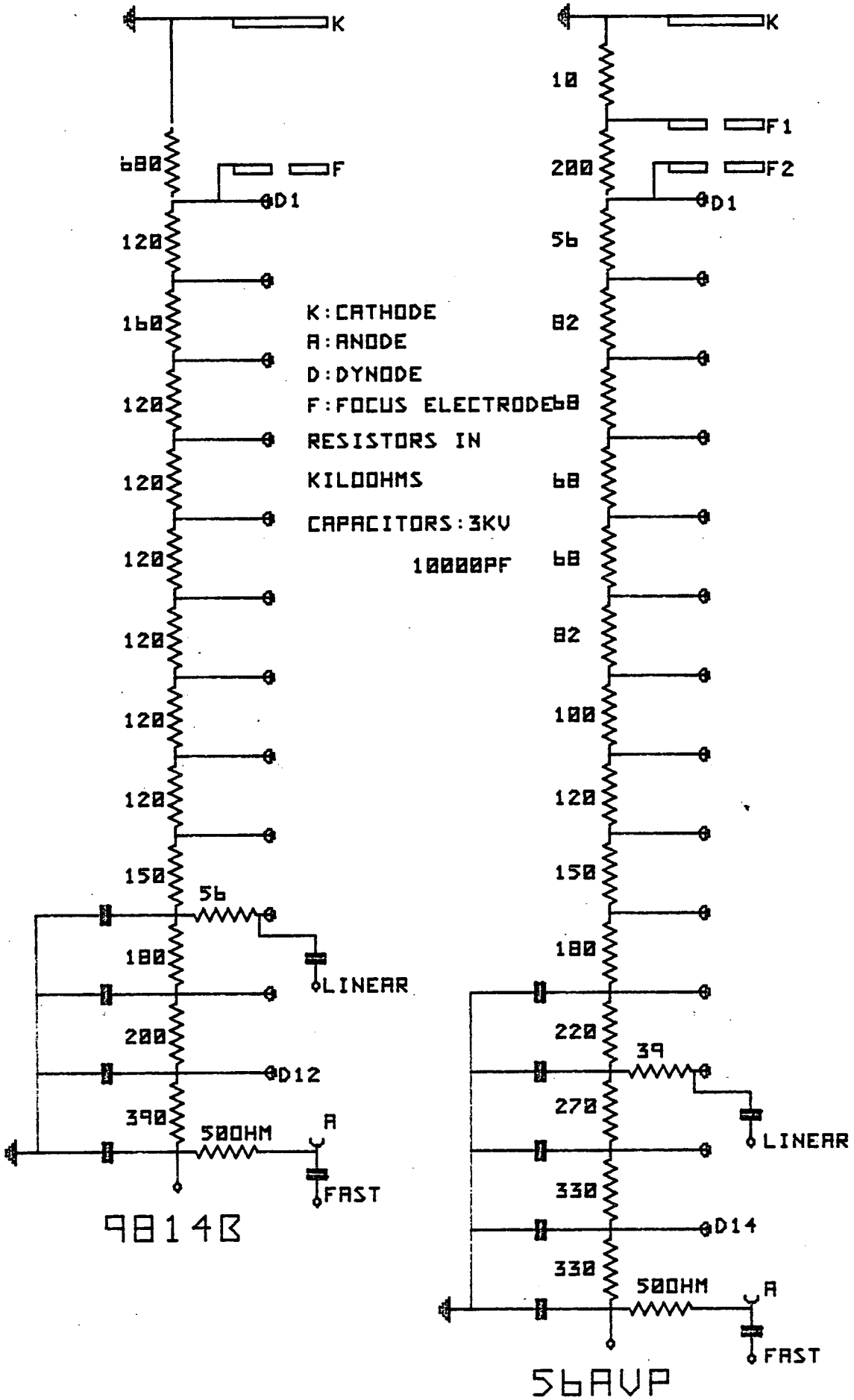

FIGURE 3.2

recoil energy spectra, while the anode provides a fast, 3ns rise time, negative pulse for possible time of flight applications.

3.2 Linearity

Before use in a scattering experiment, detectors were checked for energy/pulse height linearity, pulse height stability, and resolution. The linearity of the electronics was tested by substituting a NaI(Tl) crystal for the NE213 liquid cell, and taking pulse height spectra of the reference gamma sources, ^{137}Cs, ^{22}Na, and ^{60}Co. An energy resolution of better than 10 per cent on the 0.66MeV photo peak of ^{137}Cs was required.

3.3 Stability Tests

In any accurate measurement of left, right asymmetries, false asymmetries induced by changes in detection efficiency of scintillation counters must be minimised. A measurement by Galloway [45] on the stability of 12 liquid scintillation counters has shown count rate variation substantially greater than would be expected from Poisson statistics alone, and also large differences in performance between individual detector systems. Between best and worst cases there was almost a factor of 6 in the amount of count rate change. A consistant change in count rate when detector orientation was altered was also noted. In each case a higher count rate was measured with the detector vertical, photomultiplier facing up, than with it inverted. This was tentatively attributed to residual magnetism effecting the photomultipliers.

With the new polarimeter an automatic test procedure has been devised so that any of these effects can be easily located in detectors and the appropriate action taken. In addition to runs made with a ^{60}Co source, a ^{252}Cf source has been used in order to test for any effects

on PSD systems. The data produced here is taken from two initial detector tests. Such tests are normally carried out between experimental neutron scattering runs. To date 50 or so have been performed and the data presented is typical of what has been recorded in preliminary system tests before detectors with unacceptable performance were rejected.

3.3.1 Test Procedure

In a test run a ^{60}Co gamma or ^{252}Cf neutron source is clamped in the position normally occupied by the neutron scattering sample. Either 160 measurements with the polarimeter in one orientation or 128 measurements with the polarimeter alternately in orientation A and B were made. With individual measurement times of 1000s, the total run time for the latter was just under 2 days. ^{60}Co produces 2 gamma rays of 1.17 and 1.33 MeV, too close to be resolved, but still giving a reasonably well defined Compton edge to the recoil electron spectrum. ^{252}Cf produces neutrons with a maximum energy of 10MeV, averaging 2MeV, as well as gamma rays. The recoil proton spectra are relatively featureless with maximum counts at low energy, tailing off progressively at higher energies. Recoil proton, electron and PSD spectra are compared in figure 3.3. A pulse height discrimination level corresponding to approximately 0.6 of the ^{60}Co Compton edge was set in each case. The sensitivity of counting rate to gain varies differently with discrimination level for ^{60}Co and ^{252}Cf spectra. With this discrimination level, ^{60}Co ought to provide the more sensitive gain change test, while ^{252}Cf should give a measure of PSD stability. All liquid scintillators were checked as being bubble free, and electronics thoroughly warmed up before testing commenced.

3.3.2 Results

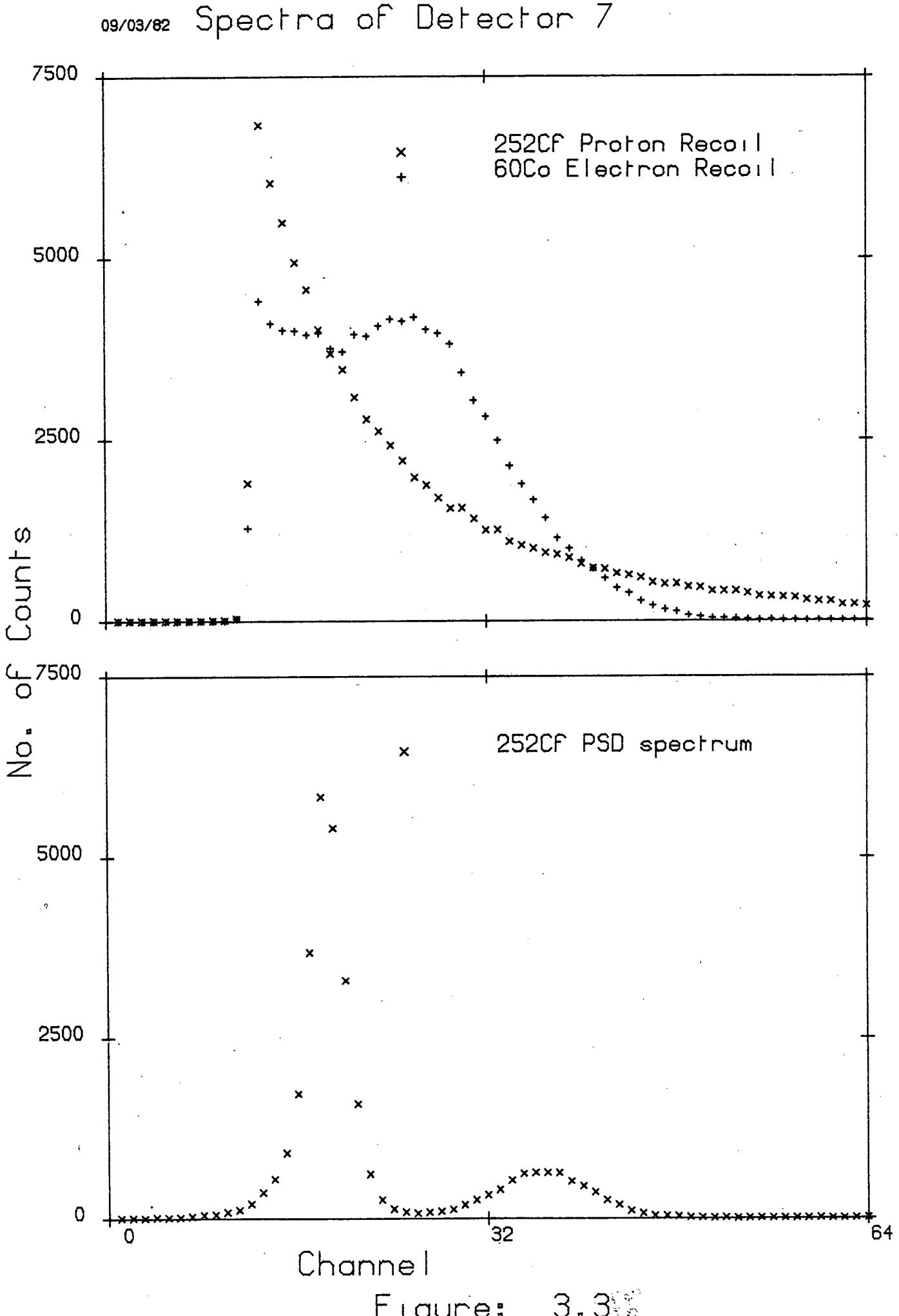
09/03/82 Spectra of Detector 7
252Cf Proton Recoil
60Co Electron Recoil
7500
5000
2500
0
Counts
No. of
252Cf PSD spectrum
7500
5000
2500
0
0
32
64
Channel

Figure: 3.3

A summary of performance with neutron and gamma tests is given in tables 3.1 and 3.2 respectively. A measure of count rate stability is obtained by comparing the standard error, the standard deviation in the mean of the 1000s counts, with the Poisson error. The asymmetry is taken as [N(A)-N(B)]/[N(A)+N(B)] for detectors 1-11 and [N(B)-N(A)]/[N(A)+N(B)] for detectors 12-22, with N(A) and N(B) the number of counts in orientations A and B respectively. It is taken this way as the left, right scattering asymmetry is the important parameter in a neutron polarisation experiment. Here it gives a useful measure of the variation in count rate when the polarimeter is rotated. The most striking result is the large difference in performance between nominally identical detector systems, especially with respect to gamma standard errors. As expected, the gamma test proved more sensitive in detecting count rate changes induced by electronic drift.

Count rate variation for best and worst cases of standard error and asymmetry, with gamma and neutron sources, is shown in figures 3.4-3.7. From these it is obvious that there is no common time dependent effect acting on all detectors, and in several cases no discernible effect at all, apart from counting statistics. Detectors 2, 13 and 18 have unacceptably bad standard errors, while 22 appears to be perfectly stable. It is also quite surprising that the 18A and B count rates should follow each other so closely, to produce the smallest asymmetry in the gamma test, while the much flatter 7A and B distributions show a marked difference.

With the neutron test, count rate was much lower and so points are more scattered. However it is possible to see a slight time dependent effect with detector 9 and a definite discrepency between 15A and B. Standard errors are all comparable with, or slightly larger than, Poissson errors, which implies that any time dependent effects on PSD are slight, except perhaps with detector 9. This has the worst

09/03/82 60Co Best and Worst Standard Error

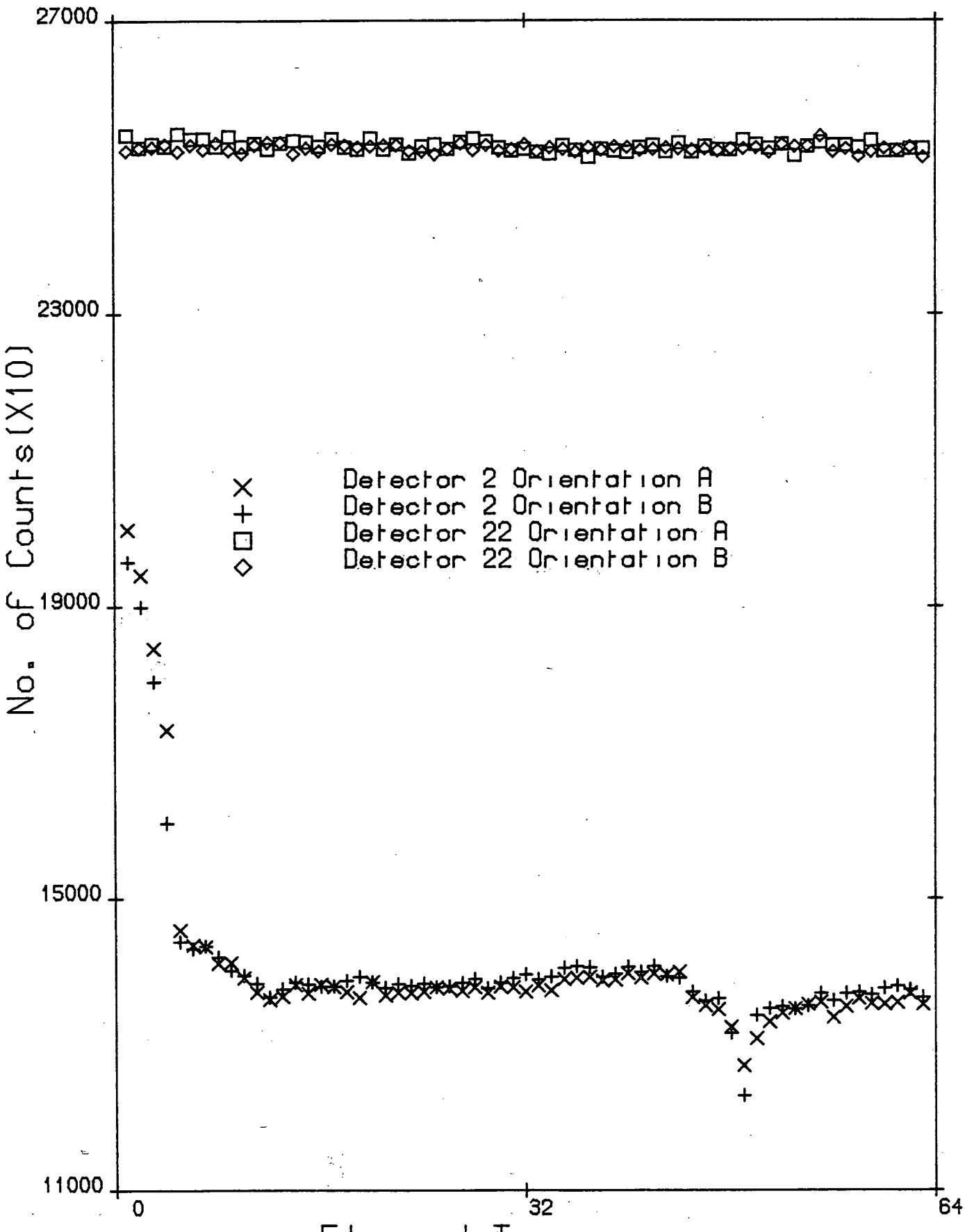

Figure: 3.4

09/03/82 60Co Best and Worst Asymmetry

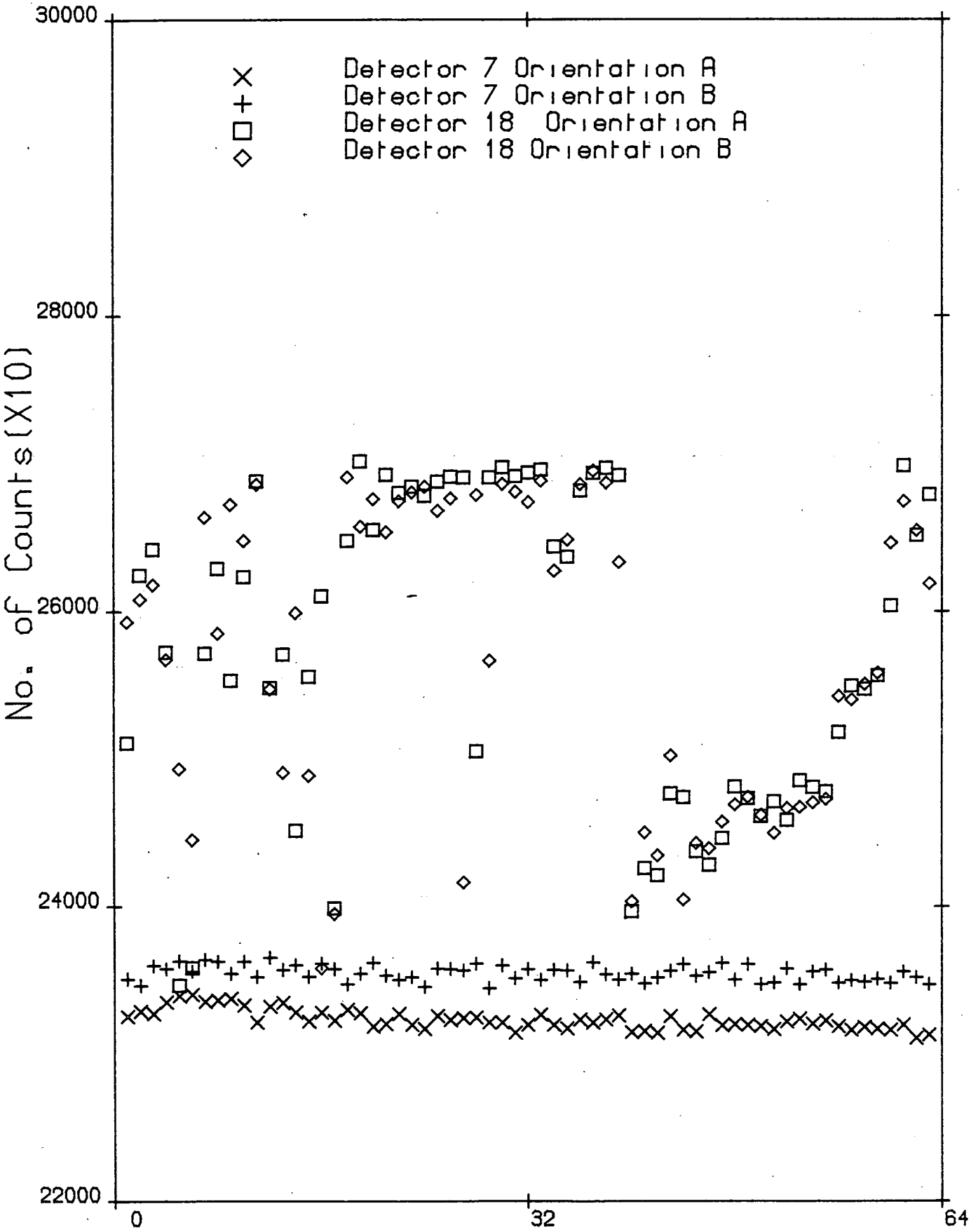

Figure: 3.5

09/03/82 252Cf Best and Worst Standard Error

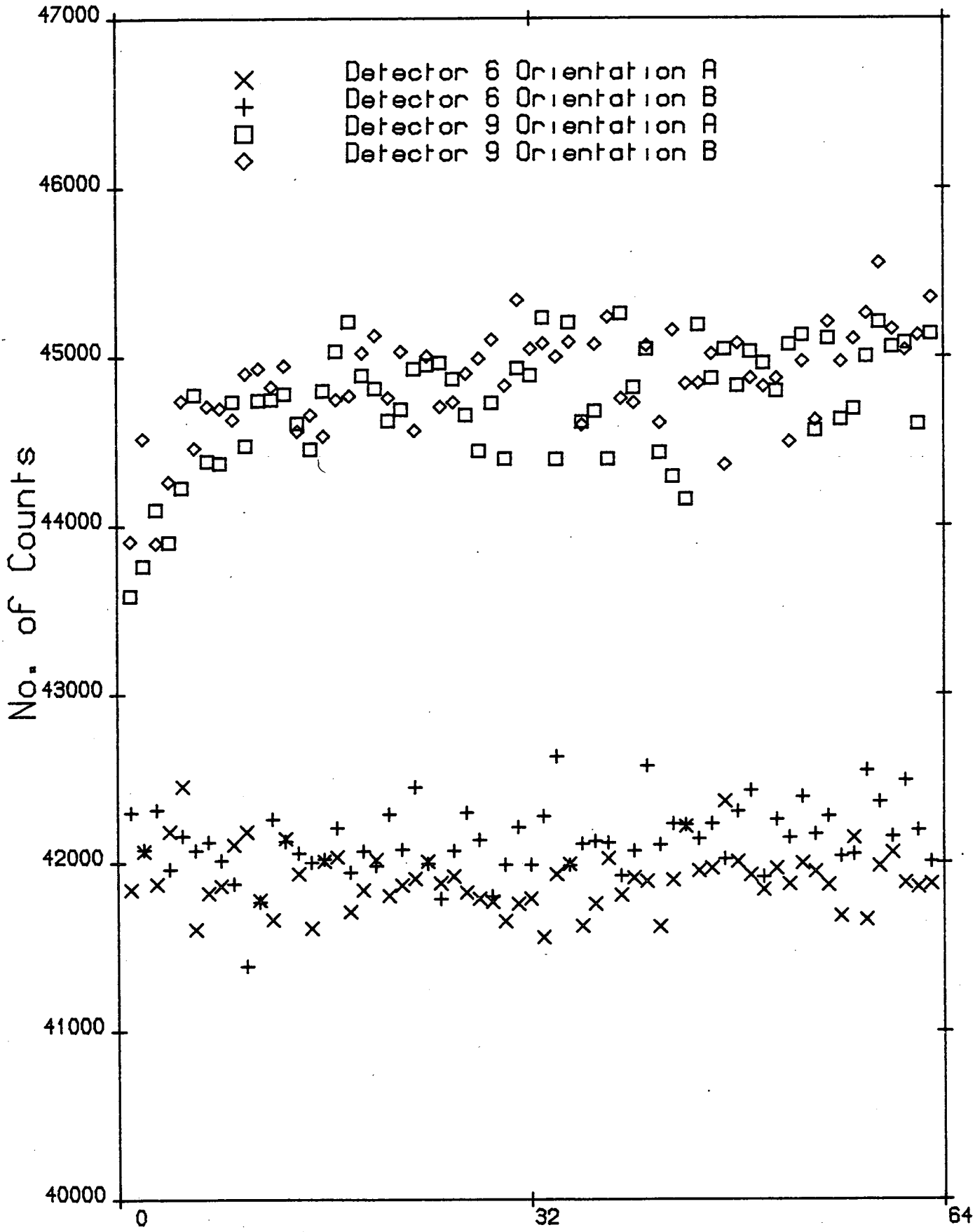

Figure: 3.6

09/03/82 252Cf Best and Worst Asymmetry

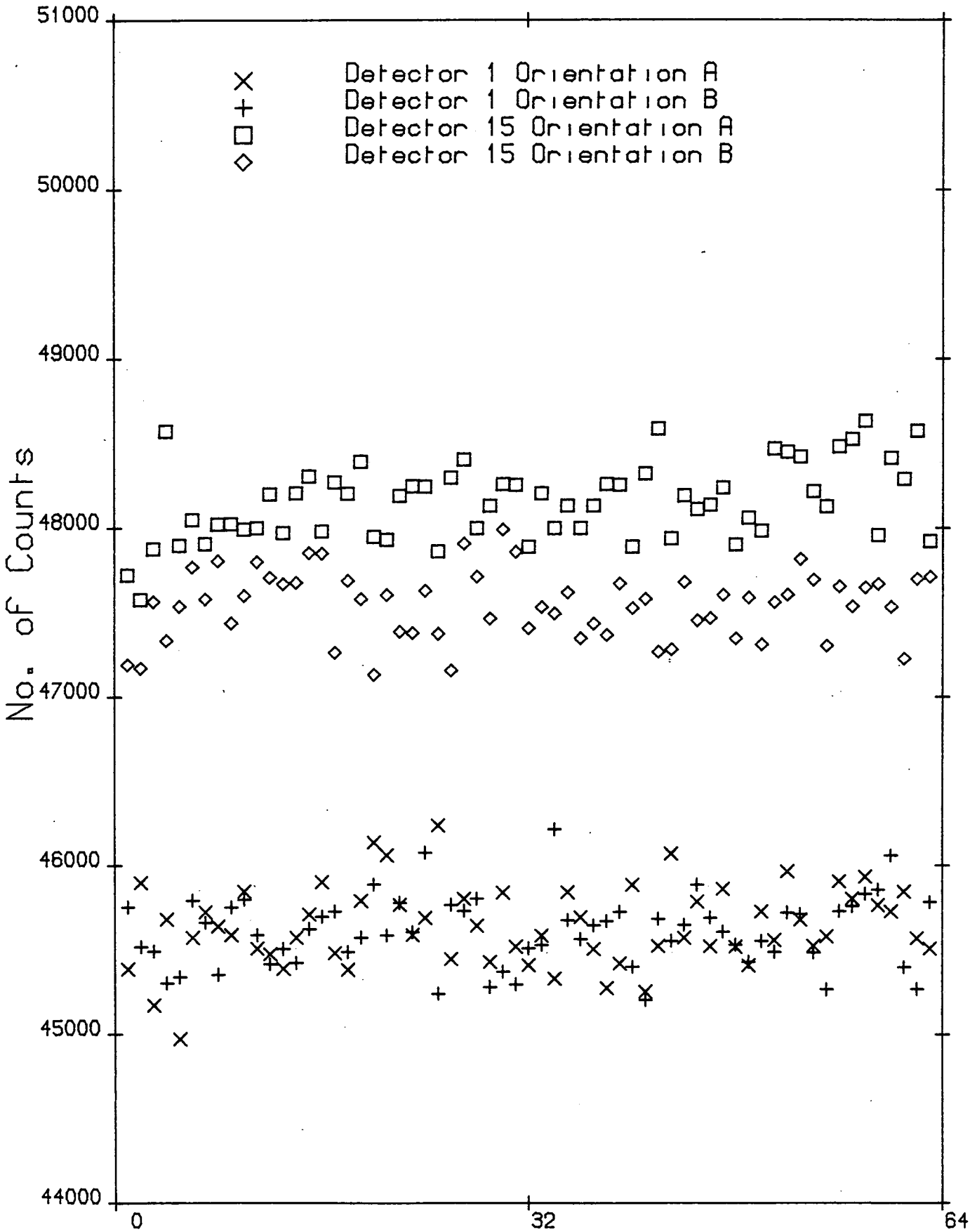

Figure: 3.7

standard error in the neutron test, but compares very favourably in the gamma test.

Although the average asymmetry over all detectors is practically the same for the two tests, the values for individual detectors do not agree well. Eight show a different sign and detectors 4,15 and 21 have the largest discrepancies. There is no obvious pattern to the detector asymmetries and certainly not the alternate positive, negative sequence observed by Galloway. The polarimeter described by Galloway [45] was built of steel as opposed to aluminium, some of which may have become magnetised in machining. With the new polarimeter another outside cause of asymmetry might be slight inhomogeneity in background levels. A massive concrete pillar,which is incorporated in the polarimeter shielding, sits less than 1m from some detectors. It produces gamma rays from ^{40}K and Uranium Thorium series decays and may also scatter some of the radiation coming from the source. Tests with weaker gamma sources do indeed show an effect attributable to the former, but in these cases detectors 10-13 always show up worst, as they have the greatest degree of movement with respect to the pillar. They do not behave particularly badly in either of the tests recorded here where the source was much stronger. For experimental running the tolerable maximum asymmetry was set as +—0.5per cent. Detectors which stubbornly refused to come below this limit were completely stripped down and carefully reassembled. This usually had the desired result.

In an attempt to find some of the causes for the very bad behaviour of one of the detectors in the gamma test, simultaneous measurements of detector temperature and of mains supply voltage were made during a measurement sequence. The temperature variation is quite small, less than one degree centigrade, and mains fluctuates within the statutary 10 per cent limit. The supply was measured both in the "machine room" where the polarimeter and common pre-amplifier supply

sit, and the "control room" where the rest of the electronics are situated. Figures 3.8-3.10 illustrate the variations. Interestingly, there is a discrepancy between control and machine room voltage shortly after the start of the run. No obvious correlation between count rate and either mains voltage or detector temperature is discernible . Inherently the most unstable component in the system, the photomultiplier, has a gain very strongly dependent on applied HT. One would expect some correlation with mains fluctuation and also correlation between individual detectors if this was the prime cause. Occasionally detectors do show similar time dependence in count rate, although in varying degrees of severity, suggesting a common cause. However it is just as likely that the distributions will be completely different, as with detectors 2 and 18 in the gamma run. This would seem to imply other possible external causes.

After those detectors with unacceptable instrumental asymmetries and stability were replaced or rebuilt, the polarimeter was thought ready to perform measurements on scattered neutrons. With care it was possible to have all detectors well within the 0.5 per cent asymmetry limit. An upper limit of 0.3 per cent was more usual.

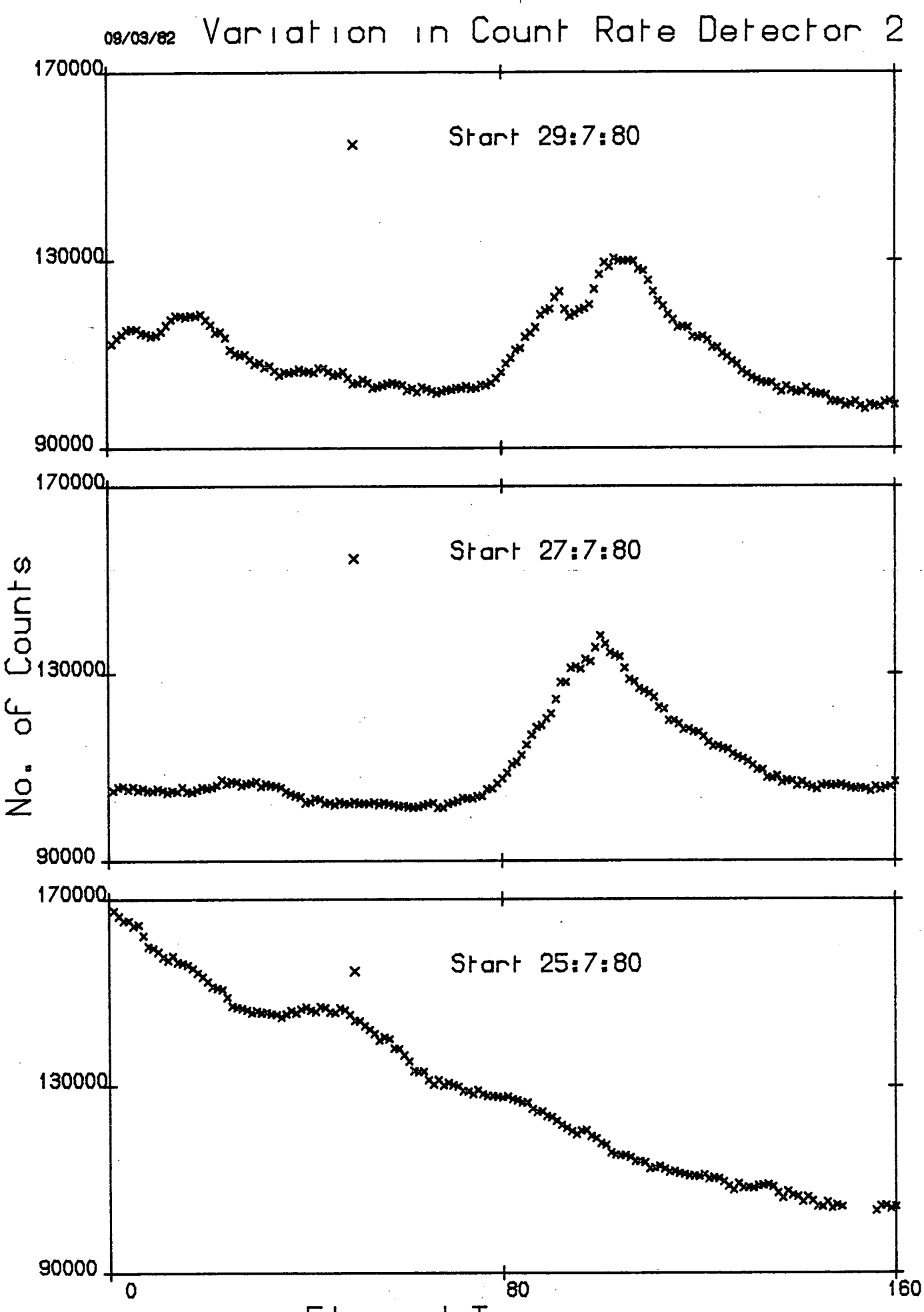
09/03/82 Variation in Count Rate Detector 2
170000
130000
90000
Start 29:7:80
170000
130000
90000
Start 27:7:80
170000
130000
90000
Start 25:7:80
No. of Counts
0
80
160
Elapsed Time

Figure: 3.8

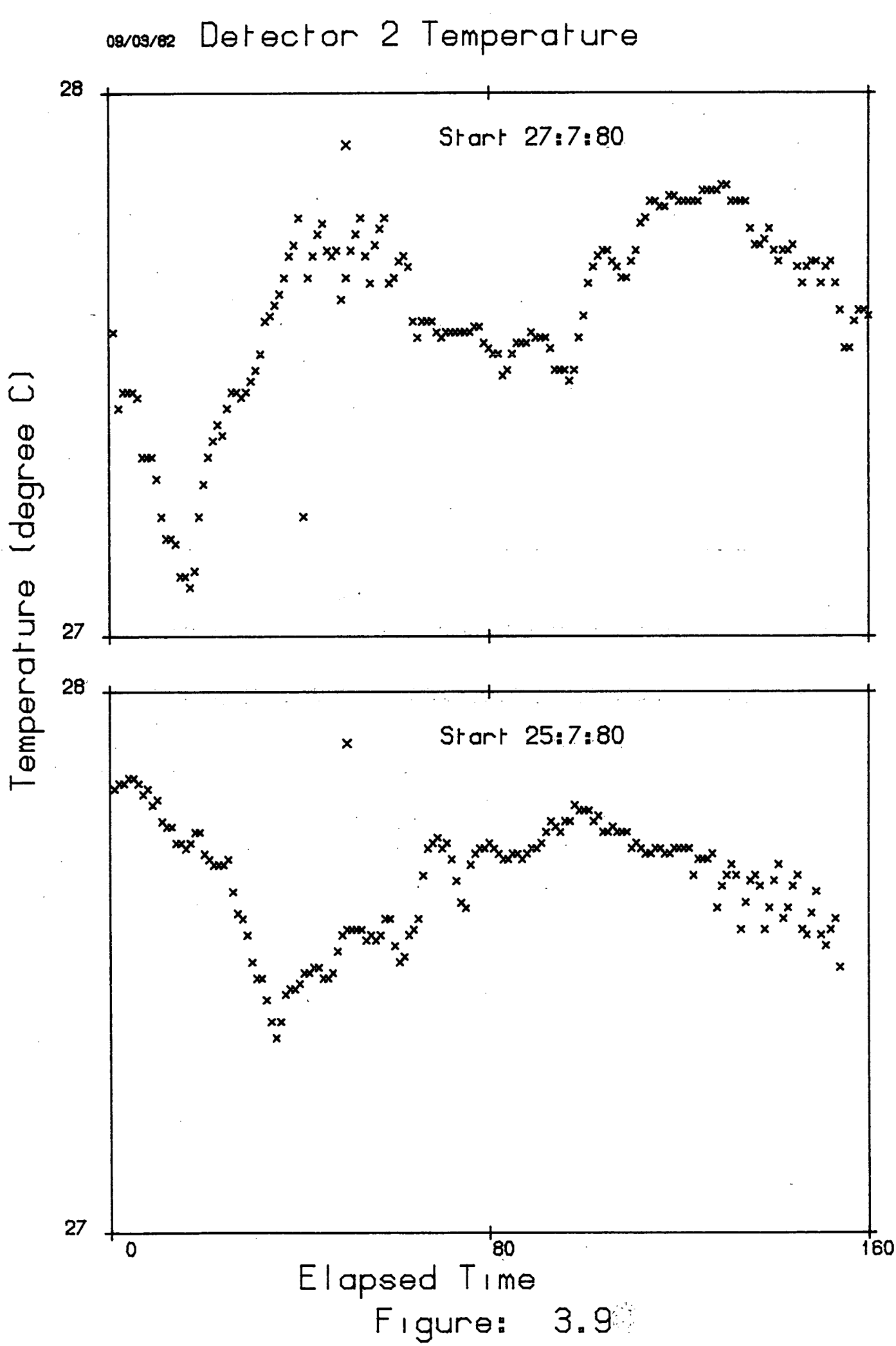
09/03/82 Detector 2 Temperature
28
Start 27:7:80
27
28
Start 25:7:80
27
0
80
160
Temperature (degree C)
Elapsed Time

Figure: 3.9

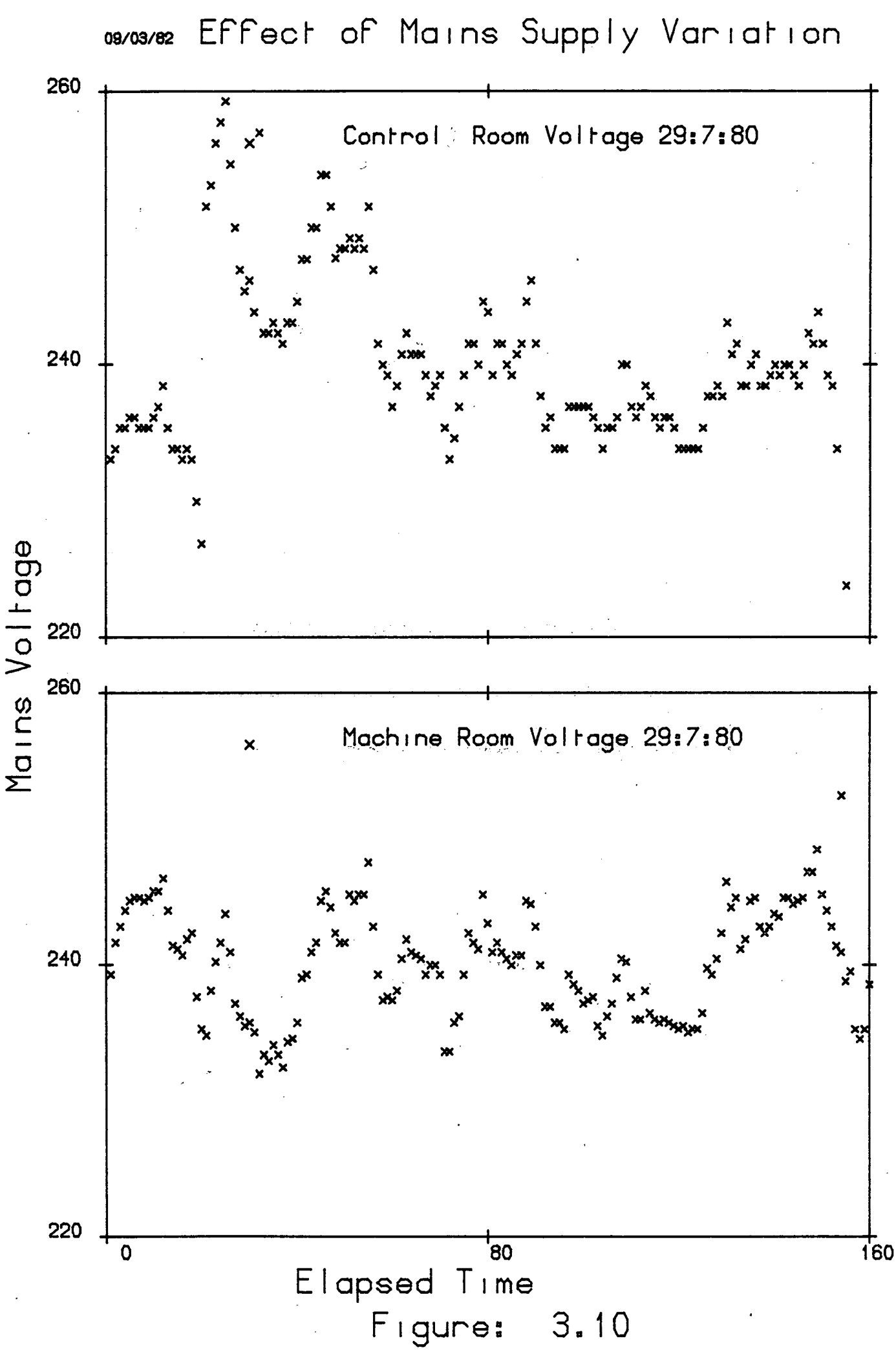
09/03/82 Effect of Mains Supply Variation
Control Room Voltage 29:7:80
Machine Room Voltage 29:7:80
Mains Voltage
260
240
220
0
80
160
Elapsed Time

Figure: 3.10

Table 3.1
^{252}Cf Source 1000sec Counts

Detector	Polarimeter Orientation	Mean Count	Standard Error	Poisson Error	Asymmetry(per c
1	A	45640	26	27	0.037
	B	45606	21	27	
2	A	43741	28	26	-0.079
	B	43810	30	26	
3	A	45570	26	27	-0.051
	B	45616	20	27	
4	A	36926	43	24	-0.022
	B	36942	27	24	
5	A	37209	28	24	-0.273
	B	37412	16	24	
6	A	41899	18	26	-0.274
	B	42129	20	26	
7	A	36678	25	24	-0.367
	B	36948	36	24	
8	A	40126	27	25	-0.115
	B	40218	30	25	
9	A	44728	43	27	-0.138
	B	44851	36	27	
10	A	45232	36	27	-0.219
	B	45431	36	27	
11	A	42113	28	26	-0.269
	B	42340	24	26	
12	A	43718	25	26	0.129
	B	43832	26	26	
13	A	37969	27	25	-0.077
	B	37911	32	25	
14	A	33184	27	23	-0.231
	B	33031	29	23	
15	A	48151	26	28	-0.636
	B	47542	20	27	
16	A	46194	25	27	-0.269
	B	45946	18	27	
17	A	45222	37	27	-0.353
	B	44904	25	27	
18	A	39448	35	25	0.230
	B	39630	34	25	
19	A	40251	20	25	-0.355
	B	39966	24	25	
20	A	42539	31	26	-0.422
	B	42181	30	26	
21	A	38943	35	25	-0.322
	B	38693	34	25	
22	A	40678	26	25	0.163
	B	40811	25	25	

Table 3.2

^{60}Co Source 1000sec Counts

Detector	Polarimeter Orientation	Mean Count	Standard Error	Poisson Error	Asymmetry(per cent
1	A	255797	46	63	0.136
	B	255104	59	63	
2	A	140454	1644	47	-0.109
	B	140760	1460	47	
3	A	265260	73	64	0.128
	B	264584	110	65	
4	A	179494	290	53	0.537
	B	177576	293	53	
5	A	210628	135	58	-0.100
	B	211048	261	58	
6	A	220166	144	59	-0.399
	B	221929	33	59	
7	A	232299	27	61	-0.671
	B	235437	43	61	
8	A	236518	59	61	0.122
	B	235990	57	61	
9	A	252989	63	63	-0.064
	B	253313	52	63	
10	A	196616	262	56	-0.337
	B	197945	263	56	
11	A	251604	165	63	-0.103
	B	252124	120	63	
12	A	235064	390	61	0.361
	B	236769	293	61	
13	A	208907	761	57	0.294
	B	210139	462	58	
14	A	173863	235	53	-0.136
	B	173390	229	52	
15	A	257249	73	64	0.175
	B	258151	73	64	
16	A	248469	54	63	-0.152
	B	247714	49	63	
17	A	267048	75	65	-0.235
	B	265798	49	65	
18	A	257410	1344	64	-0.068
	B	257043	1285	64	
19	A	201759	187	57	-0.079
	B	201442	117	57	
20	A	270141	80	65	-0.240
	B	268849	59	65	
21	A	209621	128	58	0.430
	B	211432	150	58	
22	A	252873	37	63	-0.071
	B	252529	40	63	

3.4 Energy Resolution and Light Output

A rather long cylindrical detector has been used in the present polarimeter and previous models [21,28], in order to maximise scattered neutron count rate while maintaining acceptable angular resolution. The radius of the cylinder is also limited in the present apparatus by the available space. However these detectors have noticeably poorer energy resolution than a similar Nuclear Enterprises manufactured 5cm by 5cm detector. Since proton recoil spectra are taken, inelastic neutrons are excluded, where possible, by setting a high enough pulse height discrimination level. When energy resolution is poor, the discrimination level has to be set higher to ensure the same degree of inelastic exclusion. Therefore the drop in elastic count rate through using a shorter detector is partially compensated by the ability to use a lower discrimination level. In situations where it is not feasible to exclude inelastic neutrons completely because of insufficient energy separation of ground and excited states of the nucleus under investigation, the relative detection efficiency for inelastic neutrons must be known. This is usually calculated from Monte Carlo simulations of the detector response to neutrons if a variable energy neutron source is not available.

It has been shown [46,47,48], that light attenuation effects are important in large and moderately sized liquid scintillation counters. The 5cm long and 15cm long detectors differ only with respect to their length. Differences in the pulse height and energy resolution obtained using a reference gamma source, the same photomultiplier and pulse electronics, set at the same gain, were attributed to differences in the amount of light transmitted to the photomultiplier window. This was tested by irradiating localised sectors of the active volume of the detector, and collecting the associated recoil electron spectra.

A simulation program was written which includes the results of

the light attenuation tests, and the calculated response compared with measured proton and electron recoil spectra. The final results are used to predict if any advantage might be gained by using a detector less than 15.4cm long, and also to calculate the energy dependence of the detection efficiency. Knowledge of the latter is necessary to the data corrections described in Chapter 4.

3.4.1 Light Output Test Apparatus

The liquid scintillation cells used in the light output test were thin walled aluminium cylinders of 5cm diameter and 5cm, 10cm and 15.4cm in length. The 5cm by 5cm cell is made by Nuclear Enterprises. It is filled with NE213 and the inside walls are made more reflective with NE562 TiO_2 paint. The 15.4cm and 10cm detectors were coated with NE562 and filled with NE213. Also an extra 15.4cm and 10cm detector were made, coated with NE561 reflector, and filled with NE213. NE561 uses the same grade of TiO_2 but in an epoxy base as opposed to a water base. All scintillation cells were mounted on the same EMI 9814B photomultiplier for the purposes of the test and connected to the same NIM pulse amplifier.

In the localised irradiation test, monoenergetic gamma rays were used in preference to monoenergetic neutrons. Fast neutrons are difficult to collimate into a fine beam, and being produced indirectly by a charged particle accelerator, tend to fluctuate in intensity. They are also more likely to suffer multiple scattering inside the scintillator thus delocalising the scintillations. A ^{137}Cs source giving 0.66 MeV gamma rays was chosen. This was housed in a lead castle with a collimating slit 0.3cm wide. The liquid scintillation cell was traversed accurately across the slit on a screw mechanism (figure 3.11) so that successive discs, roughly 0.5cm thick, were irradiated. Source activity of 3mC was high enough to give acceptable

Light Output Test Apparatus

scale 1:3

One turn of screw = 0.241 cm

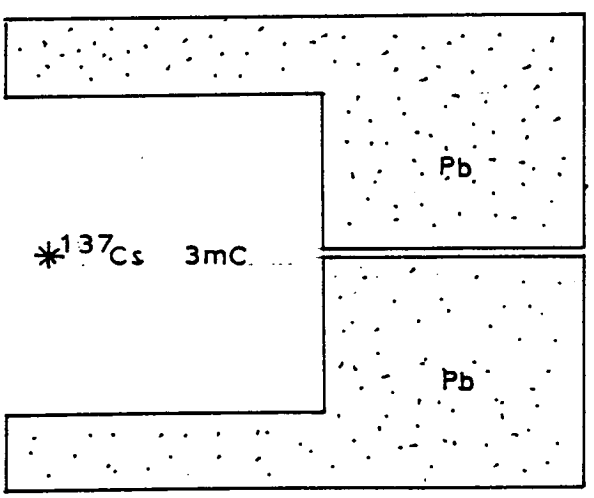

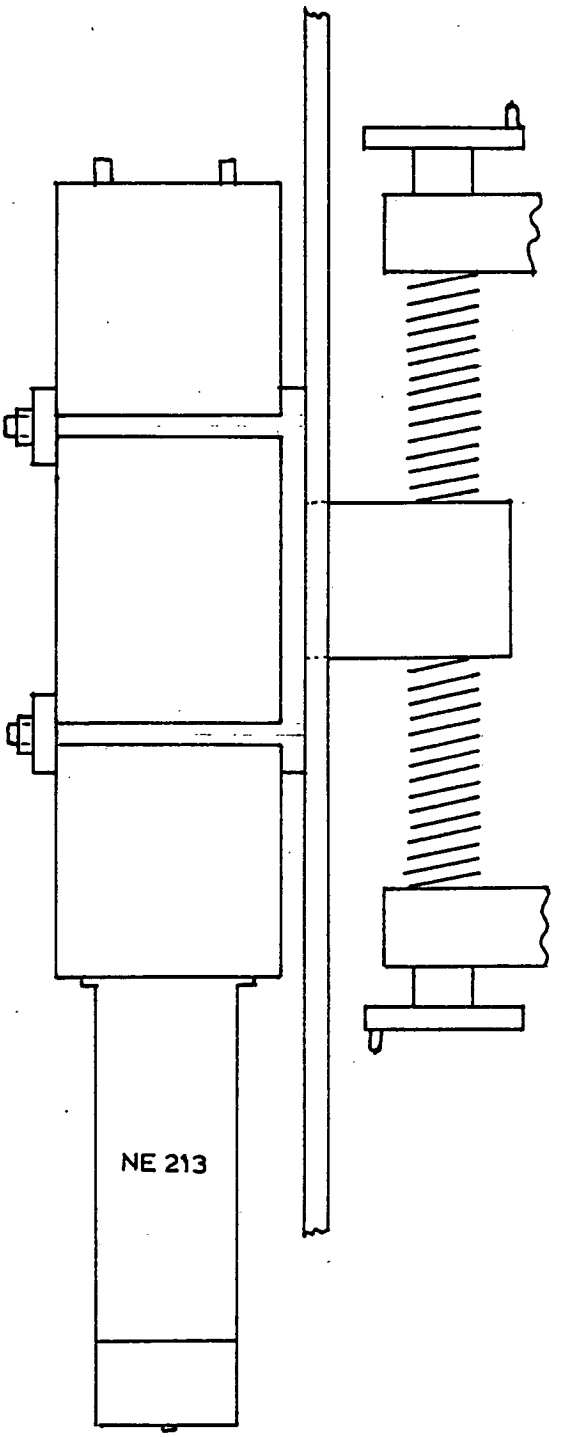

Figure 3.11

counting statistics after counts of 100s for each disc, so that long term electronic drifts could be discounted. In taking spectra for comparison with Monte Carlo simulations, an uncollimated ^{137}Cs source and 3.0 MeV neutrons from the $^{2}H(d,n)^{3}He$ reaction were used.

3.4.2 Localised Irradiation Test

The measure of intensity of light collected at the photomultiplier was taken as the channel at which the half maximum number of counts in the recoil edge occured, denoted C_{50}. The energy resolution of the spectrum was defined as $R_{90} = (C_{90} - C_{10})/C_{50}$ where C_{90} and C_{10} are the channels at which 90 per cent and 10 per cent respectively of the maximum number of counts in the recoil edge occur. A summary of pulse height and energy resolution, using gamma rays from a ^{137}Cs source is given in table 3.3 for the various detectors tested. Near denotes collimated gamma ray spectra localised near to the photomultiplier window, and far, localised at the opposite end of the detector. The figures in brackets show the length of the light pipe where used , and R_{90} is given as a per centage. In figure 3.12 the channels at which recoil edges occured are plotted against the average distances of the irradiated disc in the active scintillation area from the photomultiplier window. The detectors with the flattest distributions are those which produce the best energy resolution. It is immediately obvious that NE562 gives superior performance to NE561. Insertion of a short cylindrical light pipe flattens the distributions considerably but at the expense of reduced pulse height. There is little to choose between the 1.5, 2.5, and 3.5cm light pipes and most of the reduction in the amount of light collected is probably due to the extra optical coupling. This could be dispensed with by using a thicker window at the end of the scintillation cell.

15/04/82 Light Attenuation Effects

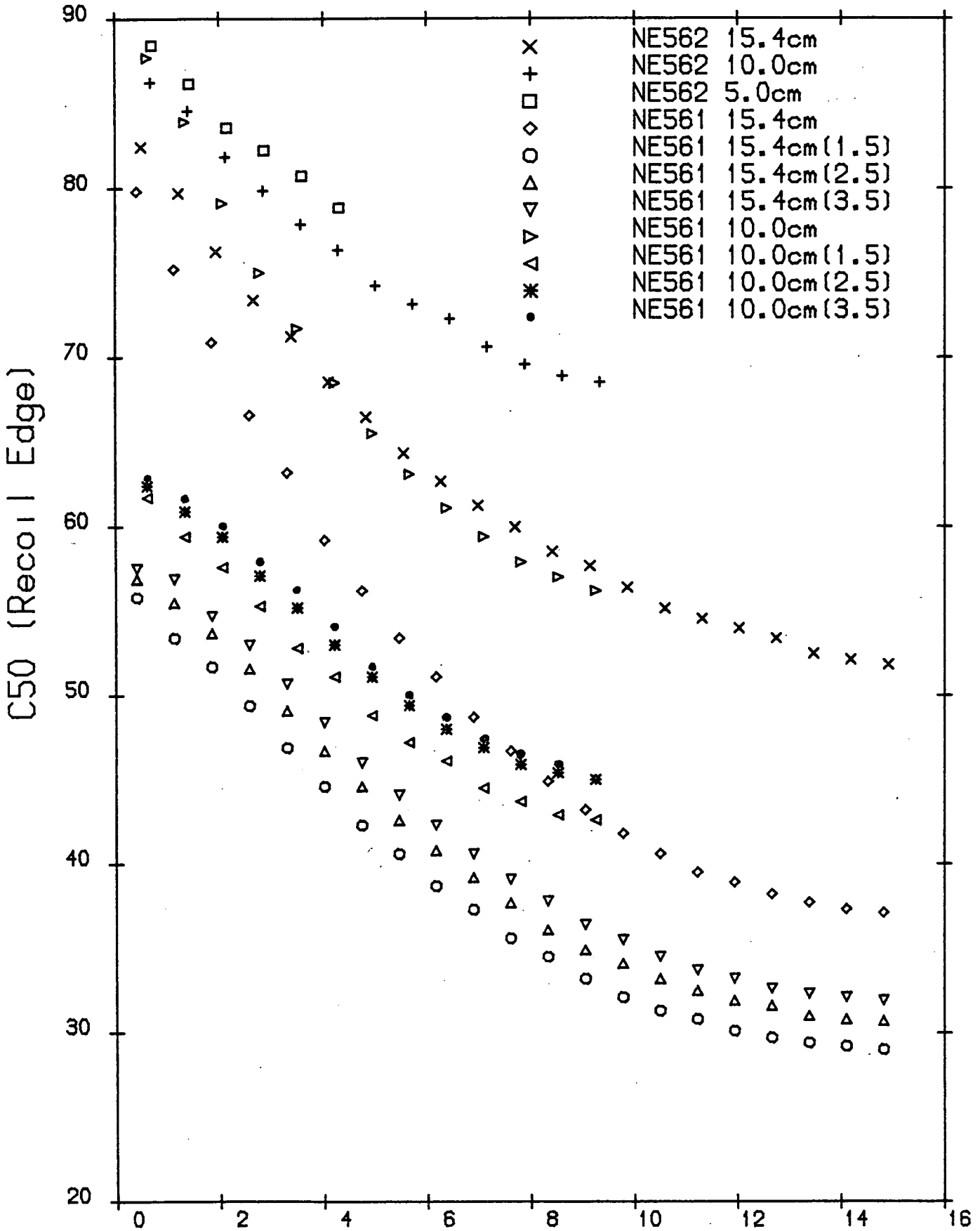

Figure: 3.12

Table 3.3

Detector Characteristics

	Uncollimated		Near		Far	
Detector	C_{50}	R_{90}	C_{50}	R_{90}	C_{50}	R_{90}
NE562 15.4	59.7	47	82.4	23	51.8	26
NE561 15.4	51.9	75	85.7	23	37.2	26
NE561 15.4(1.5)	39.7	67	55.2	22	29.0	26
NE561 15.4(2.5)	36.7	66	58.4	23	30.7	27
NE561 15.5(3.5)	39.7	64	58.6	24	31.9	27
NE562 10.0	74.6	30	86.2	22	68.5	24
NE561 10.0	68.0	49	93.1	22	56.2	24
NE561 10.0(1.5)	51.5	40	62.9	22	42.6	24
NE561 10.0(2.5)	53.7	38	62.8	22	45.0	24
NE561 10.0(3.5)	53.8	36	63.5	23	45.2	24
NE562 5.0	83.3	26	88.4	21	78.9	22

Clark [50] has produced a simple formula relating position of the scintillation in the active volume to fraction of total light output collected by the photomultiplier.

$$F = s_0\langle t\rangle / [1 - r\langle t\rangle(1-s_0)] \qquad (3.1)$$

s_0: fraction of the total solid angle subtended by the window at the scintillation point

r: reflection coefficient of the cell walls

$\langle t\rangle = \exp(-a\langle p\rangle)$

$\langle p\rangle = 4V/S$

V: cell volume

S: total surface area of the cell

$\langle p\rangle$: average path length between successive multiple reflections

<t>: average probability of photon not being absorbed between reflections

a: light absorption coefficient of NE213

The absorption coefficient was taken as 1/150 cm^{-1} following Kuijper [47]. Equation 3.1 has been used successfully in simulating the response of a 12.7cm diameter by 3.8 cm long NE213 cell to 14 MeV neutrons [48]. Nuclear Enterprises quote a coefficient of reflection of 0.96 for NE562 at 425nm the wavelength of maximum emission intensity for NE213. Using this value for the coefficient of reflection of the cell walls equation 3.1 failed to fit accurately the distributions depicted in figure 3.12 . De Leo et al used a value of 0.96 for r in their calculations. The solid angle was calculated accurately using a numerical approximation [69] and this was averaged over the volume of the irradiated discs when attempting to fit equation 3.1. The predicted drop in collected light intensity was always greater than actually observed. Attempts at varying r to improve the fit resulted in unreal values of greater than 1. For the detectors used here, equation 3.1 seems to be an oversimplification.

The amount of light reaching the photomultiplier from a scintillation will be the sum of that received directly and that received after successive reflections.

$$F = s_0 t + (1-s_0) r s_1 t_0 t_1 + (1-s_0)(1-s_1) r^2 s_2 t_0 t_1 t_2 + \ldots\ldots + \prod_{j=0}^{n-1} (1-s_j) t_j r^n s_n t_n + \qquad (3.2)$$

s_n: fractional solid angle subtended by the window at nth reflection

t_n: probability of photon being absorbed between reflections n-1 and n

Clark's formula, equation 3.1,is obtained from equation 3.2 by setting all of the s_n equal to s_0 and the t_n equal to $\langle t \rangle$. As the s_n and t_n are difficult to calculate , other approximations to equation 3.2 were tried. The first was

$$F = st + (1-s)r\langle s\rangle\langle t\rangle^2\{\sum_{n=0}^{\infty}[r(1-\langle s\rangle)\langle t\rangle]^n\}$$

$$= st + (1-s)r\langle s\rangle\langle t\rangle^2/\{1 - [r(1-\langle s\rangle)\langle t\rangle]\} \qquad (3.3)$$

t= exp(-ap), the probability of a photon travelling directly to the photomultiplier without being absorbed

p: distance between scintillation point and photomultiplier window

$\langle s \rangle$: the fractional solid angle subtended by a point on the reflecting wall averaged over the total reflecting surface area.

Equation 3.3 is obtained by setting all s_n and t_n equal to $\langle s \rangle$ and $\langle t \rangle$ for n greater than 0. It gives superior fits to equation 3.1. However the quality of fit indicated by the quantity X^2

$$X^2 = \sum_n\{[(C_{50})_{cal} - (C_{50})_{exp}]/\delta(C_{50})_{exp}\}^2/n$$

deteriorates noticeably as detector length increases. F is not a particularly sensitive function of the t_n which are always close to unity with the small detectors used. Thus the t_n n>0 were left as $\langle t \rangle$. However F is sensitive to the s_n. Acceptably good fits were achieved for the detectors considered using the approximation

$$F = s_0t_0 + (1-s_0)r\langle s\rangle\langle t\rangle^2\{s_1/\langle s\rangle$$

$$- 1 + r\langle t\rangle[\langle s\rangle - s_1] + 1/[1-r(1-\langle s\rangle)\langle t\rangle]\} \qquad (3.4)$$

$$s_1 = a s_0^{\,b}$$

Better fits were possible if a and b were allowed to vary with detector length as follows

15.4cm: a=0.3, b=0.49

10cm: a=0.22, b=0.46

5cm: a=0.19, b=0.42

A more general relationship which might confidently be applied to other sizes and shapes of detector was not attempted as the energy dependence of detection efficiency and optimum length of detectors which might be used in the polarimeter was of prime importance here. Figures 3.13, 3.14 and 3.15 illustrate the quality of fit obtained with equations 3.1, 3.3 and 3.4 for the 15cm, 10cm and 5cm detectors respectively. A value of 0.96 was used for r in all cases.

3.4.3 Monte Carlo Simulations

The use of 0.66 MeV gamma rays and 3.0 MeV neutrons in the tests eased calculation of the response of the detectors to electrons and protons considerably. Thus it was possible to use a relatively simple model of particle detection processes with some confidence so that light attenuation effects would not be obscured. At these energies only Compton scattering of electrons and $^{12}C(n,n)^{12}C$ and $^{1}H(n,n)^{1}H$ reactions need be considered. Incident particles can be started from any point relative to the detector and their maximum angular range may be confined to produce localised irradiation so that conditions of the light output test may be simulated. Particles were tracked through the detector using the "forced first collision weight sampling method" [51]. Multiple scattering is explicitly considered, with n-p scattering assumed isotropic in the centre of mass frame, and cross

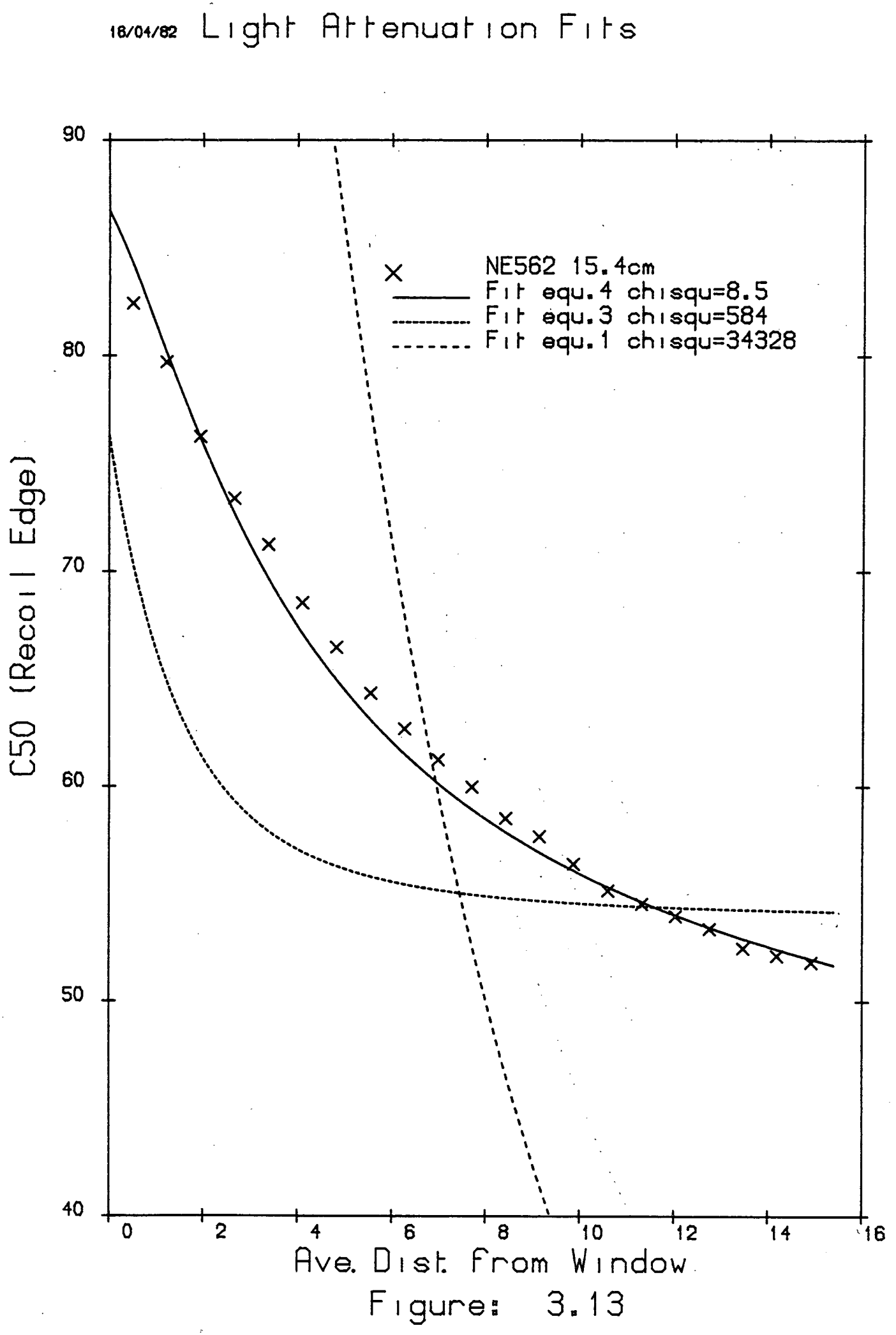
16/04/82 Light Attenuation Fits
NE562 15.4cm
Fit equ.4 chisqu=8.5
Fit equ.3 chisqu=584
Fit equ.1 chisqu=34328
C50 (Recoil Edge)
90
80
70
60
50
40
0
2
4
6
8
10
12
14
16
Ave. Dist From Window

Figure: 3.13

16/04/82 Light Attenuation Fits

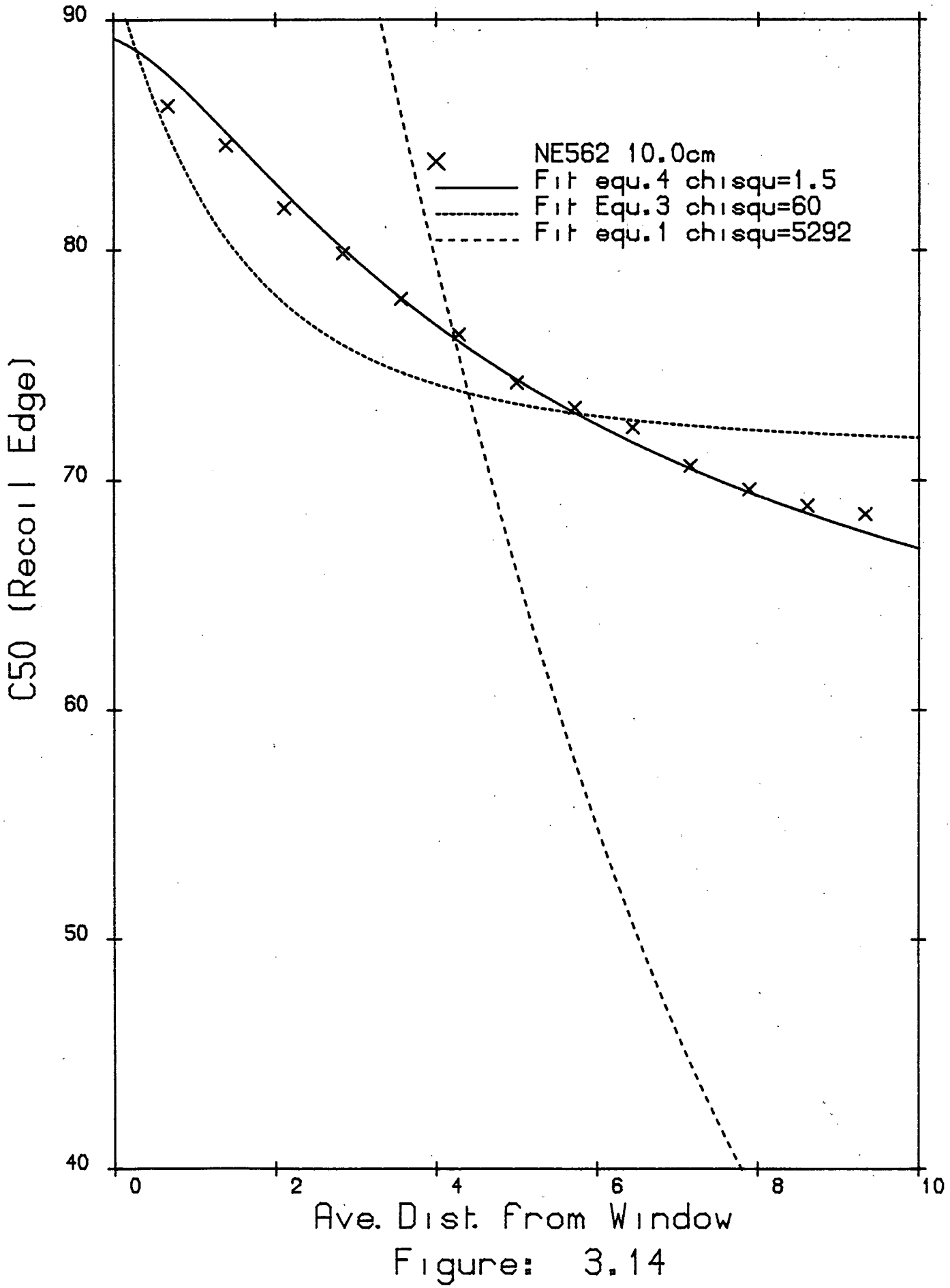

Figure: 3.14

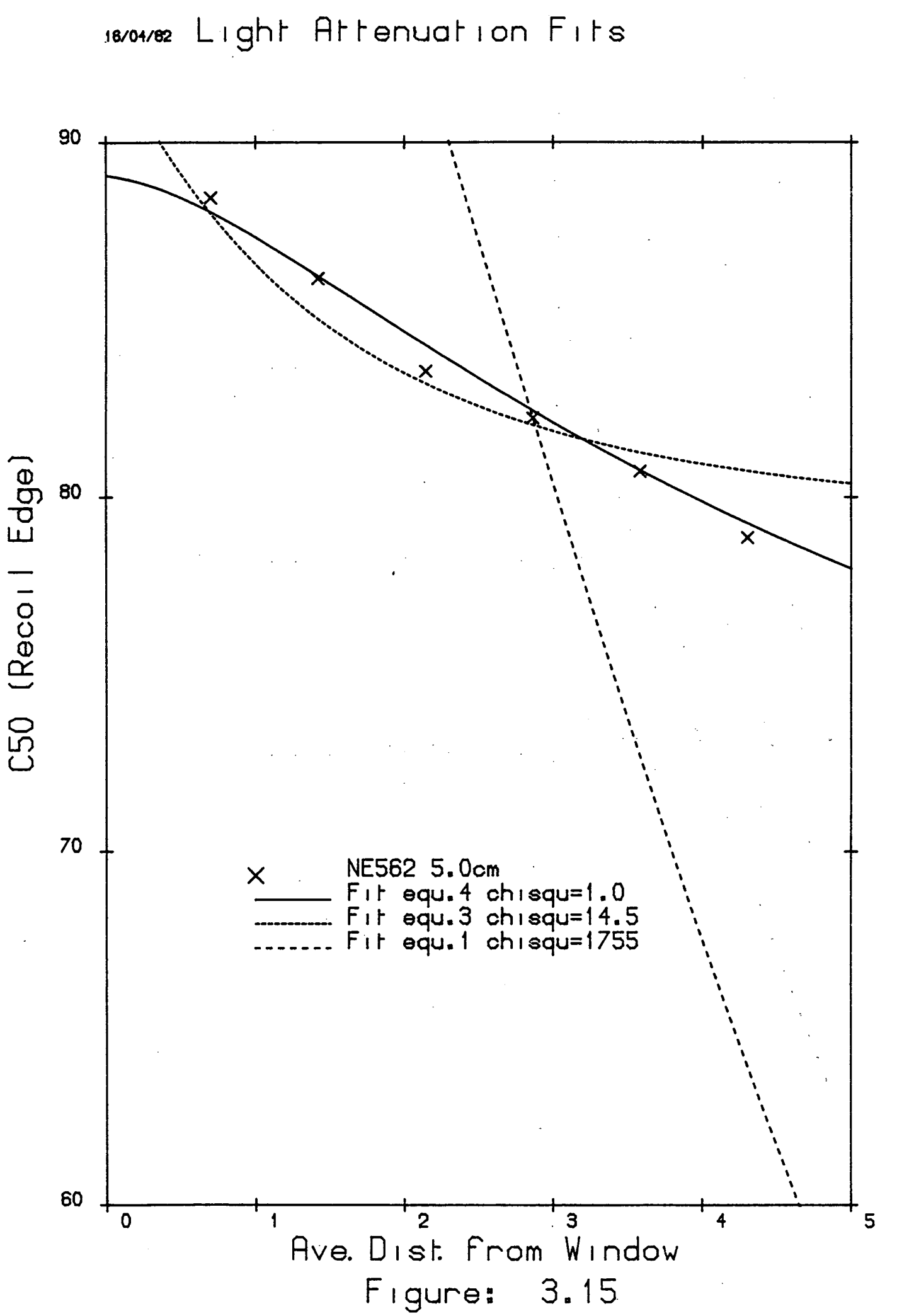
16/04/82 Light Attenuation Fits
90
80
70
60
C50 (Recoil Edge)
0
1
2
3
4
5
Ave. Dist. From Window
NE562 5.0cm
Fit equ.4 chisqu=1.0
Fit equ.3 chisqu=14.5
Fit equ.1 chisqu=1755

Figure: 3.15

sections taken from [52]. The differential cross sections and total cross sections for n-^{12}C scattering were generated using the R function parameters of Fu and Perey [53]. Compton cross sections were calculated using the Klein Nishina equations.

The ranges of the recoil charged particles, less than 2mm for electrons and 0.2mm for protons, were thought small enough to neglect escape and to assume a point source of scintillation light. The light output from electrons was assumed linear with energy, and that of protons calculated using the formula [54]

$$E_e = 0.83E_p - 2.82[1-\exp(-0.25E_p^{0.93})] \qquad (3.5)$$

where E_e is the equivalent electron energy producing the same light output. The numerical values are for NE213 only and are taken from [55]. The predictions of equation 3.5 were checked against the data of Craun and Smith [70] and found to be in agreement.

Attenuation of light was described by equation 3.4 . Other finite energy resolution effects were cumulatively represented by a jitter in the number of photoelectrons produced by the photocathode of the photomultiplier. Following De Leo et al [48] this is parameterised by the factor L_0 which is defined as the amount of energy deposited in the scintillator by an electron which will produce enough light to eject one photoelectron from the cathode. It is given in units of KeVee(KeV electron equivalent). If the parameter L is proportional to the pulse produced by the detector in the absence of light attenuation or jitter, then the pulse height accounting for these two effects is described by

$$L' = R[F.L, d(F.L)]$$

R(x,dx): pseudo random number taken from a Gaussian

distribution centred on x

with standard deviation dx

$$d(F.L) = (F.L.L_0)^{1/2}$$

F: fraction of total scintillation light reaching the photocathode.

The effect of the ith neutron or gamma photon started is calculated as follows

$$N_1 = \mathrm{Int}(kL'_1) \text{ , 1st collision}$$

$$N_j = \mathrm{Int}(k \sum_{j=1}^{jmax} L'_j) \text{ , multiple scattering}$$

N: spectrum channel

k: input constant

Int: nearest integer function

$$W(N_j) = W(N_j) + w_{ij}$$

$$W(N_{j-1}) = W(N_{j-1}) - w_{ij} \text{ , } j>1$$

W(N): the accumulated weight in channel N

w_{ij}: detected weight from jth scattering of ith particle

L_0 is determined by comparison of calculated and measured gamma response. Best results were obtained with L_0 equal to 4.0KeVee. De Leo et al quote a value of 1KeVee in their calculations which may in part be due to their use of a photomultiplier with superior quantum efficiency. However they used equation 3.1 to describe light attenuation which at least for the scintillation counters investigated, gives too large a drop in light intensity. This would tend to be compensated by a smaller value of L_0

Experimental and calculated ^{137}Cs spectra are shown for the

15.4cm, 10cm and 5cm detectors in figures 3.16, 3.17 and 3.18 respectively. Spectra resulting from non-localised irradiation and localised irradiation close to and far from the detector window are illustrated in each. The channel axes of the calculated spectra were multiplied by the same factor of 1.732 for comparison with the experimental spectra and the calculated spectra were normalised to give the same integrated counts above a lower limit of 40.

Agreement is good around the Compton Edge but the calculated values are low for lower recoil electron energies. A possible cause is scattering of gamma rays from the lead collimator or non-active parts of the detector.

Calculated and experimental response to 3.0MeV neutrons is shown in figure 3.19. The calculated response reproduces quite well the shape of the recoil edge and also fits lower energy recoils. The neutron energy dependence of detection efficiency is displayed in figures 3.20, 3.21 and 3.22 for the 15.4, 10.0 and 5.0cm detectors respectively. The curves show the detection efficiency in arbitrary units for various pulse height discrimination levels. Following the experimental situation these were calculated by assigning 3.0MeV to the edge (C_{50}) of the 3.0MeV neutron distribution and assuming a linear channel energy relationship. The recoil proton energy, light output relationship is markedly non-linear as can be seen from the efficiency curves of the 10.0 and 5.0cm detectors where a nominal bias level of 1.5MeV completely cuts out proton recoils from 1.5MeV neutrons. It can be seen from the curves that the 15.4cm detector does as expected need a higher bias level than the shorter detectors to exclude neutrons of a given energy. The calculated relative count rates of the detectors for 3.0MeV and 2.3MeV neutrons are compared in figure 3.23. Equal fluxes at both energies are assumed. The relative count rates for the three detectors is obtained by simply multiplying the detection efficiency by

the solid angle subtended by the detector. If the detectors are biased high enough to completely exclude 2.3MeV neutrons then the 5.0cm detector provides to highest 3.0MeV neutron count rate. In practise however, complete exclusion of inelastically scattered neutrons is often not demanded. If a relative count rate of 0.1 for the 2.3MeV neutrons is tolerated then the bias levels are such that the 15.4cm detector has the highest count rate and the 5.0cm detector the lowest.

In most situations therefore the 15.4cm detector will produce the highest count rate, although where inelastically scattered neutrons of energy above 2.5MeV are encountered the 10.0cm detector may prove marginally better. The marginal advantage of the 10.0cm detector in situations where one is counting elastically scattered neutrons in the presence of inelastically scattered groups from low lying excited states, was not considered enough to justify conversion of existing 15.4cm detectors which were already in use in the polarimeter.

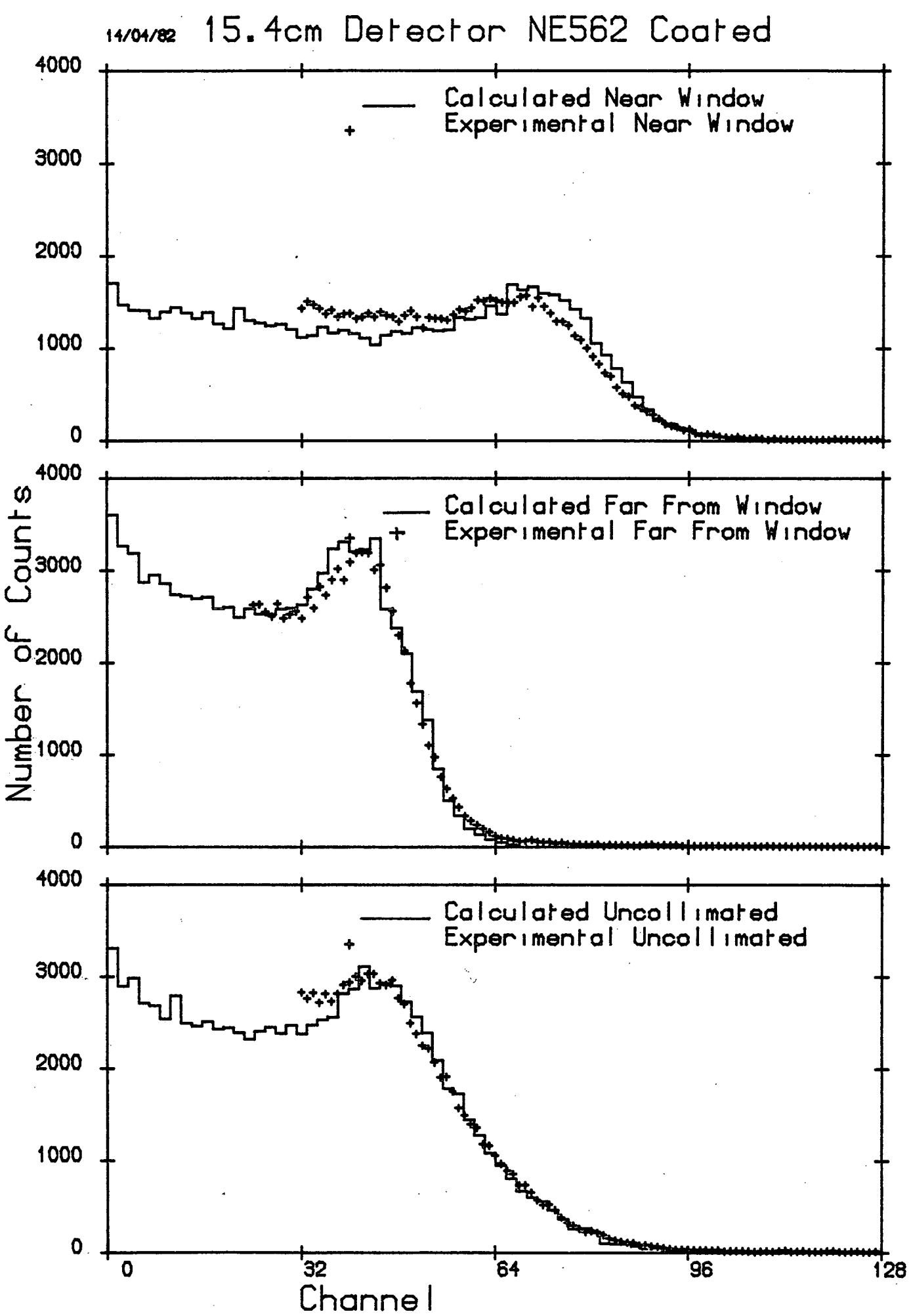
14/04/82 15.4cm Detector NE562 Coated
Calculated Near Window
Experimental Near Window
Calculated Far From Window
Experimental Far From Window
Calculated Uncollimated
Experimental Uncollimated
Number of Counts
Channel
0
1000
2000
3000
4000
0
32
64
96
128

Figure: 3.16

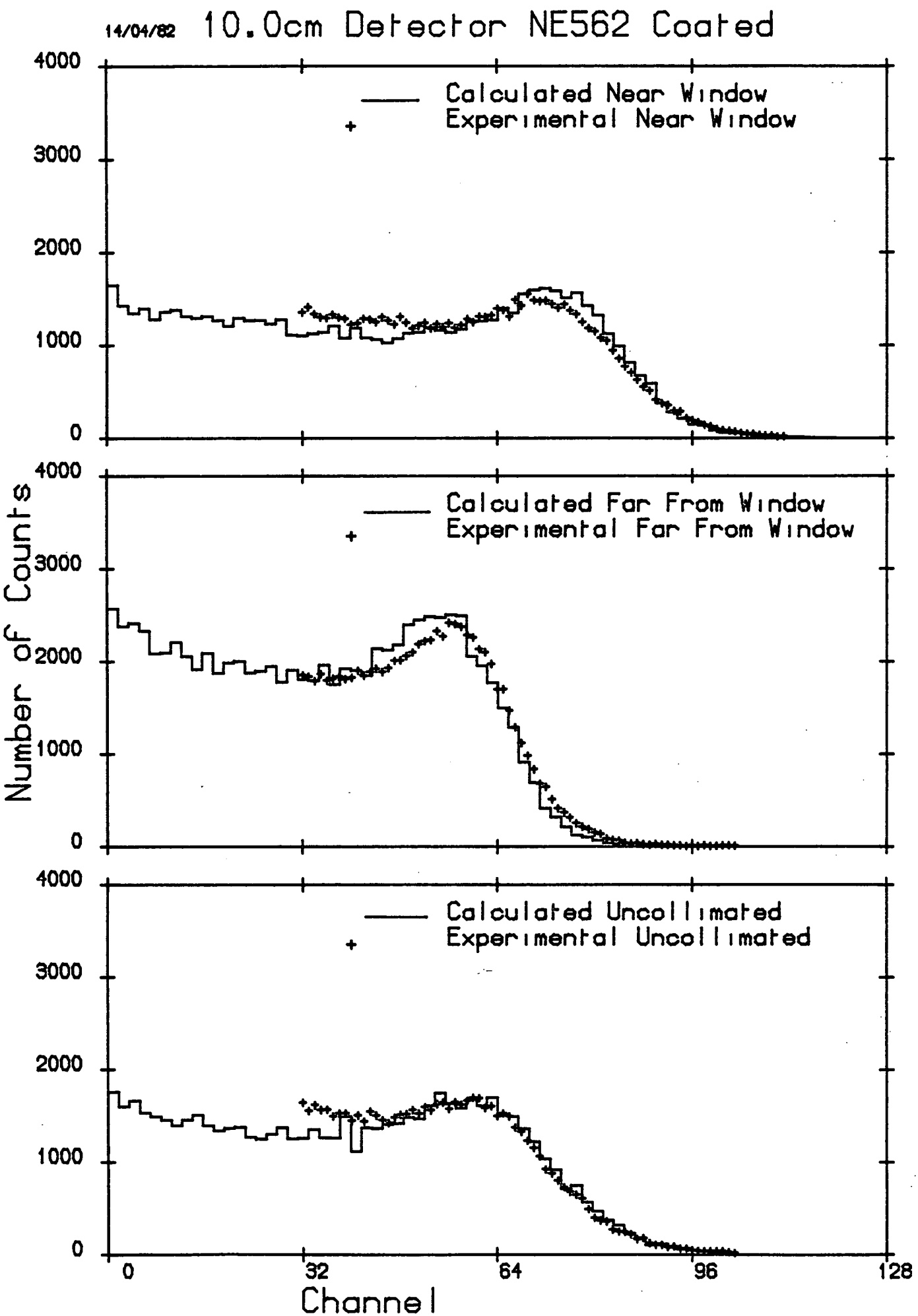
14/04/82 10.0cm Detector NE562 Coated
Calculated Near Window
Experimental Near Window
Calculated Far From Window
Experimental Far From Window
Calculated Uncollimated
Experimental Uncollimated
Number of Counts
Channel
0
1000
2000
3000
4000
32
64
96
128

Figure: 3.17

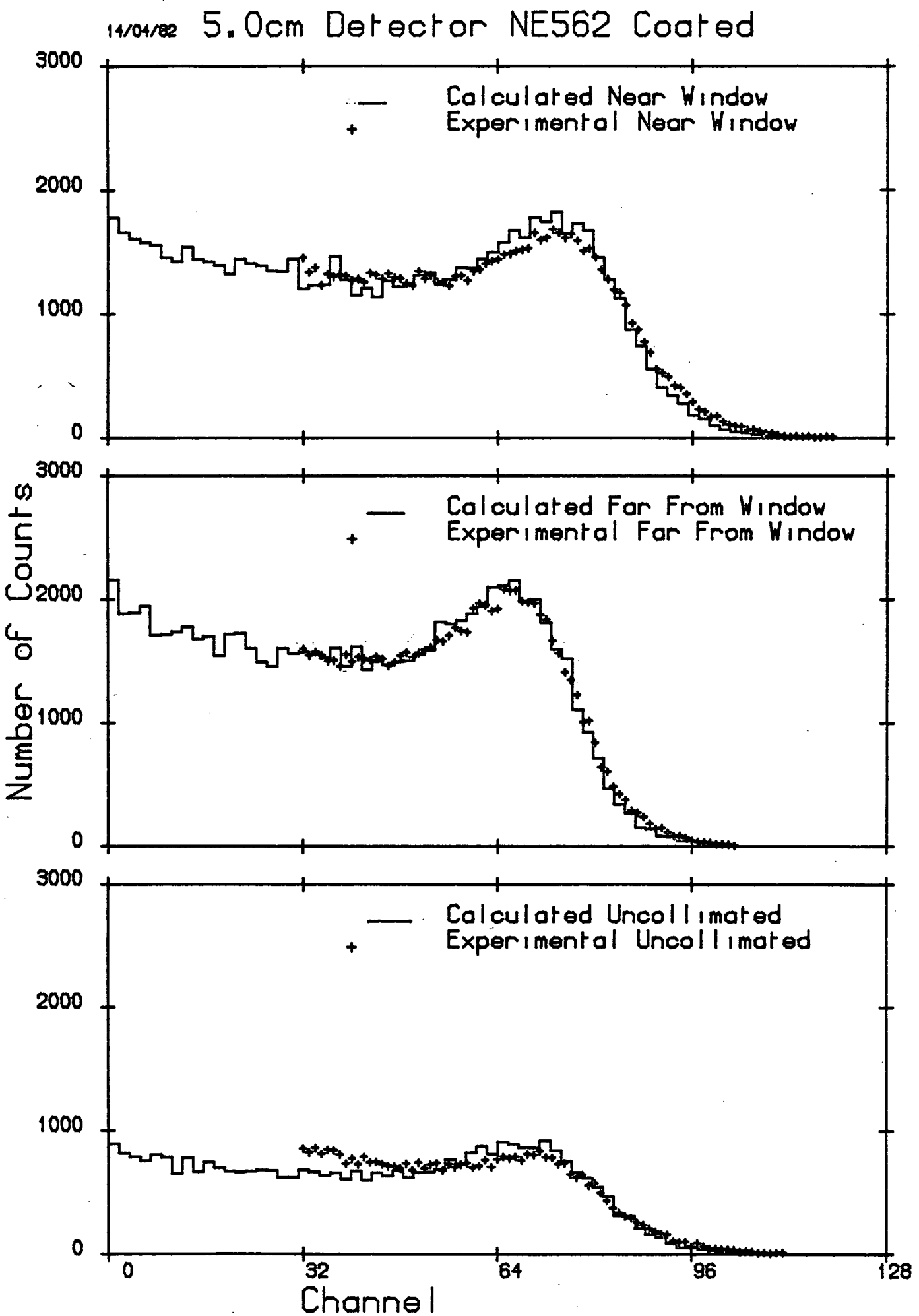
14/04/82 5.0cm Detector NE562 Coated
Calculated Near Window
Experimental Near Window
Calculated Far From Window
Experimental Far From Window
Calculated Uncollimated
Experimental Uncollimated
Number of Counts
Channel
3000
2000
1000
0
32
64
96
128

Figure: 3.18

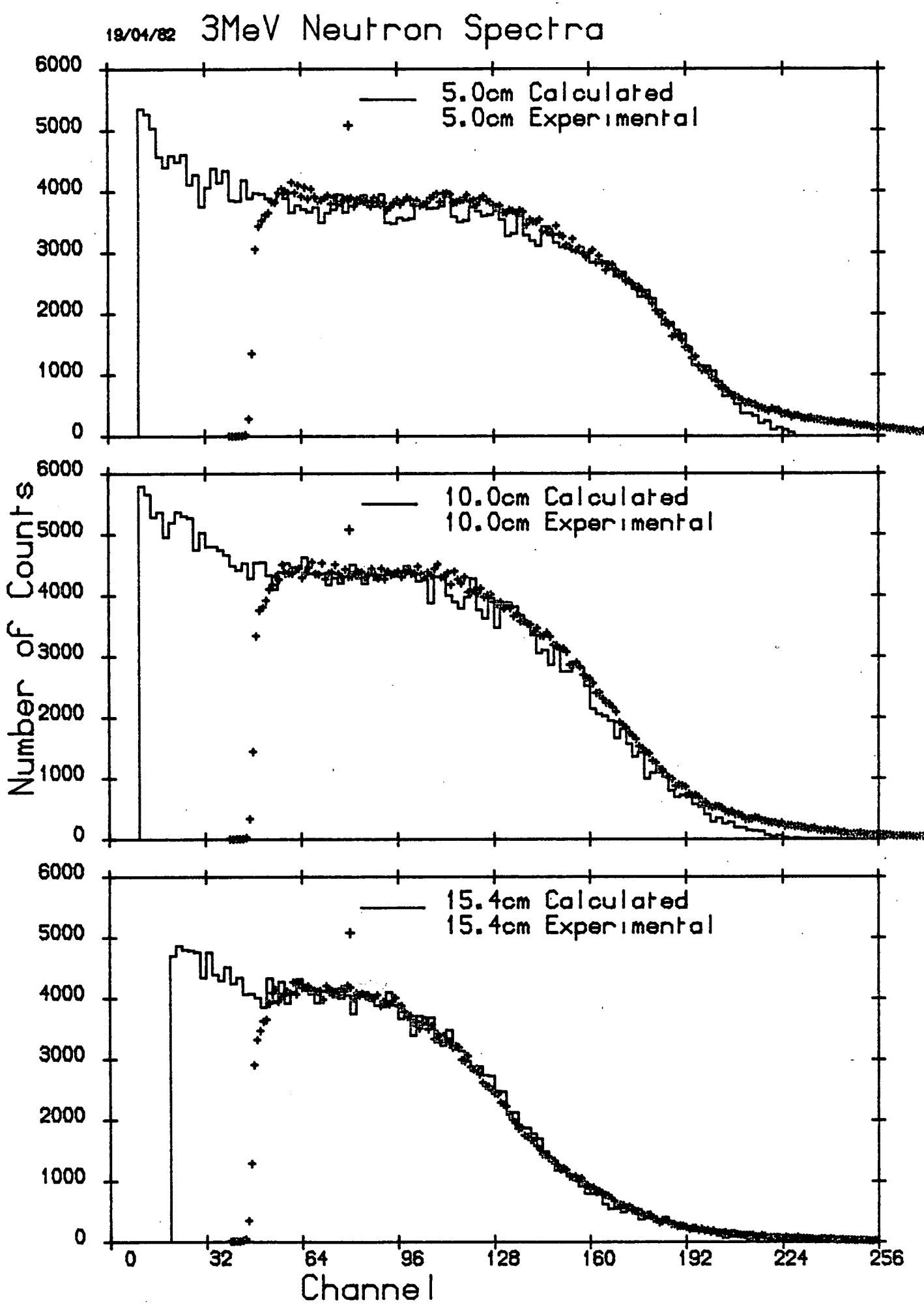
19/04/82 3MeV Neutron Spectra
5.0cm Calculated
5.0cm Experimental
10.0cm Calculated
10.0cm Experimental
15.4cm Calculated
15.4cm Experimental
Number of Counts
Channel
0
1000
2000
3000
4000
5000
6000
32
64
96
128
160
192
224
256

Figure: 3.19

17/04/82 15.4 cm Detector

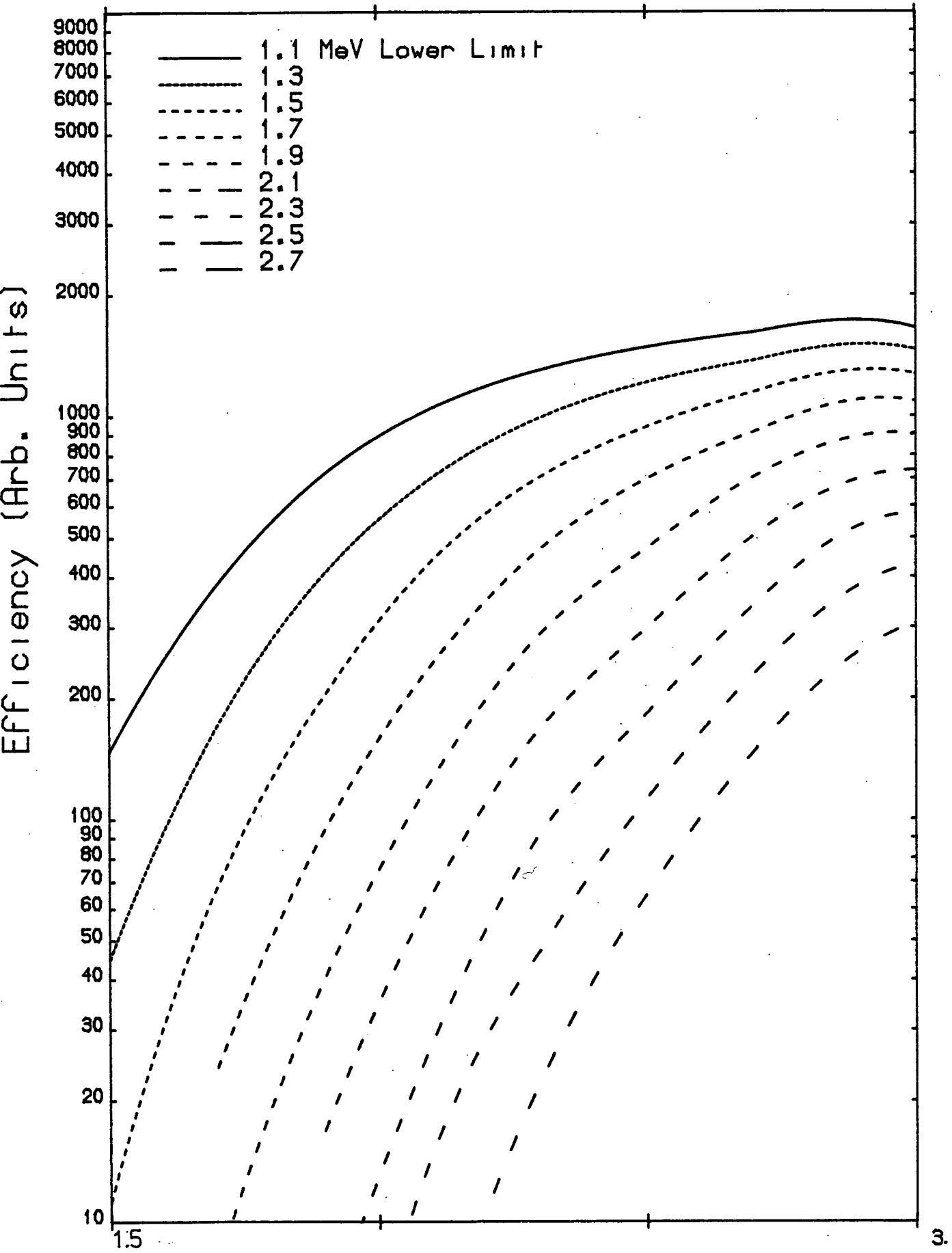

Figure: 3.20

17/04/82 10.0 cm Detector

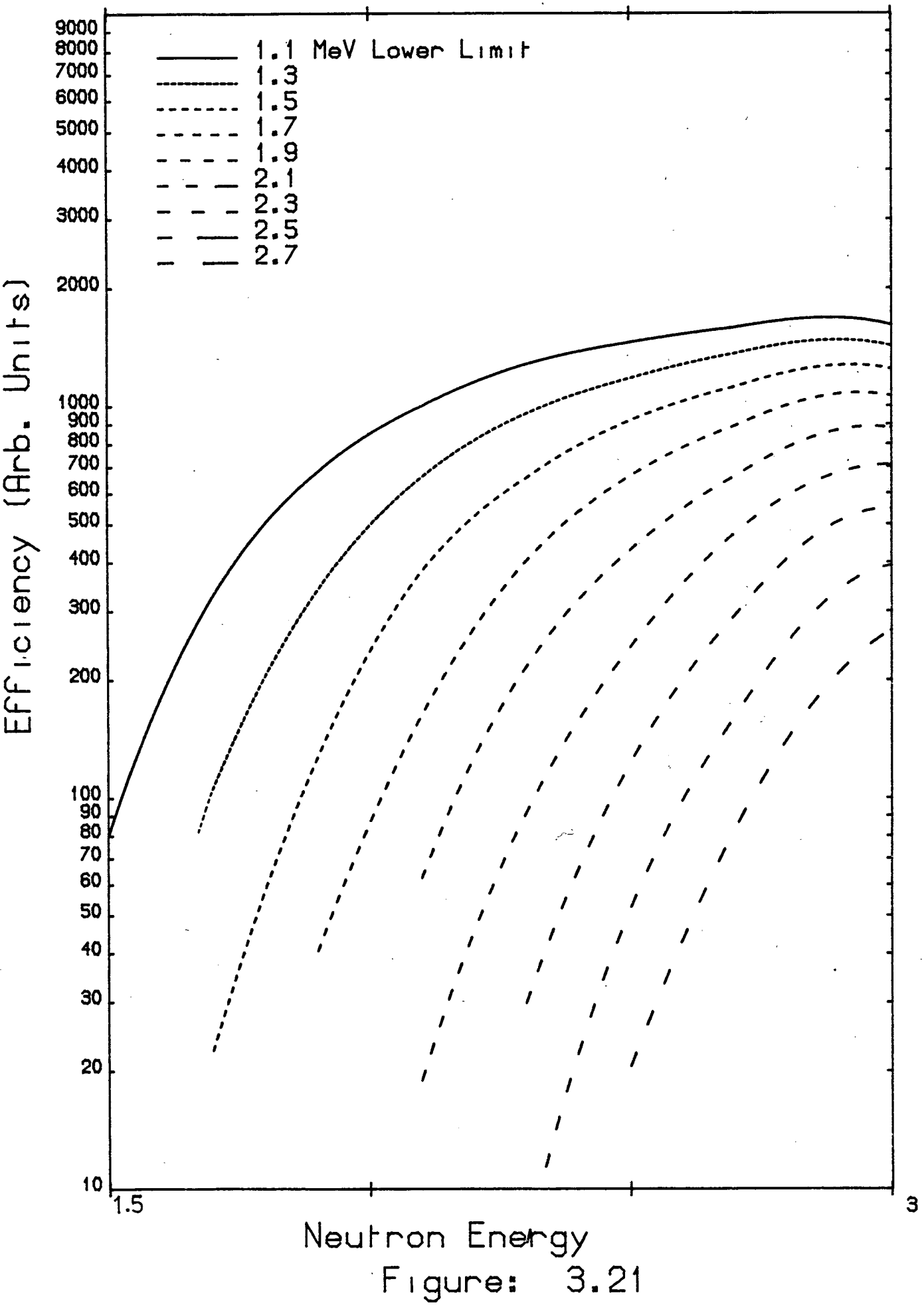

Figure: 3.21

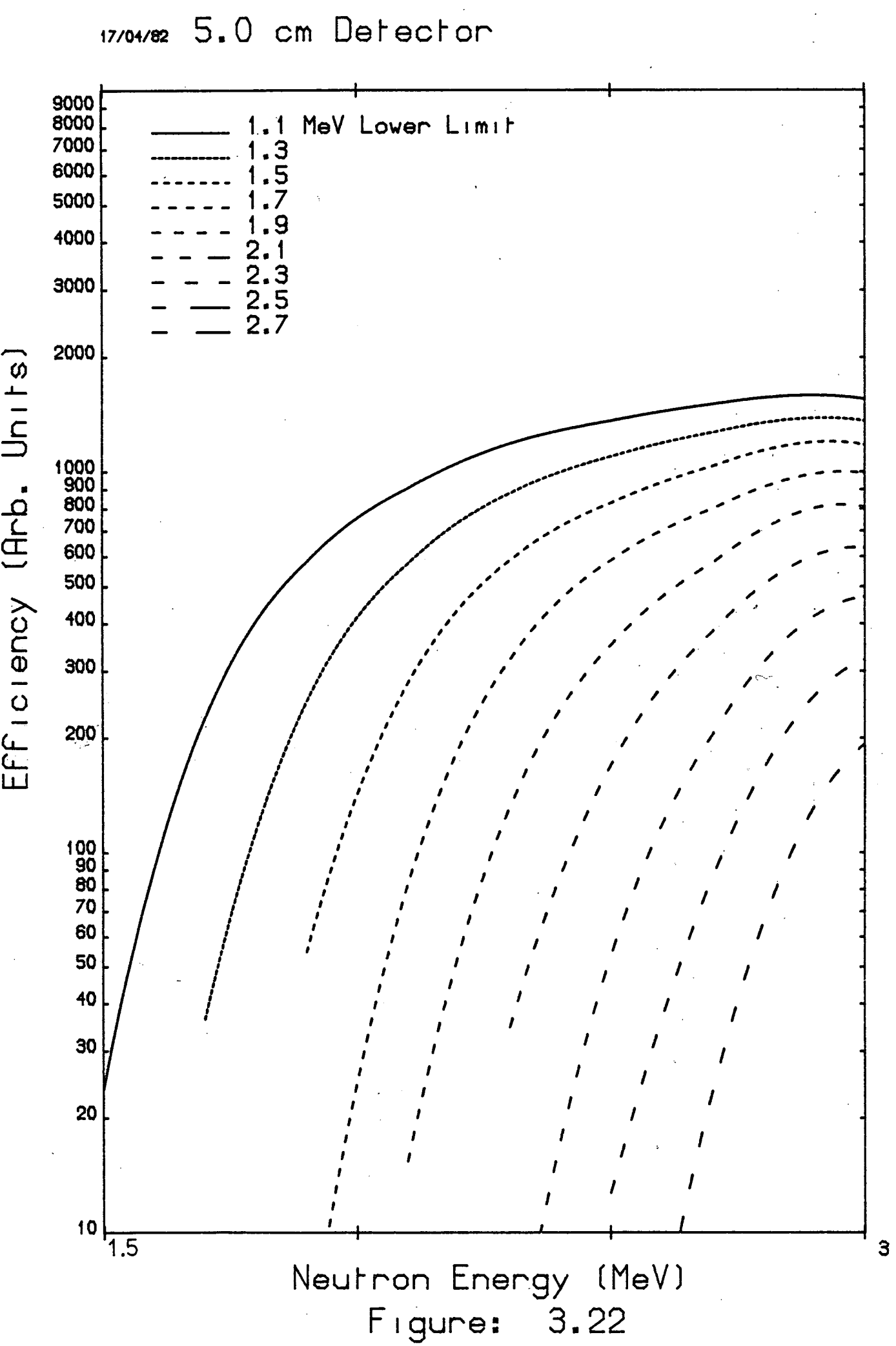
17/04/82 5.0 cm Detector
1.1 MeV Lower Limit
1.3
1.5
1.7
1.9
2.1
2.3
2.5
2.7
9000
8000
7000
6000
5000
4000
3000
2000
1000
900
800
700
600
500
400
300
200
100
90
80
70
60
50
40
30
20
10
Efficiency (Arb. Units)
1.5
3
Neutron Energy (MeV)

Figure: 3.22

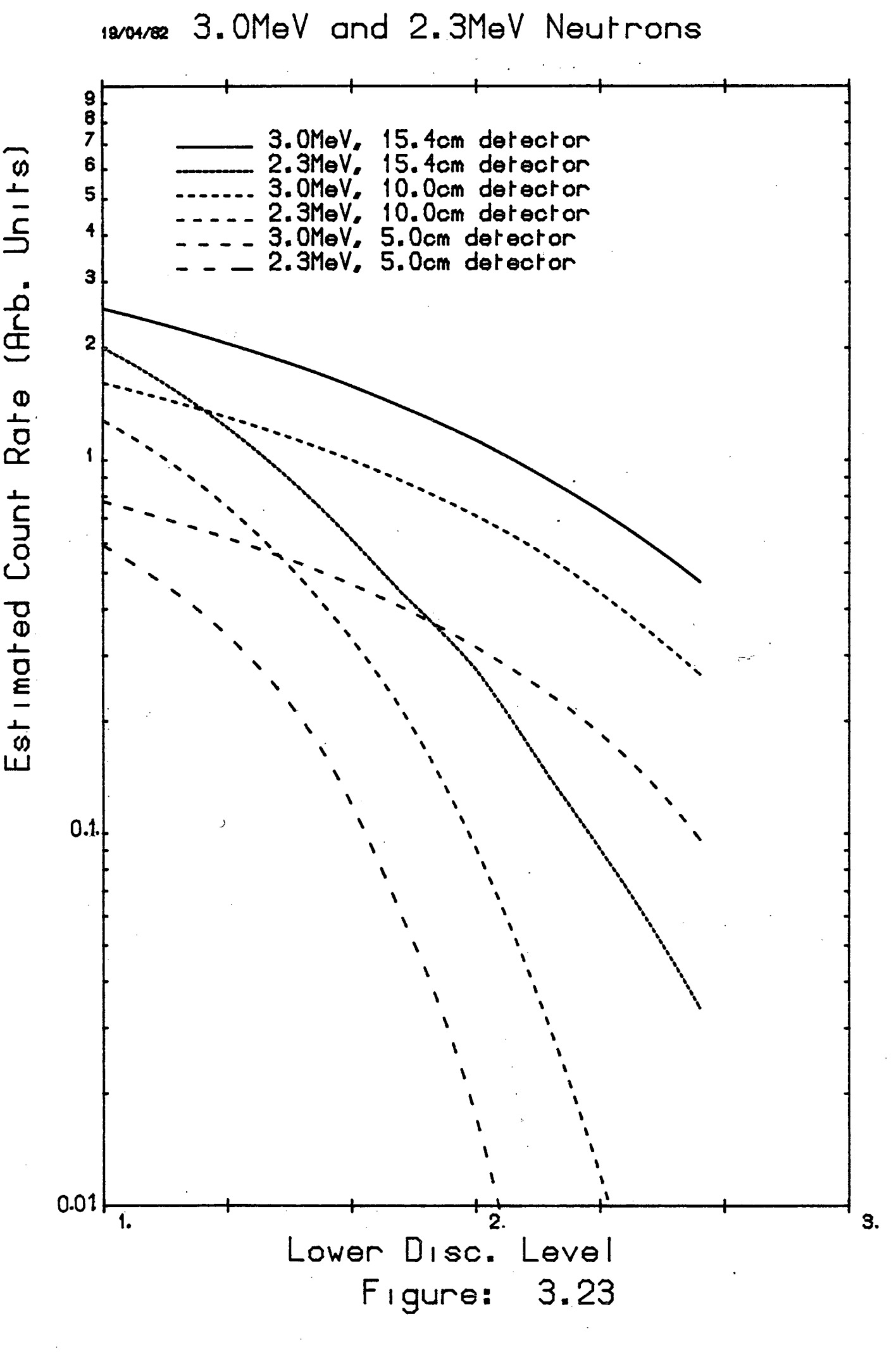
19/04/82 3.0MeV and 2.3MeV Neutrons
3.0MeV, 15.4cm detector
2.3MeV, 15.4cm detector
3.0MeV, 10.0cm detector
2.3MeV, 10.0cm detector
3.0MeV, 5.0cm detector
2.3MeV, 5.0cm detector
Estimated Count Rate (Arb. Units)
9
8
7
6
5
4
3
2
1
0.1
0.01
1.
2.
3.
Lower Disc. Level

Figure: 3.23

Chapter 4

Corrections for Finite Sample Size Effects

4.1 Introduction

Corrections for flux attenuation and multiple scattering of neutrons in solid and bored out cylindrical samples have been attempted by several experimenters in the field of fast neutron scattering [56-66]. Methods of correction fall into two broad categories, analytical and Monte Carlo, although a combination of the two is often taken. The former always involves some simplifying assumption, which may sometimes appear quite drastic, but is comparatively quick to calculate; while the latter may in principle be made as exact as is needed at the expense of greatly prolonged calculation time. It is impossible without some computing backup.

Early straight analytical methods [56] can be calculated without computers but are not good enough for accurate highly anistropic cross-sections. However refinements developed by Cox [57] and Kinney [62] have enabled the use of this method on fairly recent time of flight neutron differential cross sections [66] with some success, provided the sample size is not too large.For analysing powers a combined analytical/Monte Carlo method has been tried by Zijp and Jonker [16], and one involving successive volume integrations by Stinson et al [65]. The latter has the drawback of taking potentially longer to calculate than the Monte Carlo method, as computing time is roughly proportional to N^k where N is the number of volume elements used and k the number of multiple scatterings considered.

Monte Carlo corrections to both analysing power and differential cross section measurements have been formulated. For differential cross sections the program "Maggie" [64], whose very comprehensiveness can make it somewhat unwieldy to use, and the method of Holmquist et al

[60] have been used to correct data from previous polarimeters in the Edinburgh Neutron Physics Laboratory. A method which explicitly accounts for depolarisation of neutrons during the multiple scattering process was developed by Aspelund et al [61] but its use seems to have been confined to correction of ^{4}He and ^{12}C analysing power data. This is also true of a similar program by Millar [63].

It was decided to investigate finite sample size effects more carefully for the following reasons. Most cross section corrections are formulated on the assumption that time of flight neutron spectra are taken. Here recoil proton spectra are recorded so that elastic and inelastic neutrons are not conveniently separated if it is not feasible to exclude inelastic neutrons by raising the pulse height discrimination level. Thus the methods to be described here are concerned with the extraction of elastic scattering data only. Reports of Monte Carlo polarisation corrections have concentrated on ^{4}He and ^{12}C analysing power distributions which have a less complex structure than those of heavier elements. Most data on medium to heavy nucleus analysing powers give the size of corrections but omit to describe in detail the method of correction. One exception [16] used a combined Monte Carlo, analytical approach. However they, in common with all other workers have used smaller scattering samples than is being attempted here. The large size, up to 0.8 Mean Free Path Radius(MFPR) was used so that analysing power data of good statistical accuracy might be taken within reasonable measurement times of up to 100hr. MFPR is a convenient measure of sample size, taken as

$$MFPR = \sigma_T pR$$

σ_T: total cross section in barns

p: number nuclei/Å^3

R: sample radius in cm.

Two approaches were tried, one similar to the semi-analytical methods of Kinney and Cox and the other incorporating the ideas of Aspelund et al and Holmquist et al. The expectation was that corrections using large scattering samples would be large and so the analytical method would provide a reasonable initial guess at analysing powers and differential cross sections for use in the Monte Carlo correction. Corrections presented here relate to solid cylindrical scattering samples and assume the same experimental geometry as depicted in figure 1.2.

4.2 The Analytical Approach

This is in fact a combined analytical and Monte Carlo approach as some parameters are difficult to calculate sufficiently accurately solely from analytical formulae. Instead empirical fits to the output of Monte Carlo calculations are made. For the sake of convenience of calculation it is normally assumed that neutron flux attenuation, multiple scattering and angular spread corrections are separable, combining after calculation to give the full correction.

4.2.1 Flux Attenuation

This was calculated for each angle, to the left and right of the scattering sample, at which data was taken, denoted μ.

$$F(\mu)=\int_V\{\sigma_d(E_d,\mu_0)\exp-[\sigma_T(E_0)pl + \sigma_T(E)pl']\}dV/r^2 \Big/ \int_V\{\sigma_d(E_d,\mu_0)\}dV/r^2 \qquad (4.1)$$

σ_d: source reaction cross section

E_d: charged particle energy

μ_0: angle at which source neutrons selected

p: nuclear density in scattering sample

σ_T: total cross section

l: distance in sample before 1st collision

l′: distance in sample before exit from sample

r: distance from neutron source to collision point

E_0: source neutron energy

E: neutron energy after collision

E may be set equal to E_0 if elastic scattering is dominant or the energy dependence of the total cross section is slight . Source anisotropy generally has a negligible effect on differential cross sections but may effect analysing power measurement, by inducing a spurious right, left scattering ratio.

$$R_f(\mu) = F_R(\mu)/F_L(\mu) \qquad (4.2)$$

The effect is largest when the sample is close to the neutron source and of large radius, with incident neutrons coming at an angle where the differential cross section is varying rapidly. The flux attenuation shows an angular dependence which becomes more marked as MFPR increases. Calculated values of $F(\mu)$ and $R_f(\mu)$ are illustrated in figures 4.1 and 4.2 for samples of 2.5cm radius, 5.0cm height ,0.7 MFPR and 1.3cm radius, 5cm height, 0.36 MFPR, both situated 100cm from the neutron source. The source neutrons are of energy 3.0 MeV produced by the $^2H(d,n)^3He$ reaction at 49 degrees with deuteron energy of 390 KeV. Reaction cross sections are generated from the data of [67]. Correction for flux attenuation is made by dividing experimental cross sections by $F(\mu)$ and experimental right left scattering ratios by $R_f(\mu)$

4.2.2 Multiple Scattering Correction

The experimental differential cross section is least squares

12/04/82 Angular Dependence Flux Attenuation

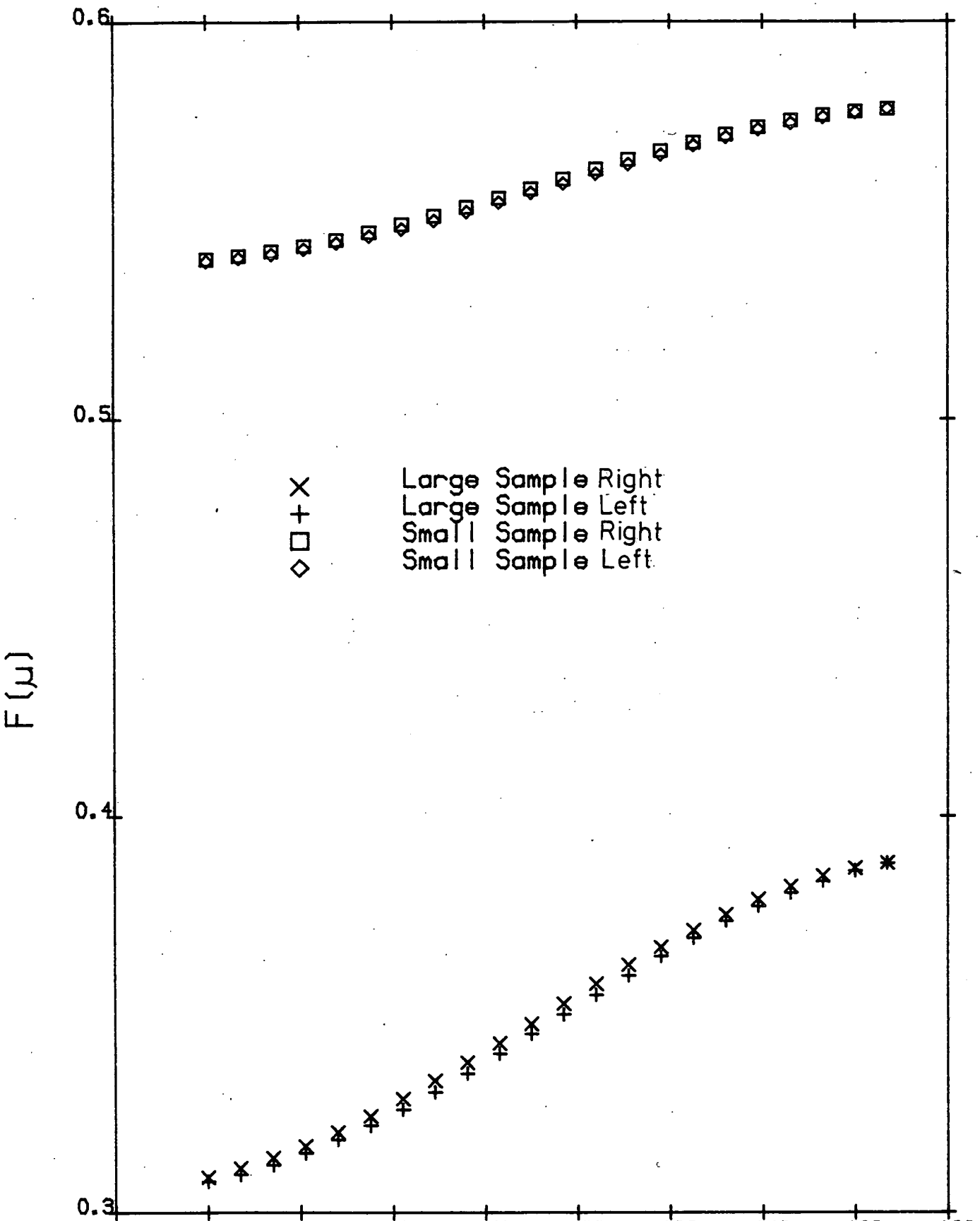

Figure: 4.15

12/04/82 Effect of Source Anisotropy

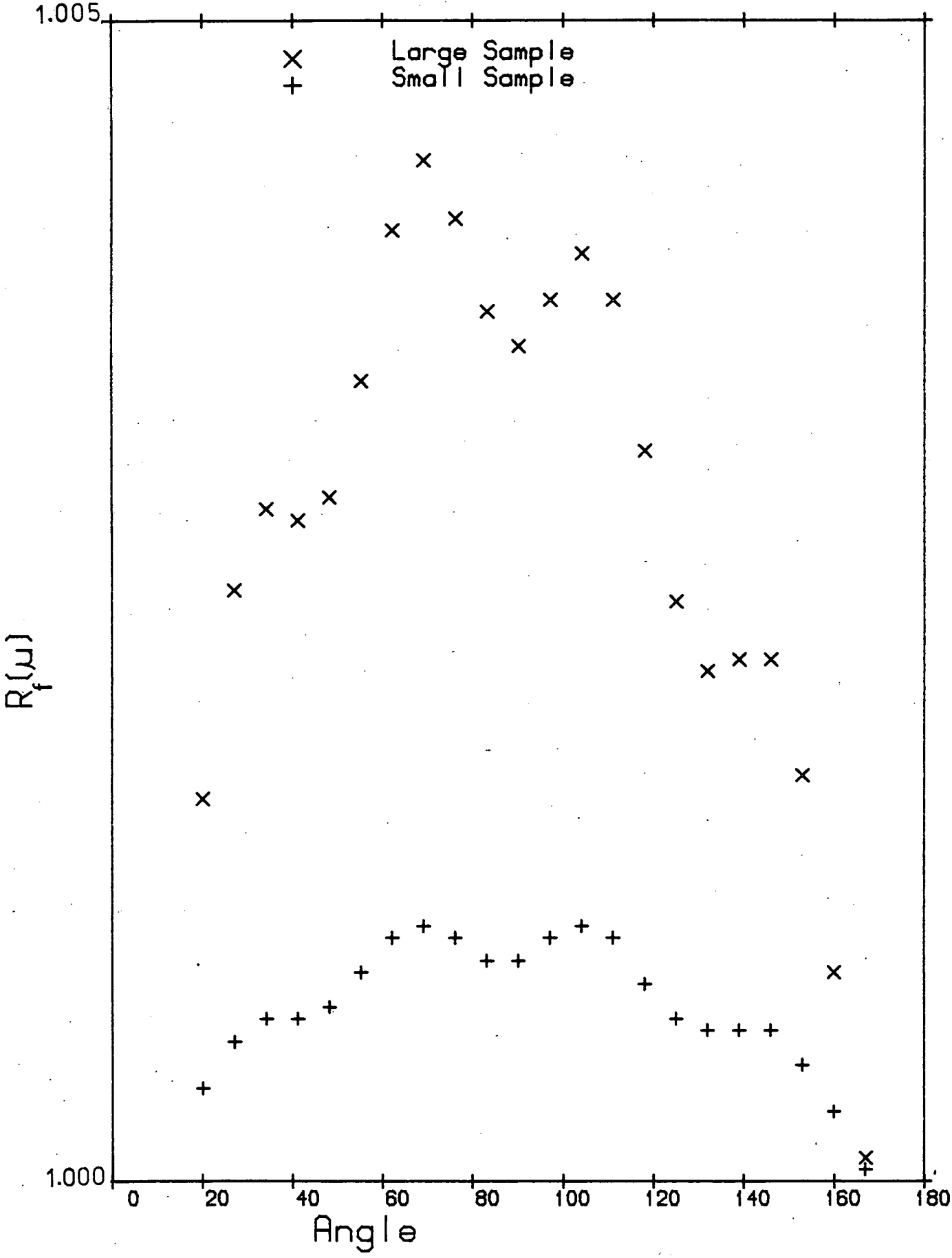

Figure: 4.2

fitted by a legendre polynomial expansion in the cosine of the lab angle, μ

$$U_{exp} = \sum_{l} a_l P_l(\mu) \tag{4.3}$$

The correction is then made on the coefficients a_l which are normalised to a_0 equal to unity. When using proton recoil spectra, the experimental distribution includes, as well as the single scattering elastic events of interest, non-elastic singles events and various combinations of elastic and inelastic multiple events. Thus U_{exp} is a weighted sum of the open channel single scattering distributions U_i, double scattering distributions, U_{ij}, triple scattering distributions, U_{ijk}, and so on. The subscripts i,j,k denote either elastic or any of the energetically possible inelastic channels in the first second and third collisions respectively. The number of channels accounted for is reduced to manageable proportions by raising the pulse height discrimination level on the recoil spectra. The U may also be expressed as legendre polynomial expansions.

$$U_i = \sum_{l} b_{il}(E_0) P_l(\mu) \tag{4.4}$$

$$U_{ij} = \sum_{l} b_{il}(E_0) b_{jl}(E_i) P_l(\mu)/(2l+1) \tag{4.5}$$

$$U_{ijk} = \sum_{l} b_{il}(E_0) b_{jl}(E_i) b_{kl}(E_{ij}) P_l(\mu)/(2l+1)^2 \tag{4.6}$$

The extension to higher scattering orders is obvious. E_i and E_{ij} are respectively the average energy after scattering "i" and the average energy after scattering "i" followed by scattering "j". They are taken as

$$E_i = \{\int E_{lab}(\mu, E_0) U_i d\mu\} / \{\int U_i d\mu\} \tag{4.7}$$

$$E_{ij} = \{\int E_{lab}(\mu, E_i) U_{ij} d\mu\} / \{\int U_{ij} d\mu\} \tag{4.8}$$

Making a generalisation of the expression given by Kinney [62], the experimental differential cross section can be expressed as

$$\begin{aligned} \sigma_{exp} U_{exp} = K[&\sum_i \sigma_i U_i Q_{1i} e_i \\ &+ \sum_{ij} \sigma_i \sigma_{jT} U_{ij} R_{1i} Q_{2j} e_{ij} \\ &+ \sum_{ijk} \sigma_i \sigma_{jT} \sigma_{kT} R_{1i} R_{2j} Q_{3k} e_{ijk} U_{ijk}] \end{aligned} \tag{4.9}$$

$\sigma_i = \sigma_i(E_0)$, angle integrated cross section

σ_T: total cross section

$\sigma_{jT} = \sigma_j(E_i)/\sigma_T(E_i)$

$\sigma_{kT} = \sigma_k(E_{ij})/\sigma_T(E_{ij})$

$Q_{1i} = Q_1(E_i, \mu_i)$, the escape probability after the 1st collision

$Q_{2j} = Q_2(E_{ij}, \mu_j)$, the escape probability after the 2nd collision

$Q_{3k} = Q_3(E_{ijk}, \mu_k)$, the escape probability after the 3rd collision

e_i: the detection efficiency after 1 collision

e_{ij}: the detection efficiency after 2 collisions

e_{ijk}: the detection efficiency after 3 collisions

$R_{1i} = R_1(E_i, \mu_i)$, the probability of further collision after the 1st collision

$R_{2j} = R_2(E_{ij}, \mu_j)$, the probability of further collision after the 2nd collision

K: a constant of proportionality

The detection efficiencies are taken from the results of Chapter 3. Following Kinney [62], R_{1i} and R_{2j} are taken to depend on energy and average angle of previous scattering only. This has also been carried over to the Q which Kinney assumed constant. Generally these parameters will have explicit angle dependence instead of just being taken to depend on an average angle of scattering, but some of this has been absorbed into the flux attenuation correction. Extracting U_l from the single scattering terms of equation 4.9, substituting equations 4.4, 4.5 and 4.6 into 4.9, and equating terms of equal l in the Legendre expansions. the multiple scattering corrected Legendre coefficients can be expressed as

$$b_{ll} = \{\sigma_{exp} a_l/K - \sum_{i\neq l} \sigma_i Q_{li} e_i b_{il} - \sum_{ij} \sigma_i \sigma_{jT} R_{1i} Q_{2j} e_{ij} b_{il} b_{jl}/(2l+1) - \sum_{ijk} \sigma_i \sigma_{jT} \sigma_{kT} R_{1i} R_{2j} Q_{3k} e_{ijk} b_{il} b_{jl} b_{kl}/(2l+1)^2\}/ /\{\sigma_l Q_{ll} e_l\} \quad (4.10)$$

K may be found by setting l to zero and hence all the a_l and b_l to 1. Again extension to higher scattering order is obvious. Equation 4.10 is solved by substituting an initial guess for b_{ll} on the right hand side and iterating until convergence is achieved. The guess values may be the a_l but faster convergence was achieved using the output from OM calculations. The final value does not depend on the input guess as long as this is not too far out. The speed of convergence is faster for small samples where corrections are smaller, 3 iterations for the 0.36 MFPR sample and 5 iterations for the 0.7 MFPR sample.

Correction of analysing powers is based on the assumption that processes other than single shape elastic scattering cause complete depolarisation. Where compound inelastic scattering dominates and multiple shape elastic events produce neutrons which are substantially

depolarised, this should be a fairly good approximation. It is left to the Monte Carlo correction to account for polarisation in multiple shape elastic events. The correction therefore can be derived from equation 4.9. If right,left ratios are not unity only when i,j and k equal 1,then the experimental right/left ratio can be expressed as

$$R_{exp}(\mu) = [\sigma_{R1}(\mu)+\sigma_m(\mu)]/[\sigma_{L1}(\mu)+\sigma_m(\mu)] \qquad (4.11)$$

$\sigma_m(\mu)$: multiple scattering and inelastic correction to the experimental differential cross section

The experimental analysing power is

$$A_{exp}(\mu) = (R_{exp}(\mu)-1)/(R_{exp}(\mu)+1)/P_1$$

P_1 : polarisation of incident neutron beam

The corrected right, left ratio is therefore

$$R_c(u) = \{\sigma_{exp}(\mu)[1+P_1A_{exp}(\mu)]-\sigma_m(\mu)\}/\{\sigma_{exp}(u)[1-P_1A_{exp}(\mu)]-\sigma_m(\mu)\} \qquad (4.12)$$

4.2.3 Angular Spread Corrections

A full account of finite sample and detector size effects would require the evaluation of a double integral over the sample volume and detector surface, which would require large amounts of computing time, several times more than the rest of the combined analytical correction procedure. As finite sample size effects are accounted for in the Monte Carlo procedure, and the scattering sample is far enough away from the neutron source for this correction to be small compared with flux attenuation and multiple scattering, it was neglected for the analytical correction.

Detector size effects which were not accounted for in the Monte Carlo correction, were calculated using an iterative procedure. The distributions corrected for flux attenuation and multiple scattering were integrated over the angle subtended at the sample by the detector and compared with the value of the distribution at the nominal detector angle. The distributions for integration were then corrected until the angle integrated value agreed with the nominal detector angle value.

4.3 The Monte Carlo Approach

In principle no artificial separation need be made between the various effects which modify differential cross sections and analysing power measurements. This however can lead to an inefficient program with respect to calculational time and a compromise is often reached. Here it was found simpler to calculate the flux attenuation first and then perform a combined calculation on multiple scattering and finite size effects. Detector size effects were not included as they were considered small enough to approximate analytically, and would have greatly increased the time for a calculation coming at the end of a chain of calculations. Angle dependence was not included in the flux attenuation as this is absorbed into the Monte Carlo routine. An attempt was made to simulate the experimental set up in so far as this did not impair the mathematical efficiency of the program, and to track the neutron as it passes through the sample, eventually scattering into the detector. Randomly varying parameters are calculated using a function Z(a,b) which yields values in the range a to b inclusive , all values having equal probability.

Neutrons are started from the source at energy E_0 with mathematical weight w which depends on the reaction cross section.

$$w = w_0 \sigma_d(E_d, \mu_0) \tag{4.13}$$

The cos of the polar angle, μ_0, and the asimuthal angle are calculated using the function Z(a,b), subject to the constraint that the neutron hits the scattering sample. The first collision point is calculated using the following [51]

$$d' = -(1/\sigma_T p)\ln\{1-Z(0,1)[1-\exp(-\sigma_T d)]\} \tag{4.14}$$

d': distance to collision point

d: thickness of sample material in path of neutron

Neutron direction after scattering is calculated using Z(a,b) weighted by the differential scattering cross section, with the next collision point evaluated using equation 4.14. The neutron scattering channel, elastic or inelastic, is sampled at each collision according to its angle integrated cross section. Probable scattered weights to each left and right detector are calculated and stored at each collision.

$$w_p = w\exp(-\sigma_T(E)1'p)U_i(E,\mu)R(E,\mu,\phi)e(E)/r^2 \tag{4.15}$$

R(E,μ,ϕ): scattering ratio (equals 1 for unpolarised neutrons)

ϕ : asimuthal angle

The weight at the collision point, w, is not effected. This is reduced on each successive collision according to the probability of escape from the scattering sample. Both w and w_p may be made polarisation dependent to any scattering order using the formulae of Aspelund et al [61]. Polarisation was accounted for in the 1st and 2nd collisions. Extension to a 3rd collision makes a negligible difference to the final results. The number of collisions is kept to a minimum to speed the calculation. Three collisions was adequate for both samples.

Uncertainties in accumulated detector neutron weights were found by taking the standard deviation of the results of several sub-runs.

Cross sections and right, left ratios are corrected by comparing experimental and simulated distributions.

$$R_c = R_{exp} W_L / W_R \; R_I \tag{4.16}$$

$$U_c = U_{exp} / (W_L W_R)^{1/2} \; U_I \tag{4.17}$$

Where W_L and W_R are the accumulated detector weights suitably normalised. This approximate method tends to overestimate the magnitude of the correction and so if the initial guess at the distribution is too far out, the whole process must be iterated until satisfactory convergence is achieved. The error in the corrected distribution takes into account both the experimental and Monte Carlo errors. The subscript I denotes the initial guess

$$dU_c = U_c \{ (dU_{exp}/U_{exp})^2 + 1/2[(W_R dW_L)^2 + (W_L dW_R)^2] \}^{1/2} \tag{4.18}$$

$$dR_c = R_c \{ (dR_{exp}/R_{exp})^2 + (dW_L/W_L)^2 + (dW_R/W_R)^2 \}^{1/2} \tag{4.19}$$

To find the absolute magnitude of the corrected cross section, the simulated cross section was fitted with a legendre polynomial expansion and normalised to the same integrated cross section as the flux attenuation corrected experimental cross section. The accumulated detector weights from single elastic scattering were stored separately. These were multiplied by the same normalising factor and fitted with a legendre polynomial expansion, thus yielding the integrated elastic cross section.

4.4 Calculation and Results

Programs to implement the two correction procedures were written in Fortran IV. Although the semi-analytical method appears to be

mathematically more complicated, calculation time is of the order of 50 to 100 times faster than one iteration of the Monte Carlo method. Sufficient accuracy in the analysing power correction requires the starting of a large number of neutrons, many times more than needed for the cross section correction. In this respect the program follows the experimental situation. The number of neutrons required also increases with increasing scattering sample size.

The reliability of Monte Carlo errors was tested by varying an initial input parameter in the pseudo-random number generator so that a different number sequence was obtained. The variation in simulated distributions was consistant with the calculated errors. As the analytically corrected distributions were usually used as input data for the Monte Carlo correction, no analysis of errors induced by this method was made.

In both programs cross sections and analysing powers were input at discrete energies and energy dependence approximated by interpolation, between the energy points. Experimental distributions could optionally be used as a starting approximation to the corrected distribution. However where the correction was large , output from a previous correction run, or distributions calculated from suitable Optical Potentials were used. Inelastic cross sections were taken from previous experimental data or, if not available calculated as described in Chapter 5.

Numerical integrations used in averaging energy and scattering angle in the analytical method were made using the Romberg method, and volume integrations were performed by dividing the sample into small volume sections of equal volume. The shape of the sections followed the cylindrical geometry of the scattering sample, and a 10x10x10 mesh was found adequate to ensure convergence of the calculation for the largest sample sizes considered. The values of the further collision

probabilities and escape probabilities used in the semi-analytical method were deduced from the results of previous Monte Carlo calculations. Instead of fitting these with power series expansions [57,62] in MFPR, height/radius ratio and average scattering angle, they were held as block data in a three dimensional array. The dimensions specify MFPR, height/radius ratio and cosine of the average scattering angle. Deduction of a value at a specific MFPR, height /radius ratio and angle was made by quadratic interpolation between the array elements. This is likely to be more accurate than overall quadratic fits to Monte Carlo values.

The accuracy of the correction procedures was tested on data taken using two differently sized iron scattering samples, one 2.5cm radius by 5cm high, and the other 1.3cm radius by 5.25cm high. Neutrons from the $^{2}H(d,n)^{3}He$ reaction emitted at 49 degrees with an energy of 3.0 MeV and polarisation of -0.15 were used. The MFPR of the large sample is 0.7 and for the small sample 0.36. Data was collected with a lower discrimination level of 1.9MeV on the proton recoil spectra so that only inelastic scattering associated with the first excited state (0.85 MeV) was considered

Uncorrected analysing powers and differential cross sections were calculated by the methods described in Chapter 5. Analytical and Monte Carlo corrections to the analysing power are illustrated in figures 4.3 and 4.4. There is not much difference between the Monte Carlo and analytical corrections except in the angular range 60-100 degrees. The Monte Carlo corrected analysing powers taken with small and large samples are in agreement. The detector angular spread correction can be seen to be negligible except where the distribution varies sharply.

Analytical and Monte Carlo corrections to differential cross sections are shown in figures 4.5 and 4.6. Errors shown in the former are statistical only arising from count rate and efficiency calibration

15/04/82 Analytical Correction

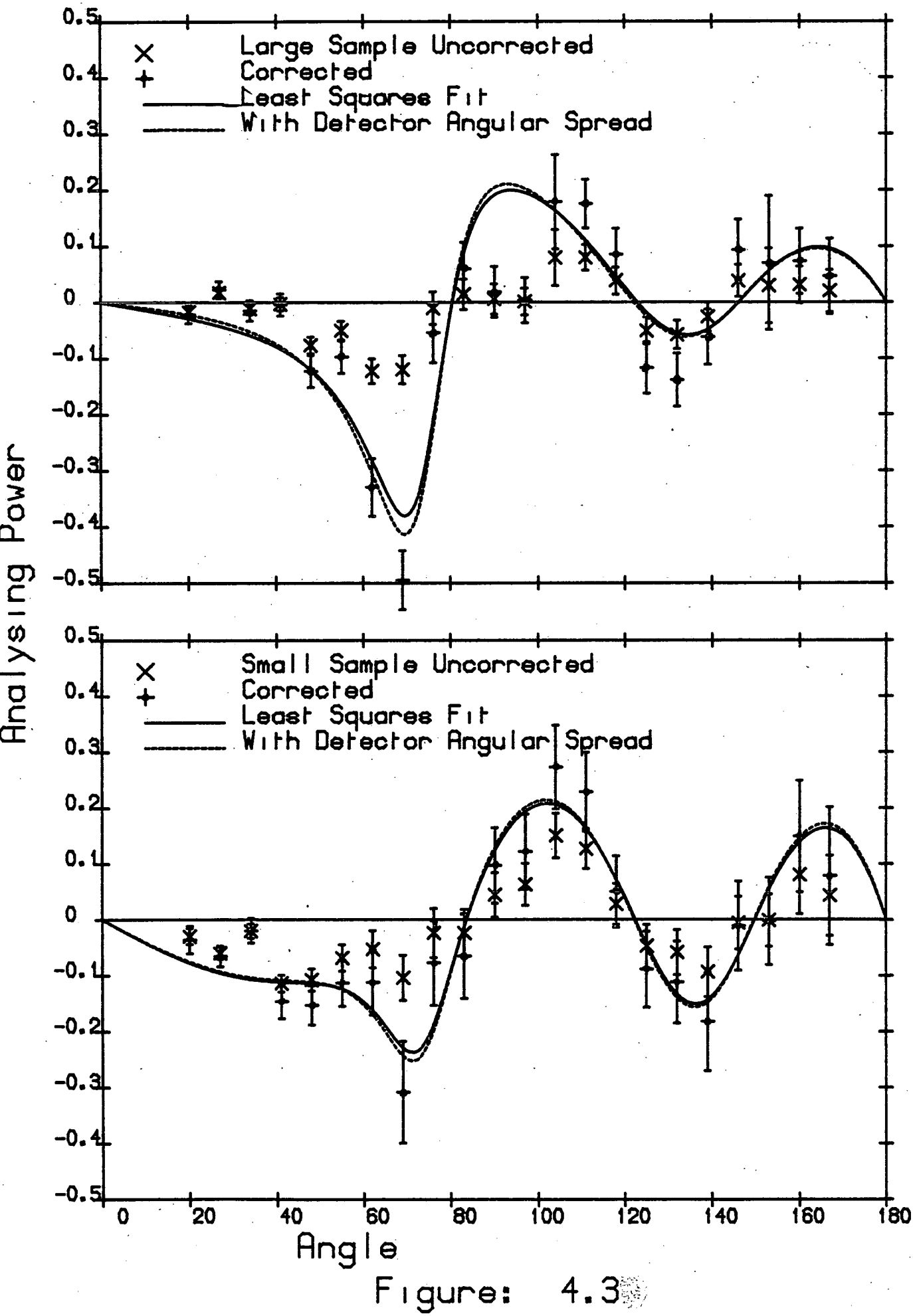

Figure: 4.3

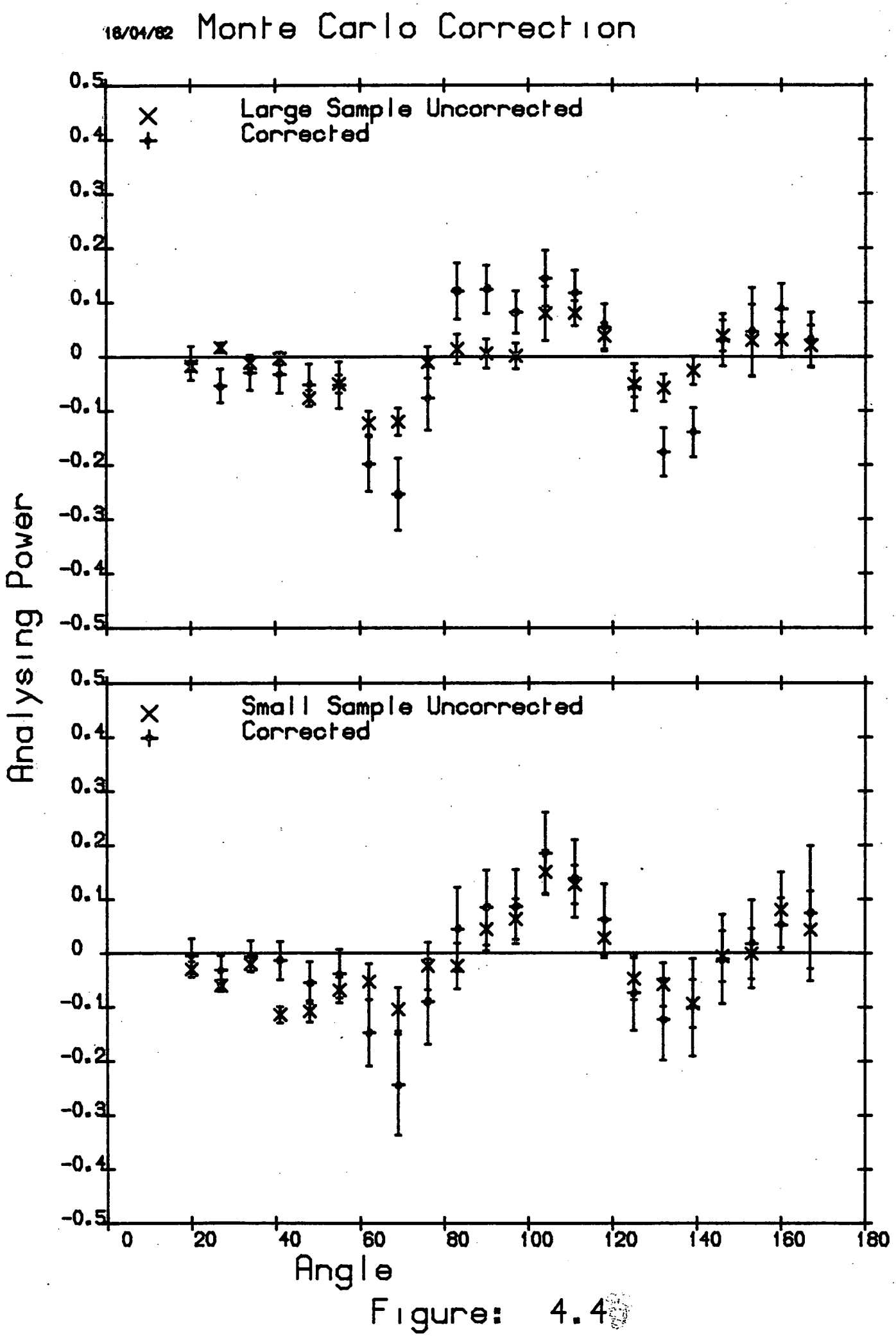
16/04/82 Monte Carlo Correction
Large Sample Uncorrected
Corrected
Small Sample Uncorrected
Corrected
Analysing Power
Angle
0.5
0.4
0.3
0.2
0.1
0
-0.1
-0.2
-0.3
-0.4
-0.5
0
20
40
60
80
100
120
140
160
180

Figure: 4.4

uncertainties. The analytical corrections tend to produce too deep a minimum in the angular region 60-100 degrees and also values which are too low at backward angles. The Monte Carlo corrected differential cross sections are in agreement.

The large sample Monte Carlo corrected analysing power is compared with the data of Ellgehausen et al [12] and Galloway and Waheed [21]. Agreement is quite good, although the distributions show differences in detail. The small sample Monte Carlo corrected differential cross section is compared with the data of Smith et al [25]. This was an accurate time of flight measurement using a small 2cm long by 2cm diameter (0.15 MFPR) scattering sample. Error bars on the present data include distance and area measurement uncertainties described in Chapter 5. Agreement here is very good.

The agreement between small and large sample corrected data and also the agreement with previous data confirm that the polarimeter is functioning correctly and that the data correction procedure is valid for the size of scattering samples used here.

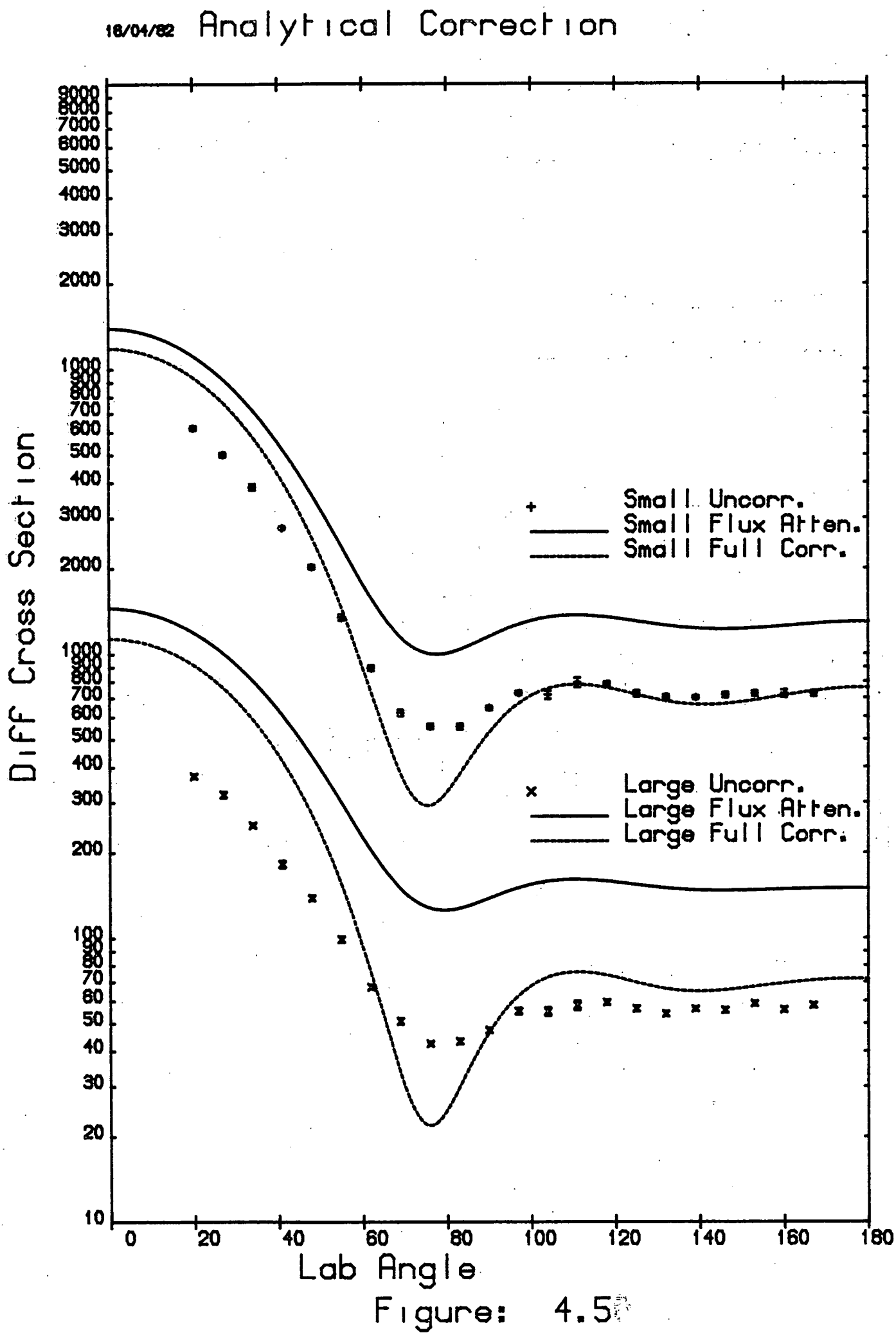
16/04/82 Analytical Correction
Diff Cross Section
Lab Angle
Small Uncorr.
Small Flux Atten.
Small Full Corr.
Large Uncorr.
Large Flux Atten.
Large Full Corr.
9000
8000
7000
6000
5000
4000
3000
2000
1000
900
800
700
600
500
400
300
200
100
90
80
70
60
50
40
30
20
10
0
20
40
60
80
100
120
140
160
180

Figure: 4.5

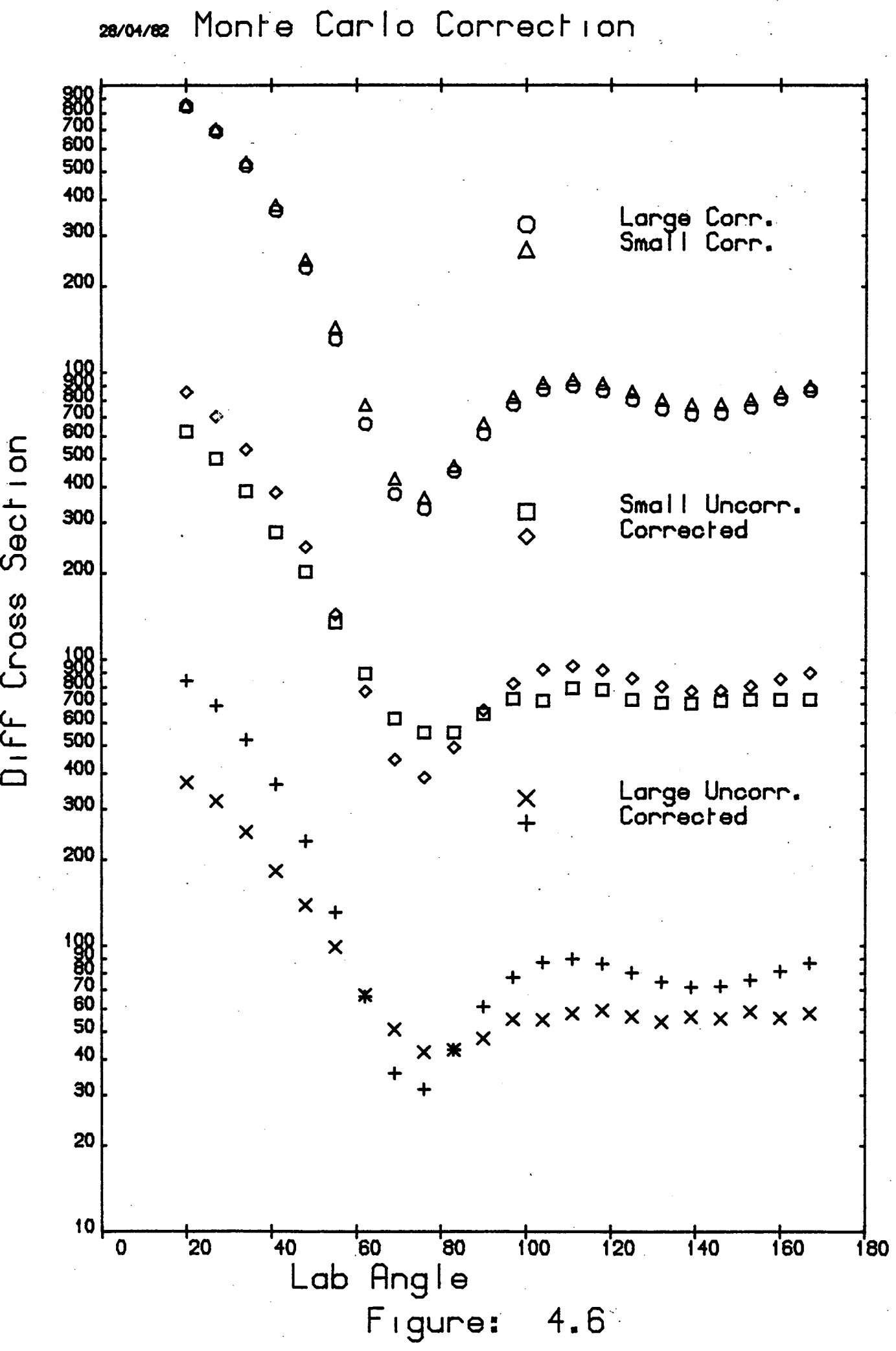
28/04/82 Monte Carlo Correction
Large Corr.
Small Corr.
Small Uncorr.
Corrected
Large Uncorr.
Corrected
Diff Cross Section
Lab Angle
0
20
40
60
80
100
120
140
160
180

Figure: 4.6

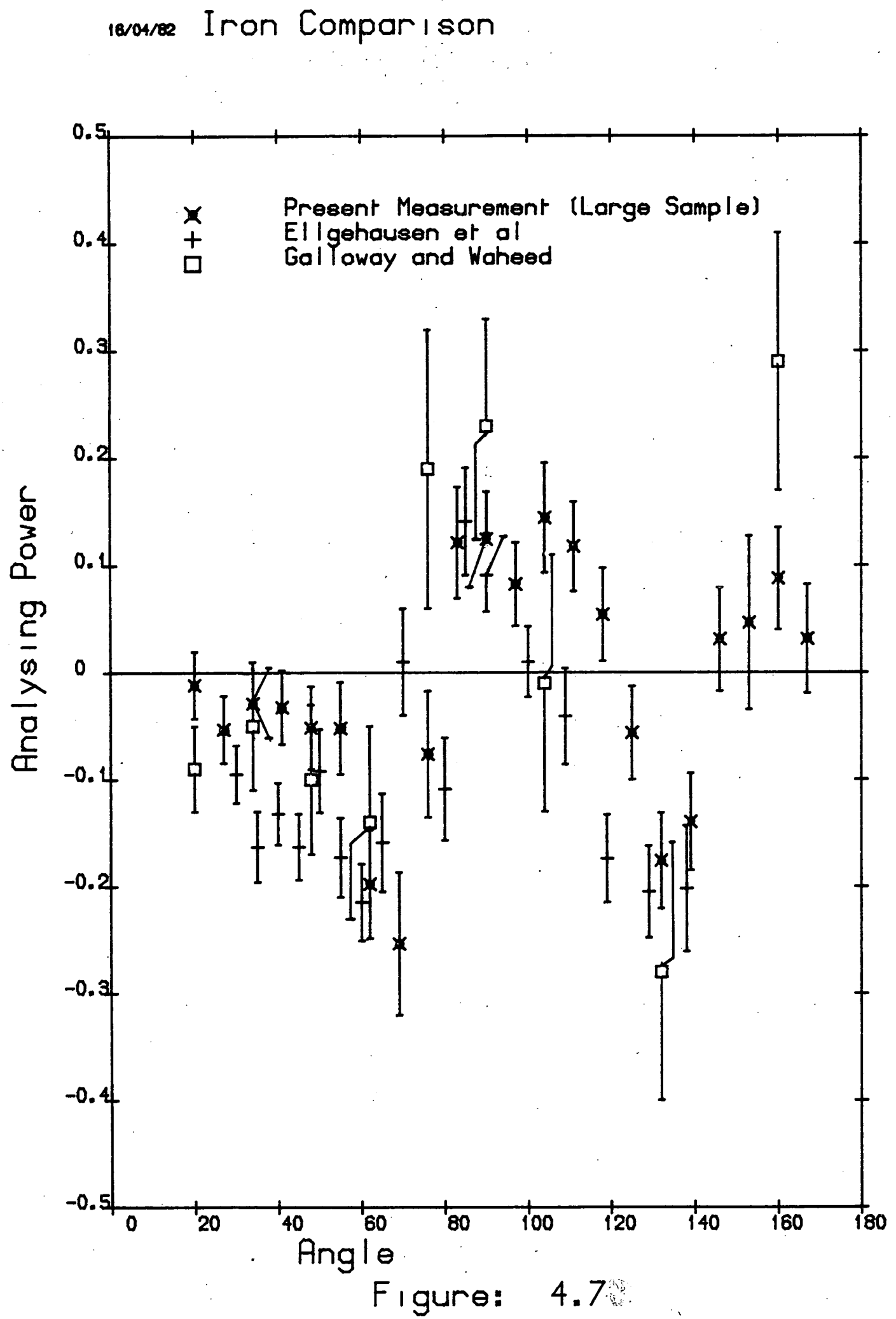
16/04/82 Iron Comparison
Present Measurement (Large Sample)
Ellgehausen et al
Galloway and Waheed
Analysing Power
Angle
0.5
0.4
0.3
0.2
0.1
0
-0.1
-0.2
-0.3
-0.4
-0.5
0
20
40
60
80
100
120
140
160
180

Figure: 4.7

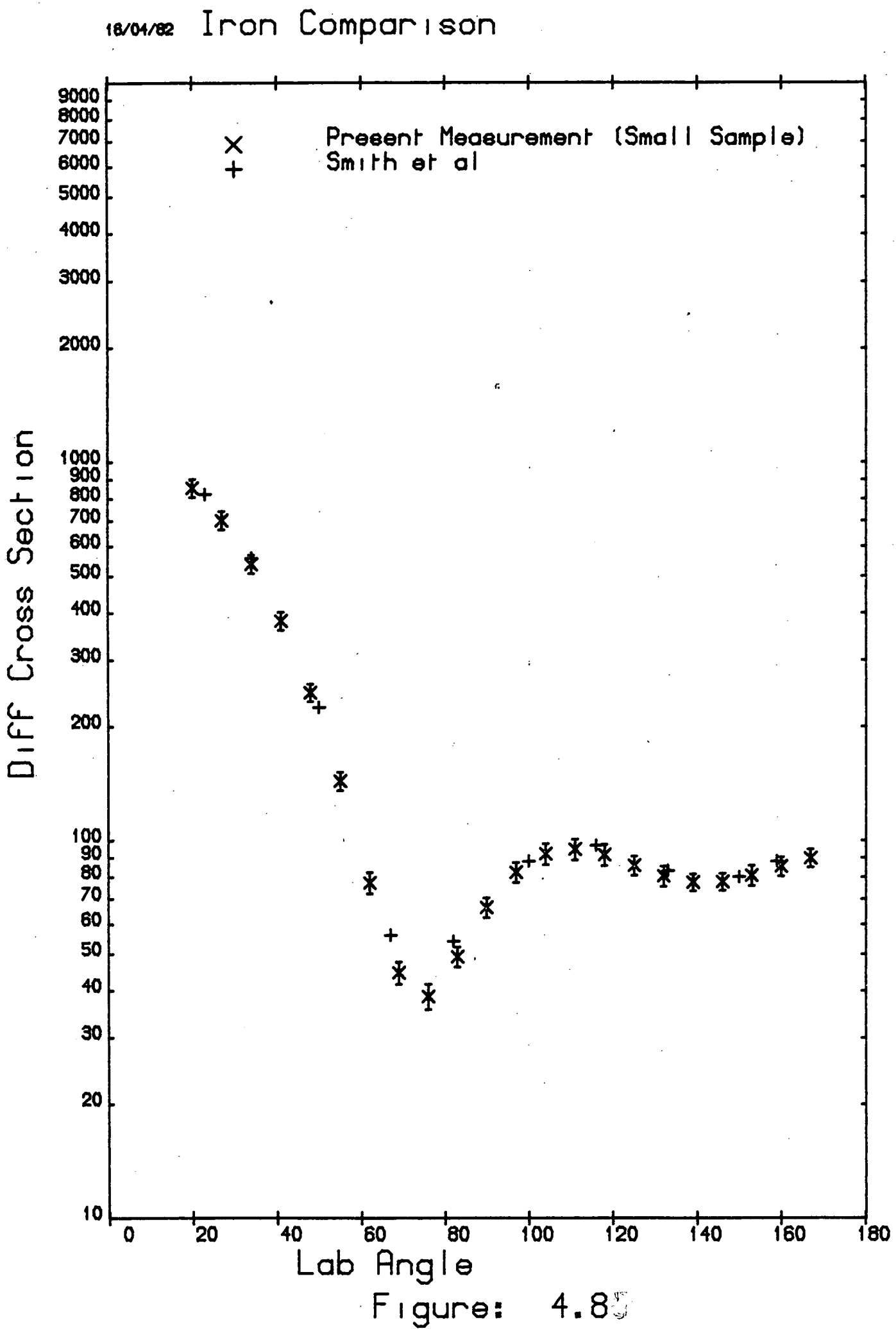
16/04/82 Iron Comparison
Present Measurement (Small Sample)
Smith et al
Diff Cross Section
9000
8000
7000
6000
5000
4000
3000
2000
1000
900
800
700
600
500
400
300
200
100
90
80
70
60
50
40
30
20
10
0
20
40
60
80
100
120
140
160
180
Lab Angle

Figure: 4.8

Chapter 5

Experimental Data

5.1 Data Collection

Data was collected using the polarimeter and Van de Graaff accelerator continuously for periods upwards of 1 week. Experimental runs were made in two halves, one covering the angles 20,34,...,160 degrees and the other the angles 27,41,...,167 degrees. The 13 degree angle was not used as in this position detectors were too close to the direct neutron beam, when using the circular cross section collimator. Collecting data at alternate angle sets in alternate runs gave a usefull check on the reproducibility of measurements and both sets were required to mesh together smoothly. The larger number of angles also helped to define the shapes of angular distributions more accurately, especially in some backward angle analysing power measurements where there were sharp swings from negative to positive polarisation. Runs were made with the polarimeter performing a four position sequence:

Orientation A, Sample In, Count Rate:$N(A_I)$

Orientation A, Sample Out,Count Rate:$N(A_O)$

Orientation B, Sample In, Count Rate:$N(B_I)$

Orientation B, Sample Out,Count Rate:$N(B_O)$

The count rate for neutrons scattered from the scattering sample is the count rate with the sample out subtracted from the count rate with the sample in

$$N(A) = N(A_I) - N(A_O)$$

$$N(B) = N(B_I) - N(B_O)$$

$$dN(A) = \{N(A_I) + N(A_O)\}^{1/2}$$

$$dN(B) = \{N(B_I) + N(B_O)\}^{1/2}$$

where N(A) and N(B) are the count rates with the polarimeter in orientations A and B respectively, and dN(A) and dN(B) are the associated statistical uncertainties

Figure 2.8 shows the detector numbering system employed. In orientation A detector 1 is situated at the left hand scattering angle, 22 at the right hand and so on.

5.2 Analysing Power Calculation

The right left ratio is taken as the geometric mean of the ratios of the two detectors at each angle

$$R_i = \{N_j(A)N_i(B)/N_j(B)N_i(A)\}^{1/2}$$

i: 1-11

j= 23-i

The statistical error in R_i will be

$$dR_i = 0.5R_i\{[dN_i(A)/N_i(A)]^2+[dN_i(B)/N_i(B)]^2+[dN_j(A)/N_j(A)]^2+ [dN_j(B)/N_j(B)]^2\}^{1/2}$$

The analysing Power is then

$$P_i = (R_i-1)/(R_i+1)/P_r$$

P_r: reaction polarisation

The error in the analysing power is

$$dP_i = P_i\{[dR_i/(R_i-1)+dR_i/(R_i+1)]^2+[dP_r/P_r]^2+D^2\}^{1/2}$$

dP_r: the error in P_r

D: the systematic error caused by instrumental asymmetries

The polarisation of neutrons from the $^2H(d,n)^3He$ reaction has been measured many times [71-76] for deutron energies of less than 1 MeV. At energies around 0.5 MeV the reaction neutron polarisation is weakly energy dependent. A value of -0.15 ± 0.01 has been used by Begum and Galloway [28] using 0.315 MeV deutrons and Zijp and Jonker [16] using 0.65 MeV deutrons. This value was used in the present calculations.

The systematic error D was estimated from the results of the instrumental asymmetry tests described in section 3.3. The maximum acceptable instrumental asymmetry was quoted there as 0.005, but by the time experimental running was taking place it was possible to have all detectors within 0.003. D was taken from the instrumental asymmetry measured using a ^{60}Co source with a pulse height discrimination level set at 2/3 of the Compton edge channel number. This roughly corresponds to running with 3.0 MeV neutrons with a 2.0 MeV discrimination level. To give D the instrumental asymmetry must be divided by P_r. An average instrumental asymmetry of about 0.0015 gives a value of 0.01 for D, which in most of the measurements is larger than the statistical uncertainty in the 20 degree measurement. Away from the forward angles D is less important.

5.3 Differential Cross Section Calculation

The differential cross section can be expressed as

$$\sigma(\theta) = Sr^2/IN$$

N: number of nuclei in the scatterer

I: incident neutron flux

S: scattered neutron flux

r: distance from scatterer to detector

Practical evaluation requires the following substitutions

$S = n_d / e_d A_d$

n_d: count rate at the scattered neutron(side) detector

e_d: efficiency of side detector

A_d: area of side detector presented to scattered neutrons

$I = n_0 / A_s$

n_0: number of neutrons incident on the scatterer/unit time

A_s: area of the scatterer presented to the incident beam

$n_0 = (n_m A_s / e_m A_m) \cdot (r_m / r_s)^2$

n_m: CBM count rate

e_m: CBM detection efficiency

A_m: CBM area irradiated by the direct beam

r_m: distance from CBM to neutron source

r_s: distance from scatterer to neutron source

Making these substitutions therefore

$$\sigma(\theta) = (e_m / e_d) \cdot (r_s r / r_m)^2 \cdot (n_d / n_m) \cdot (A_m / A_d) / N$$

n_d and (e_m / e_d) refer to measurement at each angle which has two detectors so that

$$n_d = \{N_i(A) N_j(A) N_i(B) N_j(B)\}^{1/4}$$

$$dn_d = n_d\{[dN_i(A)/N_i(A)]^2+[dN_j(A)/N_j(A)]^2+[dN_i(B)/N_i(B)]^2 + [dN_j(B)/N_j(B)]^2\}^{1/2}/4$$

$$e_i = e_m/e_d \text{ for one detector}$$

$$e = \{e_i e_j\}^{1/2}$$

$$de = 0.5e\{[de_i/e_i]^2+[de_j/e_j]^2\}^{1/2}$$

In using this method of differential cross section determination much of the total error results from measurement errors in distances and areas. A_m, A_d, r_s, r and r_m were measured as having the following values in this series of experimental runs.

A_m: 101.1+—5.0 cm^2

A_d: 77.4+—1.0 cm^2

r_s: 170.4+—0.4 cm

r: 30.0+—0.1 cm

r_m: 117.1+—0.3 cm

These errors do not effect the shape of the angular distribution, but will change the absolute magnitude of the cross section. The dominating factor is the error in the irradiated area of the CBM which is a consequence of uncertainty in the neutron beam width. Errors in count rate and detection efficiency effect both angular distributions and absolute magnitudes. In a polarisation experiment where large numbers of scattered neutron counts have to be accumulated, errors in n_d and n_m are small compared to other experimental uncertainties. The ratio of detection efficiencies, e_m/e_d, is determined by the in-beam calibration runs, with the ratio taken as

$$e_m/e_d = n'_m M_d / n'_d M_m$$

n'_m: CBM count rate

n'_d: in-beam side detector count rate

M_d: TYM count rate when the side detector is in-beam

M_m: TYM count rate when measuring n_m

n'_d was measured by rotating each side detector in-beam and counting for 30s. n'_m was determined by taking 30s counts at the start and finish of the in-beam calibration run. Typically two calibrations were performed each day with a minimum of six for each experiment. e_m/e_d was taken as the mean value and the error taken as the standard deviation in the mean. With stable accelerator running conditions one per cent accuracy in e_m/e_d was possible for individual detectors. However variations in machine voltage somtimes caused a wavering in the beam which effected the neutron flux and led to larger errors in e_m/e_d.

5.4 Spectrum Integration and Correction

Proton recoil spectra are shown in figure 5.1 . Channel to energy calibration is made by assigning 3.0 MeV to the recoil edge channel (arrowed) in the direct neutron beam spectrum. This is compared with the spectrum of neutrons scattered through 20 degrees by the Bismuth sample, which was obtained by subtracting the sample out from the sample in spectrum . Counting times are 30s for the direct beam spectrum and a total of 50000s (sample in and sample out) for the scattered neutron spectrum. Neutron selector pulse height discrimination levels were set to correspond to 1.3 MeV proton energy approximately. At lower levels quality of PSD suffered. The PSD level was set fairly high for improved gamma rejection, but this has resulted in reduced detection efficiency for proton recoils between 1.3 and 1.8 MeV. Recoil spectrum integration was performed starting with a lower energy limit of 1.5 MeV and raising the limit in 0.1 MeV steps up to 2.9 MeV. Differential cross sections and analysing powers were

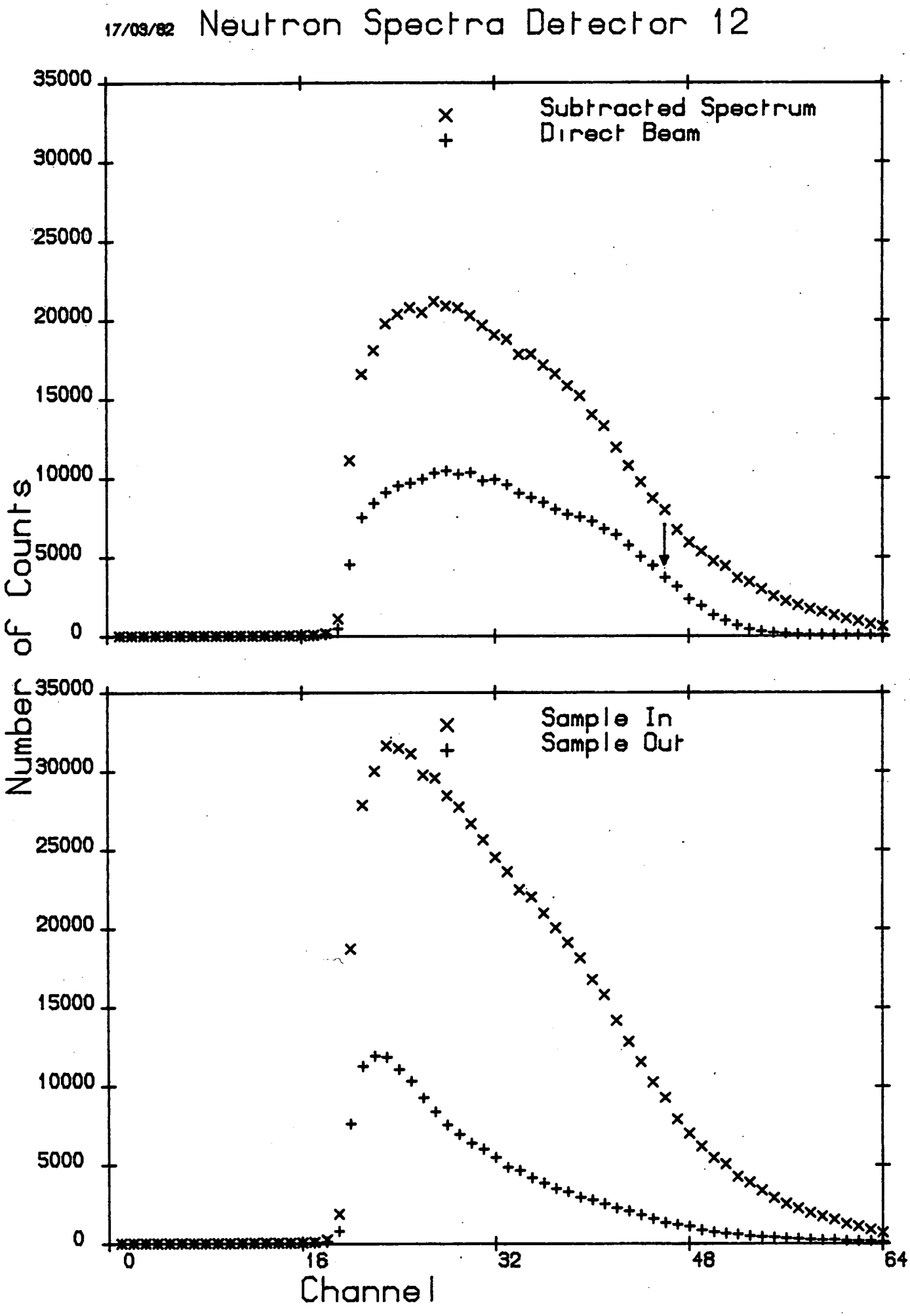
17/03/82 Neutron Spectra Detector 12
Subtracted Spectrum
Direct Beam
Sample In
Sample Out
Number of Counts
Channel
35000
30000
25000
20000
15000
10000
5000
0
0
16
32
48
64

Figure: 5.1

calculated after each integration. The lower limit, where calculated values had ceased to change, was chosen as the final value. This was in general around 2.2 MeV. The subtracted spectrum shows a slight high energy tail, not noticeable in the direct beam spectrum, which is possibly due to leakage of gamma rays, from neutron capture in the shielding. Thus the upper integration limit was set at 3.1 MeV.

A summary of the physical characteristics of the scattering samples is given in table 5.1. The term MFPR is explained in Chapter 4. Tables 5.2-5.13 give the uncorrected and corrected values of analysing powers and differential cross sections for Tungsten, Mercury, Thalium, Lead, Bismuth and Uranium. The uncorrected values are just those values calculated according the procedure described previously, while the corrected values were calculated by the methods of Chapter 4. In the following data tables "Stat." denotes the statistical errors in the uncorrected distributions, "Inst." denotes errors in analysing power due to instrumental asymmetry and "Syst." denotes errors in uncorrected differential cross section due to uncertainty in distances and areas. The initial corrections were made using the semi-analytical method and these were then used as input data for the Monte Carlo correction, which yielded the final results. Thus the number of Monte Carlo iterations necessary to achieve satisfactory agreement between experimental and simulated distributions was reduced, saving a large amount of computing time. In the tables "M.C." denotes the uncertainty in the corrected distribution due to uncertainties in the simulated Monte Carlo distribution. The unit of cross sections tabulated and plotted in this and the next chapter is mb/sr.

Except with Bismuth it was not considered practical to completely exclude inelastically scattered neutrons by raising the lower integration limit, as this would have entailed serious loss of accuracy in the analysing power measurements. Wherever data was available this

was used to estimate the inelastic contribution to recoil spectrum counts. If not available, inelastic cross sections were calculated using the program "CINDY" (see Chapter 6). These cross sections were then used as input data for both the analytical and Monte Carlo calculations. Corrected and Uncorrected distributions are compared in the figures which follow. Uncorrected distributions show statistical errors only, while corrected distributions show the total estimated errors . Comparison of the present data with previous measurements is included for each sample after the figures showing corrected and uncorrected data.

Table 5.1

Scattering Sample Characteristics

Element	Height (cm)	Diameter (cm)	Density (gcm^{-3})	MFPR	Comments
Tungsten	5.66	5.05	15.14	0.88	Cylindrical, Sintered
Mercury	5.00	5.00	13.59	0.76	Cylindrical, Thin Stainless Steel Container
Thalium	5.35	5.08	10.79	0.61	Cylindrical,Cast
Lead	4.92	4.88	10.99	0.62	Cylindrical,Cast
Bismuth	5.08	5.08	9.73	0.53	Cylindrical,Cast
Uranium	5.45	2.86	19.00	0.55	Cylindrical,Cast Supplied UKAEA

5.5 The Data

Data is presented as follows:

Tungsten: Tables 5.2,5.3, Figures 5.2,5.3,5.4,5.5

Mercury: Tables 5.4,5.5, Figures 5.6,5.7,5.8,5.9

Thalium: Tables 5.6,5.7, Figures 5.10,5.11,5.12,5.13

Lead: Tables 5.8,5.9, Figures 5.14,5.15,5.16,5.17

Bismuth: Tables 5.10,5.11, Figures 5.18,5.19,5.20,5.21

Uranium: Tables 5.12,5.13, Figures 5.22,5.23,5.24,5.25

5.5.1 Tungsten

The scattering sample was a cylinder, 5.66 cm high by 5.05 cm diameter, of scintered natural tungsten, density 15.14gm/cm^3, about 80 per cent of the accepted value. Inspection of a second broken sample showed that it was homogeneous in constitution. Foster and Glasgow [77] give total cross sections of 7.2b and 7.0b at neutron energies 2.3 and 3.0 MeV respectively, which result in sample MFPR's (see Chapter 4) of 0.90 and 0.88.

Natural Tungsten consists principally of four isotopes, ^{182}W, ^{183}W, ^{184}W and ^{186}W, with fractional abundances of 0.26, 0.14, 0.31 and 0.29 respectively. With a lower integration limit of 2.3 MeV the following excited states need to be considered:

^{182}W: 0.100, 0.329 MeV [78]

^{183}W: 0.046, 0.099, 0.207, 0.209, 0.292, 0.309, 0.412, 0.515 MeV [79]

^{184}W: 0.111, 0.364 MeV [80]

^{186}W: 0.122, 0.396 MeV [81]

Since it would be impractical to account for each excited state individually, and since detection efficiency does not vary appreciably over small energy intervals, closely spaced levels were combined to give two effective excited states for the purposes of inelastic event correction:

State 1: Effective energy 0.11 Mev; Constituent States
0.099(^{183}W), 0.100(^{182}W),
0.111(^{184}W), 0.122(^{186}W)

State 2: Effective energy 0.35 MeV; Constituent States
0.329(^{182}W), 0.364(^{184}W),
0.396(^{186}W)

The 0.046 level of ^{183}W was considered on its own. Two sets of data on differential inelastic cross sections are available close to the energy

region of interest. One by Tsukada et al [82] at 2.01 Mev using natural tungsten, and the other by Delaroche et al [68] at 3.4 MeV using separated isotopes. The former observed two inelastic groups due to scattering from combinations of excited states, probably not unlike that proposed for the correction. The latter measured cross sections for excitation of the 1st two excited states of each isotope. Cross sections for the scattering of neutrons from excited states of ^{183}W above 0.099MeV are not available. However ^{183}W is the least abundant of the common isotopes and calculation indicates that these cross sections are small. They were thus neglected in the correction. This is further discussed in Chapter 6. The effective contribution of neutrons from the 0.046MeV state varies between 5 and 1mb/sr, from state 1 it drops from 62mb/sr at forward angles to 7mb/sr at backward angles and from state 2 it is close to 5mb/sr. These values do not include the effect of decreased detection efficiency.

The data is listed in tables 5.2 and 5.3 and illustrated in figures 5.2 and 5.3. In figure 5.4 the corrected analysing power is compared with measurements by Zijp and Jonker [16], and Begum and Galloway [28]. Agreement with the data of the former is reasonable where their errors are within reasonable bounds. Agreement with the latter, which have significantly poorer accuracy, is not good and the present measurements stay definitely negative until the very backward angles are reached. The corrected differential cross section is compared in figure 5.5 with those of Begum and Galloway [28], Becker et al [9] and Delaroche et al [68]. The present measurements are closest to those of Delaroche et al, but it is difficult to assess the importance of the 0.4 MeV difference in energy. This will be investigated more fully in Chapter 6. Both of the other two data sets show significantly higher cross sections, which can partially be attributed to inelastic neutron contamination.

Table 5.2

Tungsten

Analysing Power

	Uncorrected				Corrected
Angle	P(θ)	Stat.	Inst.	M.C.	P(θ)
20	-0.031	0.006	0.003	0.013	-0.037+- 0.015
27	-0.062	0.006	0.009	0.015	-0.075+- 0.019
34	-0.092	0.008	0.007	0.017	-0.119+- 0.022
41	-0.099	0.009	0.011	0.021	-0.153+- 0.028
48	-0.163	0.014	0.007	0.026	-0.256+- 0.035
55	-0.109	0.016	0.012	0.032	-0.244+- 0.041
62	-0.157	0.023	0.009	0.036	-0.298+- 0.048
69	-0.126	0.023	0.002	0.036	-0.230+- 0.045
76	-0.068	0.023	0.017	0.033	-0.170+- 0.045
83	-0.053	0.023	0.014	0.030	-0.155+- 0.041
90	-0.106	0.026	0.012	0.029	-0.195+- 0.043
97	-0.077	0.023	0.007	0.030	-0.154+- 0.040
104	-0.078	0.030	0.011	0.034	-0.144+- 0.047
111	-0.051	0.028	0.020	0.040	-0.105+- 0.053
118	-0.069	0.036	0.002	0.048	-0.101+- 0.060
125	-0.026	0.037	0.002	0.055	-0.012+- 0.066
132	-0.100	0.048	0.005	0.058	-0.052+- 0.075
139	0.002	0.051	0.006	0.056	0.083+- 0.077
146	0.079	0.063	0.022	0.053	0.231+- 0.087
153	0.030	0.056	0.018	0.049	0.243+- 0.078
160	0.140	0.080	0.002	0.043	0.328+- 0.093
167	0.077	0.057	0.003	0.037	0.202+- 0.070

Table 5.3

Tungsten

Differential Cross Section

	Uncorrected				Corrected
Angle	$\sigma(\theta)$	Stat.	M.C.	Syst.	$\sigma(\theta)$
20	867.9	15.1	5.4	47.7	2161.1+- 124.8
27	622.3	16.3	3.6	34.2	1443.9+- 88.0
34	417.9	11.2	2.2	23.0	841.9+- 51.6
41	270.8	15.4	1.3	14.9	423.6+- 33.5
48	180.6	2.8	0.7	9.9	182.7+- 10.5
55	112.3	2.8	0.4	6.2	69.5+- 4.2
62	75.4	1.1	0.2	4.1	29.1+- 1.7
69	60.4	1.0	0.2	3.3	23.5+- 1.4
76	58.2	1.0	0.2	3.2	34.1+- 2.0
83	58.3	1.1	0.3	3.2	51.0+- 3.0
90	61.8	0.8	0.4	3.4	65.3+- 3.7
97	60.6	0.9	0.4	3.3	69.2+- 4.0
104	53.0	0.8	0.4	2.9	60.0+- 3.4
111	46.6	1.0	0.3	2.6	42.6+- 2.5
118	43.2	0.7	0.2	2.4	26.0+- 1.5
125	35.1	0.7	0.1	1.9	16.3+- 1.0
132	33.0	0.5	0.1	1.8	14.0+- 0.8
139	29.2	0.7	0.1	1.6	15.4+- 0.9
146	30.1	0.6	0.2	1.7	18.0+- 1.1
153	29.1	0.9	0.2	1.6	22.4+- 1.4
160	30.4	1.0	0.3	1.7	30.4+- 2.0
167	32.8	1.0	0.3	1.8	41.5+- 2.6

04/04/82 Tungsten

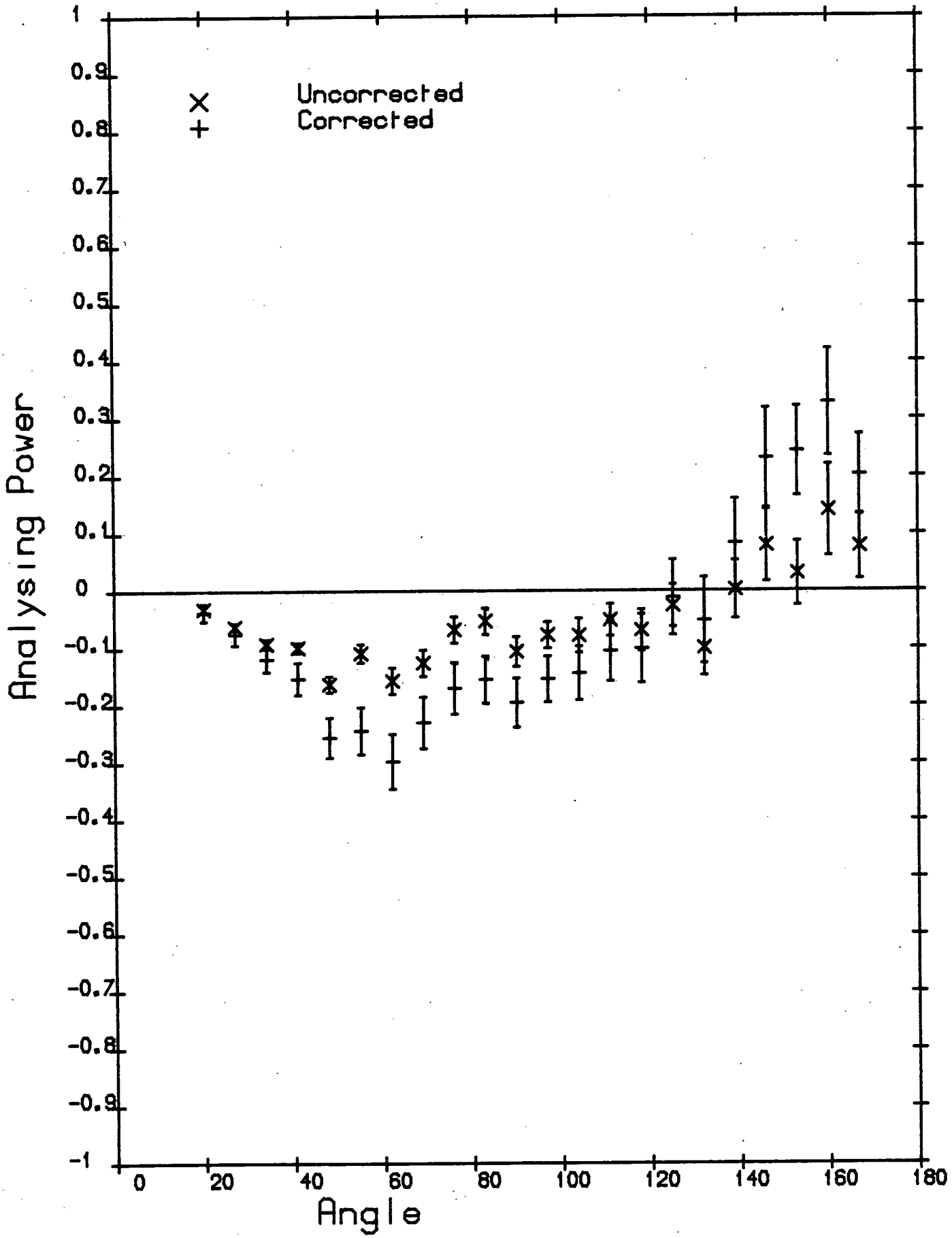

Figure: 5.2

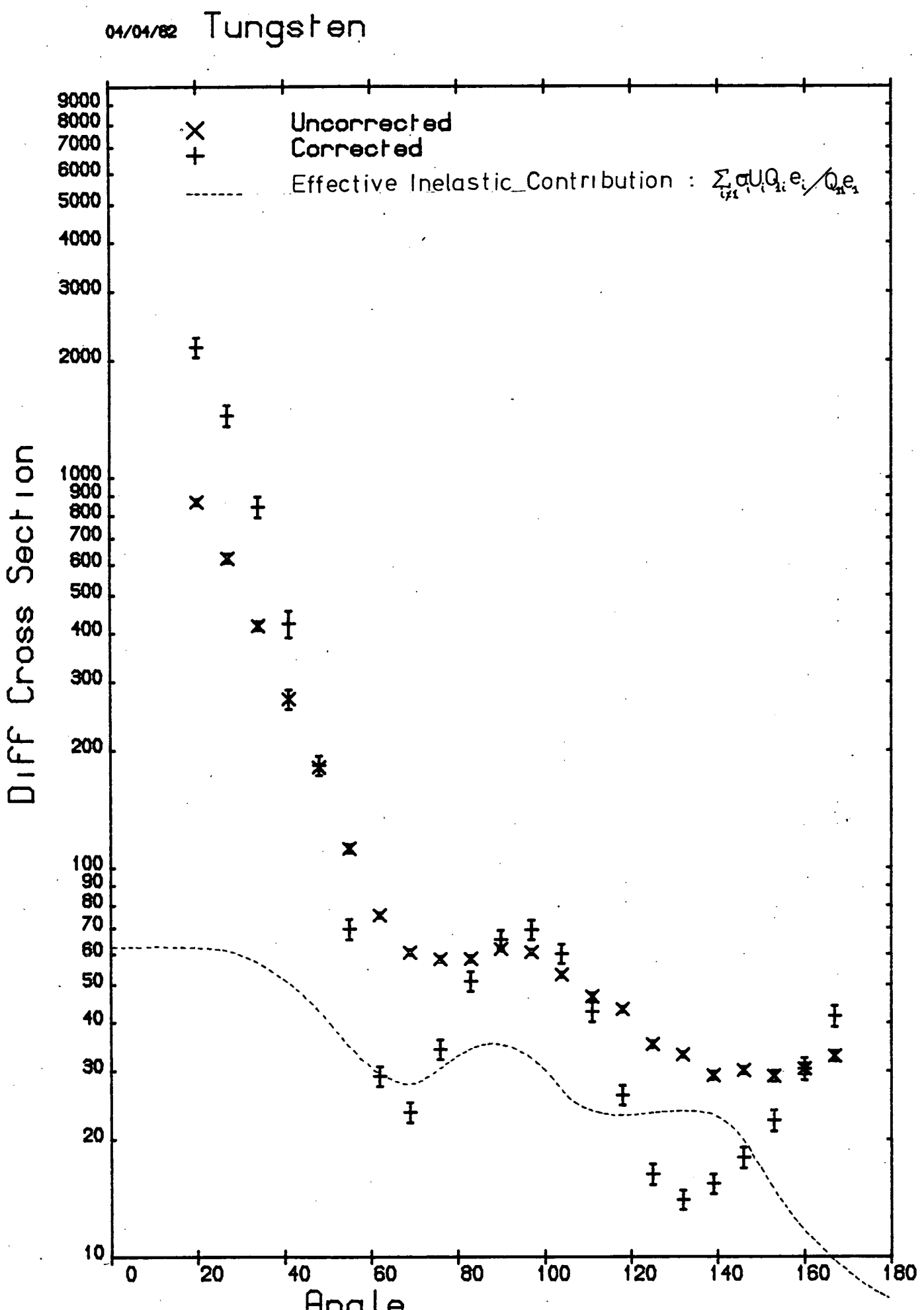
04/04/82 Tungsten
Uncorrected
Corrected
Effective Inelastic_Contribution : $\sum_{i\neq 1}\sigma_1 U_i Q_{1i} e_i / Q_{11} e_1$
Diff Cross Section
9000
8000
7000
6000
5000
4000
3000
2000
1000
900
800
700
600
500
400
300
200
100
90
80
70
60
50
40
30
20
10
0
20
40
60
80
100
120
140
160
180
Angle

Figure: 5.3

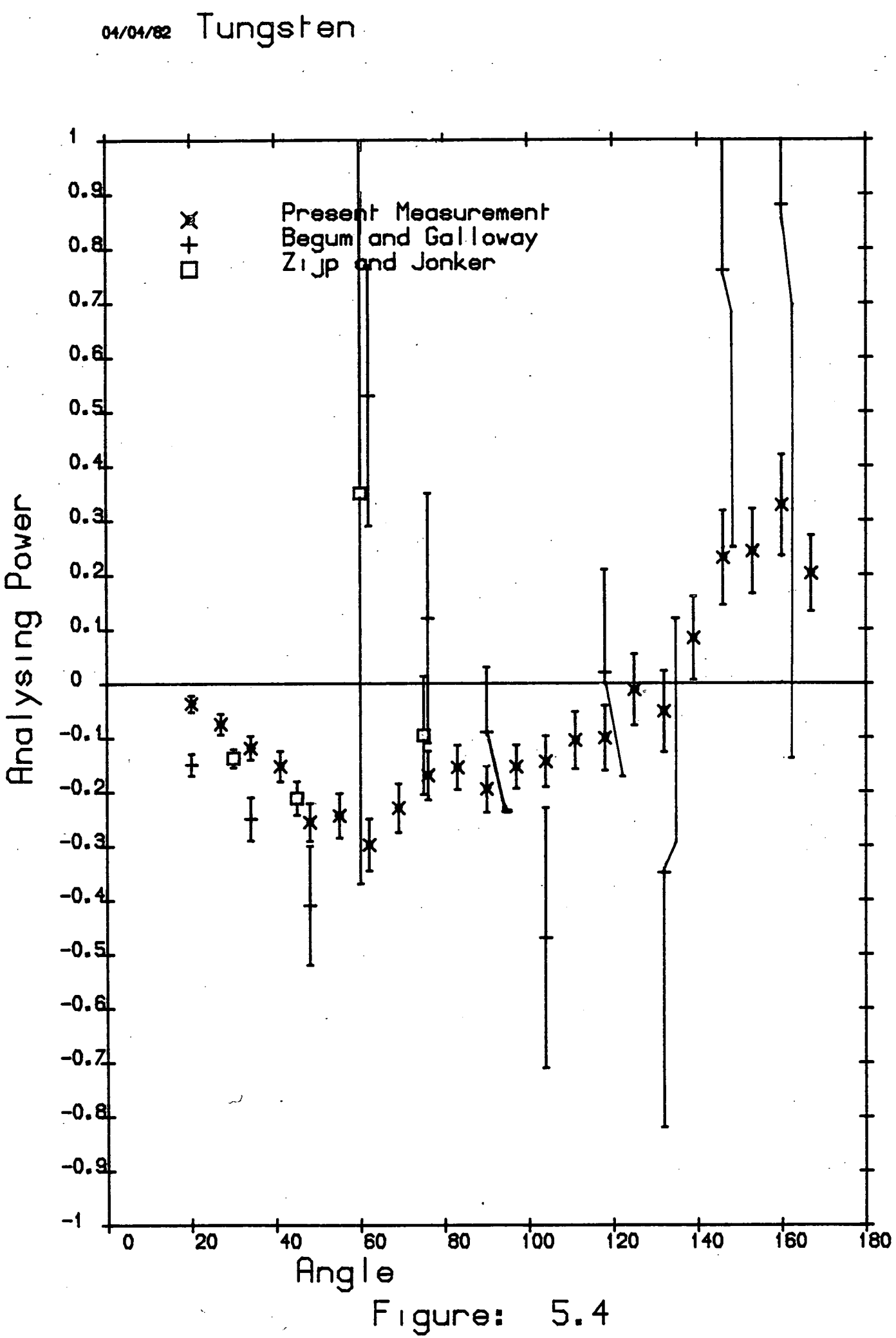
04/04/82 Tungsten
Present Measurement
Begum and Galloway
Zijp and Jonker
Analysing Power
Angle
1
0.9
0.8
0.7
0.6
0.5
0.4
0.3
0.2
0.1
0
-0.1
-0.2
-0.3
-0.4
-0.5
-0.6
-0.7
-0.8
-0.9
-1
0
20
40
60
80
100
120
140
160
180

Figure: 5.4

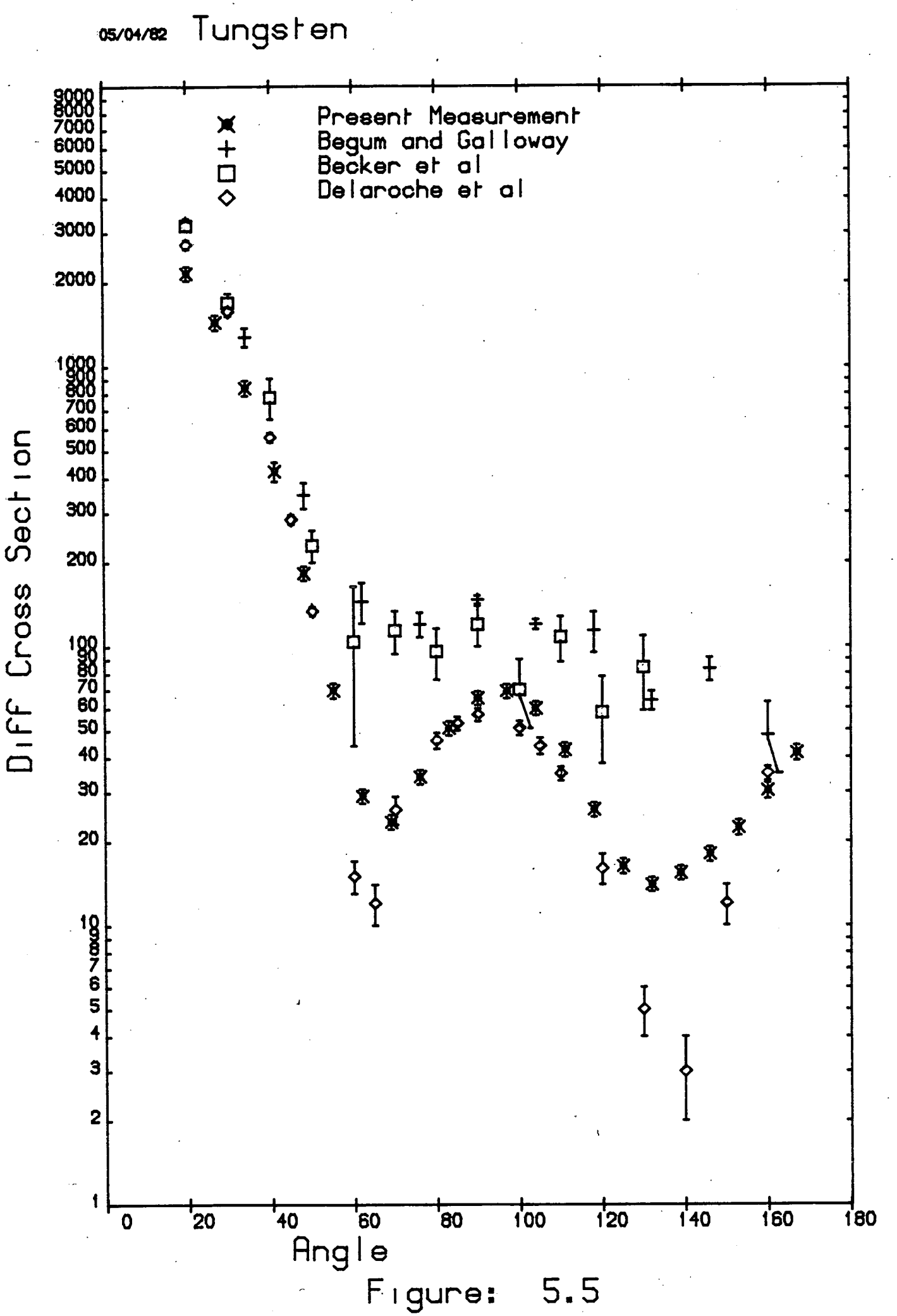
05/04/82 Tungsten
Present Measurement
Begum and Galloway
Becker et al
Delaroche et al
Diff Cross Section
Angle
9000
8000
7000
6000
5000
4000
3000
2000
1000
900
800
700
600
500
400
300
200
100
90
80
70
60
50
40
30
20
10
9
8
7
6
5
4
3
2
1
0
20
40
60
80
100
120
140
160
180

Figure: 5.5

5.5.2 Mercury

The scattering sample is a cylinder of natural mercury, 5 cm high by 5 cm diameter, held in a stainless steel container. The mass of stainless steel in the path of the neutron beam was estimated as 50gm, small compared to the 1335gm of mercury. The contribution of the container to the cross section was estimated using the cross section data of Smith et al [25] for iron, and then subtracted from the experimental value. For the worst case, around the backward angle minimum in the cross section, the correction amounted to about 5 per cent, slightly less than the systematic error in the cross section , and small compared to finite sample size corrections. Effects on analysing power were considered negligible and neglected. Foster and Glasgow [77] give total cross sections of 6.9b and 7.4b at energies 2.5 and 3.0 Mev respectively, which result in sample MFPR's of 0.71 and 0.76.

Natural mercury consists principally of 6 isotopes, ^{198}Hg, ^{199}Hg, ^{200}Hg, ^{201}Hg, ^{202}Hg and ^{204}Hg in fractional abundances of 0.1, 0.168, 0.231, 0.132, 0.298 and 0.069 respectively. The even-odd isotopes have many low energy excited states, the lowest quoted at 1.5 KeV, and no measurements of neutron inelastic cross sections have apparently been published. No existing aparatus could separate out the 1.5 KeV excited state inelastic group at 3 MeV in any case. Total inelastic event rejection is plainly impossible, but the size of the correction was reduced by raising the lower integration limit to 2.5 MeV. Several excited states must still be considered. They are:

^{198}Hg: 0.412 MeV [83]

^{199}Hg: 0.158, 0.208, 0.404, 0.414, 0.455, 0.492 MeV [84]

^{200}Hg: 0.368 MeV [85]

^{201}Hg: 0.0015, 0.027, 0.032, 0.167, 0.382, 0.415, 0.465 MeV [86]

^{202}Hg: 0.439 MeV [87]

^{204}Hg: 0.437 MeV [88]

As with the tungsten corrections, inelastic contributions were summed over several closely spaced levels, this time to give 4 effective inelastic groups scattering from the following effective states:

State 1: Effective energy 0.02 MeV, Contributing states
0.0015, 0.027, 0.032 MeV (^{201}Hg)

State 2: Effective energy 0.18 Mev, Contributing states
0.158, 0.208 MeV (^{199}Hg), 0.167 MeV (^{201}Hg)

State 3: Effective energy 0.375 MeV, Contributing states
0.368 MeV (^{200}Hg), 0.382 MeV (^{201}Hg)

State 4: Effective energy 0.44 MeV, Contributing states
0.412 MeV (^{198}Hg),
0.403, 0.413,
0.455, 0.492 MeV (^{199}Hg),
0.415, 0.465 MeV (^{201}Hg),
0.439 MeV (^{202}Hg)
and 0.437 MeV (^{204}Hg).

Cross sections were calcuated using the Statistical Model with level width fluctuation correction. Moldauer's Optical potential [89] was used for the calculation as it gives a good description of Thalium low lying excited state excitation functions (see under Thalium). Use of Rosen's potential [11] altered calculated cross sectios by less than 10 per cent in most cases.

This procedure obviously casts some doubt on the corrected data. However the calculated effective inelastic cross sections were not large, close to 5mb/sr in total for states 1, 2 and 3. State 4 had the largest calculated cross section between 20 and 27mb/sr, but its contribution is greatly reduced by the low detection efficiency. The data is listed in tables 5.4 and 5.5 and illustrated in figures 5.6 and

5.7. The analysing power is compared in figure 5.8 with the measurements of Galloway and Waheed [21]. The present measurement is of superior accuracy and the two distributions completely disagree. Noticeable features of the present measurements are the large backward angle analysing powers and the sharp swing from negative to positive polarisation around 145 degrees. Figure 5.9 compares differential cross sections with those of Galloway and Waheed [21] and Becker et al [9]. There is qualitative agreement between the sets of data.

Table 5.4

Mercury

Analysing Power

	Uncorrected				Corrected
Angle	P(θ)	Stat.	Inst.	M.C.	P(θ)
20	0.003	0.007	0.015	0.016	0.034+- 0.023
27	0.009	0.008	0.013	0.016	0.048+- 0.023
34	-0.040	0.010	0.005	0.017	0.003+- 0.020
41	-0.010	0.013	0.012	0.018	0.032+- 0.026
48	-0.085	0.017	0.016	0.022	-0.059+- 0.032
55	-0.028	0.024	0.015	0.027	-0.029+- 0.039
62	-0.006	0.029	0.012	0.031	0.022+- 0.044
69	0.001	0.032	0.009	0.029	0.079+- 0.044
76	0.044	0.028	0.007	0.026	0.100+- 0.040
83	0.072	0.028	0.010	0.024	0.110+- 0.039
90	0.055	0.026	0.019	0.024	0.094+- 0.040
97	0.071	0.027	0.007	0.025	0.123+- 0.038
104	0.081	0.029	0.001	0.027	0.150+- 0.041
111	0.059	0.033	0.011	0.030	0.133+- 0.047
118	-0.058	0.034	0.015	0.034	-0.025+- 0.050
125	-0.100	0.042	0.015	0.036	-0.192+- 0.059
132	-0.162	0.049	0.006	0.037	-0.412+- 0.067
139	-0.004	0.059	0.002	0.036	-0.088+- 0.069
146	0.048	0.056	0.001	0.035	0.378+- 0.071
153	0.223	0.051	0.005	0.030	0.520+- 0.069
160	0.231	0.045	0.006	0.024	0.398+- 0.058
167	0.200	0.047	0.001	0.020	0.295+- 0.055

Table 5.5

Mercury

Differential Cross Section

	Uncorrected				Corrected
Angle	σ(θ)	Stat.	M.C.	Syst.	σ(θ)
20	1289.8	25.3	10.5	70.9	2966.5+- 173.5
27	901.2	7.4	7.2	49.6	1987.7+- 110.8
34	603.8	18.6	4.6	33.2	1163.3+- 73.5
41	379.5	3.4	2.6	20.9	587.1+- 32.8
48	234.9	5.1	1.3	12.9	252.9+- 15.0
55	137.0	1.5	0.6	7.5	97.1+- 5.5
62	95.6	2.1	0.3	5.3	47.8+- 2.9
69	83.1	0.8	0.3	4.6	53.6+- 3.0
76	91.5	2.4	0.5	5.0	84.7+- 5.2
83	97.0	0.8	0.7	5.3	121.5+- 6.8
90	108.5	3.1	0.9	6.0	147.3+- 9.2
97	108.2	1.0	1.0	6.0	150.5+- 8.5
104	95.7	3.0	1.0	5.3	130.4+- 8.3
111	83.4	0.9	0.8	4.6	97.2+- 5.5
118	75.9	2.2	0.5	4.2	64.1+- 4.0
125	61.5	0.7	0.3	3.4	39.2+- 2.2
132	52.8	1.4	0.2	2.9	23.6+- 1.5
139	47.9	0.8	0.1	2.6	17.4+- 1.0
146	52.6	1.9	0.2	2.9	25.3+- 1.7
153	68.9	0.9	0.4	3.8	55.4+- 3.2
160	87.3	3.4	0.7	4.8	109.4+- 7.4
167	115.2	1.5	0.9	6.3	174.8+- 9.9

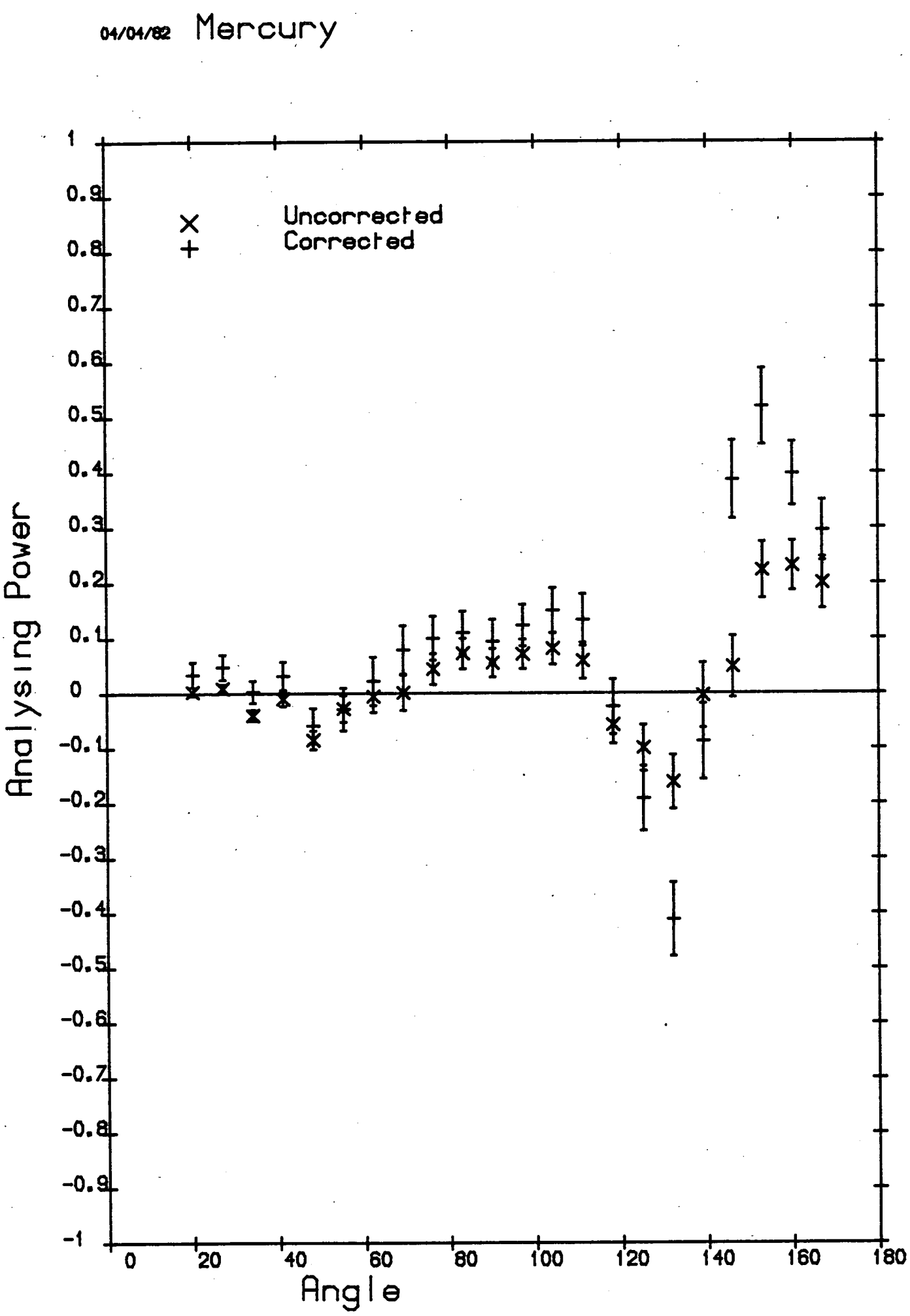
04/04/82 Mercury
Uncorrected
Corrected
Analysing Power
Angle
1
0.9
0.8
0.7
0.6
0.5
0.4
0.3
0.2
0.1
0
-0.1
-0.2
-0.3
-0.4
-0.5
-0.6
-0.7
-0.8
-0.9
-1
0
20
40
60
80
100
120
140
160
180

Figure: 5.6

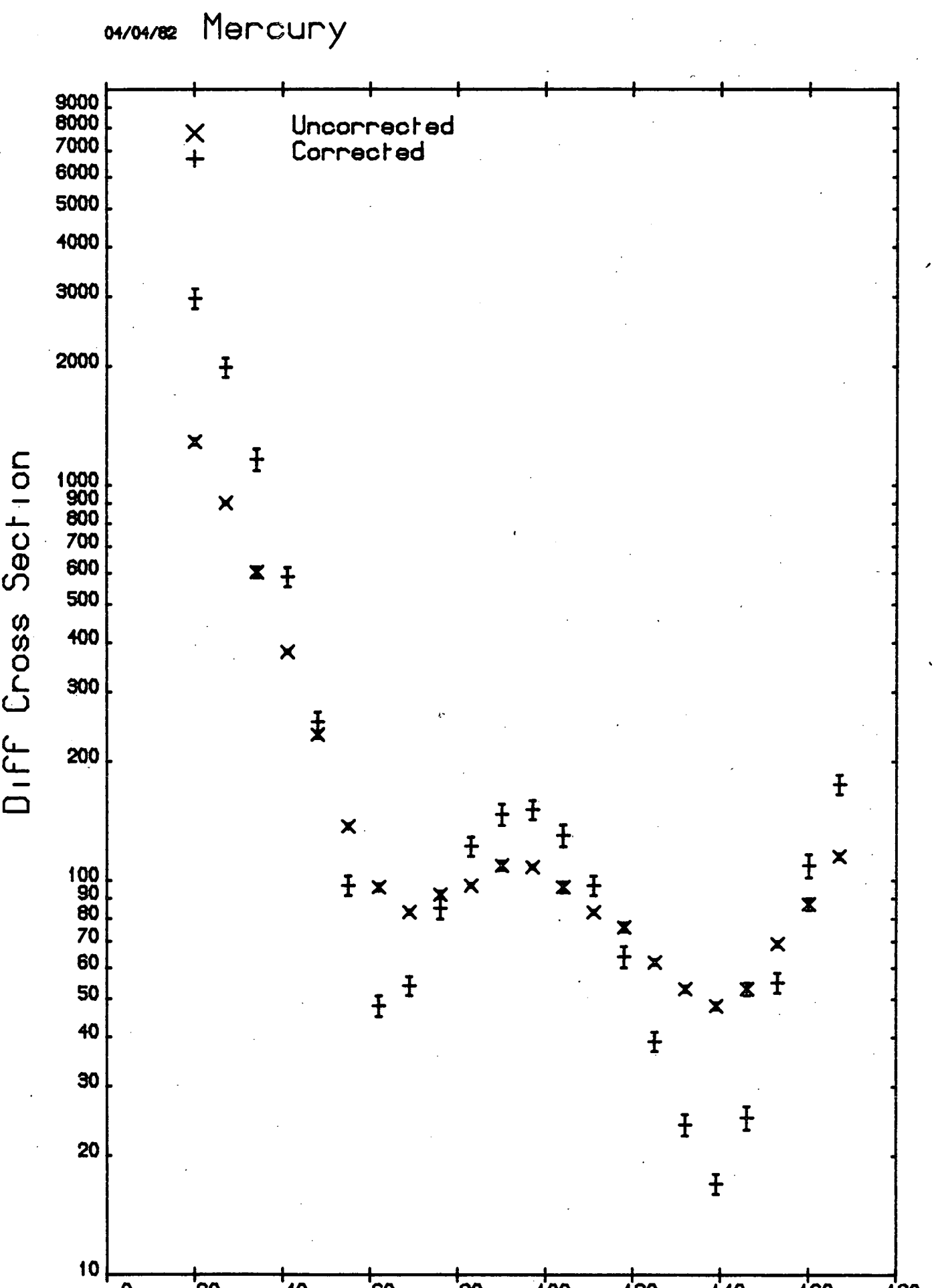
04/04/82 Mercury
Uncorrected
Corrected
Diff Cross Section
9000
8000
7000
6000
5000
4000
3000
2000
1000
900
800
700
600
500
400
300
200
100
90
80
70
60
50
40
30
20
10
0
20
40
60
80
100
120
140
160
180
Angle

Figure: 5.7

04/04/82 Mercury

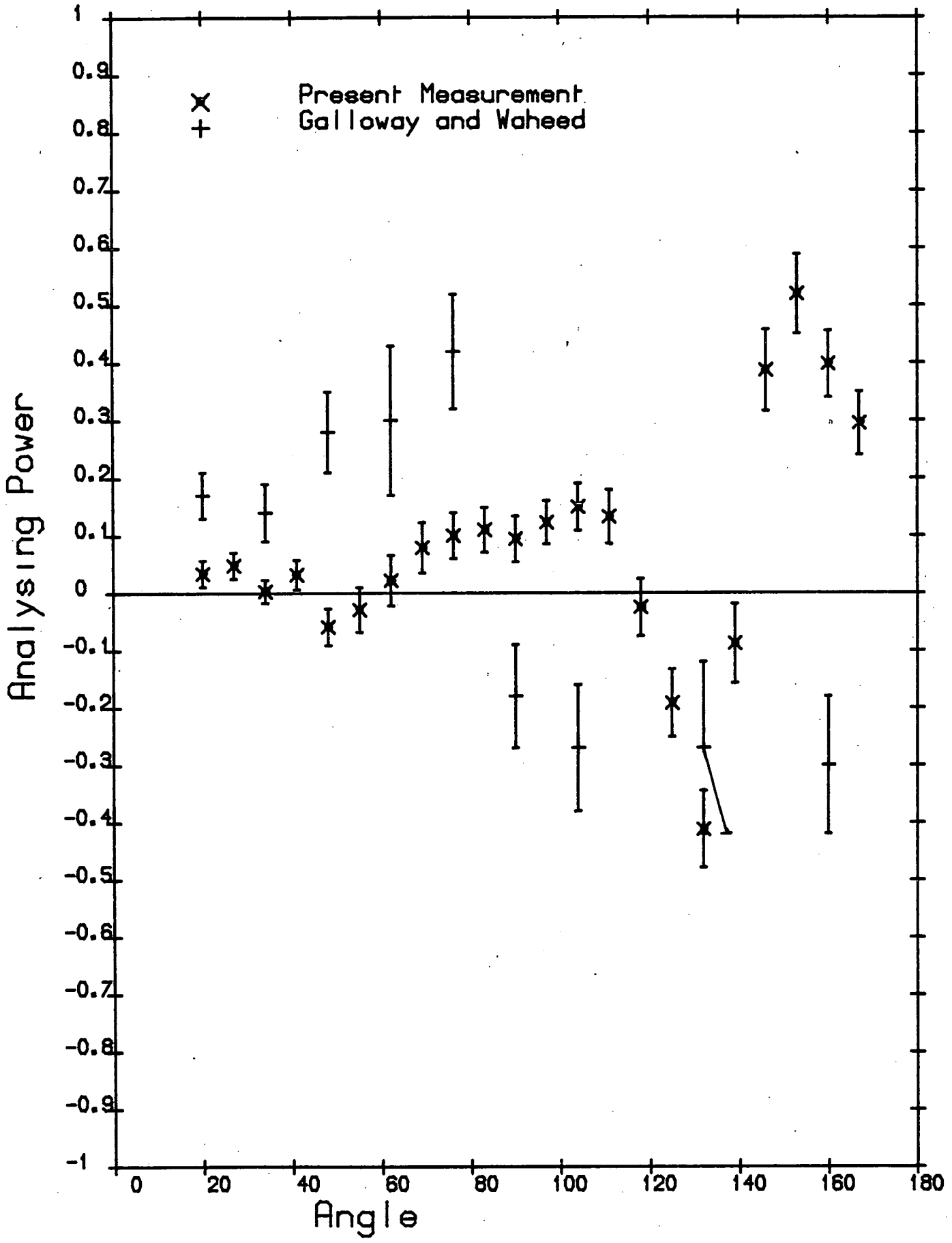

Figure: 5.8

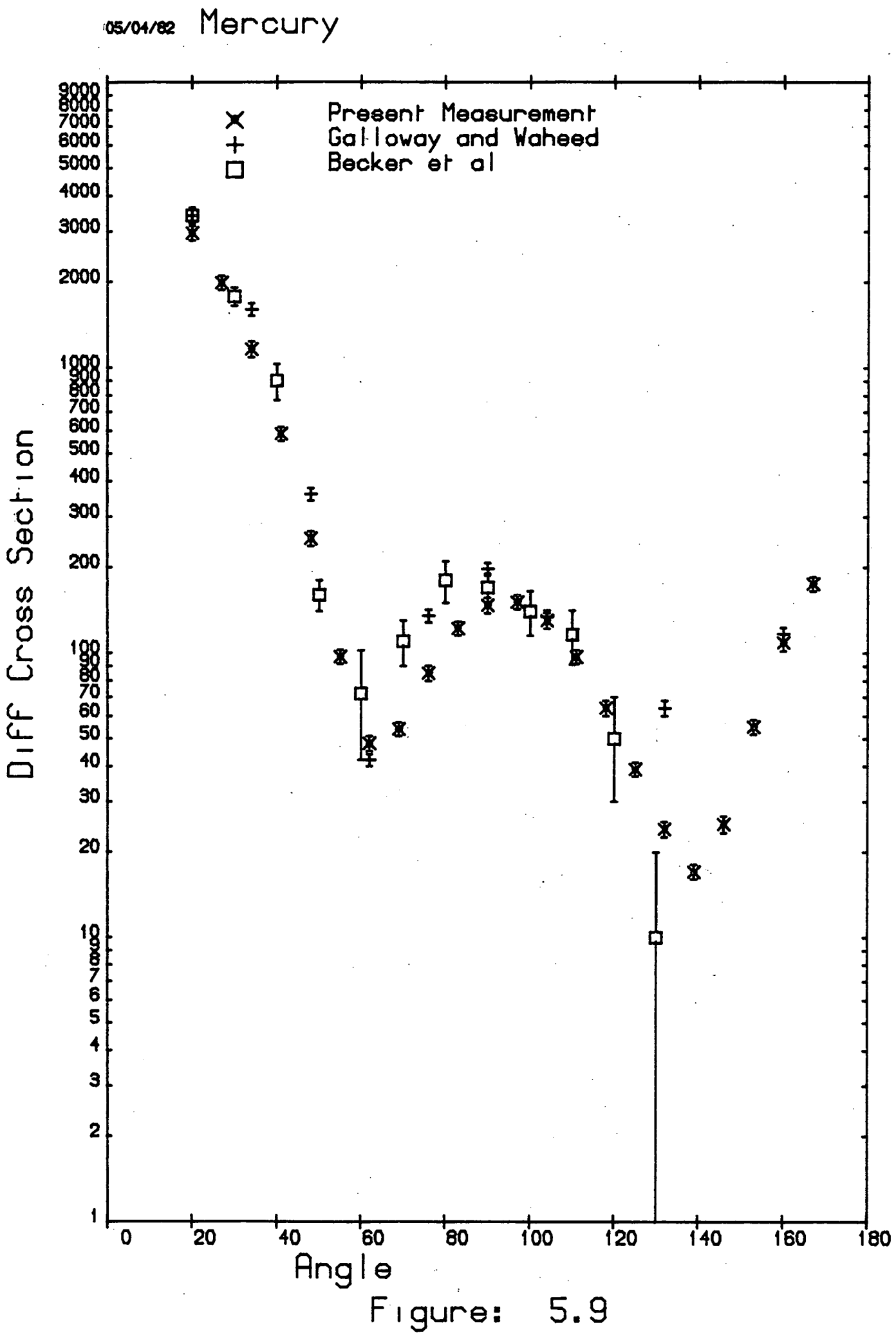
05/04/82 Mercury
Present Measurement
Galloway and Waheed
Becker et al
Diff Cross Section
Angle
9000
8000
7000
6000
5000
4000
3000
2000
1000
900
800
700
600
500
400
300
200
100
90
80
70
60
50
40
30
20
10
9
8
7
6
5
4
3
2
1
0
20
40
60
80
100
120
140
160
180

Figure: 5.9

5.5.3 Thalium

The sample is a cast cylinder of natural thalium 5.35cm high by 5.08cm diameter, and its density is 10.79gm/cm^3. Natural thalium consists of two isotopes ^{203}Tl and ^{205}Tl in fractional abundances of 0.295 and 0.705 respectively. Foster and Glasgow [77] give total cross sections of 6.9b and 7.5b at 2.2 and 3.0 MeV respectively which result in MFPR's of 0.56 and 0.61 respectively. The lower integration limit was set at 2.2 MeV so that inelastic scattering involving the excitation of four levels must be considered. They are the 0.204 MeV and 0.620 MeV levels [90] of ^{205}Tl and the 0.279 MeV and 0.681 MeV levels [91] of ^{203}Tl. The (n,n'γ) cross sections have been measured by Feicht and Gobel [92] and Ahmed et al [93]. Where the measurements coincide the cross sections agree. Neutron inelastic differential cross sections were calculated using the statistical model and normalised to give the observed total inelastic cross sections. They were then weighted according to the fractional isotopic abundances, before use in the correction. The effective contributions of the 1st excited states are both between 20 and 30mb/sr and the contributions of the 2nd excited states close to 5mb/sr. Data is listed in tables 5.6 and 5.7 and illustrated in figures 5.10 and 5.11. Figure 5.12 compares analysing powers with those of Zijp and Jonker [16] and Begum and Galloway [28]. The present measurements disagree with the other two sets at forward angles. The sequence of crossings of the zero axis is qualitatively similar to that observed by Begum and Galloway, but the cross over occurs at somewhat different angles. In figure 5.13 the differential cross section is compared with the data of Begum and Galloway [28] and Becker et al [9]. The present measurements are generally lower than these two other data sets, and show deeper minima.

Table 5.6

Thalium

Analysing Power

	Uncorrected				Corrected
Angle	P(θ)	Stat.	Inst.	M.C.	P(θ)
20	-0.049	0.008	0.015	0.014	-0.020+- 0.022
27	-0.044	0.007	0.013	0.016	-0.003+- 0.022
34	-0.014	0.011	0.005	0.019	0.038+- 0.023
41	-0.033	0.013	0.012	0.024	0.029+- 0.030
48	-0.035	0.021	0.016	0.030	0.031+- 0.040
55	-0.045	0.024	0.015	0.037	-0.027+- 0.046
62	-0.033	0.034	0.012	0.037	-0.123+- 0.052
69	0.003	0.029	0.009	0.032	-0.001+- 0.044
76	0.127	0.032	0.007	0.030	0.172+- 0.045
83	0.121	0.026	0.010	0.028	0.180+- 0.041
90	0.097	0.029	0.019	0.027	0.155+- 0.045
97	0.070	0.027	0.007	0.026	0.114+- 0.039
104	0.083	0.033	0.001	0.026	0.106+- 0.042
111	0.067	0.030	0.011	0.025	0.062+- 0.041
118	0.017	0.039	0.015	0.026	-0.032+- 0.049
125	-0.111	0.040	0.015	0.030	-0.246+- 0.054
132	-0.221	0.054	0.006	0.036	-0.496+- 0.072
139	-0.067	0.062	0.002	0.042	-0.405+- 0.080
146	0.071	0.072	0.001	0.043	0.252+- 0.086
153	0.276	0.047	0.005	0.036	0.672+- 0.074
160	0.321	0.047	0.006	0.027	0.561+- 0.065
167	0.196	0.039	0.001	0.020	0.347+- 0.049

Table 5.7

Thalium

Differential Cross Section

	Uncorrected				Corrected
Angle	σ(θ)	Stat.	M.C.	Syst.	σ(θ)
20	1403.9	13.2	8.7	77.2	2947.3+- 164.7
27	1046.2	9.6	7.3	57.5	1987.7+- 111.1
34	674.6	8.3	5.4	37.1	1152.9+- 65.2
41	395.0	7.5	3.4	21.7	550.6+- 32.2
48	219.4	2.8	1.6	12.1	198.6+- 11.3
55	140.3	4.5	0.5	7.7	49.2+- 3.2
62	98.9	1.3	0.3	5.4	28.5+- 1.6
69	100.0	1.9	0.5	5.5	67.6+- 4.0
76	110.8	1.7	0.8	6.1	117.4+- 6.8
83	114.5	2.7	1.0	6.3	150.4+- 9.1
90	120.6	1.4	1.0	6.6	157.0+- 8.9
97	114.7	1.5	0.8	6.3	140.8+- 8.0
104	105.9	1.4	0.6	5.8	113.1+- 6.4
111	93.1	1.1	0.5	5.1	85.7+- 4.8
118	82.3	1.1	0.3	4.5	64.1+- 3.6
125	68.5	1.2	0.3	3.8	46.9+- 2.7
132	56.8	0.9	0.2	3.1	30.6+- 1.8
139	52.6	0.8	0.2	2.9	17.7+- 1.0
146	57.1	1.2	0.2	3.1	19.5+- 1.2
153	76.6	1.2	0.4	4.2	49.0+- 2.8
160	107.0	1.5	0.6	5.9	108.8+- 6.2
167	147.0	2.5	0.8	8.1	183.4+- 10.6

04/04/82 Thallium

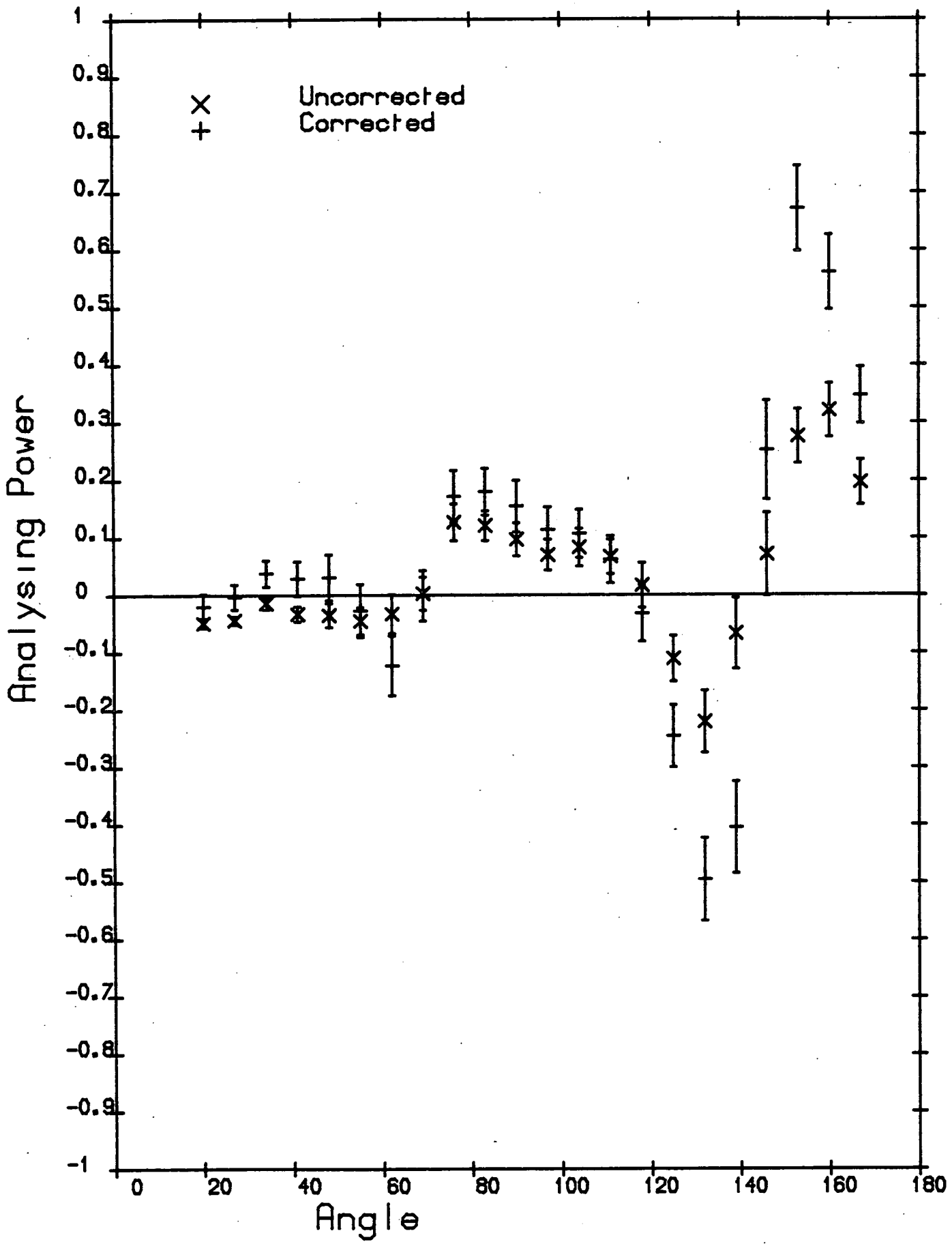

Figure: 5.10

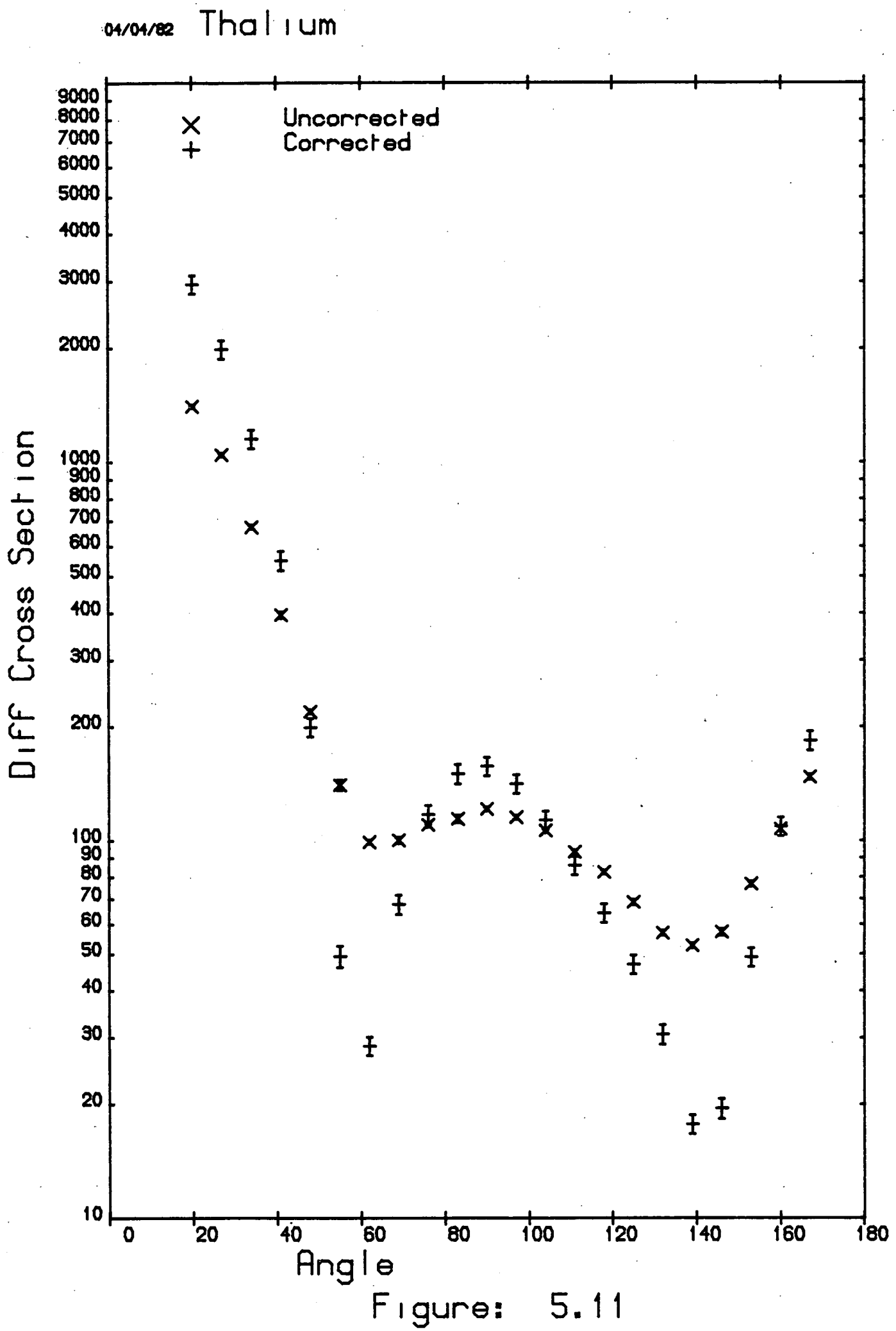
04/04/82 Thallium
Uncorrected
Corrected
Diff Cross Section
9000
8000
7000
6000
5000
4000
3000
2000
1000
900
800
700
600
500
400
300
200
100
90
80
70
60
50
40
30
20
10
0
20
40
60
80
100
120
140
160
180
Angle

Figure: 5.11

04/04/82 Thallium

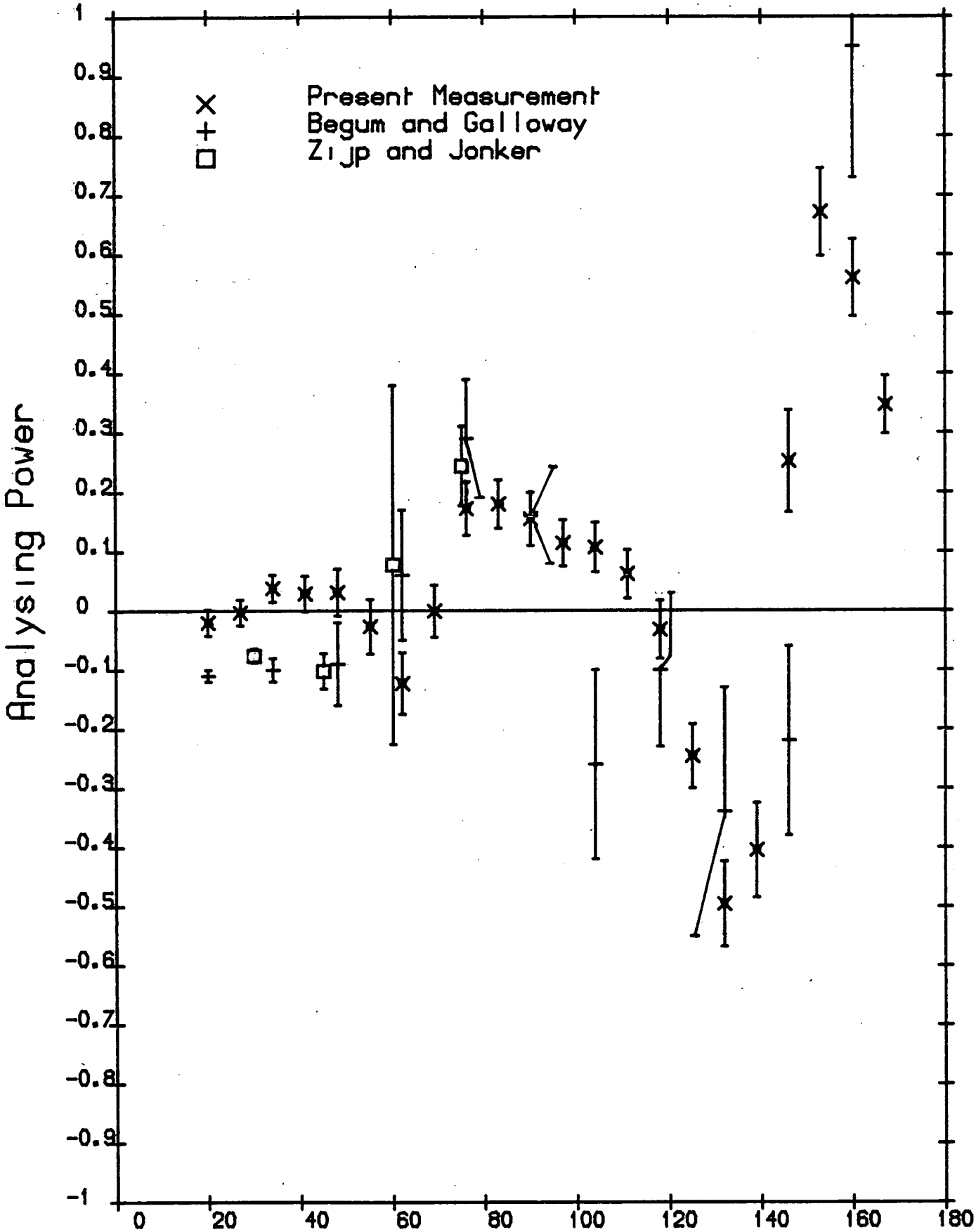

Figure: 5.12

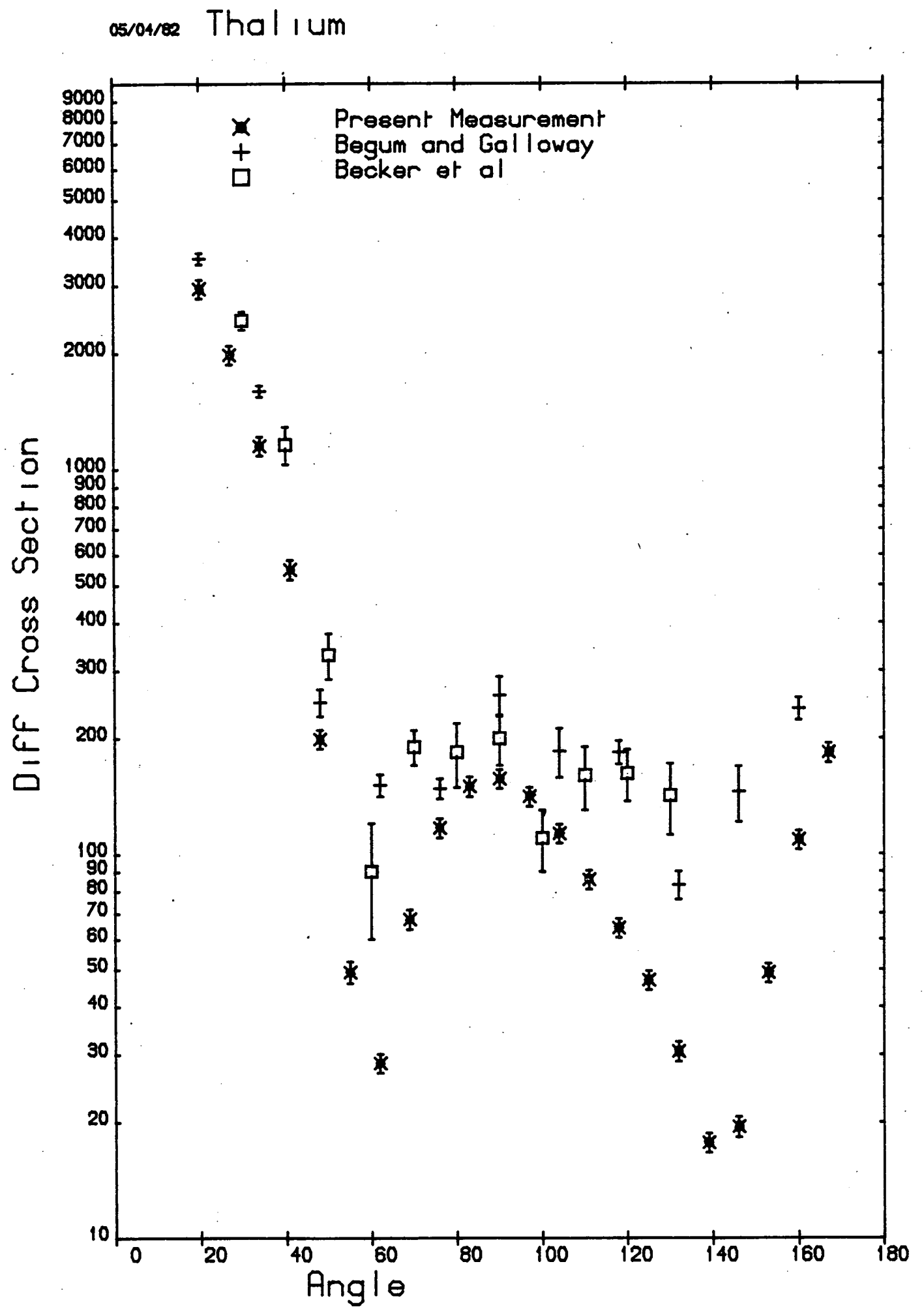
05/04/82 Thallium
Present Measurement
Begum and Galloway
Becker et al
Diff Cross Section
Angle
9000
8000
7000
6000
5000
4000
3000
2000
1000
900
800
700
600
500
400
300
200
100
90
80
70
60
50
40
30
20
10
0
20
40
60
80
100
120
140
160
180

Figure: 5.13

5.5.4 Lead

The scattering sample was machined from a piece of natural lead to a cylinder 4.82cm high by 4.92cm diameter. Its density was measured as 10.9gm/cm^3 slightly less than the accepted value.

Natural lead consists principally of three isotopes, ^{206}Pb, ^{207}Pb and ^{208}Pb in fractional abundances of 0.24, 0.23 and 0.53 repectively. With a lower integration limit of 2.2 MeV inelastic scattering involving the excitation of the 0.57 MeV level [29] of ^{207}Pb needs to be considered. Available inelastic cross section data [95] is well fitted by statistical model calculations using Fu and Pereys [29] Optical Potential. The statistical model fit to the data of Cranberg et al [95] was used to correct for inelastic scattering. The effective contribution is close to 11mb/sr before consideration of reduced detection efficiency. Data is listed in tables 5.8 and 5.9 and illustrated in figures 5.14 and 5.15. Figure 5.16 compares present data to that of Begum [38], Zijp and Jonker [16], and Galloway and Waheed [21]. Present measurements are in fair agreement with those of Zijp and Jonker and do not agree particularly well with those of Begum. The data of Galloway and Waheed look very different. Figure 5.17 compares the differential cross sections with those of Begum [38], Becker et al [9] and Galloway and Waheed [21]. The present measurements show a tendency to lower cross sections than the other sets.

Table 5.8

Lead

Analysing Power

	Uncorrected				Corrected
Angle	P(θ)	Stat.	Inst.	M.C.	P(θ)
20	-0.066	0.008	0.003	0.011	-0.060+- 0.015
27	-0.039	0.008	0.009	0.011	-0.030+- 0.016
34	-0.073	0.012	0.007	0.013	-0.066+- 0.020
41	-0.075	0.012	0.011	0.017	-0.073+- 0.024
48	-0.093	0.019	0.007	0.023	-0.100+- 0.032
55	-0.061	0.019	0.012	0.026	-0.112+- 0.035
62	-0.061	0.026	0.009	0.026	-0.117+- 0.039
69	-0.054	0.021	0.002	0.024	-0.065+- 0.032
76	0.013	0.024	0.017	0.024	0.022+- 0.038
83	-0.024	0.019	0.014	0.024	-0.010+- 0.034
90	0.037	0.024	0.012	0.024	0.049+- 0.036
97	0.031	0.020	0.007	0.025	0.045+- 0.033
104	0.041	0.028	0.011	0.026	0.070+- 0.040
111	0.020	0.024	0.020	0.027	0.039+- 0.041
118	0.028	0.031	0.002	0.028	-0.009+- 0.042
125	-0.085	0.021	0.002	0.029	-0.106+- 0.036
132	-0.074	0.035	0.005	0.029	-0.302+- 0.050
139	-0.053	0.031	0.006	0.029	-0.160+- 0.044
146	0.069	0.035	0.022	0.029	0.224+- 0.052
153	0.220	0.025	0.018	0.025	0.461+- 0.050
160	0.307	0.030	0.002	0.021	0.524+- 0.051
167	0.218	0.024	0.003	0.018	0.421+- 0.041

Table 5.9

Lead

Differential Cross Section

	Uncorrected				Corrected
Angle	σ(θ)	Stat.	M.C.	Syst.	σ(θ)
20	1674.4	53.1	7.3	92.1	3749.5+- 238.3
27	1194.5	12.8	5.3	65.7	2504.8+- 140.3
34	783.7	19.3	4.1	43.1	1470.9+- 88.7
41	497.6	4.9	3.1	27.4	787.6+- 44.1
48	330.9	7.3	2.2	18.2	424.3+- 25.2
55	231.0	3.8	1.7	12.7	224.3+- 12.9
62	193.2	6.6	1.5	10.6	171.8+- 11.1
69	192.7	1.7	1.6	10.6	200.1+- 11.2
76	199.9	5.1	1.8	11.0	234.3+- 14.3
83	206.4	1.9	1.9	11.4	258.0+- 14.5
90	210.1	4.9	2.0	11.6	271.2+- 16.4
97	198.8	2.5	1.9	10.9	245.7+- 13.9
104	175.8	5.0	1.7	9.7	192.0+- 11.9
111	161.7	1.5	1.5	8.9	162.4+- 9.2
118	154.6	4.2	1.3	8.5	149.4+- 9.3
125	141.7	2.5	1.1	7.8	118.9+- 6.9
132	137.6	4.4	1.0	7.6	105.2+- 6.7
139	141.9	1.7	1.1	7.8	105.7+- 6.0
146	166.4	4.9	1.2	9.2	148.8+- 9.3
153	209.6	4.4	1.5	11.5	231.8+- 13.7
160	262.8	8.1	1.7	14.5	336.6+- 21.3
167	323.4	3.0	1.9	17.8	461.0+- 25.8

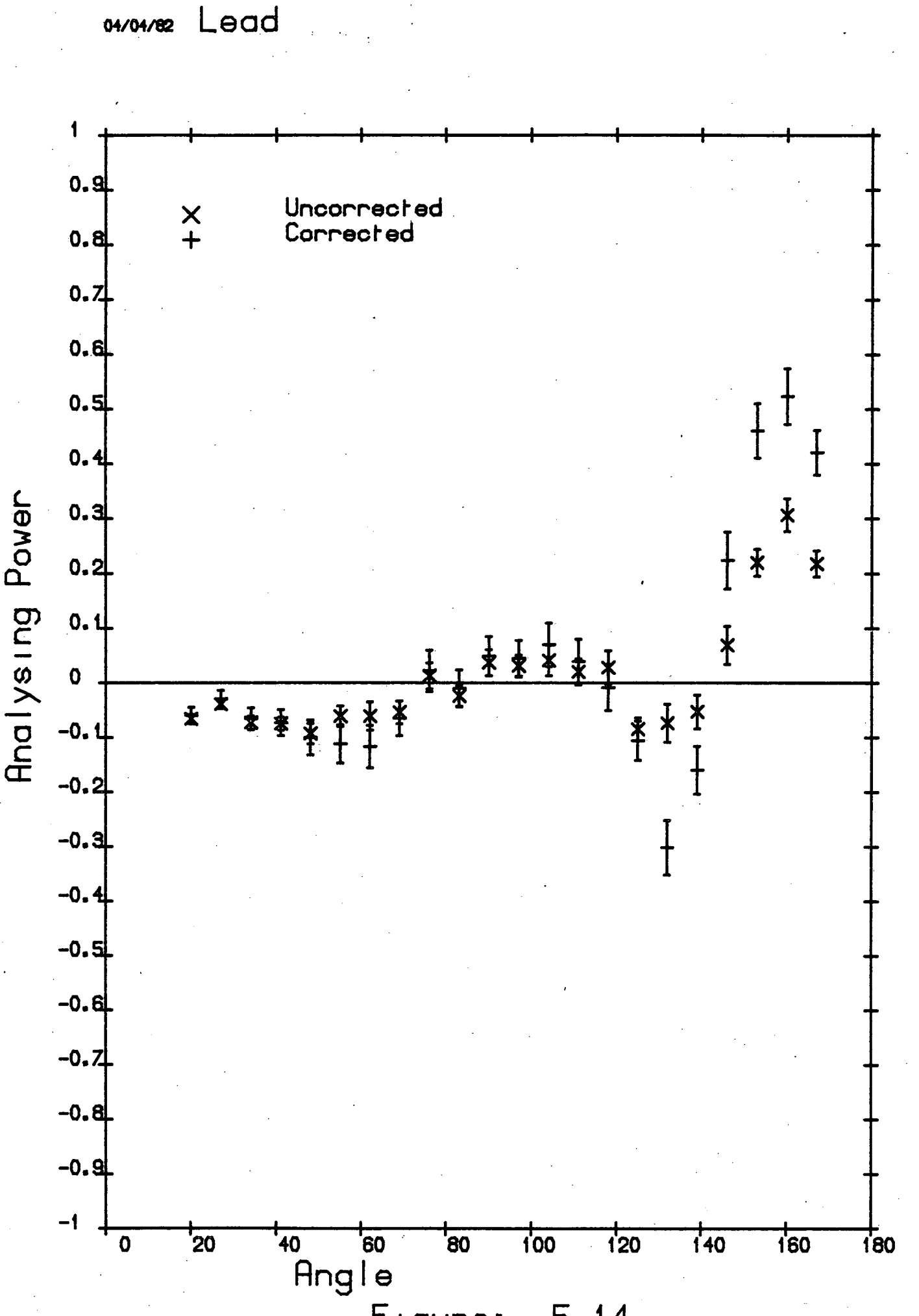
04/04/82 Lead
Uncorrected
Corrected
Analysing Power
Angle
1
0.9
0.8
0.7
0.6
0.5
0.4
0.3
0.2
0.1
0
-0.1
-0.2
-0.3
-0.4
-0.5
-0.6
-0.7
-0.8
-0.9
-1
0
20
40
60
80
100
120
140
160
180

Figure: 5.14

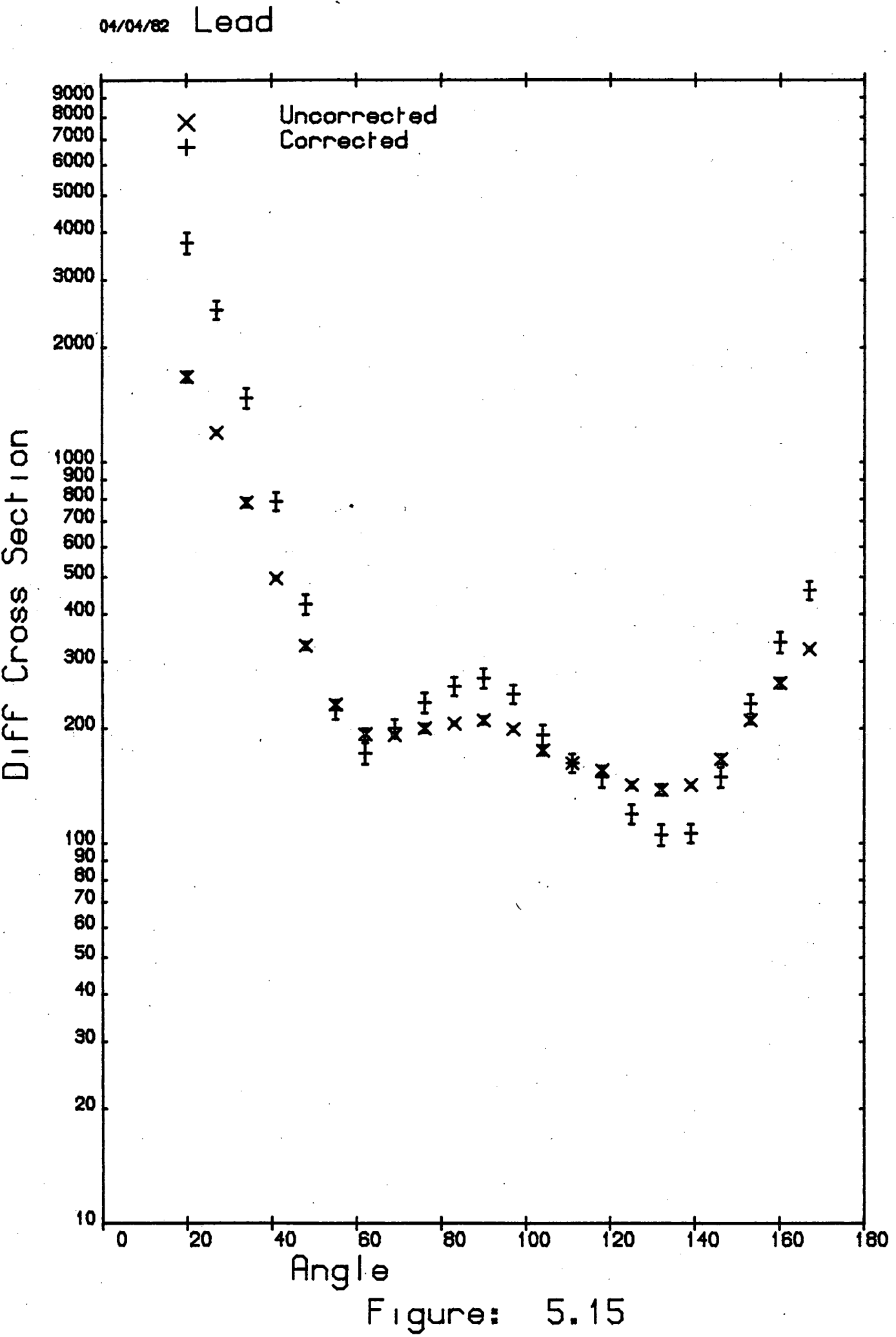
04/04/82 Lead
Uncorrected
Corrected
Diff Cross Section
9000
8000
7000
6000
5000
4000
3000
2000
1000
900
800
700
600
500
400
300
200
100
90
80
70
60
50
40
30
20
10
0
20
40
60
80
100
120
140
160
180
Angle

Figure: 5.15

05/04/82 Lead

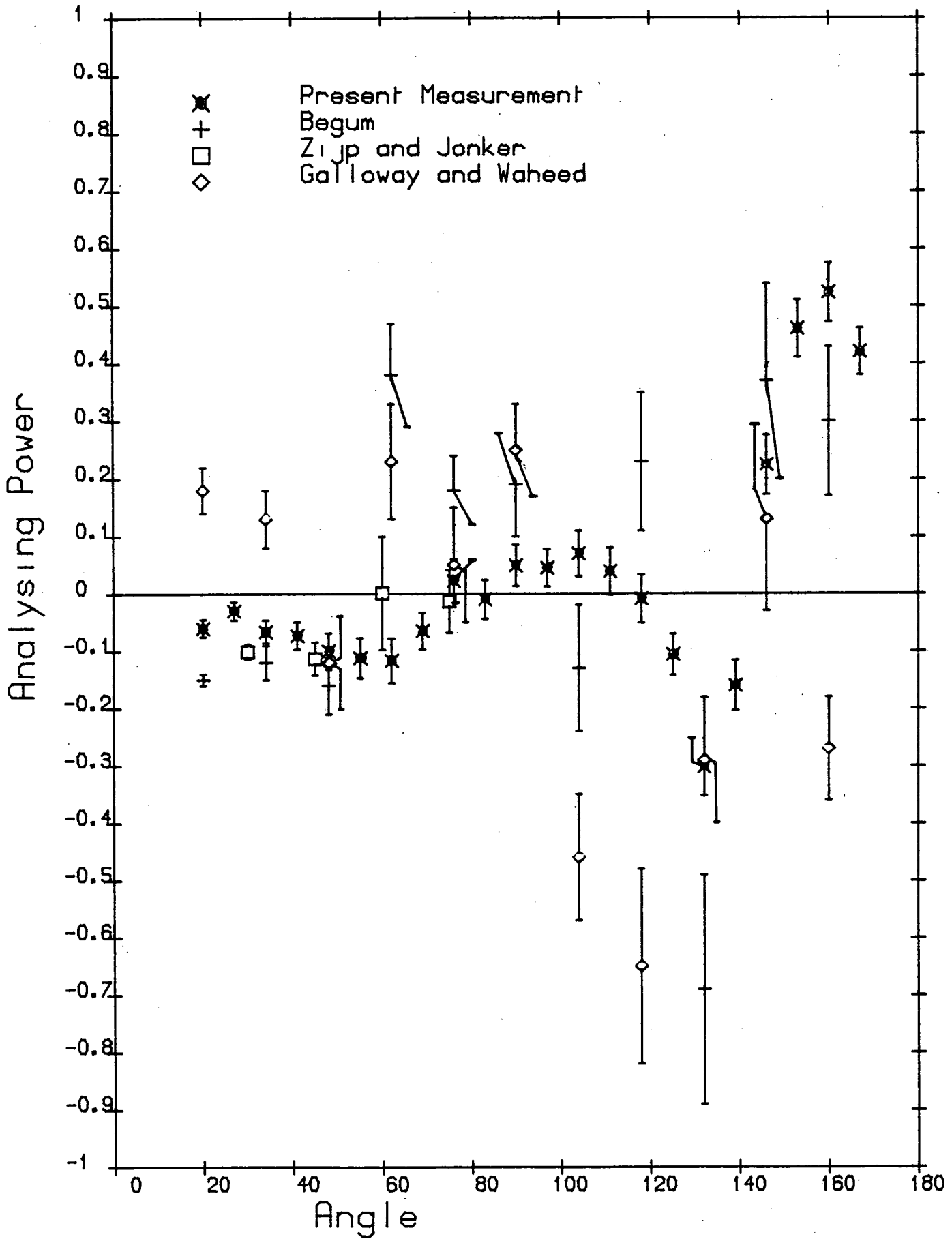

Figure: 5.16

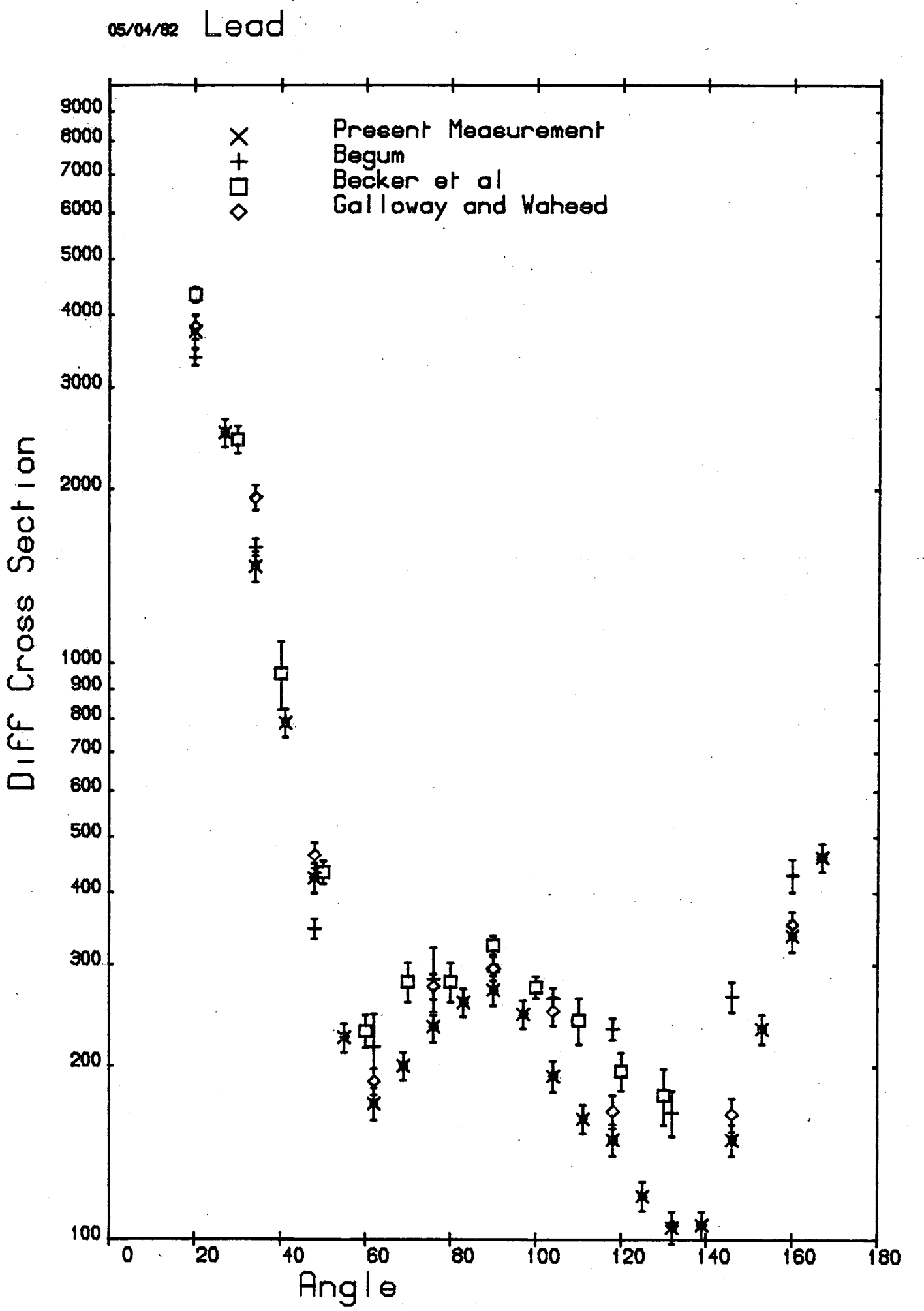
05/04/82 Lead
Present Measurement
Begum
Becker et al
Galloway and Waheed
Diff Cross Section
9000
8000
7000
6000
5000
4000
3000
2000
1000
900
800
700
600
500
400
300
200
100
0
20
40
60
80
100
120
140
160
180
Angle

Figure: 5.17

5.5.5 Bismuth

The sample is a cast cylinder of natural bismuth 5.08cm high by 5.08cm diameter, and its density is 9.734gm/cm^3, very close to the accepted value. Smith et al [26] give values of 5.90b and 7.40b for the total neutron cross sections of bismuth at 2.2 MeV and 3.0 MeV respectively, which result in sample MFPR's of 0.411 and 0.527.

Bismuth provided the easiest task of data correction as it is mono-isotopic and has, for the mass range under investigation, a high first excited state at 0.895 MeV [97]. Thus a lower integration limit of 2.1 MeV should exclude inelastic events, except for a very small residual count due to finite detector energy resolution. Correction proceeded with this lower limit under the assumption that total inelastic exclusion was achieved. Data is presented in tables 5.10 and 5.11 and illustrated in figures 5.18 and 5.19. Analysing powers are compared in figure 5.20 with those of Zijp and Jonker [16] and Begum and Galloway [28]. There is some qualitative agreement betweem the present measurements and those of Zijp and Jonker, although the former suggest more of a positive swing around 75 degrees and less of a negative swing around 130 degrees. The data of Begum and Galloway is more negative at forward angles and elsewhere is of poorer accuracy. Figure 5.21 compares the differential cross sections with those of Begum and Galloway [28], Becker et al [9] and Tanaka et al [30]. There is very good agreement between the present data and that of Tanaka et al which is a time of flight measurement of good accuracy.

Table 5.10

Bismuth

Analysing Power

	Uncorrected				Corrected
Angle	P(θ)	Stat.	Inst.	M.C.	P(θ)
20	-0.074	0.007	0.015	0.011	-0.079+- 0.021
27	-0.091	0.008	0.013	0.012	-0.096+- 0.021
34	-0.071	0.010	0.005	0.015	-0.081+- 0.020
41	-0.091	0.015	0.012	0.018	-0.115+- 0.027
48	-0.093	0.019	0.016	0.023	-0.142+- 0.034
55	-0.040	0.024	0.015	0.024	-0.102+- 0.038
62	-0.048	0.024	0.012	0.023	-0.090+- 0.036
69	-0.052	0.024	0.009	0.021	-0.068+- 0.033
76	0.029	0.022	0.007	0.021	0.028+- 0.031
83	0.040	0.022	0.010	0.021	0.042+- 0.032
90	-0.008	0.021	0.019	0.022	-0.011+- 0.035
97	-0.006	0.023	0.007	0.023	-0.014+- 0.034
104	-0.000	0.023	0.001	0.025	-0.007+- 0.035
111	0.012	0.026	0.011	0.028	0.006+- 0.039
118	0.010	0.026	0.015	0.030	-0.009+- 0.042
125	-0.125	0.030	0.015	0.031	-0.184+- 0.048
132	-0.115	0.030	0.006	0.032	-0.219+- 0.046
139	-0.073	0.038	0.002	0.031	-0.165+- 0.050
146	-0.004	0.036	0.001	0.028	0.008+- 0.046
153	0.109	0.031	0.005	0.024	0.227+- 0.043
160	0.141	0.030	0.006	0.021	0.289+- 0.042
167	0.177	0.031	0.001	0.020	0.344+- 0.044

Table 5.11

Bismuth

Differential Cross Section

	Uncorrected				Corrected
Angle	σ(θ)	Stat.	M.C.	Syst.	σ(θ)
20	1685.2	72.4	8.3	92.7	3281.0+- 229.1
27	1244.2	26.7	6.4	68.4	2316.6+- 136.9
34	792.3	18.4	4.5	43.6	1333.8+- 79.8
41	476.1	9.7	3.1	26.2	673.7+- 39.6
48	299.2	10.8	2.2	16.5	332.6+- 21.9
55	219.2	5.1	1.6	12.1	201.6+- 12.1
62	197.5	12.7	1.4	10.9	187.5+- 15.9
69	209.1	5.2	1.7	11.5	234.5+- 14.2
76	223.1	12.5	2.0	12.3	275.4+- 21.7
83	219.9	4.3	2.2	12.1	271.0+- 15.9
90	224.3	11.8	2.2	12.3	283.0+- 21.7
97	206.9	4.4	2.1	11.4	246.9+- 14.6
104	193.7	8.7	1.9	10.7	222.7+- 15.9
111	176.9	3.4	1.7	9.7	191.8+- 11.2
118	166.6	8.9	1.6	9.2	175.8+- 13.6
125	149.5	3.0	1.7	8.2	143.0+- 8.5
132	141.4	8.9	1.8	7.8	126.7+- 13.9
139	137.6	3.5	1.9	7.6	115.4+- 7.1
146	151.0	8.6	2.0	8.3	136.4+- 10.9
153	185.2	4.2	2.1	10.2	198.2+- 12.0
160	207.5	10.0	2.1	11.4	232.6+- 17.0
167	279.1	5.7	2.0	15.4	372.8+- 21.9

04/04/82 Bismuth

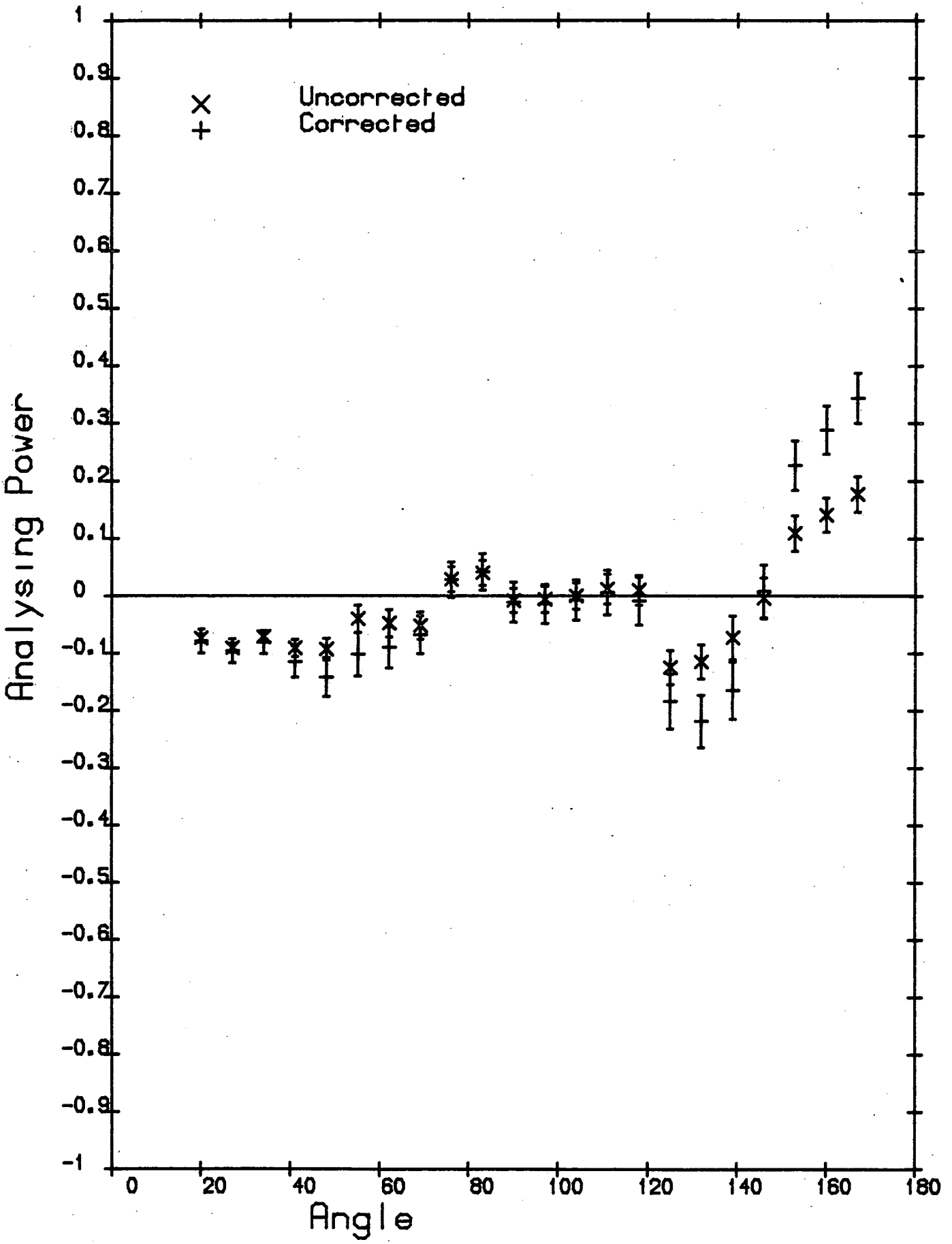

Figure: 5.18

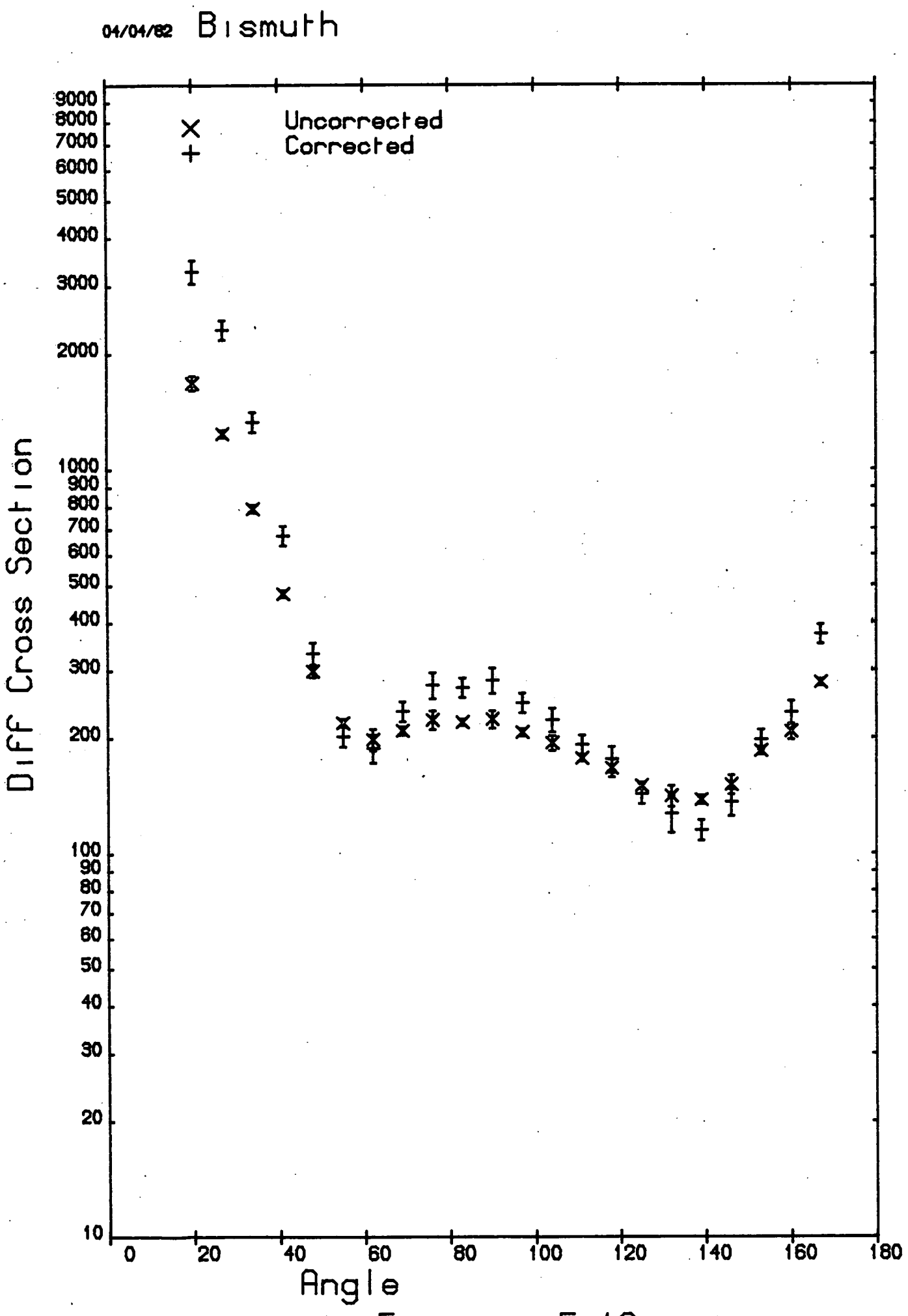
04/04/82 Bismuth
Uncorrected
Corrected
DiFF Cross Section
9000
8000
7000
6000
5000
4000
3000
2000
1000
900
800
700
600
500
400
300
200
100
90
80
70
60
50
40
30
20
10
0
20
40
60
80
100
120
140
160
180
Angle

Figure: 5.19

05/04/82 Bismuth

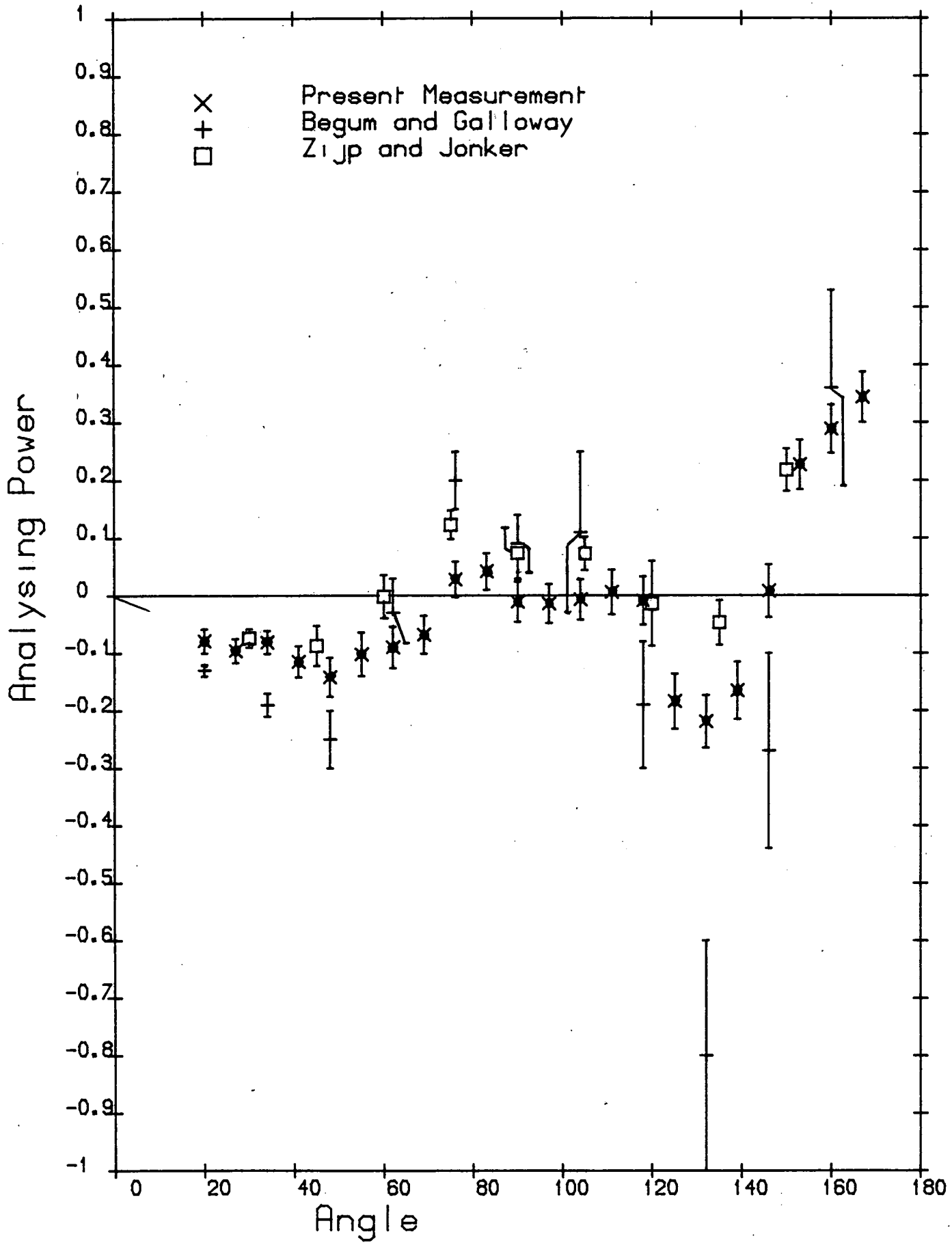

Figure: 5.20

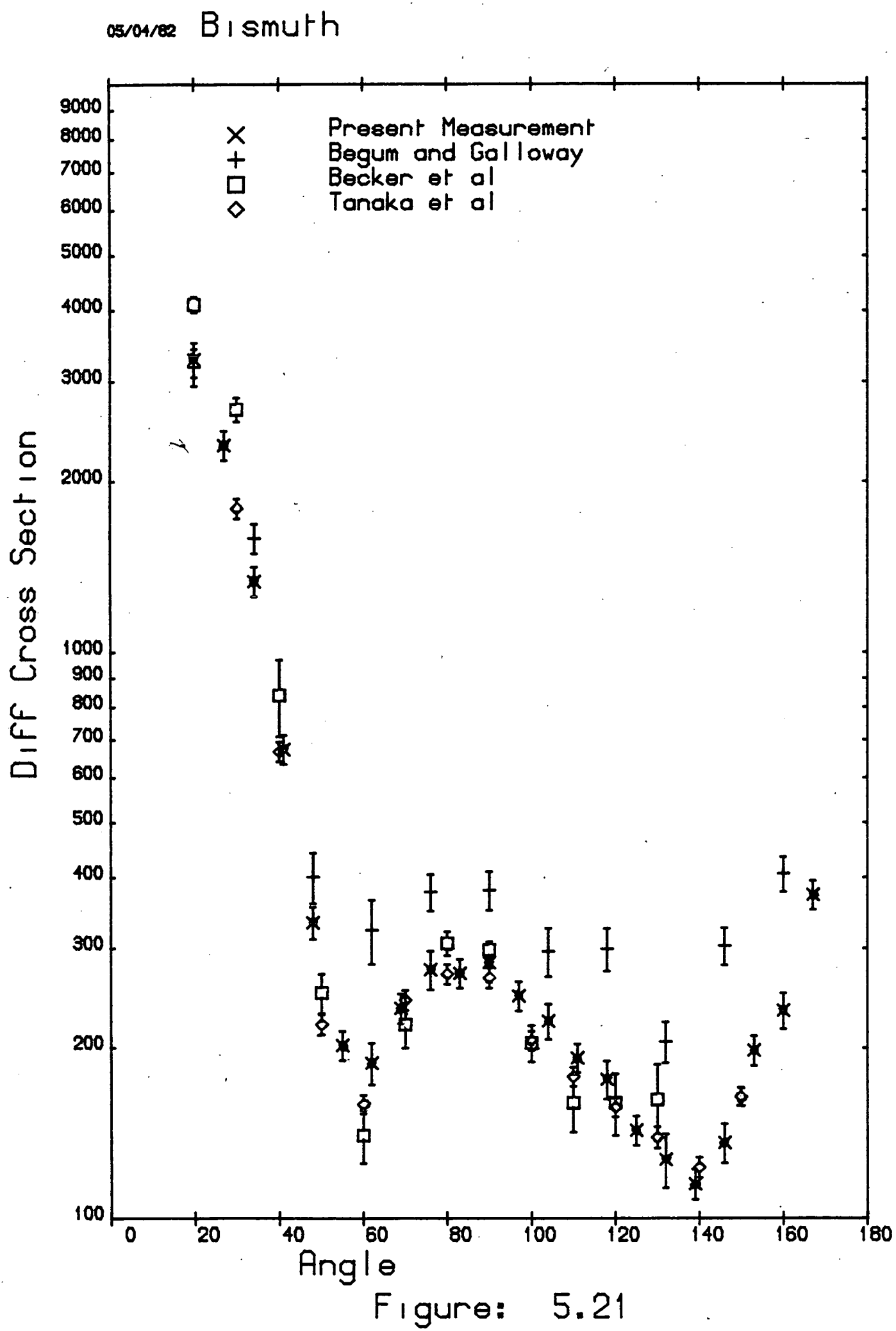
05/04/82 Bismuth
Present Measurement
Begum and Galloway
Becker et al
Tanaka et al
Diff Cross Section
9000
8000
7000
6000
5000
4000
3000
2000
1000
900
800
700
600
500
400
300
200
100
0
20
40
60
80
100
120
140
160
180
Angle

Figure: 5.21

5.5.6 Uranium

The scattering sample of uranium depleted of ^{235}U was provided by the UKAEA. It is a cylinder 5.45cm high by 2.86cm diameter, density 19.0gm/cm^3. Foster and Glasgow [77] give total cross sections of 7.4b and 8.0b at energies of 2.3 and 3.0 MeV respectively which result in sample MFPR's of 0.51 and 0.55.

With a lower integration limit of 2.3 MeV the following excited states must be considered: 0.045, 0.148, 0.308 and 0.519 MeV [98]. Beghian et al [27] have measured the inelastic cross sections of the first two excited states, at 3.1 MeV incident energy. Their data was used in the correction. No data is available for the 3rd and 4th state. These states are all components of the ground rotational band of ^{238}U and the measured cross section of the 2nd state is much smaller than that of the first state. It is therefore likely that the 3rd and 4th state excitation cross sections are not large and hence they were neglected. Without considering reduced detection efficiency, the 1st excited state contribution varies between 30 and 60mb/sr and the 2nd excited state contribution between 17 and 3mb/sr. In addition to inelastic scattering, fast neutron induced fission must be considered. At 3 MeV the cross section for this process is 0.53b [100], and given an average of 2.61 prompt neutrons emitted per fission event, the size of the contribution becomes significant. The effective fission neutron contribution to the cross section was taken as

$$\sigma_{eff} = \nu\sigma_{nf}\int_{E_1}^{E_2} N(E)e(E)dE \Big/ \int_0^{\infty} N(E)dE$$

σ_{nf}: fast neutron induced fission cross section

ν: number of neutrons per fission event

$e(E)$: detection efficiency

E_1: lower integration limit (2.3MeV)

E_2: upper integration limit (3.1MeV)

A short program was written to evaluate the integrals numerically with

N(E) assumed Maxwellian

$$N(E) = E^{1/2} \exp(-E/T) c / T^{3/2}$$

T: nuclear temperature

The sensitivity of σ_{eff} to T was investigated. Raising T from 1.5 MeV to 2.0 MeV raised σ_{eff} by about 10 per cent and further raising produced little subsequent effect in σ_{eff}. σ_{eff} was calculated as being 18.0 +— 2.0 mb/sr. Data is listed in tables 5.12 and 5.13 and illustrated in figures 5.22 and 5.23. Figure 5.24 compares the analysing power with that of Begum and Galloway [28]. The data can be said to disagree only at the forward angles where accuracy is best. Figure 5.25 compares the differential cross section with those of Beghian et al [27] , Batchelor et al [99] and Begum and Galloway [28]. The present measurements are somewhat higher than those of Beghian et al, but agree with those of Batchelor et al. However the data of Batchelor et al and Begum and Galloway are not corrected for the inelastic contribution from the 0.045MeV state and in addition the latter data contains a contribution from fission neutrons.

Table 5.12

Uranium

Analysing Power

	Uncorrected				Corrected
Angle	P(θ)	Stat.	Inst.	M.C.	P(θ)
20	-0.067	0.015	0.003	0.017	-0.057+- 0.023
27	-0.075	0.022	0.009	0.021	-0.061+- 0.032
34	-0.008	0.021	0.007	0.028	0.012+- 0.036
41	-0.034	0.019	0.011	0.035	-0.007+- 0.044
48	0.011	0.032	0.007	0.041	0.096+- 0.063
55	0.016	0.032	0.012	0.039	0.154+- 0.074
62	-0.001	0.049	0.009	0.036	0.002+- 0.074
69	-0.022	0.022	0.002	0.034	-0.045+- 0.046
76	0.070	0.032	0.017	0.032	0.074+- 0.055
83	0.001	0.028	0.014	0.030	0.021+- 0.049
90	-0.030	0.045	0.012	0.030	0.002+- 0.061
97	-0.046	0.032	0.007	0.032	-0.022+- 0.052
104	-0.052	0.044	0.011	0.038	-0.082+- 0.071
111	-0.052	0.044	0.020	0.048	-0.281+- 0.091
118	-0.091	0.067	0.002	0.055	-0.767+- 0.120
125	-0.121	0.051	0.002	0.053	-0.772+- 0.098
132	-0.111	0.057	0.005	0.045	-0.435+- 0.094
139	-0.011	0.052	0.006	0.039	-0.080+- 0.083
146	0.124	0.053	0.022	0.038	0.283+- 0.094
153	0.097	0.100	0.018	0.038	0.423+- 0.143
160	0.252	0.060	0.002	0.036	0.661+- 0.105
167	0.064	0.068	0.003	0.032	0.419+- 0.098

Table 5.13

Uranium

Differential Cross Section

	Uncorrected				Corrected
Angle	σ(θ)	Stat.	M.C.	Syst.	σ(θ)
20	1529.6	36.6	7.6	84.1	2814.3+- 171.3
27	1011.6	24.9	5.8	55.6	1738.1+- 107.2
34	603.9	14.3	3.8	33.2	880.3+- 55.1
41	320.6	12.4	1.9	17.6	344.0+- 25.6
48	199.8	3.3	0.7	11.0	102.4+- 8.2
55	148.6	2.6	0.4	8.2	54.6+- 5.4
62	144.4	2.7	0.6	7.9	92.6+- 7.7
69	160.1	2.9	0.8	8.8	143.4+- 10.6
76	167.7	3.9	0.9	9.2	175.0+- 12.8
83	164.3	3.4	0.9	9.0	180.6+- 12.9
90	156.4	2.6	0.8	8.6	162.0+- 11.6
97	141.4	2.9	0.7	7.8	124.8+- 9.6
104	110.5	2.3	0.5	6.1	79.8+- 7.0
111	90.1	2.0	0.4	5.0	42.2+- 4.8
118	85.8	2.0	0.3	4.7	24.7+- 3.8
125	82.8	2.3	0.3	4.6	29.2+- 4.1
132	85.0	2.6	0.4	4.7	46.3+- 5.3
139	95.2	2.7	0.4	5.2	63.0+- 6.2
146	98.5	3.1	0.5	5.4	73.1+- 7.0
153	102.3	2.9	0.5	5.6	80.0+- 7.3
160	104.2	3.1	0.6	5.7	90.5+- 8.0
167	112.6	3.6	0.6	6.2	106.5+- 9.2

08/04/82 Uranium

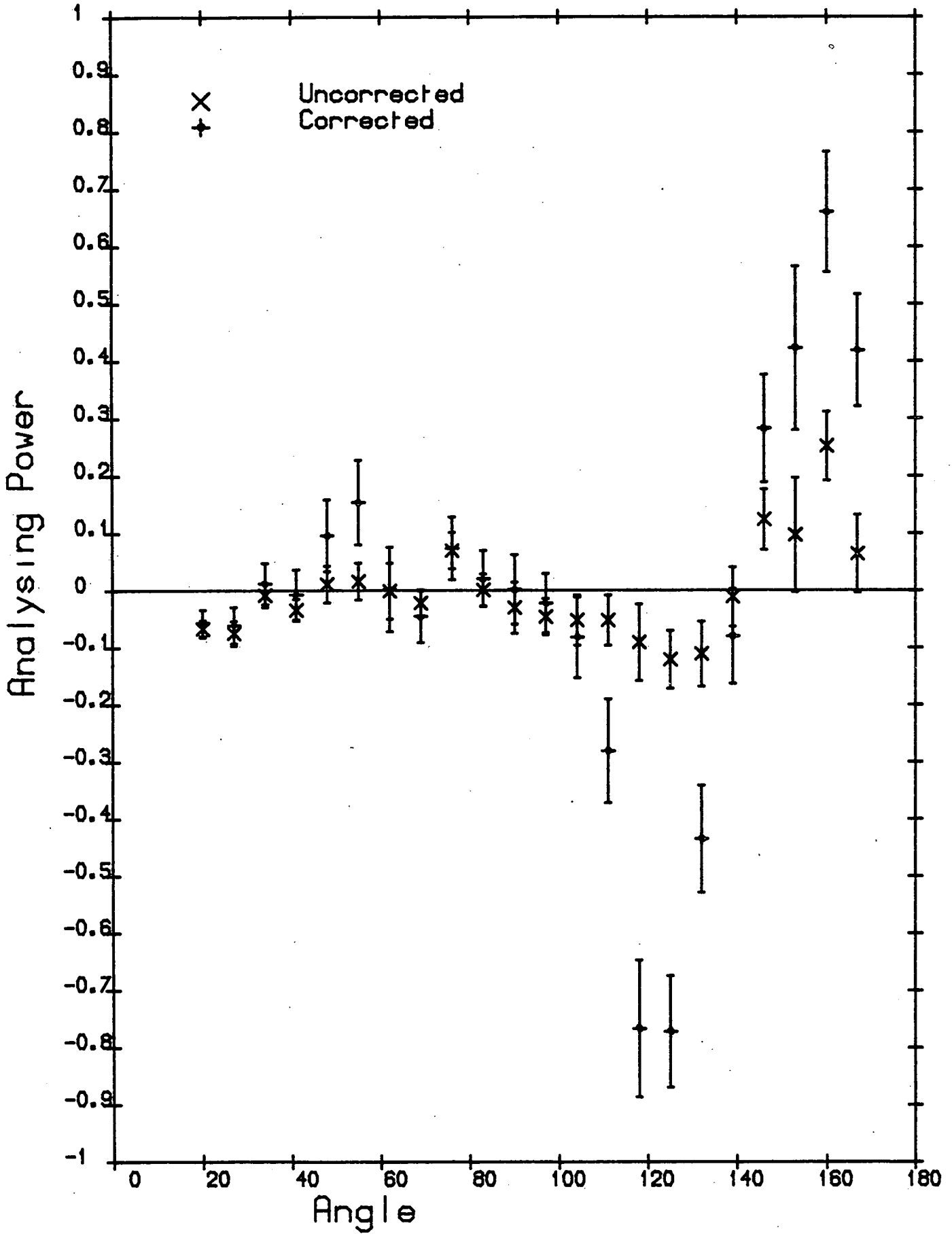

Figure: 5.22

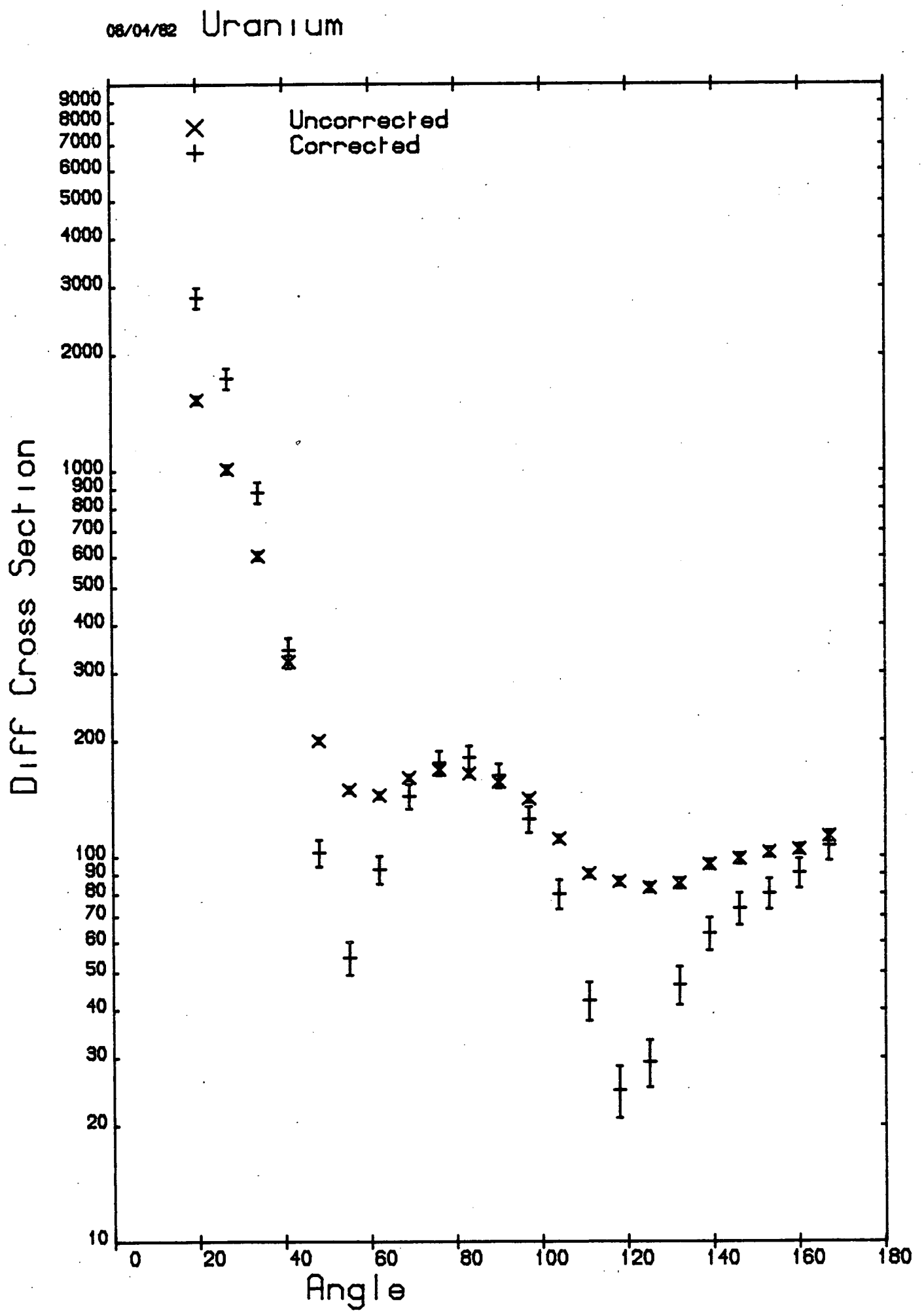
08/04/82 Uranium
Uncorrected
Corrected
Diff Cross Section
9000
8000
7000
6000
5000
4000
3000
2000
1000
900
800
700
600
500
400
300
200
100
90
80
70
60
50
40
30
20
10
0
20
40
60
80
100
120
140
160
180
Angle

Figure: 5.23

08/04/82 Uranium

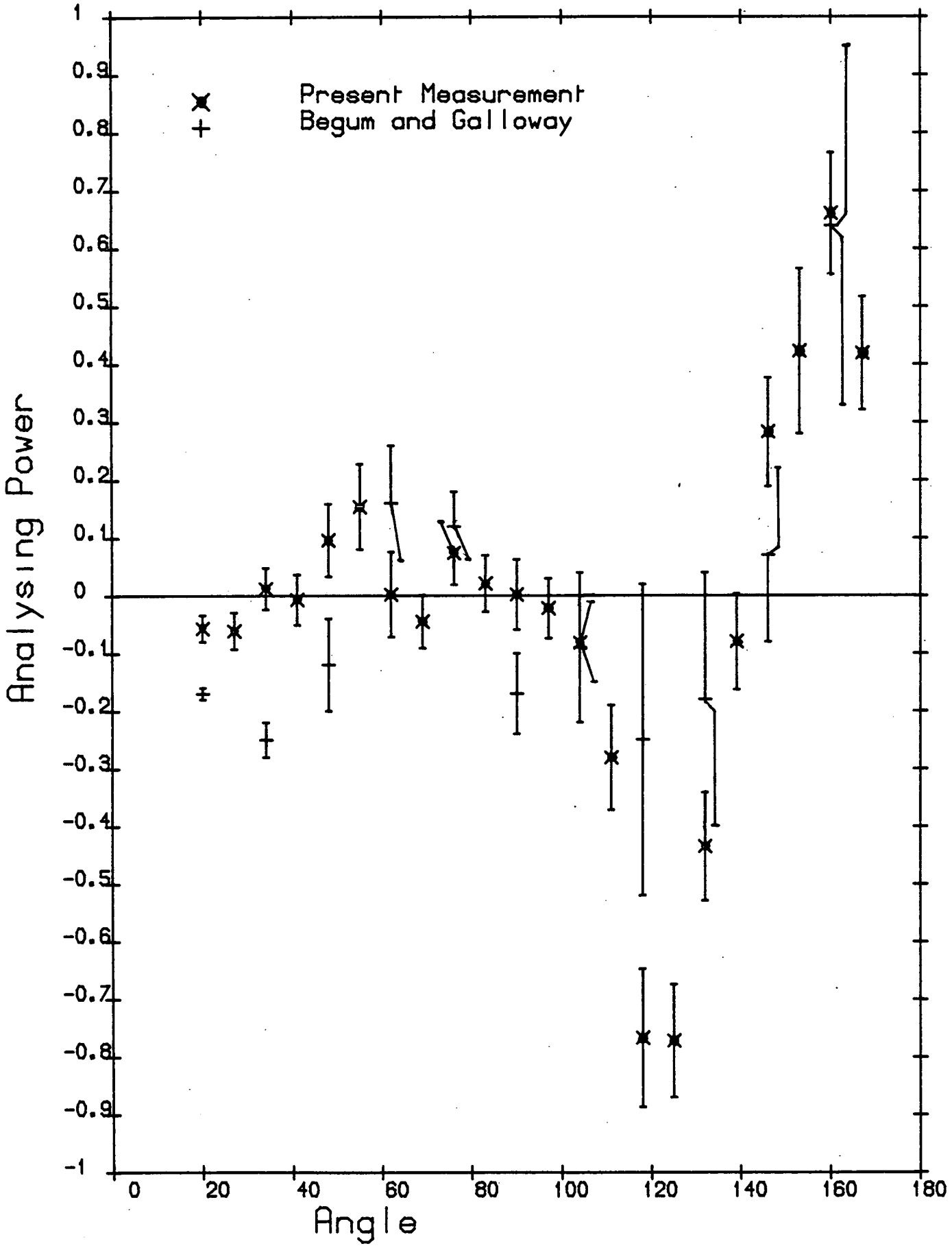

Figure: 5.24

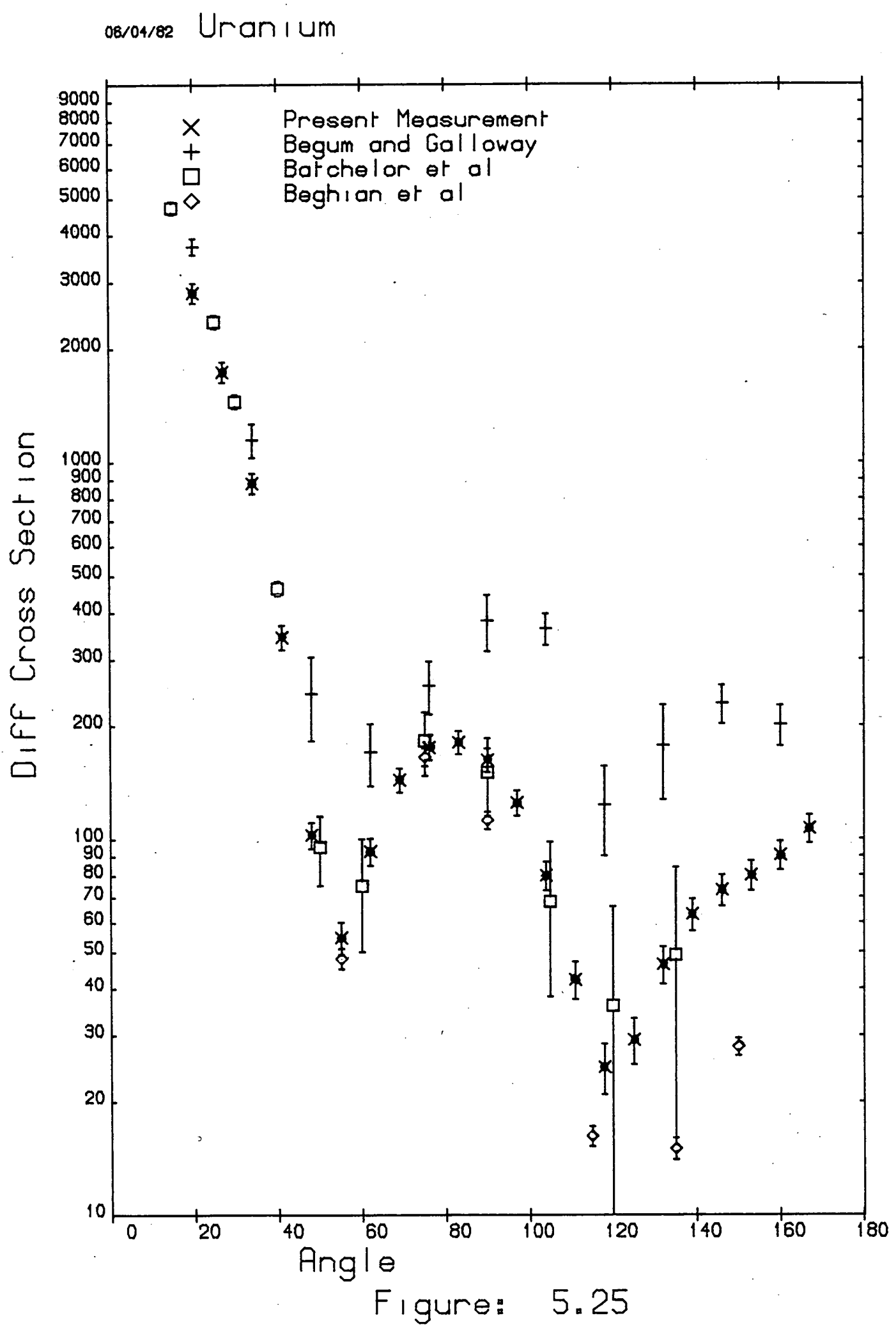
06/04/82 Uranium
Present Measurement
Begum and Galloway
Batchelor et al
Beghian et al
Diff Cross Section
9000
8000
7000
6000
5000
4000
3000
2000
1000
900
800
700
600
500
400
300
200
100
90
80
70
60
50
40
30
20
10
0
20
40
60
80
100
120
140
160
180
Angle

Figure: 5.25

Chapter 6

Reaction Model Calculations

6.1 Introduction

To date the majority of neutron scattering data analyses have been made using the Optical Model (OM) in which polarisations and cross sections are calculated after solution of a time independent Schrodinger equation into which has been inserted a complex interaction potential, the Optical Potential (OP). The use of this potential represents an amalgamation of the strong interaction (compound nucleus) and weak interaction (shell) models, and its use is equivalent to considering the nucleus as a semi-transparent medium. The real part is responsible mainly for direct or shape elastic scattering and the imaginary part accounts for all other processes where the incident neutron is absorbed to form a compound nucleus. In this framework no other possibilities are considered. To account for processes such as direct inelastic scattering at low energy, collective nucleon effects must be considered. If this is done the OP cannot be assumed spherically symmetric and polar and asimuthal angle as well as radial dependence have to be included. Good accounts of the OM and more general nuclear reaction theory are given by Hodgson [101,102]. Some refinements [103,104] have been made to the formalism since 1971 when the latter book was published, but the basic theory remains substantially unaltered to the present day.

The Spherical OP

The spherical OP is taken to have the form

$$U(r) = -Vf(r) - Wg(r) - V_S h(r) L.\sigma \qquad (6.1)$$

$$f(r) = \{1 + \exp[(r - r_R A^{1/3})/a_R]\}^{-1}$$

$$h(r) = \{h/m_{\pi}c\}^2 \, d/dr.\{1 + \exp[(r-r_S A^{1/3})/a_S]\}^{-1}$$

where f(r) and h(r) are the Woods Saxon and Thomas Fermi form factors respectively, which were introduced in Chapter 1. The imaginary factor, g(r) is usually given a surface peaked form at energies under 10 MeV as the Pauli Principle prevents absorption into the volume of the nucleus. Convenient and widely used forms are the derivative Woods Saxon and Gaussian radial dependence. The former will be used in the analysis presented here. It is

$$g(r) = 4a_I d/dr.\{1+\exp[(r-r_I A^{1/3})/a_I]\}^{-1}$$

The radius parameters r_R, r_I and r_S are often taken as equal to one another, but a_I often differs from a_R and a_S.

Solution of the Schrodinger equation using the OP yields the elements of the Scattering Matrix (S Matrix), the S_{lj}, and from these elements the total, integrated elastic, integrated absorption, differential shape elastic cross sections and differential polarisations can be calculated. The S_{lj} derived from the OP show a smooth energy dependence, which result in a smooth energy dependence of cross sections and polarisations.

This is contrary to the observed energy dependence of cross sections at low energy, especially with light nuclei , which show resonance behaviour, when isolated, well defined states of the compound system are excited. The OM therefore is not equiped to deal with these situations. At higher excitation energies and with heavier nuclei, when compound nucleus states become broader and crowd more closely together so that they tend to overlap, well defined resonances are not observed. Instead, cross sections tend to fluctuate in a highly irregular manner. However if they are averaged over a suitable energy

interval, the fluctuations can be smoothed out. The apparatus described in the previous sections has relatively poor energy resolution and the neutron beam is far from being mono-energetic. Thus the data collected has effectively been averaged over an interval large compared with the average spacing of compound nuclear states at an energy of around 3 MeV, at least for the mass region under investigation. To use the OM it is necessary to relate the energy averaged experimental data to the energy averaged S Matrix elements, the $\langle S_{lj} \rangle$, calculated from the OP. For simplicity s wave scattering and hence cross sections only are considered. Taking the non-energy averaged S Matrix element as the sum of an averaged and fluctuating component

$$S = \langle S \rangle + S_{fl}$$

$$\langle S_{fl} \rangle = 0$$

The energy averaged cross sections are then

$$\langle \sigma_t \rangle = 2\pi\pi/k^2 \langle (1-\mathrm{Re}S) \rangle$$
$$= 2\pi\pi/k^2 (1-\mathrm{Re}\langle S \rangle)$$

$$\langle \sigma_e \rangle = \pi\pi/k^2 \langle |1-S|^2 \rangle$$
$$= \pi\pi/k^2 \{|1-\langle S \rangle|^2 - |\langle S \rangle|^2 + \langle |S| \rangle^2\}$$

$$\langle \sigma_r \rangle = \pi\pi/k^2 \langle (1-|S|^2) \rangle$$
$$= \pi\pi/k^2 (1-\langle |S| \rangle^2)$$

where t,e and r refer to total,elastic and absorption cross sections respectively. Thus it can be seen that $\langle S \rangle$ gives the total cross section directly, but since $\langle |S|^2 \rangle \neq |\langle S \rangle|^2$ the elastic and reaction

cross sections have an extra term due to the fluctuations. This fluctuating term can be equated [102] to the energy averaged compound elastic cross section.

$$\langle\sigma_{ce}\rangle = \Pi/k^2(\langle|S|^2\rangle - |\langle S\rangle|^2)$$

$$\langle\sigma_{e}\rangle = \Pi/k^2(|1-\langle S\rangle|^2) + \langle\sigma_{ce}\rangle$$

$$\langle\sigma_{r}\rangle = \Pi/k^2(1-|\langle S\rangle|^2) - \langle\sigma_{ce}\rangle$$

The energy averaged compound elastic cross section may be calculated indirectly from $\langle S\rangle$ using the Hauser Feshbach formalism [31], also referred to as the Statistical Model, or a derivative accounting for level width fluctuation [32].

One of the assumptions made in the Hauser Feshbach theory is that many states are excited in the compound system and that the corresponding wave functions have random phases. This leads to the prediction that the emitted particle will be unpolarised. Thus the presence of a compound component in elastic scattering will reduce the magnitude of the measured analysing power. This dilution of analysing power can be quite marked at 3 MeV, and compound elastic effects are most noticeable for both analysing power and cross section around the angles at which diffraction minima in the direct elastic cross section occur. Here the compound component may be larger than the direct component. This is illustrated in figures 6.1 and 6.2 which show the calculated analysing power and differential cross sections for the nucleus ^{209}Bi with and without a compound elastic contribution.

6.3 Optical Model Analysis

OM calculations of analysing powers and differential cross

08/04/82 Calculated Analysing Power: Bismuth

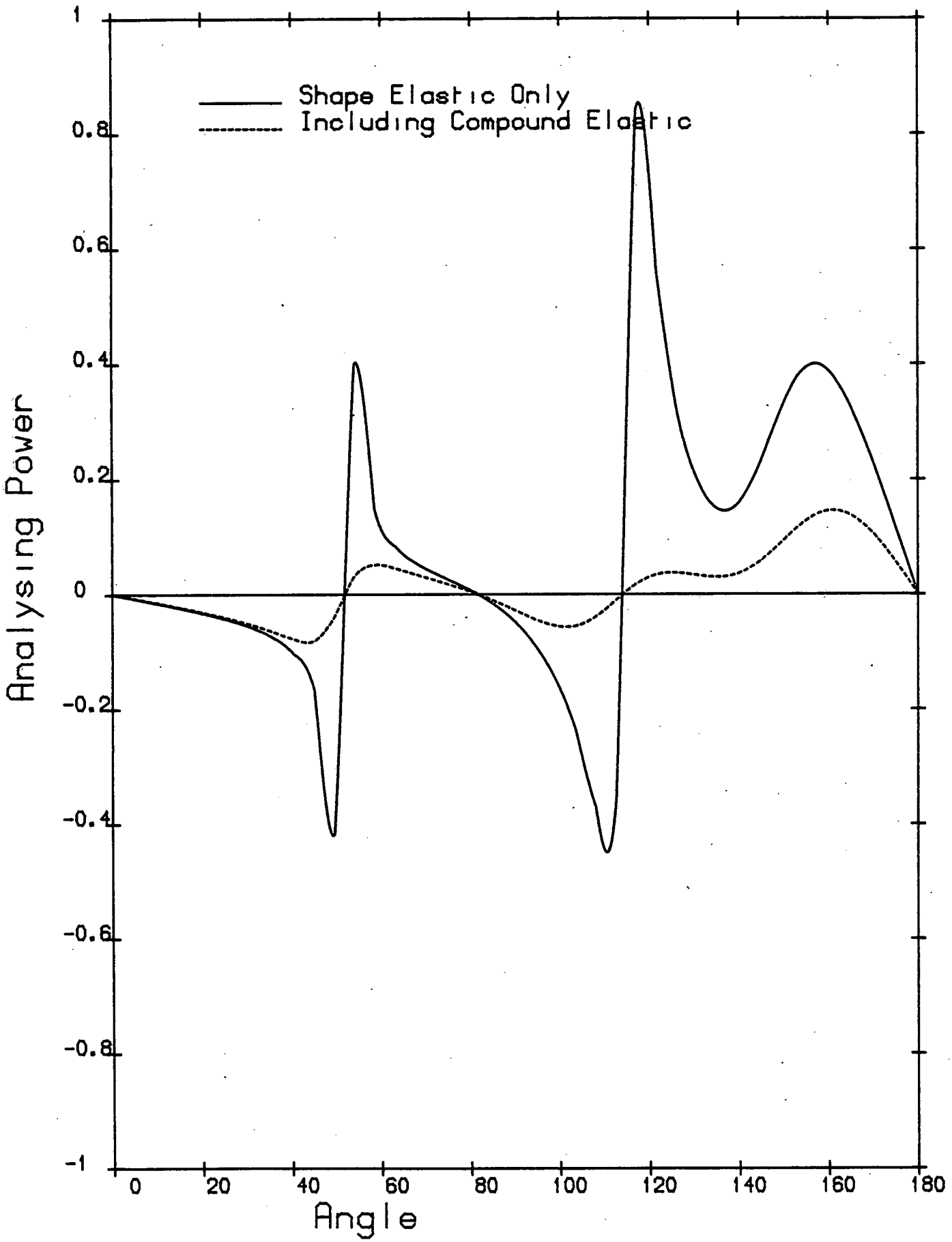

Figure: 6.1

08/04/82 Calculated Cross Sections: Bismuth

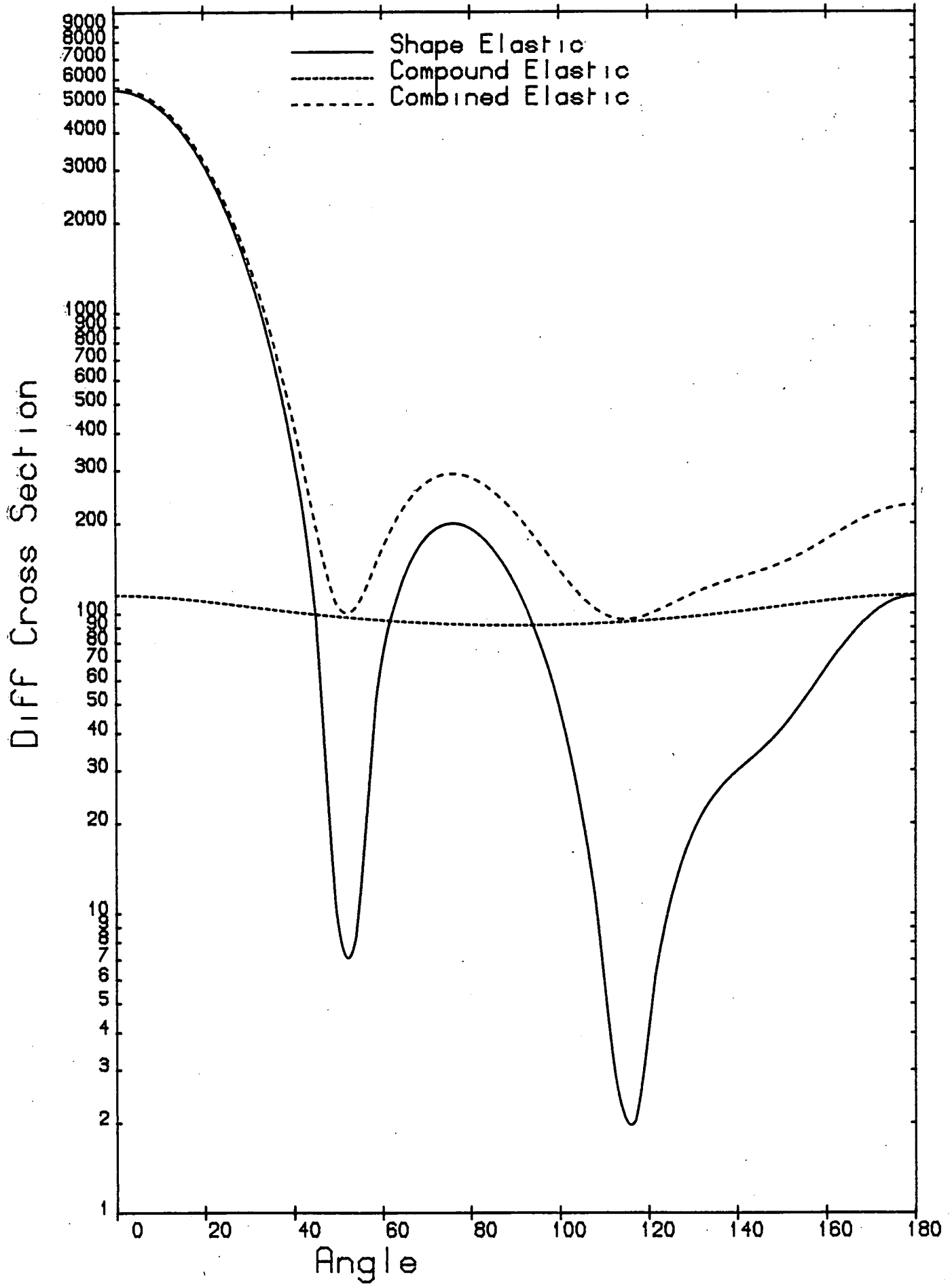

Figure: 6.2

sections were made for all nuclei on which measurements were taken. Where natural scattering samples contained more than one isotope, the calculation was taken as the sum of the contributions of the constituent nuclei weighted by their fractional abundances. Although the direct elastic component does not vary much over small mass intervals, the compound elastic cross section may vary considerably between isotopes of the same element. This is true of the lead isotopes. ^{208}Pb with one excited state below 3 MeV has a much higher compound elastic cross section than ^{206}Pb which has 20 excited states below 3 MeV. The potential of equation 6.1 was used in all cases. In more extensive OM analyses, potentials introducing energy and isospin dependence in the real and imaginary well depths have been introduced.

$$U = U_0 + U_1 E + U_2 E^2 \tag{6.2}$$

$$U = U_0 + U_1 (N-Z)/A \tag{6.3}$$

where U denotes the real or imaginary potential well depth. The isospin term, (N-Z)/A, is introduced to explain the fact that nuclei with the same mass but differing proton and neutron numbers may have differing differential cross sections and polarisations. One extensive OM analysis by Perey and Buck [8] has used a non-local potential to fit neutron differential cross sections. Non-locality is implied by microscopic calculations of the nucleon nucleus potential from the nucleon nucleon interaction [96,102]. Mathematically this means that the term $V(r)\Psi(r)$ in the Schrodinger equation must be replaced by the term $\int V(r,r')\Psi(r')dr'$. However the energy independent non-local potential can been shown [102] to be equivalent to an energy dependent local potential as of equation 6.2. The present data was not thought extensive enough to make the results of such elaborations physically significant.

The numerical parameters of all OPs used in this analysis are presented in table 6.1. The potential well depths are in MeV and the radius and diffuseness parameters in fm.

Table 6.1

OP Parameters

Best Fit	V: 44.02	W: 9.91	V_S: 4.18
Tungsten	r_R: 1.26	r_I: 1.28	r_S: 1.26
	a_R: 0.641	a_i: 0.662	a_S: 0.128
Best Fit	V: 45.84	W: 7.69	V_S: 3.86
Mercury	r_R: 1.25	r_I: 1.25	r_S: 1.25
	a_R: 0.672	a_I: 0.462	a_S: 0.518
Best Fit	V: 43.94	W: 18.99	V_S: 3.20
Thalium	r_R: 1.30	r_I: 1.32	r_S: 1.30
	a_R: 0.616	a_I: 0.199	a_S: 0.545
Best Fit	V: 43.60	W: 9.75	V_S: 6.89
Lead	r_R: 1.30	r_I: 1.32	r_S: 1.30
	a_R: 0.629	a_I: 0.193	a_S: 0.217
Best Fit	V: 43.71	W: 15.77	V_S: 6.96
Bismuth	r_R: 1.30	r_I: 1.32	r_S: 1.30
	a_R: 0.629	a_I: 0.190	a_S: 0.228
Best Fit	V: 45.08	W: 6.12	V_S: 2.86
Uranium	r_R: 1.217	r_I: 1.212	r_S: 1.217
	a_R: 0.728	a_I: 0.373	a_S: 0.824
Rosen et al	V: 49.03-0.33E	W: 5.75	V_S: 5.5
[11]	r_R: 1.25	r_I: 1.25	r_S: 1.2
	a_R: 0.65	a_I: 0.75	a_S: 0.65
Becchetti and	V: 56.3-0.32E	W: 13-0.25E	V_S: 6.2
Greenlees	- 24(N-Z)/A	- 12(N-Z)/A	
[18]	r_R: 1.17	r_I: 1.26	r_S: 1.25
	a_R: 0.75	a_I: 0.58	a_S: 0.75

Wilmore and	V: 47.01	W: 9.52	V_S: 7.2
Hodgson	- 0.217E	- 0.53E	
[105]	- $0.0012E^2$		
	r_R: 1.322	r_I: 1.266	$r_S = r_R$
	- $7.6\times10^{-4}A$	- $3.7\times10^{-4}A$	
	+ $4\times10^{-6}A^2$	+ $2\times10^{-6}A^2$	
	- $8\times10^{-9}A^3$	- $4\times10^{-9}A^3$	
	a_R: 0.66	a_I: 0.48	a_S: 0.66
Moldauer	V: 46.0	W: 14.0	V_S: 7.0
[89]	r_R: 1.25	r_I: 1.38	r_S: 1.25
	a_R: 0.62	a_I: 0.24	a_S: 0.65
Becker et al	V: 48	W: 5.5	V_S: 10.4
[9]	r_R: 1.25	r_I: 1.25	r_S: 1.25
	a_R: 0.65	a_I: 0.96	a_S: 0.65
Zijp and Jonker	V: 50.4.0(W)	W: 9.3(W)	V_S: 8.0
[16]	: 45.0(Tl)	: 13.0(Tl)	
	: 46.6(Pb)	: 6.9(Pb)	
	: 46.2(Bi)	: 8.2(Bi)	
	r_R: 1.25	r_I: 1.25	r_S: 1.12
	a_R: 0.65	a_I: 0.65	a_S: 0.65
Begum and	V: 49.13	W: 2.27	V_S: 11.39
Galloway (W)	r_R: 1.16	r_I: 1.66	r_S: 1.01
[28]	a_R: 0.67	a_I: 0.66	a_S: 0.75
Begum and	V: 49.9	W: 6.96	V_S: 16.88
Galloway (Tl)	r_R: 1.14	r_I: 1.43	r_S: 1.07
[28]	a_R: 0.63	a_I: 0.36	a_S: 0.38
Begum and	V: 47.06	W: 7.94	V_S: 11.12
Galloway (Bi)	r_R: 1.25	r_I: 1.23	r_S: 1.25
[28]	a_R: 0.63	a_I: 0.49	a_S: 0.21

Begum and	V: 42.98	W: 13.08	V_S: 17.14
Galloway (U)	r_R: 1.27	r_I: 1.08	r_S: 1.28
[28]	a_R: 0.76	a_I: 0.54	a_S: 0.52
Galloway and	V: 50.89	W: 4.63	V_S: 3.42
Waheed (Hg)	r_R: 1.17	r_I: 1.23	r_S: 1.75
[21]	a_R: 0.48	a_I: 0.8	a_S: 0.23
Galloway and	V: 38.65	W: 29.05	V_S: 6.2
Waheed (Pb)	r_R: 1.32	r_I: 1.23	r_S: 1.01
[21]	a_R: 0.47	a_I: 0.14	a_S: 0.75
Smith et al	V: 43.296	W: 11.91	V_S: 4.35
(Bi) [26]	r_R: 1.30	r_I: 1.32	r_S: 1.30
	a_R: 0.58	a_I: 0.20	a_S: 0.58
Guenther	V: 46.824	W: 4.03	V_S: 8.0
et al(Bi) [22]	- 0.261E	+ 0.215E	
	r_R: 1.217	r_I: 1.212	r_S: 1.217
	a_R: 0.758	a_I: 0.485	a_S: 0.758
Tanaka et al	V: 46.11	W: 3.59	V_S: 7.0
(Bi) [30]	r_R: 1.25	r_I: 1.25	r_S: 1.25
	a_R: 0.65	a_I: 0.48	a_S: 0.65
Fu and Perey	V: 47-0.25E	W: 3.5+0.43E	V_S: 6.0
(Pb) [29]	r_R: 1.25	r_I: 1.25	r_S: 1.25
	a_R: 0.65	a_I: 0.47	a_S: 0.65
Delaroche	V: 49.9-0.25E	W: 4.93-1.3E	V_S: 6.0
et al(W)	- 16(N-Z)/Z	- 8(N-Z)/A	
[68]	r_R: 1.26	r_I: 1.28	r_S: 1.26
	a_R: 0.63	a_I: 0.47	a_S: 0.63

The potentials of Rosen et al, Becchetti and Greenlees, Wilmore and Hodgson and Moldauer are "semi-global" in that they have attempted fits over a range of nuclear mass and incident particle energy. The "Moldauer" potential is the one attributed to Moldauer by Ahmed et al [93] in their attempt to fit thalium inelastic excitation functions. It appears to differ slightly from that produced in Moldauer's publication [89]. Moldauer also used a Gaussian imaginary form factor not used here. The potential of Becker et al covers a large mass range but at a fixed energy of 3.2 MeV, and that of Fu and Perey, the lead isotopes in the energy range 0-20 MeV. Other potentials result from a fit to data taken at fixed energy close to 3 MeV on one isotope (or the set of isotopes found in a natural sample). Where this is so, the element is included in brackets. The best fit potentials are those resulting from least squares parameter searches on the present data. In the search procedure S Matrix elements were calculated from the OP by the routine "SCAT" [106]. These were then used to calculate the shape elastic analysing power, differential cross section and the compound elastic differential cross section. The latter was calculated by a modified version of the program "CINDY" [107] which is called as a subroutine by the search routine. Thus as well as the experimental data and OP parameters, spins, parities and excitation energies for other open reaction channels are required as input data for each isotope ocurring naturally.

Parameters were varied to minimise the quantity X^2

$$X_\sigma^2 = \sum_n \{(\sigma_{exp}-\sigma_{cal})/d\sigma_{exp}\}^2/n \qquad (6.4)$$

OR

$$X_P^2 = \sum_n \{(P_{exp}-P_{cal})/dP_{exp}\}^2/n \qquad (6.5)$$

OR

$$X_{comb}^2 = \{X_P^2+X_\sigma^2\}/2 \qquad (6.6)$$

The best fit parameters are those which minimise X_{comb}^2. Any number of parameters from 1 to 9 can be varied simultaneously and in any order. Comparison of X^2 for a particular data set shows the relative success of the various potentials used in predicting cross sections and polarisations. Comparison between different data sets, and between cross sections and analysing powers, can however be misleading as X^2 depends strongly on the precision of the data. In optimising potential parameters it is possible to obtain equally good fits with differing parameters. Ambiguities in V and r_R and also W and a_I are well known. Radius parameters were kept fixed during a search so that only 6 parameters were allowed to vary, and several searches were conducted with various sets of radius parameters which have been used in previous analyses. When varying several parameters simultaneously, a variation of one parameter could sometimes be seen to be partially compensated by a variation in another so that X^2 changed little while the parameters veered off to unphysical values. This was avoided by initially searching on single parameters and then fine tuning by searching on several parameters simultaneously. Spin orbit parameters were initially searched to minimise X_P^2, real and imaginary parameters to minimise X_σ^2. Searches were then made to minimise X_{comb}^2.

6.3.1 Tungsten

None of the potentials tried produced good fits to the tungsten data. Apart from the Best Fit potential the parameters of Becchetti and Greenlees were the most successful. The overall optimised potential gives substantially better analysing power than any other fit , but still looks pretty unconvincing. Reproduction of cross sections is better but still does not give detailed agreement. The relative success of the various potentials is sumarised in table 6.2, and the predictions of the most successful are compared with the present data in figures 6.3 and 6.4 (analysing power) and 6.5 and 6.6 (differential cross section)

Table 6.2

Tungsten: Quality of OM Fits

Potential	X^2_{comb}	X^2_P	X^2_σ
Best Fit	25.7	9.2	42.3
Becchetti and Greenlees	35.4	37.1	33.1
Zijp and Jonker(W)	57.7	38.6	76.8
Becker et al	135.5	46.5	224.6
Rosen et al	159.8	34.8	284.7
Moldauer	162.3	43.7	280.9
Wilmore and Hodgson	232.6	68.4	396.8
Begum and Galloway(W)	360.9	73.7	648.1
Delaroche et al(W)	414.2	69.0	759.4
Fu and Perey(Pb)	664.5	77.5	1251.5

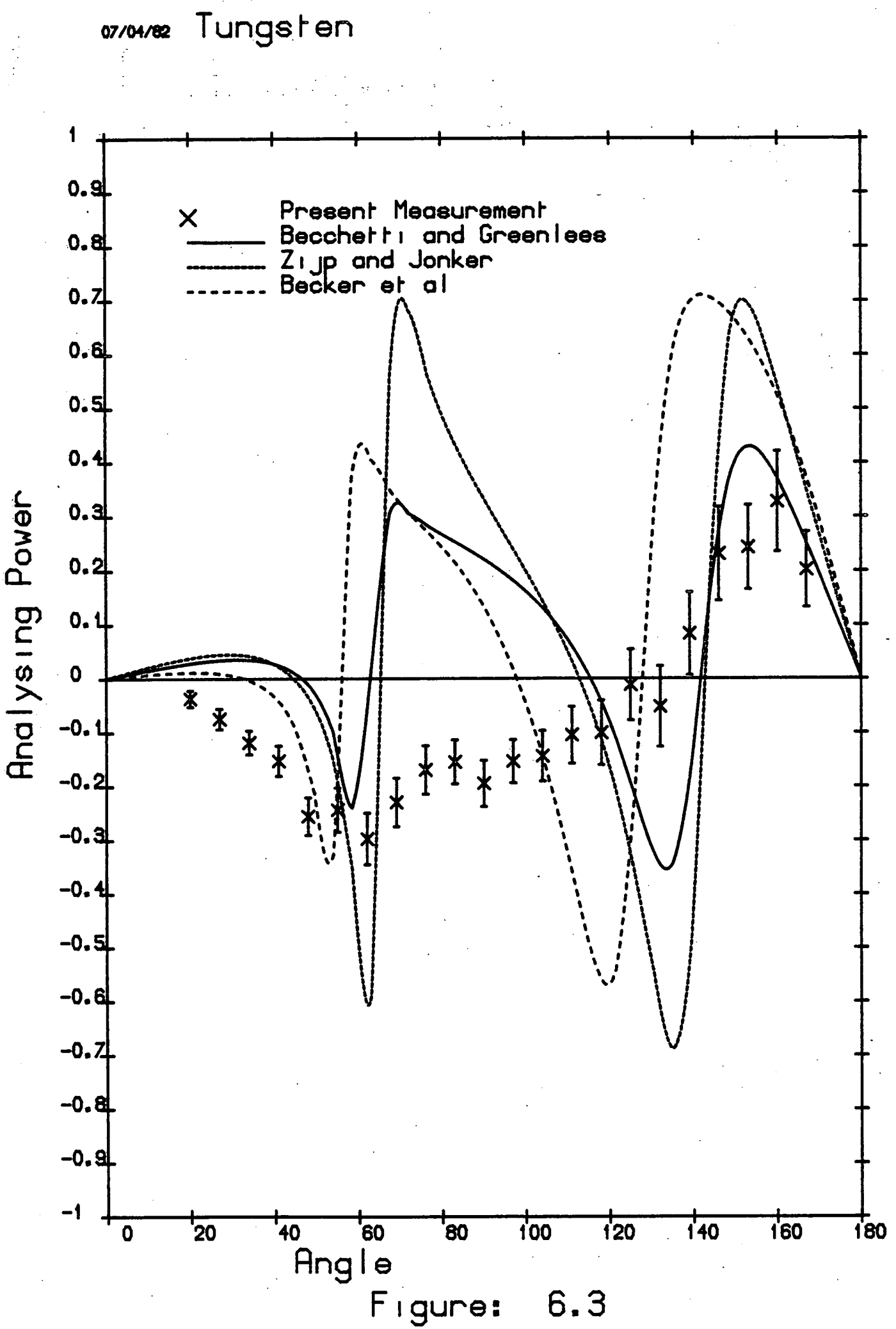
07/04/82 Tungsten
Present Measurement
Becchetti and Greenlees
Zijp and Jonker
Becker et al
Analysing Power
Angle
1
0.9
0.8
0.7
0.6
0.5
0.4
0.3
0.2
0.1
0
-0.1
-0.2
-0.3
-0.4
-0.5
-0.6
-0.7
-0.8
-0.9
-1
0
20
40
60
80
100
120
140
160
180

Figure: 6.3

07/04/82 Tungsten

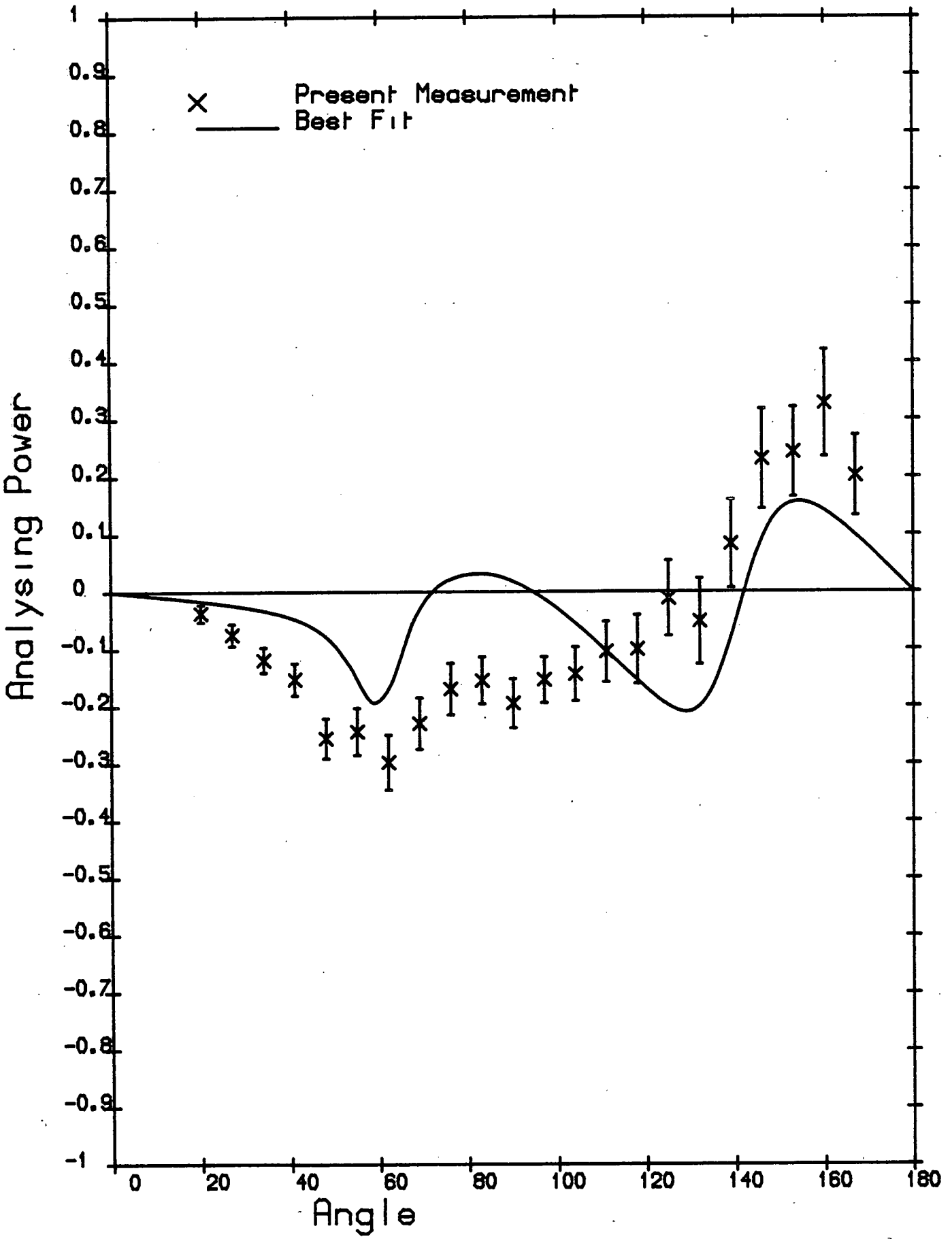

Figure: 6.4

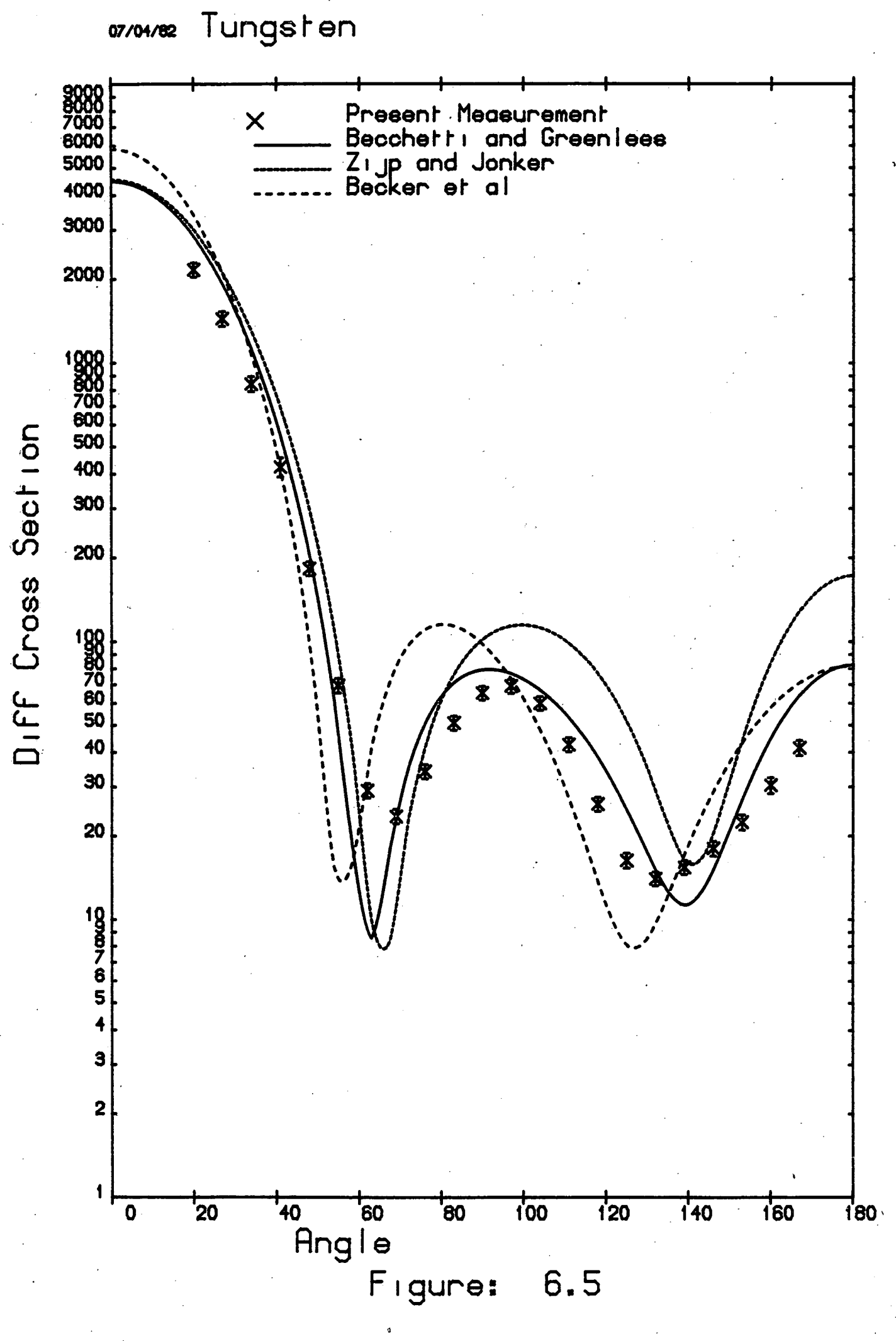
07/04/82 Tungsten
Present Measurement
Becchetti and Greenlees
Zijp and Jonker
Becker et al
Diff Cross Section
Angle
0
20
40
60
80
100
120
140
160
180

Figure: 6.5

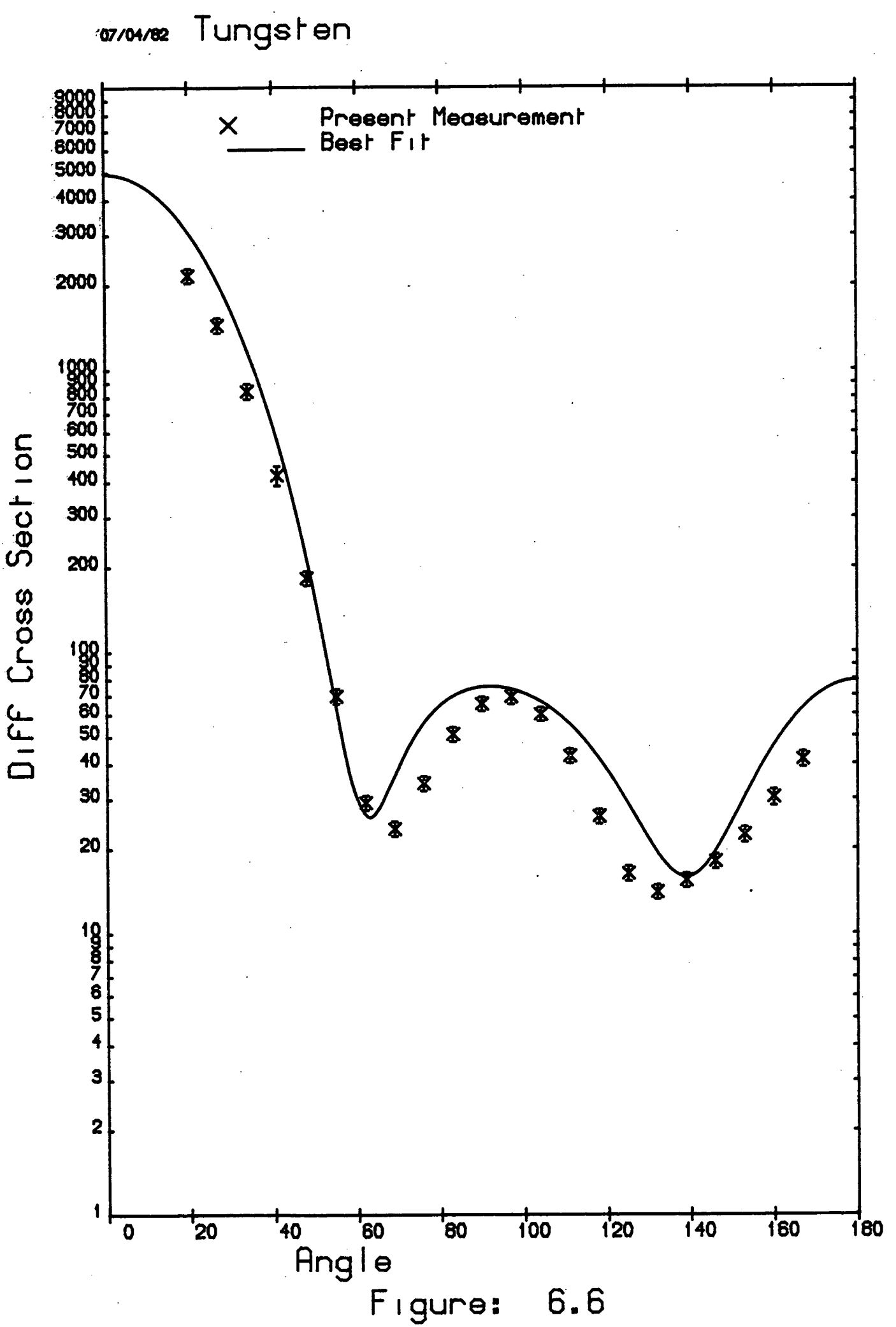
07/04/82 Tungsten
Present Measurement
Best Fit
Diff Cross Section
9000
8000
7000
6000
5000
4000
3000
2000
1000
900
800
700
600
500
400
300
200
100
90
80
70
60
50
40
30
20
10
9
8
7
6
5
4
3
2
1
0
20
40
60
80
100
120
140
160
180
Angle

Figure: 6.6

6.3.2 Mercury

The relative success of various potential parameters is summarised in table 6.3. The predictions of the most successful are compared with the present data in figures 6.7 and 6.8 (analysing power) and 6.9 and 6.10 (differential cross section). OM fits to the Mercury data look much better than in the case of tungsten. The potential of Wilmore and Hodgson reproduces the shape of the analysing power distribution quite well, although at some angles it tends to overestimate the magnitude. The best fit potential reproduces the cross section quite well and the analysing power is also reasonably well fitted apart from a few points where the measured analysing power is slightly greater than the calculated value

Table 6.3

Mercury: Quality of OM Fits

Potential	X^2_{comb}	X^2_P	X^2_σ
Best Fit	6.6	1.6	11.5
Zijp and Jonker(Bi)	12.6	6.3	19.0
Moldauer	21.0	15.7	27.0
Wilmore and Hodgson	25.9	3.5	48.4
Becchetti and Greenlees	26.0	7.4	44.0
Smith et al(Bi)	33.0	7.9	58.0
Fu and Perey(Pb)	48.0	13.0	84.0
Rosen et al	64.0	13.0	116.0
Becker et al	86.0	32.0	139.0

07/04/82 Mercury

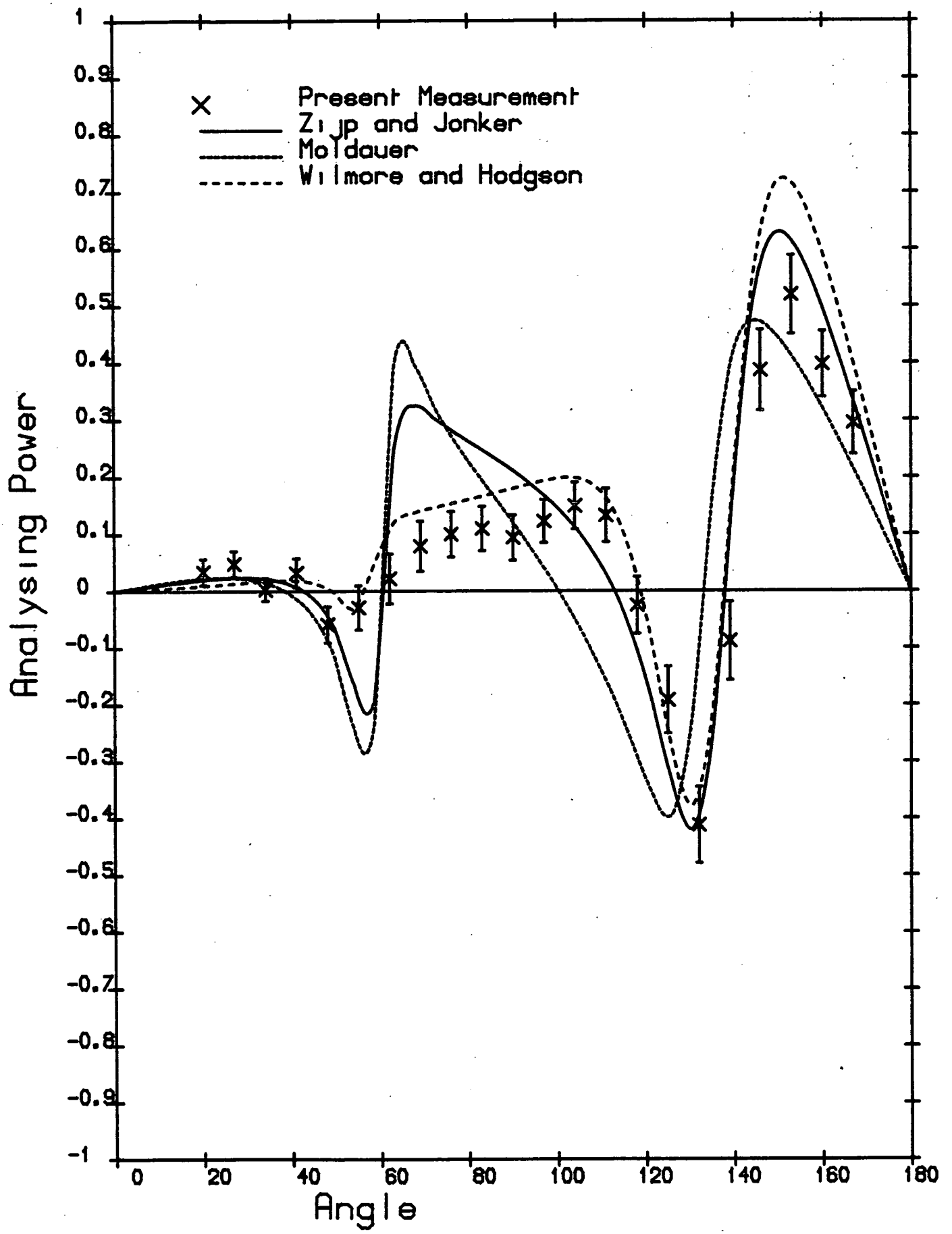

Figure: 6.7

07/04/82 Mercury

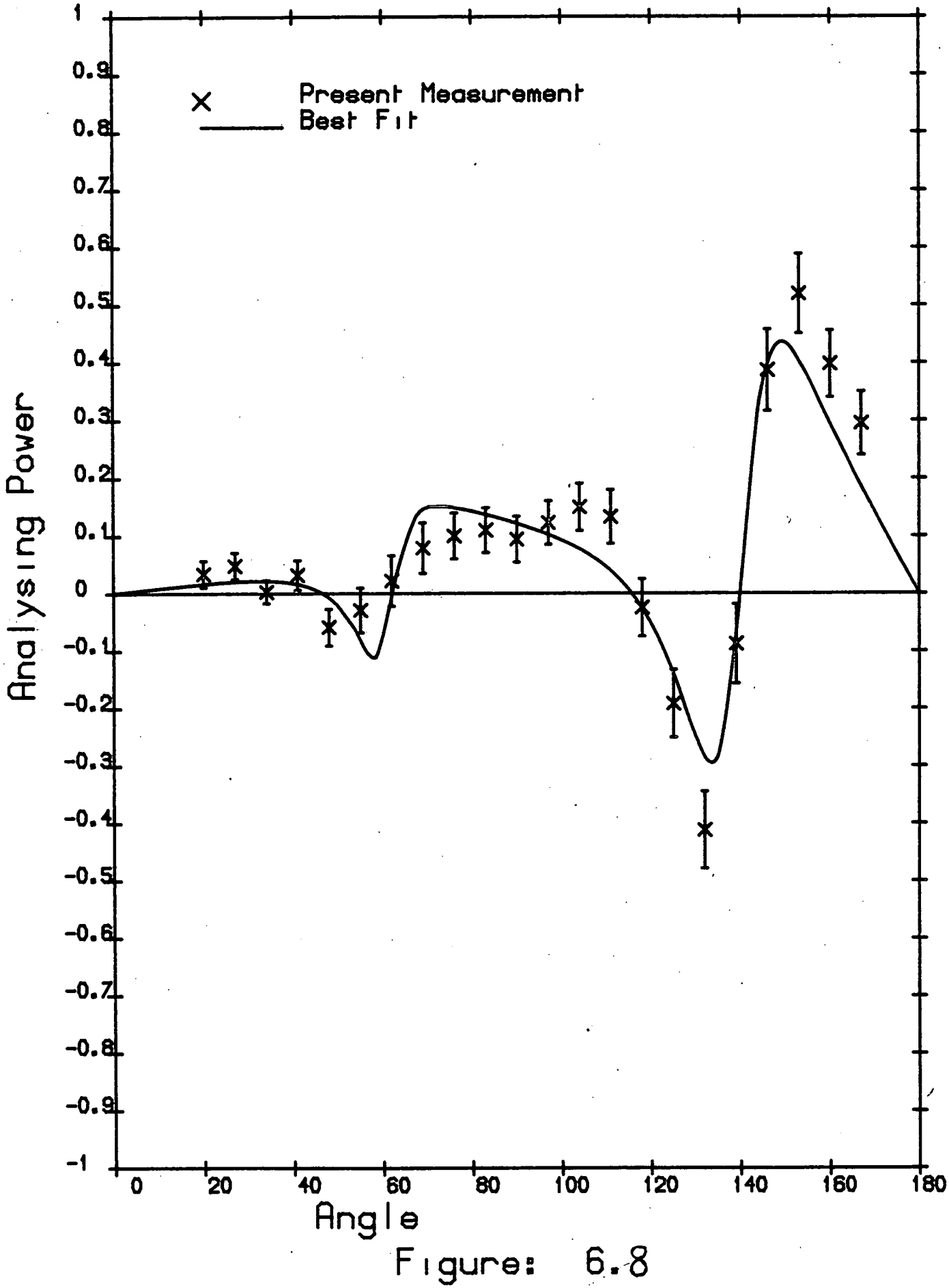

Figure: 6.8

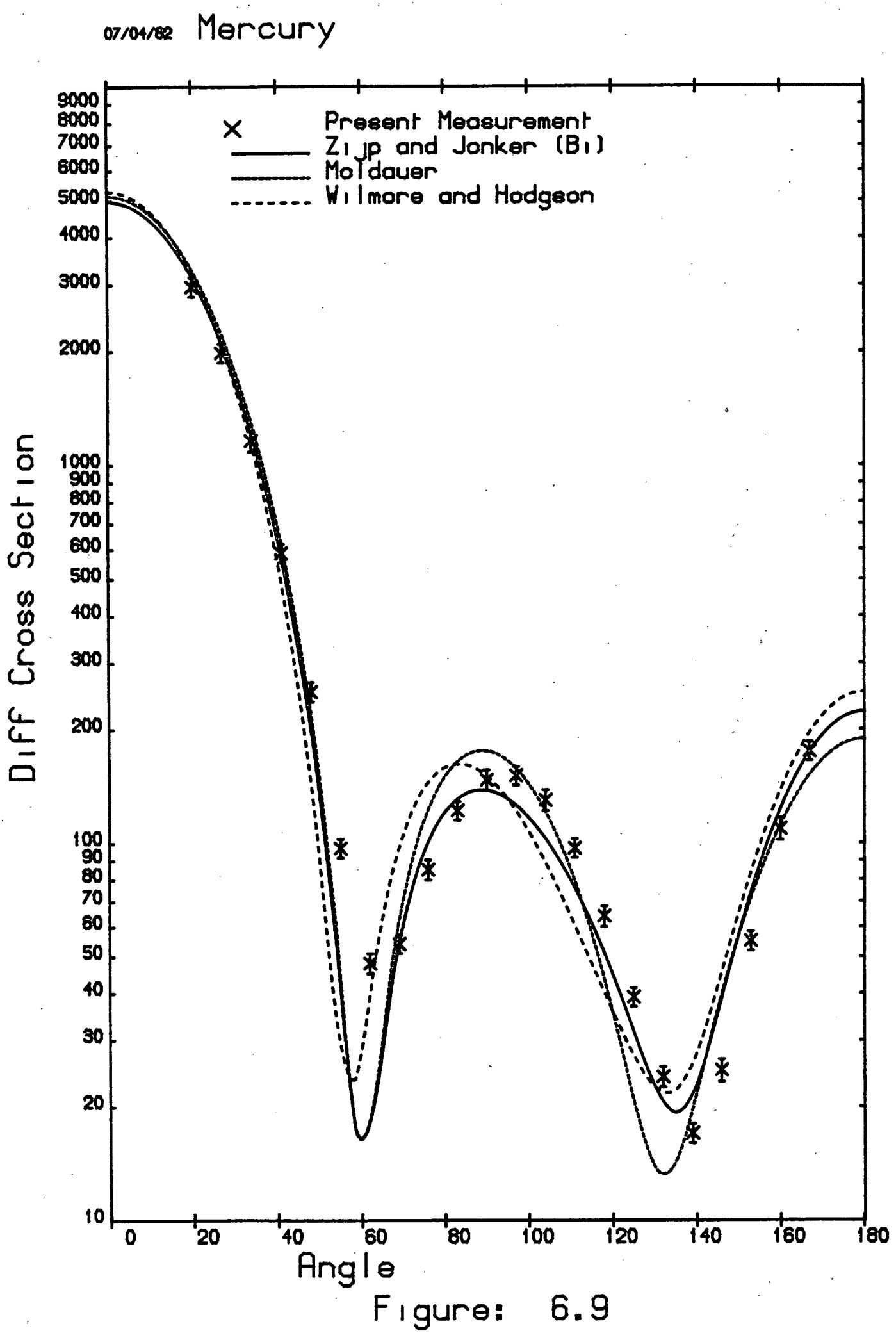
07/04/82 Mercury
Present Measurement
Zijp and Jonker (B1)
Moldauer
Wilmore and Hodgson
Diff Cross Section
9000
8000
7000
6000
5000
4000
3000
2000
1000
900
800
700
600
500
400
300
200
100
90
80
70
60
50
40
30
20
10
0
20
40
60
80
100
120
140
160
180
Angle

Figure: 6.9

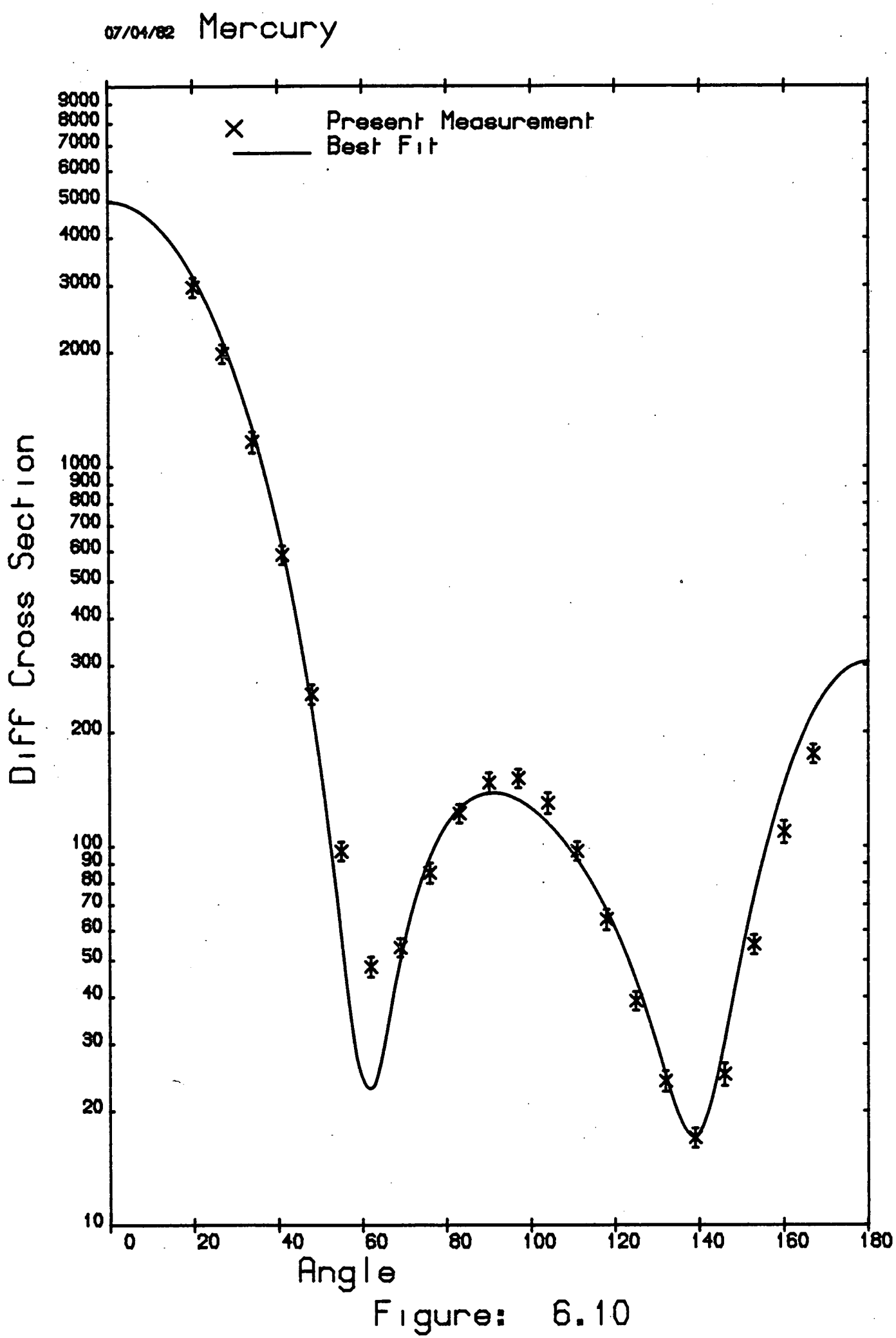
07/04/82 Mercury
Present Measurement
Best Fit
Diff Cross Section
9000
8000
7000
6000
5000
4000
3000
2000
1000
900
800
700
600
500
400
300
200
100
90
80
70
60
50
40
30
20
10
0
20
40
60
80
100
120
140
160
180
Angle

Figure: 6.10

6.3.3 Thalium

Table 6.4 summarises the relative success of potentials tried for thalium. The predictions of the most successful are plotted against the present data in figures 6.11, 6.12 (analysing power) and 6.13, 6.14 (differential cross section). The overall quality of OM fits to thalium data is not very good. The potential of Smith et al gives a reasonable fit to the analysing power, which is rather surprising considering that it was derived from a fit to bismuth cross section data. The best fit potential gives a good fit to the differential cross section except around 140 degrees, but reproduces the analysing power rather poorly.

Table 6.4

Thalium: Quality of OM Fits

Potential	X^2_{comb}	X^2_{P}	X^2_{σ}
Best Fit	12.3	7.4	17.2
Zijp and Jonker(Bi)	21.0	7.8	35.0
Smith et al(Bi)	33.0	3.1	62.9
Becchetti and Greenlees	43.4	15.9	71.1
Moldauer	43.7	22.9	64.6
Wilmore and Hodgson	47.2	5.7	88.8
Begum and Galloway(Tl)	64.0	44.0	83.0
Fu and Perey(Pb)	89.0	7.4	171.0
Rosen et al	103.6	19.1	198.0
Becker et al	141.9	36.6	247.3

08/04/82 Thallium

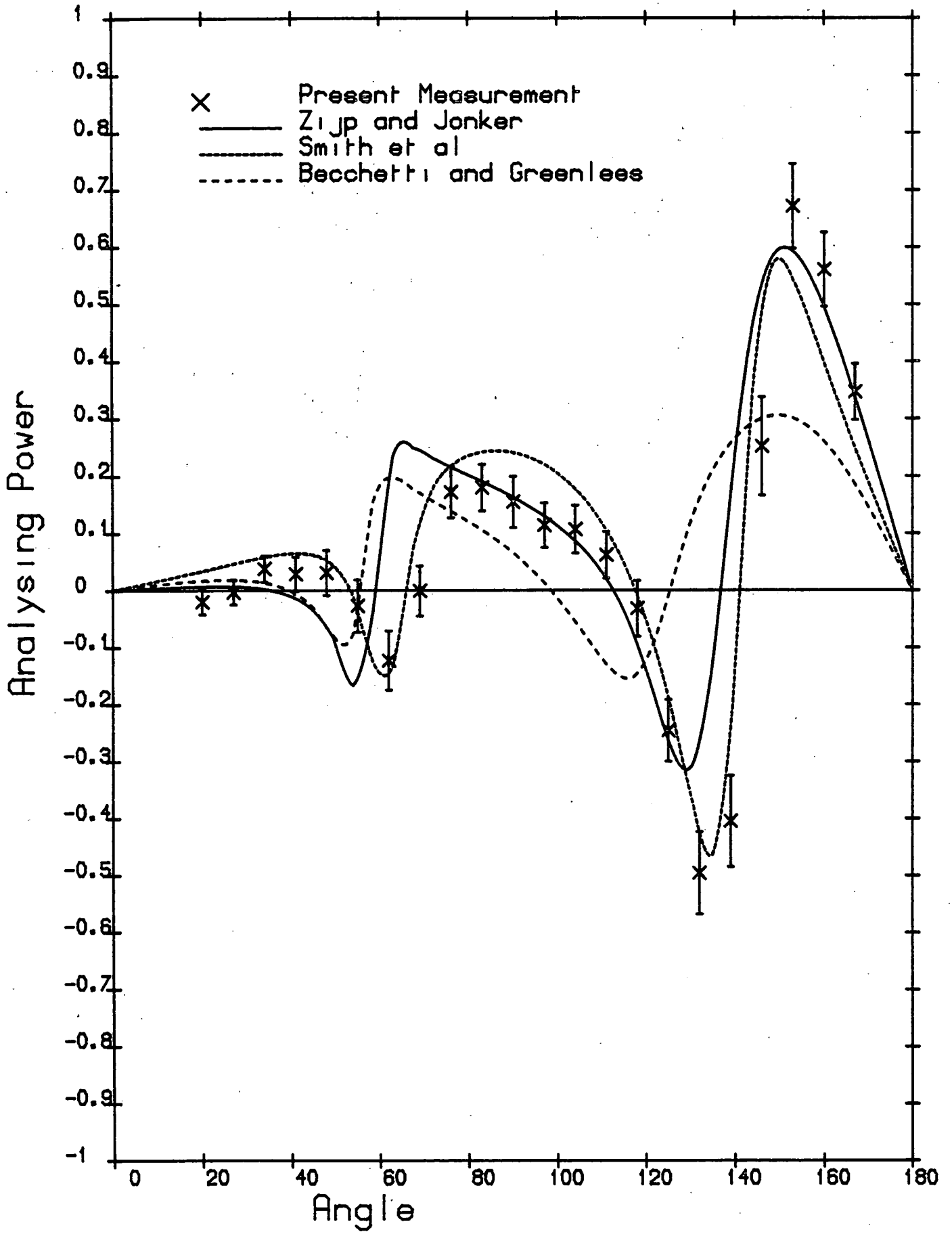

Figure: 6.11

07/04/82 Thallium

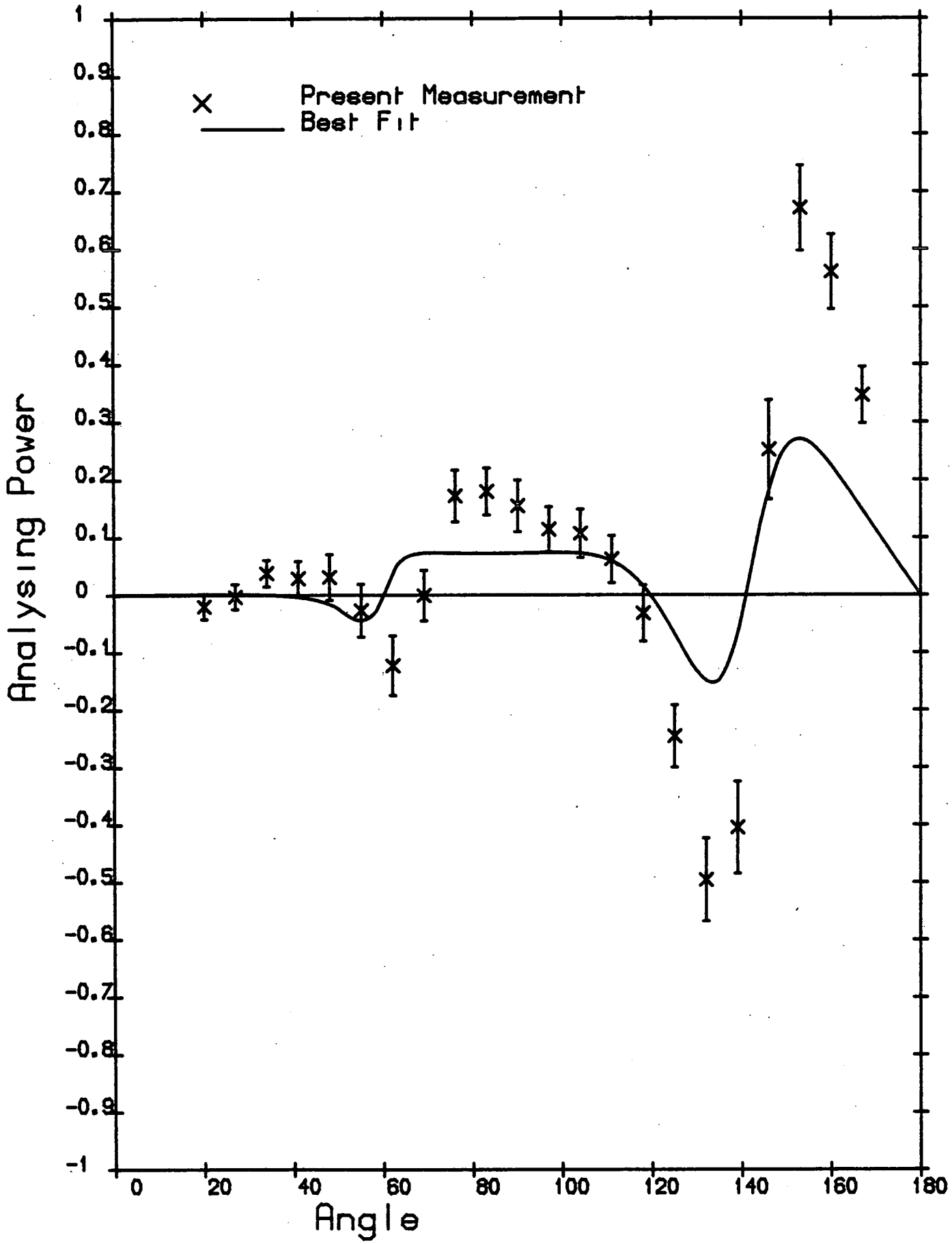

Figure: 6.12

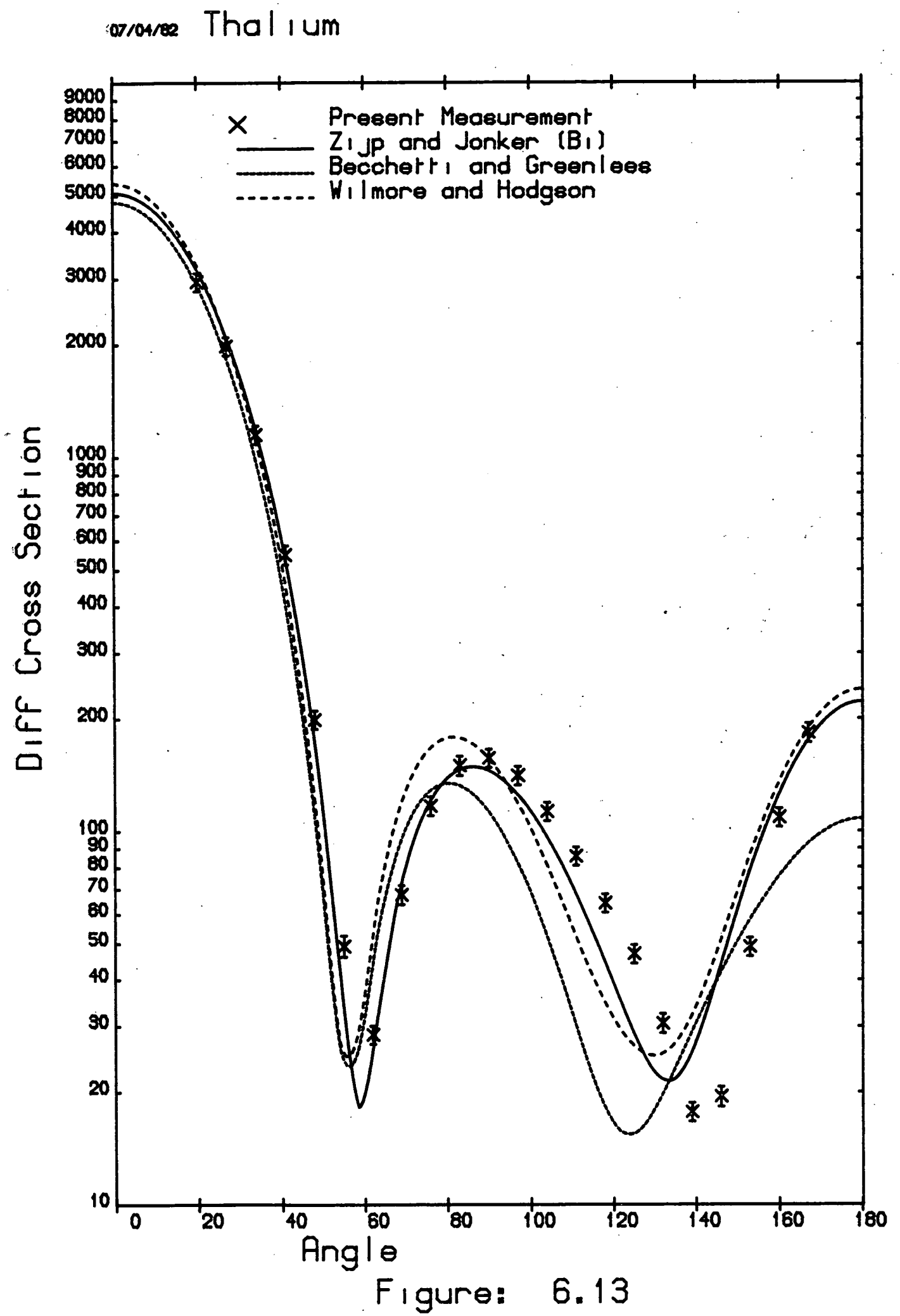
07/04/82 Thalium
Present Measurement
Zijp and Jonker (Bi)
Becchetti and Greenlees
Wilmore and Hodgson
Diff Cross Section
9000
8000
7000
6000
5000
4000
3000
2000
1000
900
800
700
600
500
400
300
200
100
90
80
70
60
50
40
30
20
10
0
20
40
60
80
100
120
140
160
180
Angle

Figure: 6.13

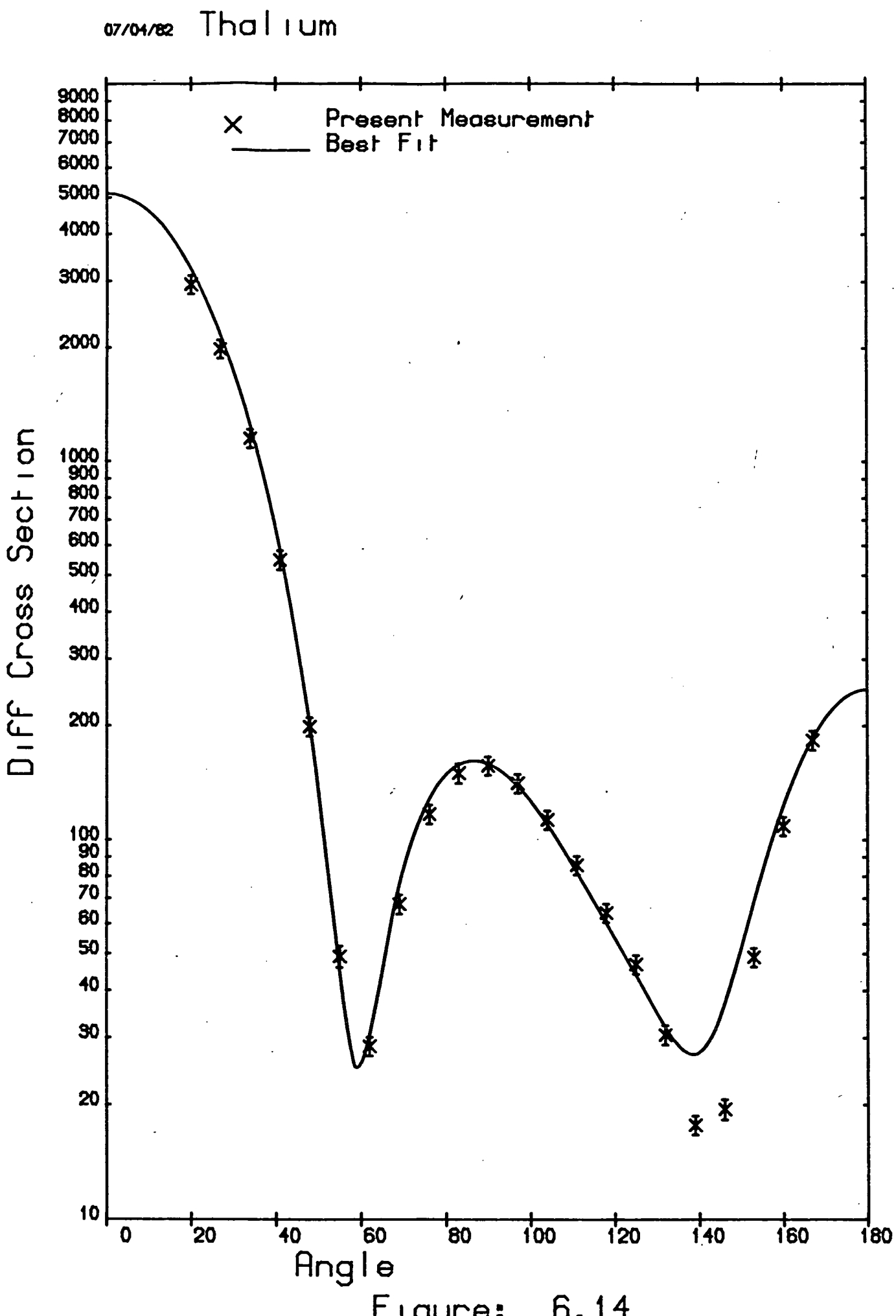
07/04/82 Thallium
Present Measurement
Best Fit
DiFF Cross Section
9000
8000
7000
6000
5000
4000
3000
2000
1000
900
800
700
600
500
400
300
200
100
90
80
70
60
50
40
30
20
10
0
20
40
60
80
100
120
140
160
180
Angle

Figure: 6.14

6.3.4 Lead

The quality of fit of various potentials is summarised for lead in table 6.5. The most successful are plotted against the present lead data in figures 6.15, 6.16 (analysing power) and 6.17, 6.18 (differential cross section). The potential of Fu and Perey reproduces the overall features of the differential cross section quite well, but the analysing power rather poorly. The best fit potential gives a better looking fit to the analysing power, but is at variance with the measurements in the angular range 50-70 degrees. It also gives a lower X_{σ}^{2} although its predictions are low around 60 degrees and 90 degrees.

Table 6.5

Lead Quality of OM Fits

Potential	X^2_{comb}	X^2_{P}	X^2_{σ}
Best Fit	4.6	4.3	5.0
Fu and Perey(Pb)	11.5	15.3	7.7
Smith et al(Bi)	11.7	8.9	14.6
Wilmore and Hodgson	15.3	8.8	22.2
Tanaka et al(Bi)	15.4	22.9	7.9
Zijp and Jonker(Bi)	17.5	11.9	23.1
Begum and Galloway(Bi)	24.1	12.6	35.7
Rosen et al	26.1	16.8	35.4
Galloway and Waheed(Pb)	32.0	33.8	30.2
Becker et al	32.9	22.9	42.8
Becchetti and Greenlees	52.9	19.4	86.5

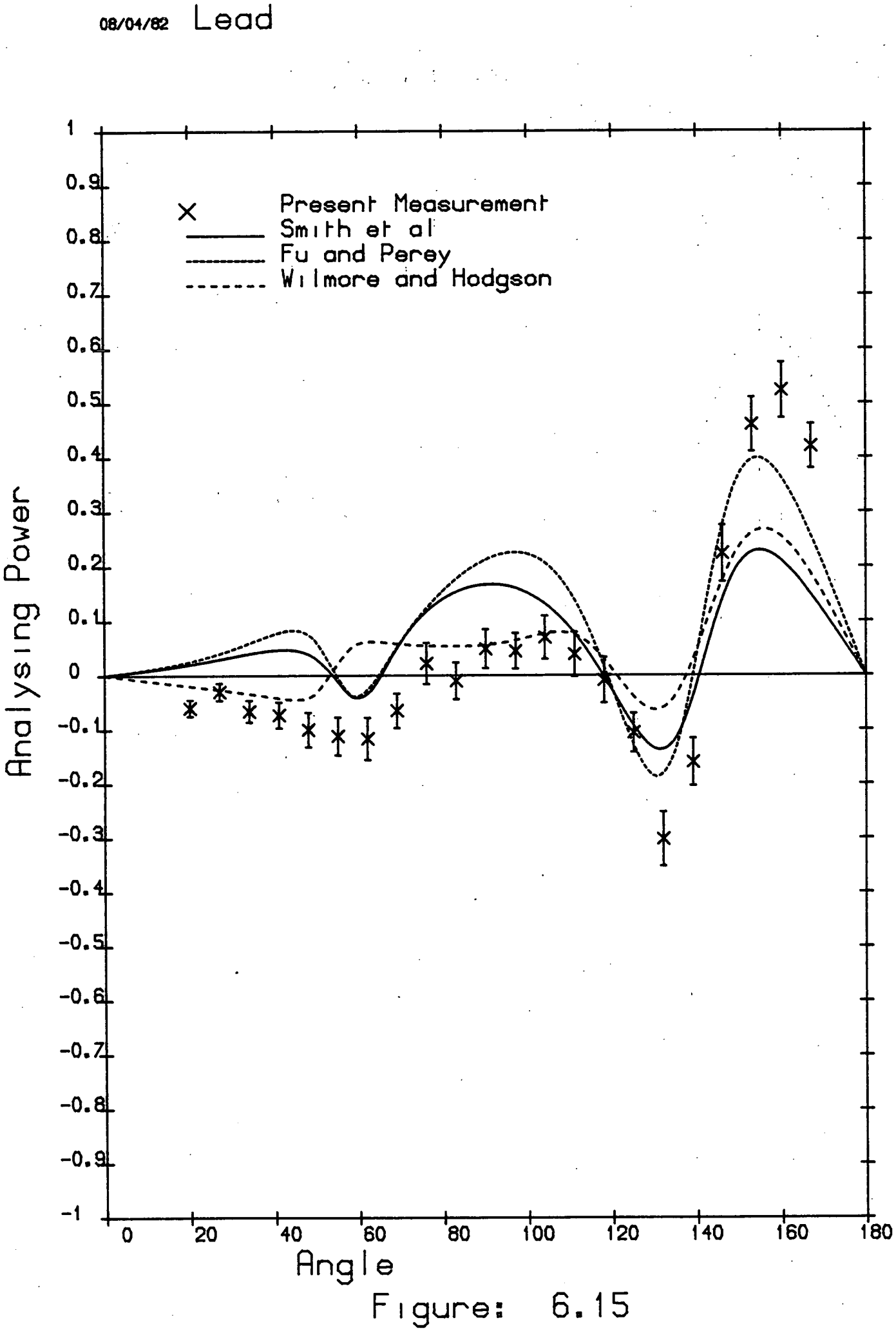
Lead
Present Measurement
Smith et al
Fu and Perey
Wilmore and Hodgson
Analysing Power
Angle
1
0.9
0.8
0.7
0.6
0.5
0.4
0.3
0.2
0.1
0
-0.1
-0.2
-0.3
-0.4
-0.5
-0.6
-0.7
-0.8
-0.9
-1
0
20
40
60
80
100
120
140
160
180

Figure: 6.15

08/04/82 Lead

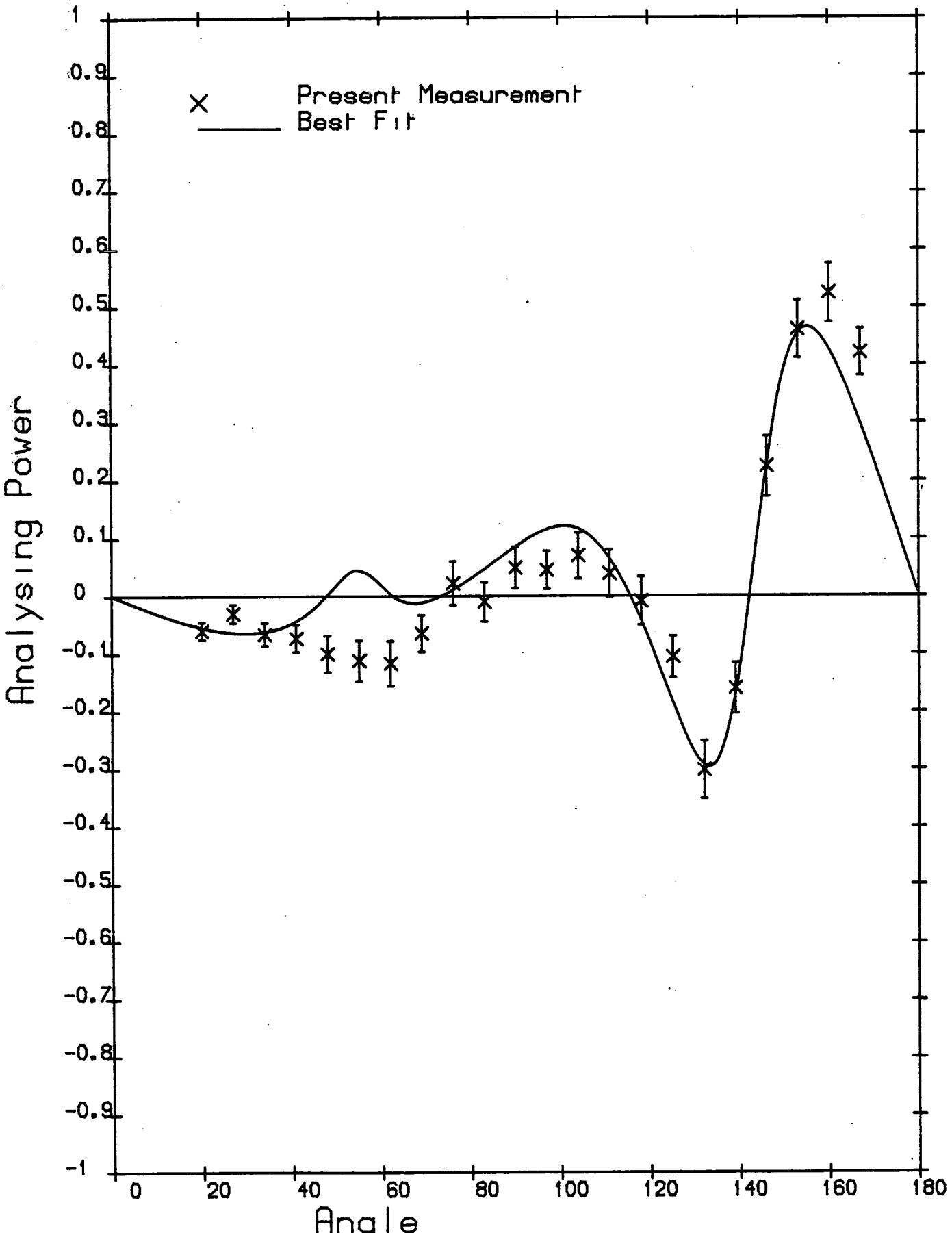

Figure: 6.16

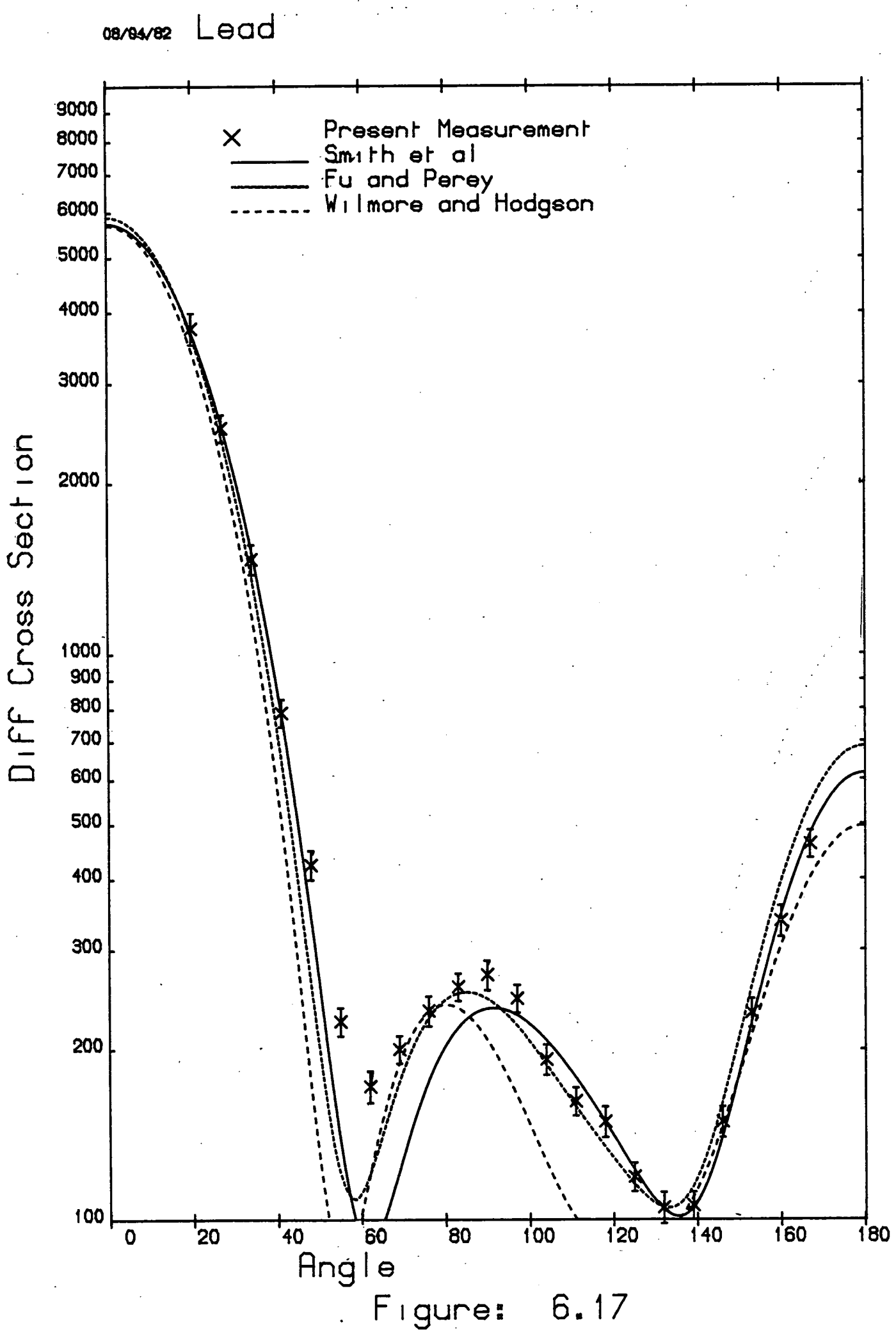
08/04/82 Lead
Present Measurement
Smith et al
Fu and Perey
Wilmore and Hodgson
DiFF Cross Section
9000
8000
7000
6000
5000
4000
3000
2000
1000
900
800
700
600
500
400
300
200
100
0
20
40
60
80
100
120
140
160
180
Angle

Figure: 6.17

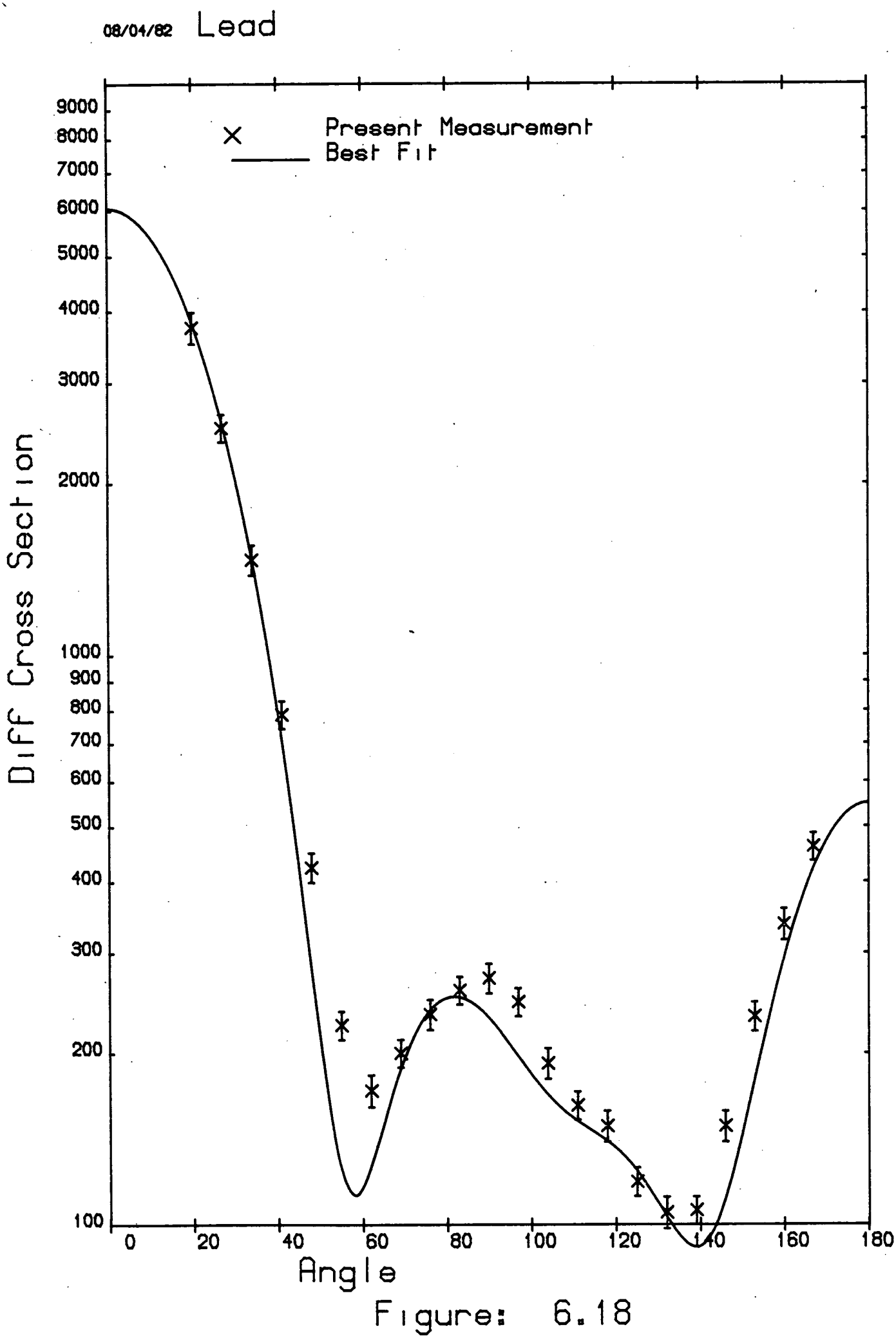
08/04/82 Lead
Present Measurement
Best Fit
Diff Cross Section
9000
8000
7000
6000
5000
4000
3000
2000
1000
900
800
700
600
500
400
300
200
100
0
20
40
60
80
100
120
140
160
180
Angle

Figure: 6.18

6.3.5 Bismuth

A summary of the quality of fit for various potentials used with bismuth is presented in table 6.6. The closest fits are compared with the present bismuth data in figures 6.19, 6.20 (analysing power) and 6.21, 6.22 (differential cross section). The potential of Smith et al fits the differential cross section data quite well but is at odds with the analysing power. None of the potentials, including the best fit, gives a good reproduction of the analysing power.

Table 6.6

Bismuth: Quality of OM Fits

Potential	X^2_{comb}	X^2_P	X^2_σ
Best Fit	3.7	4.2	3.2
Wilmore and Hodgson	7.0	6.1	7.9
Zijp and Jonker(Bi)	7.4	8.4	6.4
Smith et al(Bi)	8.4	12.7	4.0
Begum and Galloway(Bi)	10.9	8.0	13.7
Moldauer	11.2	14.1	8.4
Fu and Perey(Pb)	11.6	18.9	4.3
Becchetti and Greenlees	11.8	12.5	11.1
Becker et al	15.9	10.5	21.3
Rosen et al	15.9	7.4	24.4
Tanaka et al(Bi)	18.9	28.9	8.9

07/04/82 Bismuth

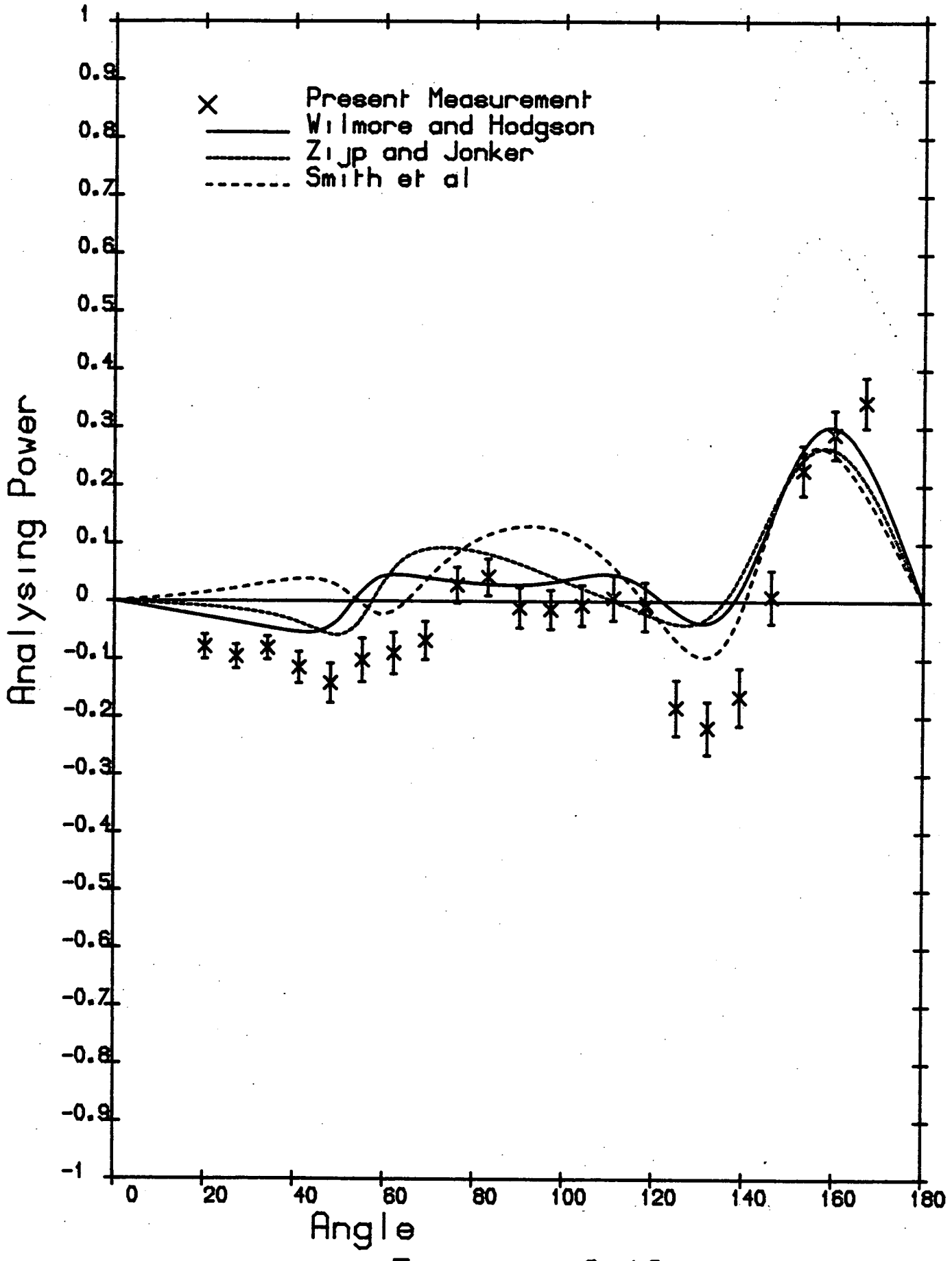

Figure: 6.19

09/04/82 Bismuth

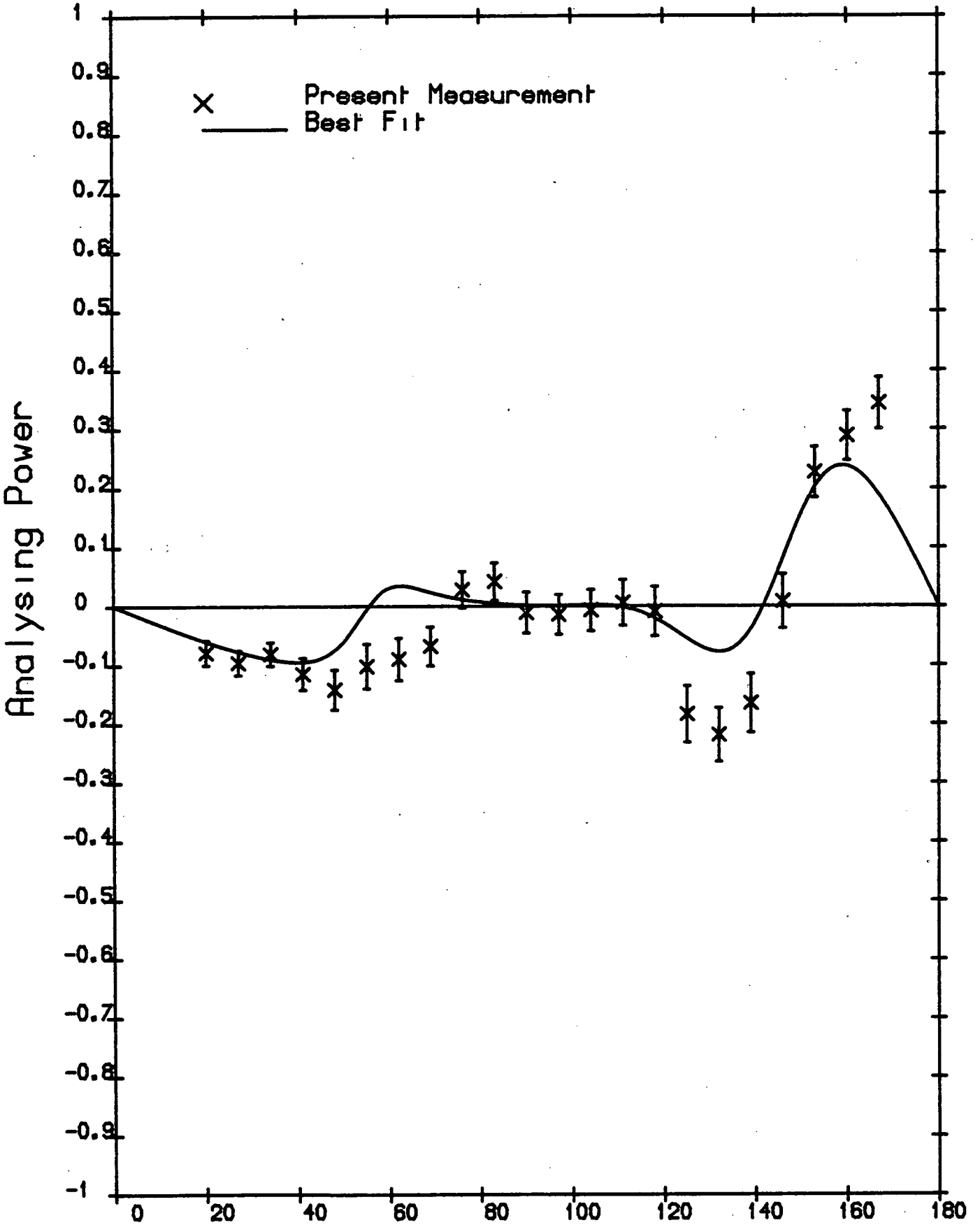

Figure: 6.20

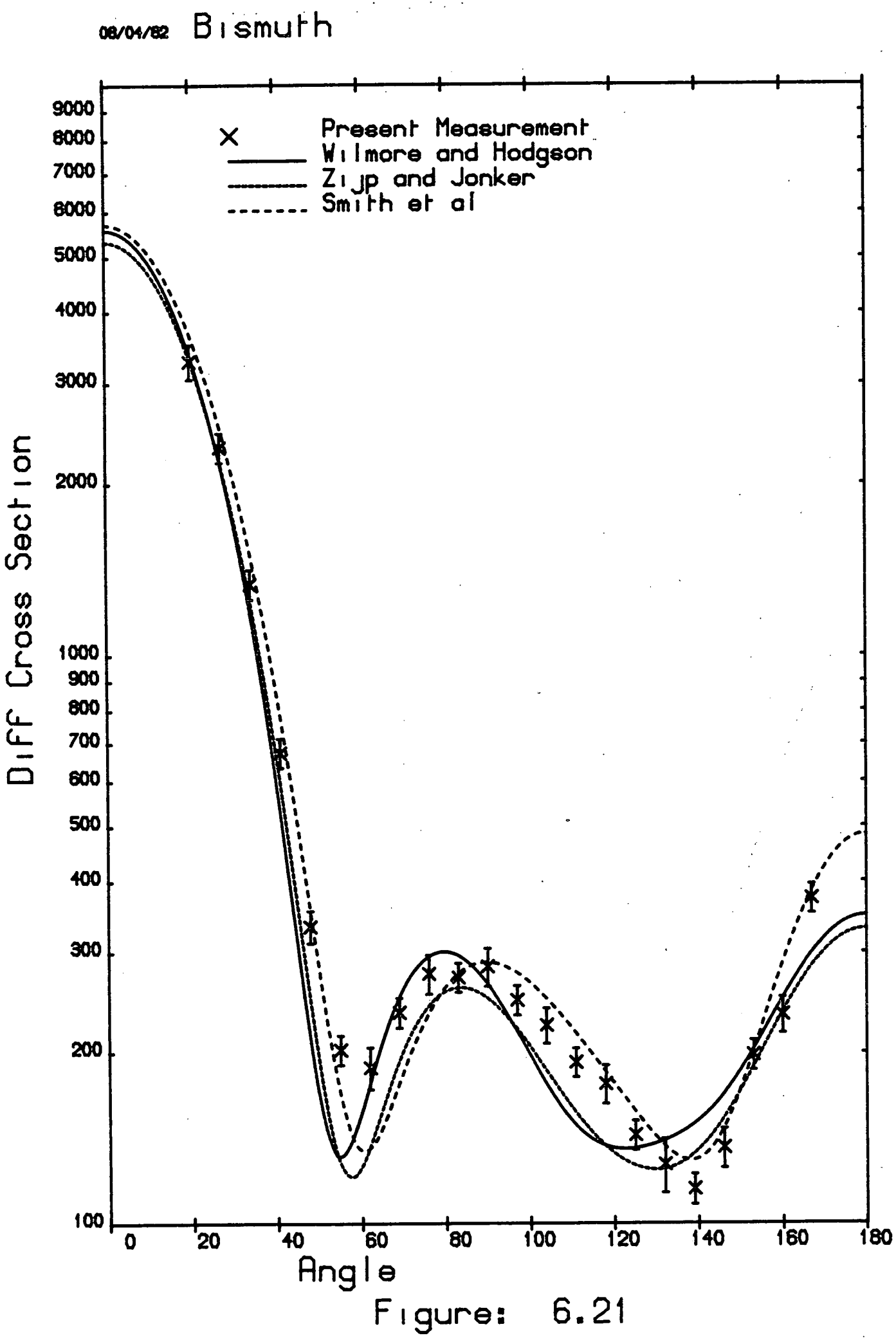
08/04/82 Bismuth
Present Measurement
Wilmore and Hodgson
Zijp and Jonker
Smith et al
Diff Cross Section
9000
8000
7000
6000
5000
4000
3000
2000
1000
900
800
700
600
500
400
300
200
100
0
20
40
60
80
100
120
140
160
180
Angle

Figure: 6.21

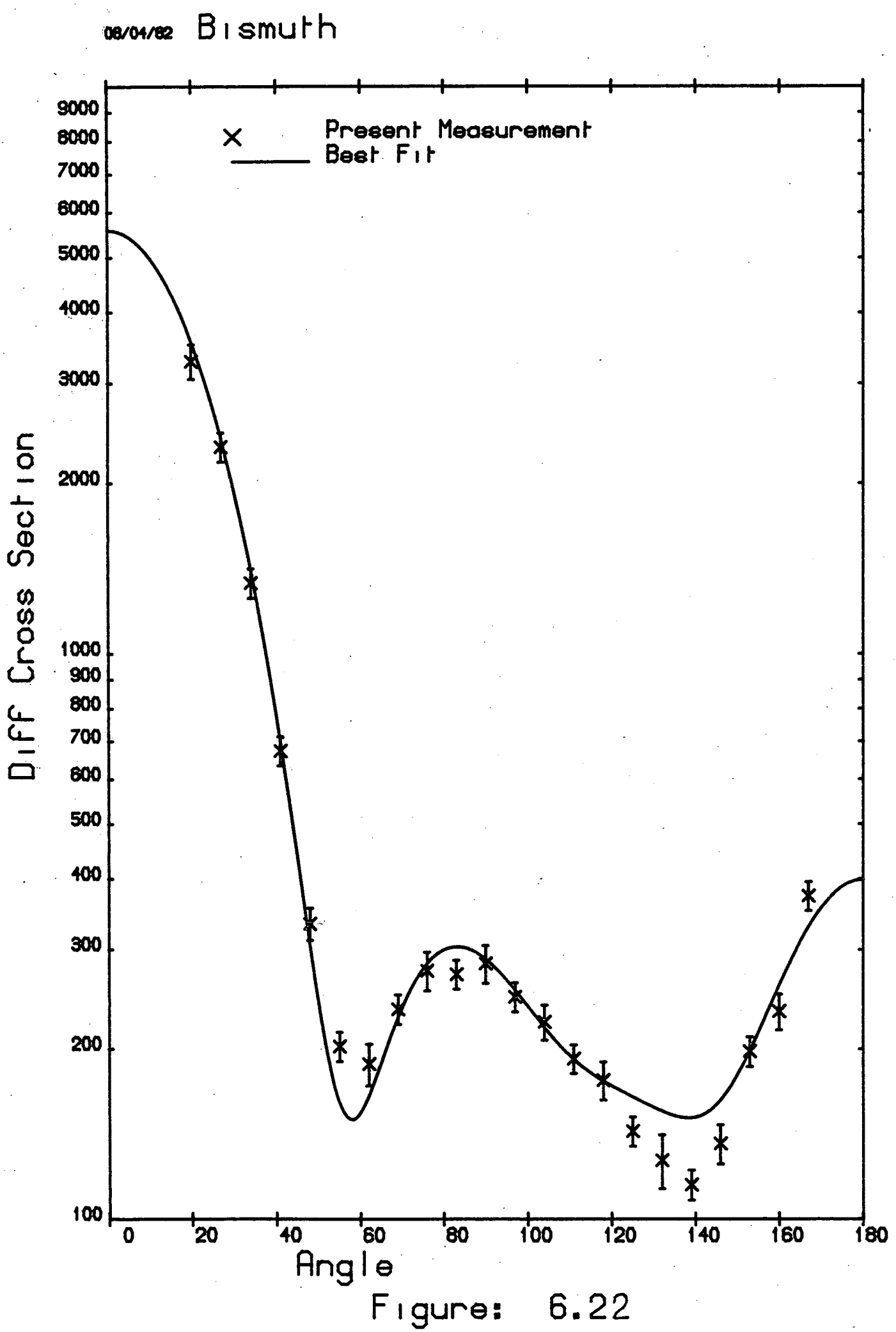
08/04/82 Bismuth
Present Measurement
Best Fit
DiFF Cross Section
9000
8000
7000
6000
5000
4000
3000
2000
1000
900
800
700
600
500
400
300
200
100
0
20
40
60
80
100
120
140
160
180
Angle

Figure: 6.22

6.3.6 Uranium

The quality of OM fits to the uranium data is summarised in table 6.7. The closest fits are compared with the present data in figures 6.23, 6.24 (analysing power) and 6.25, 6.26 (differential cross section). OM fits to the uranium analysing power are not good. There is a tendency for the OM to predict more positive negative swings than are observed. The best fit is reasonably close to the analysing power except in the angular range 100-140 degrees. Differential cross section fits are somewhat better although there is similarly a tendency to produce an unobserved peak and valley in the distribution.

Table 6.7

Uranium: Quality of OM Fits

Potential	X^2_{comb}	X^2_P	X^2_σ
Best Fit	12.5	8.4	16.7
Moldauer	28.3	21.5	35.2
Wilmore and Hodgson	33.5	30.8	36.2
Smith et al(Bi)	33.7	19.1	58.2
Becchetti and Greenlees	41.5	15.9	67.2
Zijp and Jonker(Bi)	42.6	30.7	54.4
Begum and Galloway(Bi)	56.2	61.5	50.9
Fu and Perey	56.7	39.9	73.5
Rosen et al	58.3	23.0	93.7
Becker et al	70.4	46.8	94.0
Guenther et al(Bi)	73.0	36.0	109.9

08/04/82 Uranium

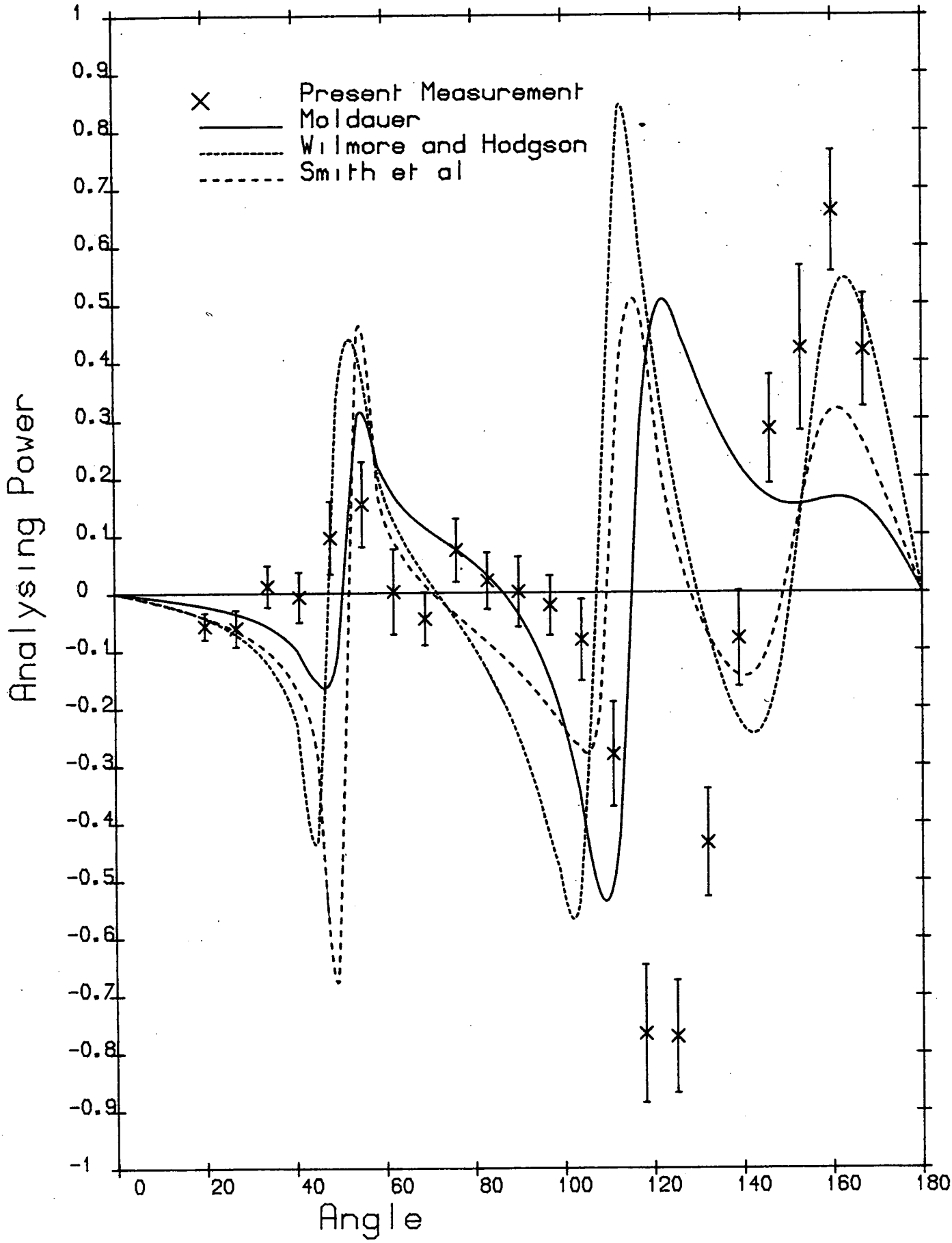

Figure: 6.23

08/04/82 Uranium

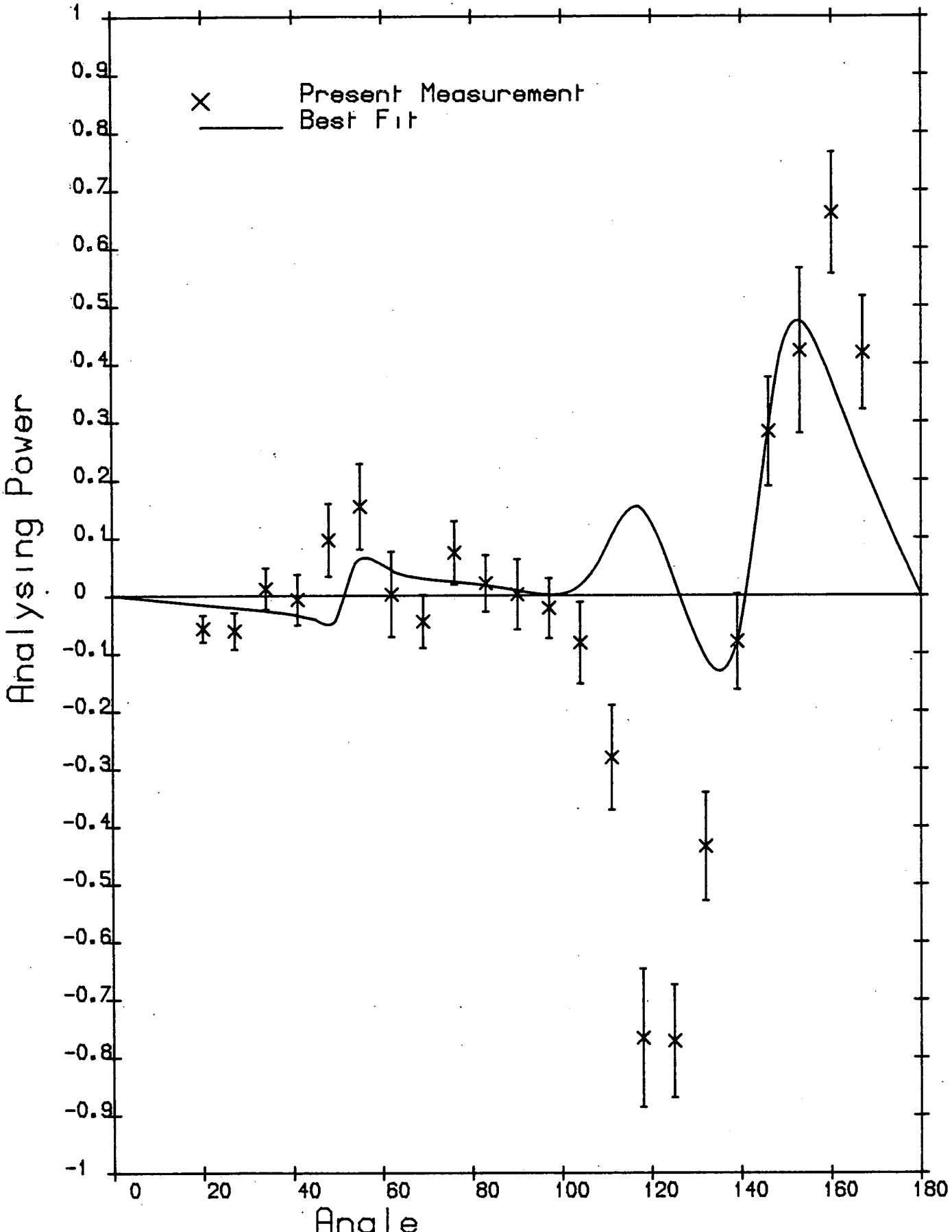

Figure: 6.24

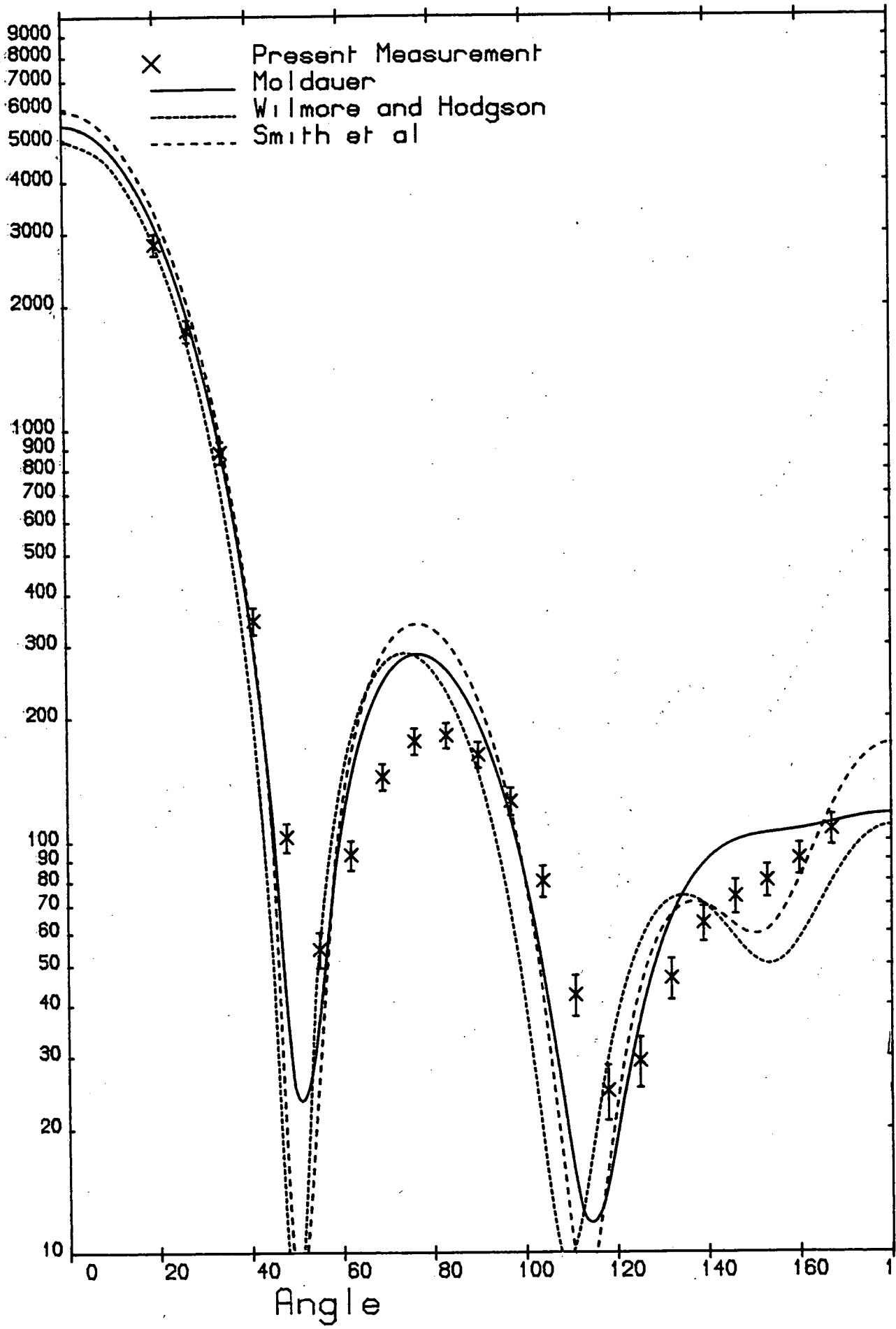
08/04/82 Uranium
Present Measurement
Moldauer
Wilmore and Hodgson
Smith et al
9000
8000
7000
6000
5000
4000
3000
2000
1000
900
800
700
600
500
400
300
200
100
90
80
70
60
50
40
30
20
10
0
20
40
60
80
100
120
140
160
180
Angle

Figure: 6.25

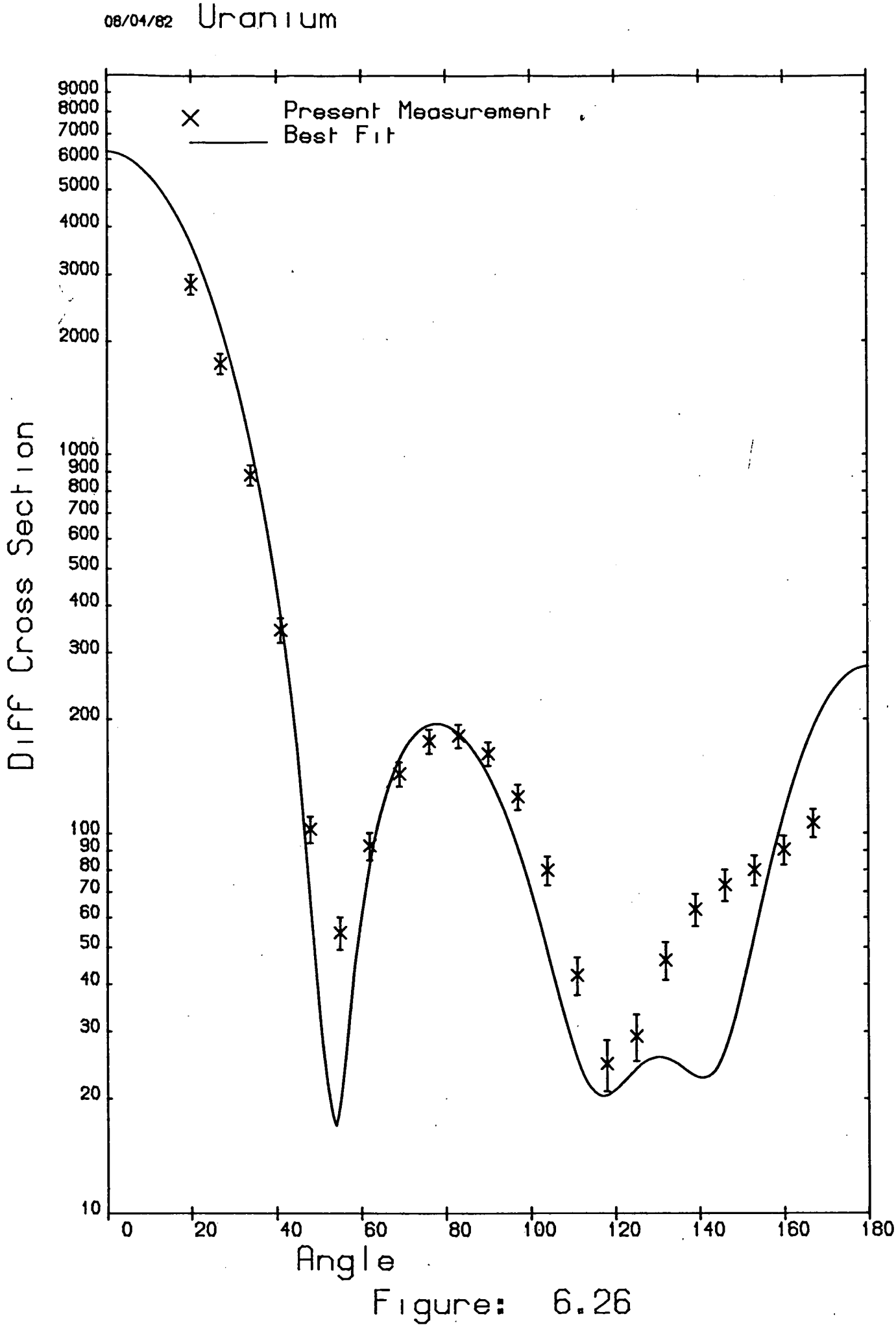
08/04/82 Uranium
Present Measurement
Best Fit
Diff Cross Section
9000
8000
7000
6000
5000
4000
3000
2000
1000
900
800
700
600
500
400
300
200
100
90
80
70
60
50
40
30
20
10
0
20
40
60
80
100
120
140
160
180
Angle

Figure: 6.26

From the above analysis it is apparent that there is some difficulty in obtaining good OM fits to both analysing powers and differential cross sections over the full angular range measured, even for those nuclei thought to be spherically symmetrical. Fits to the differential cross sections are generally better than analysing power fits, and although fitting the latter over a limited angular range was not unduly difficult, good reproduction of measured values over the full 20-167 degrees was not in general possible. The data best fitted by the OM was that of mercury where agreement was tolerably good for both analysing power and differential cross section using the best fit potential. Apart from the best fit potentials, the most successful set of parameters were those derived by Zijp and Jonker from their analysing power data and the differential cross section data of Becker et al. Of the "semi-global" potentials, that of Wilmore and Hodgson was relatively successful. The potential of Rosen et al which has had some success in fitting medium mass nucleus analysing powers [12], was not particularly good here. Neither was that of Becchetti and Greenlees, except for a comparatively close fit to tungsten differential cross sections.

6.4 The Non-Spherical OP

Many nuclei exibit collective nucleon effects which cause the nucleus to be deformed from spherical symmetry. These deformations may be permanent or dynamic, and often manifest themselves in characteristic sequences of excitation energies, spins and parities of the non-continuum states of the nuclei. In a systematic study of the energy dependence of the neutron total cross section throughout the periodic table, Foster and Glasgow [77] have observed that there are mass regions where spherical OM fits to the data are substantially poorer. In two of these regions, the rare earths and the actinides,

the nuclei are known to be permanently deformed. ^{238}U falls in the latter region and the isotopes of tungsten come at the high mass edge of the former. The low lying levels of both form a rotation band characteristic of deformed nuclei. An account of the non-spherical OP and Coupled Channels (CC) calculations is given by Tamura [33].

Deformations may be represented by substituting the following for the radius parameters

$$r = r_0[1+\sum_L B_L Y_{L0}(\theta,\phi)] \tag{6.7}$$

r_0: OP radius parameter r_R, r_I or r_S

B_L: deformation parameter

Substituting equation 6.7 in equation 6.1 and expanding the resulting expression in terms of Legendre polynomials, which is the recommended expansion for permanently deformed potentials, the result is a potential consisting of two components

$$V(r,\theta,\phi) = V_{diag} + V_{couple} \tag{6.8}$$

V_{diag} is just the usual OP and V_{couple} is the coupling potential between elastic and inelastic channels. The result of V_{couple} is that none of the quantum numbers $l, j, (-)^l$ of the incident neutron or I_n, Π_n of the target nucleus are good quantum numbers. The good quantum numbers are now

$$J = j + I_n$$
$$\Pi = \Pi_n (-)^l$$

In general several combinations of j and l will satisfy the above relations depending on the number of states assumed coupled, so that

instead of the Schrodinger equation, one has a set of coupled differential equations to solve. In the calculations made on deformed nuclei, quadrupole (B_2) and hexadecapole (B_4) deformations were considered. The effects of higher order deformations on neutron scattering data will be comparatively small [68] and are neglected. Their inclusion would in any case make the calculation intolerably long. The parameter B_2 couples the ground(0^+) and 1st excited(2^+) states of the ground rotation band, and B_4 couples the ground and 2nd excited(4^+) states for even even nuclei. With the even odd nucleus ^{183}W the ground and first two excited states are $1/2^-$, $3/2^-$ and $5/2^-$ respectively.

The nuclei in the mass region 198-209 are usually assumed spherically symmetrical. However this does not exclude the possibility of collective vibrational states of these nuclei. In this case the radius parameter may be expressed as

$$r = r_0[1+\sum_{LM} a_{LM} Y_{LM}(\theta,\phi)] \qquad (6.9)$$

Substituting equation 6.9 in 6.1 and this time expanding in powers of $\sum_{LM} a_{LM} Y_{LM}(\theta,\phi)$ up to the 2nd order one arrives at an expression of the same type as equation 6.8. The deformation parameter is given by

$$B_L = \sum_M a^2_{LM}$$

For the vibrational calculations only coupling of the ground and first collective excited state was considered. Deformation parameters where known, tend to be smaller for the vibrational nuclei in the mass range of interest here. The bulk of the collective effect is likely to result from this coupling of ground and 1st collective excited state. Besides the CC analysis was not expected to provide a definitive set of

potential and deformation parameters. It was undertaken to test if the difficulties encountered with the OM, especially in fitting analying powers might be due to collective effects. For similar reasons the complex part of V_{couple} was neglected in both rotational and vibrational nucleus calculations.

CC calculations were made with the program "JUPITOR1" [33,108], modified to remove dependence on scratch tapes which significantly slow the calculation. Calculations were made for the isotopes of tungsten and lead and for ^{238}U. As in the spherical OM case, a compound elastic contribution calculated by "CINDY" was added and calculations for single isotopes combined where applicable, before comparison with data. The relative success of the spherical OM and CC calculations, as exemplified by the X^2 tests of equations 6.4-6.6 are summarised in table 6.8.

Table 6.8

Comparison Spherical OM and CC Calculations

	CC			OM		
	X^2_{comb}	X^2_P	X^2_σ	X^2_{comb}	X^2_P	X^2_σ
Tungsten						
Delaroche et al	29.9	14.9	44.9	414.2	69.0	759.4
Best Fit	29.9	11.9	48.0	25.7	9.2	42.3
Wilmore and Hodgson	40.6	16.9	64.4	232.6	68.4	396.8
Uranium						
Guenther et al	22.3	12.0	32.6	73.0	36.0	109.9
Wilmore and Hodgson	28.0	19.2	36.8	33.5	30.8	36.2
Best Fit	29.2	15.4	43.1	12.5	8.4	16.7
Lead						
Best Fit	7.25	9.8	4.7	4.6	4.3	5.0
Fu and Perey	10.9	14.6	7.2	11.5	15.3	7.7
Wilmore and Hodgson	17.1	13.6	20.5	15.3	8.8	22.2

Tungsten and uranium, as previously mentioned, are known to be permanently deformed, and CC calculations have been performed in order to fit measured differential elastic and inelastic cross sections [68,22,27].

For tungsten the B_L of Delaroche et al were used

^{182}W: $B_2=0.223$, $B_4=-0.054$

^{183}W: $B_2=0.220$, $B_4=-0.075$

^{184}W: $B_2=0.209$, $B_4=-0.056$

^{186}W: $B_2=0.203$, $B_4=-0.057$

Three potentials were tried, those of Delaroche et al, Wilmore and Hodgson, and the Best Fit Potential. In figure 6.28 the present differential cross section and that of Delaroche(3.4MeV data on separated isotopes combined for comparison) are compared with CC calculations at 3.0 and 3.4 MeV. The 3.4MeV curve follows the latter data quite well indicating that the calculations are reliable. Although the calculations show a slight difference in the depth of the 135 degree diffraction minimum, they indicate that a real discrepancy exists between the two sets of data. There is also a discrepancy at forward angles. As the latter is a high resolution time of flight measurement which completely separates out elastically scattered neutrons, then it must be assumed more reliable. A possible cause is the neglection of the contribution of several inelastic groups to the experimental cross section (5.5.1), scattering from excited states of W^{183} above 0.099MeV. However the present data is not uniformly high. The low cross section at forward angles and the insufficiently deep minima may indicate a slight inadequacy in the finite sample size correction. The tungsten sample was certainly the largest in terms of neutron MFPR. This cannot however explain the discrepancy between measured and calculated analysing powers in the angular range 70-110 degrees (figure 6.29), where the present cross section appears to be

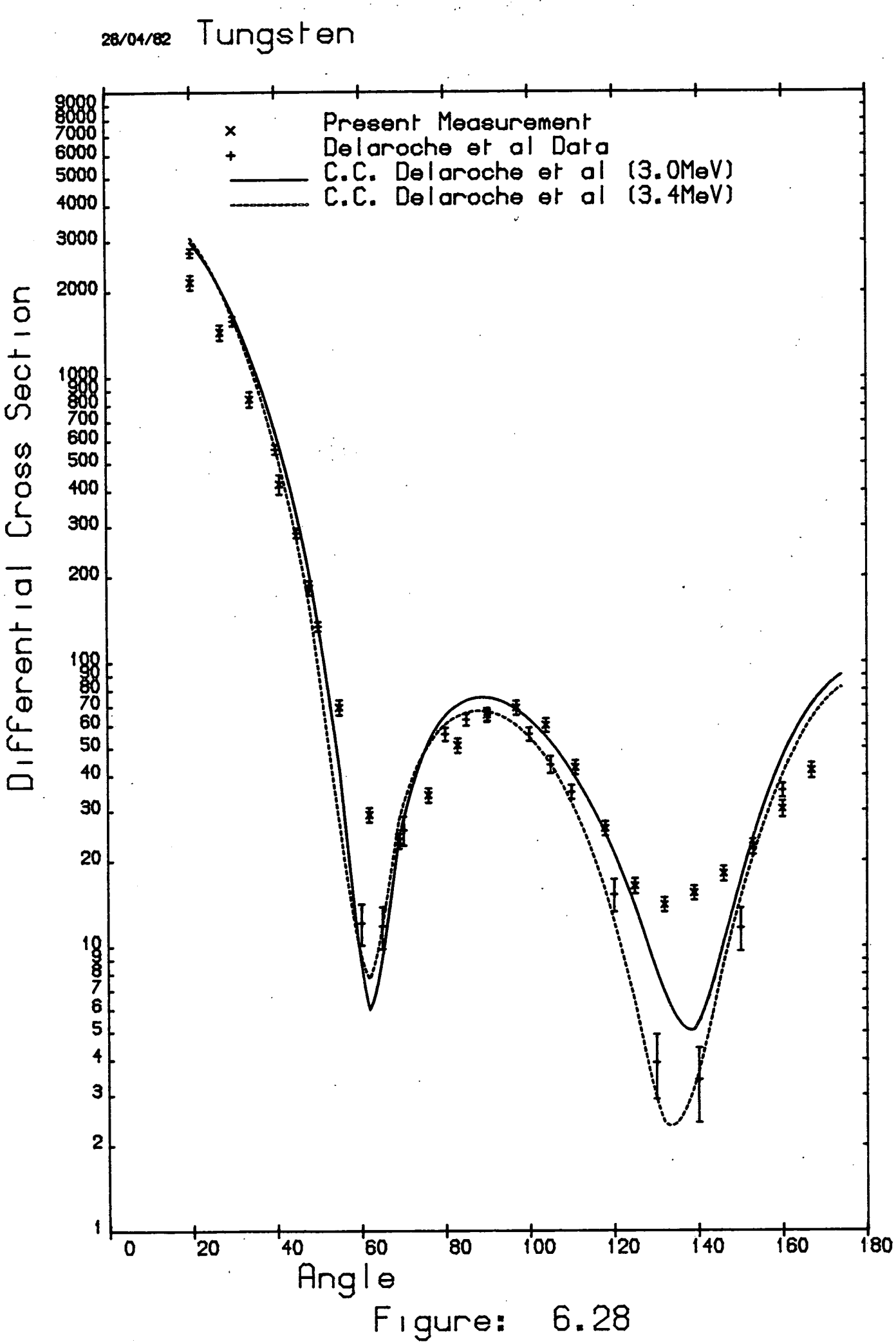
28/04/82 Tungsten
Present Measurement
Delaroche et al Data
C.C. Delaroche et al (3.0MeV)
C.C. Delaroche et al (3.4MeV)
Differential Cross Section
Angle
9000
8000
7000
6000
5000
4000
3000
2000
1000
900
800
700
600
500
400
300
200
100
90
80
70
60
50
40
30
20
10
8
7
6
5
4
3
2
1
0
20
40
60
80
100
120
140
160
180

Figure: 6.28

28/04/82 Tungsten

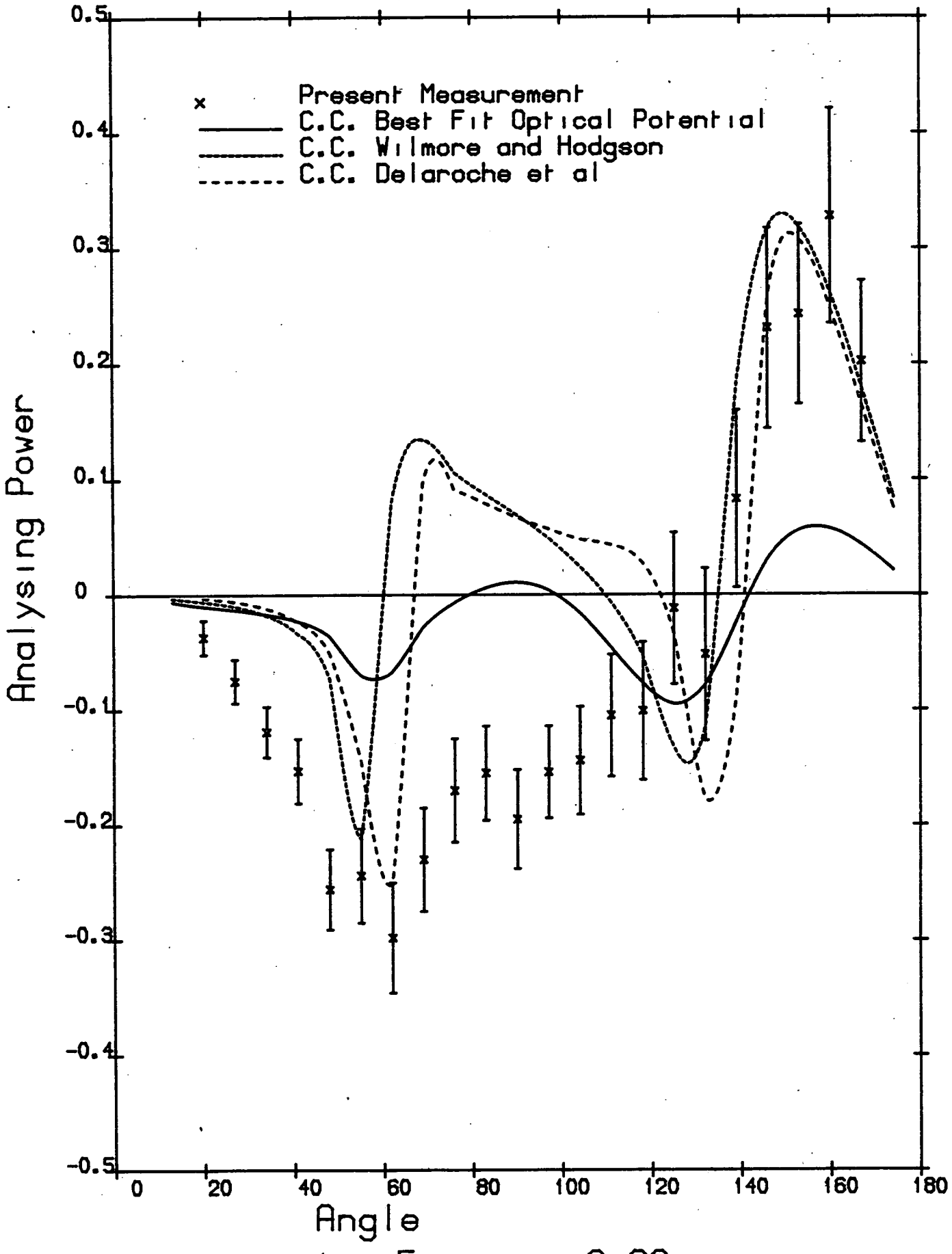

Figure: 6.29

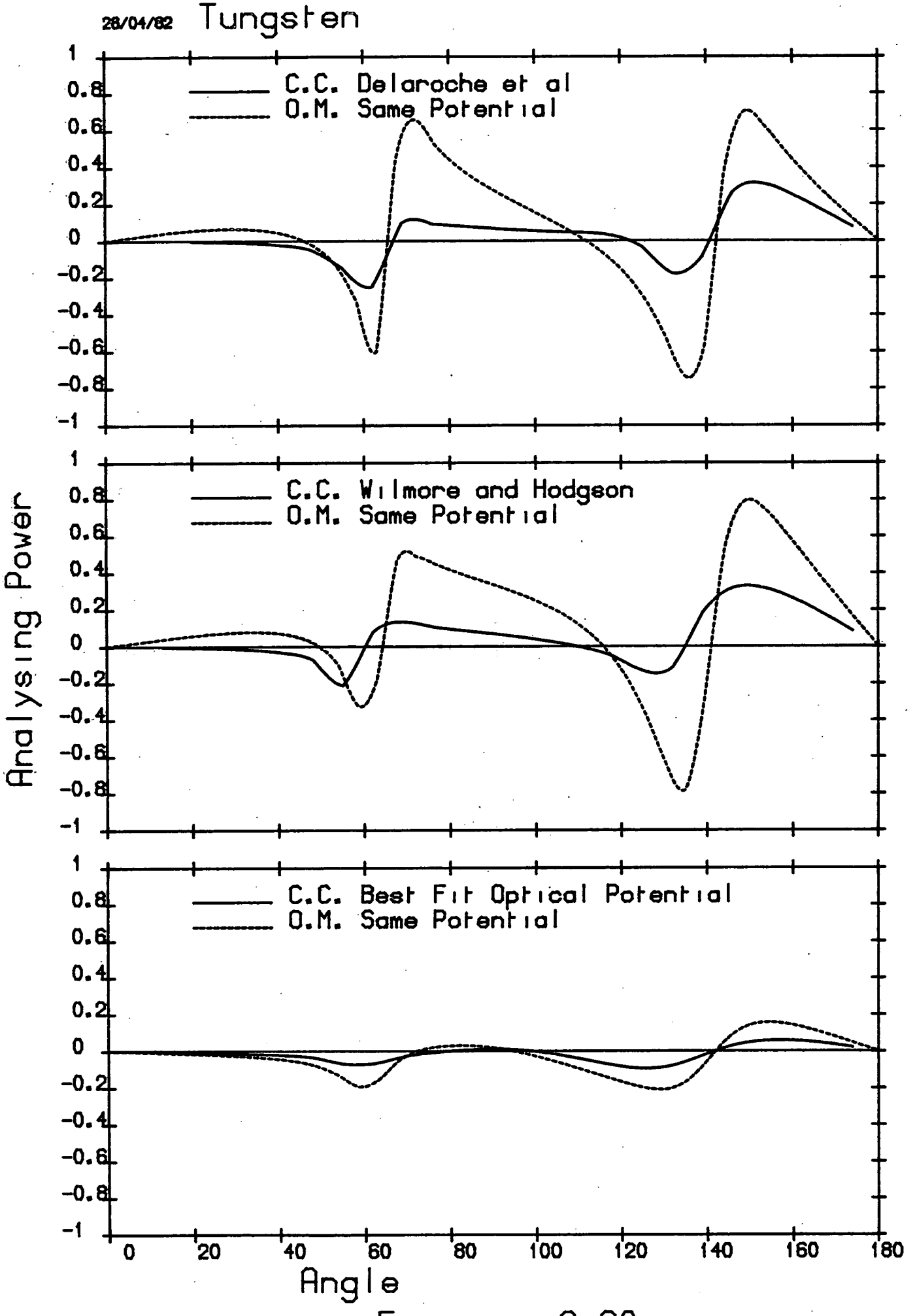
28/04/82 Tungsten
C.C. Delaroche et al
O.M. Same Potential
C.C. Wilmore and Hodgson
O.M. Same Potential
C.C. Best Fit Optical Potential
O.M. Same Potential
Analysing Power
Angle
1
0.8
0.6
0.4
0.2
0
-0.2
-0.4
-0.6
-0.8
-1
0
20
40
60
80
100
120
140
160
180

Figure: 6.30

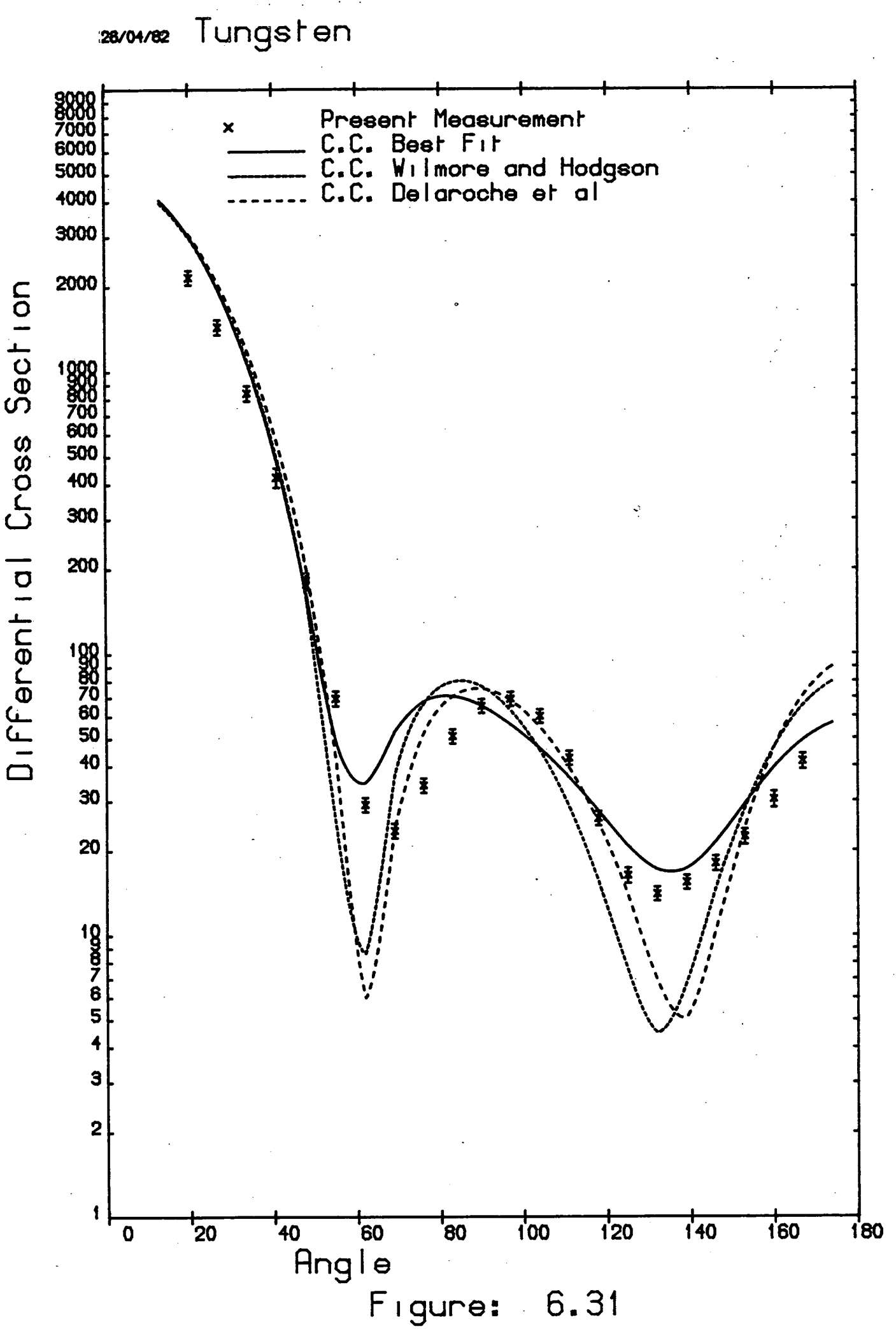
28/04/82 Tungsten
Present Measurement
C.C. Best Fit
C.C. Wilmore and Hodgson
C.C. Delaroche et al
Differential Cross Section
Angle
9000
8000
7000
6000
5000
4000
3000
2000
1000
900
800
700
600
500
400
300
200
100
90
80
70
60
50
40
30
20
10
8
7
6
5
4
3
2
1
0
20
40
60
80
100
120
140
160
180

Figure: 6.31

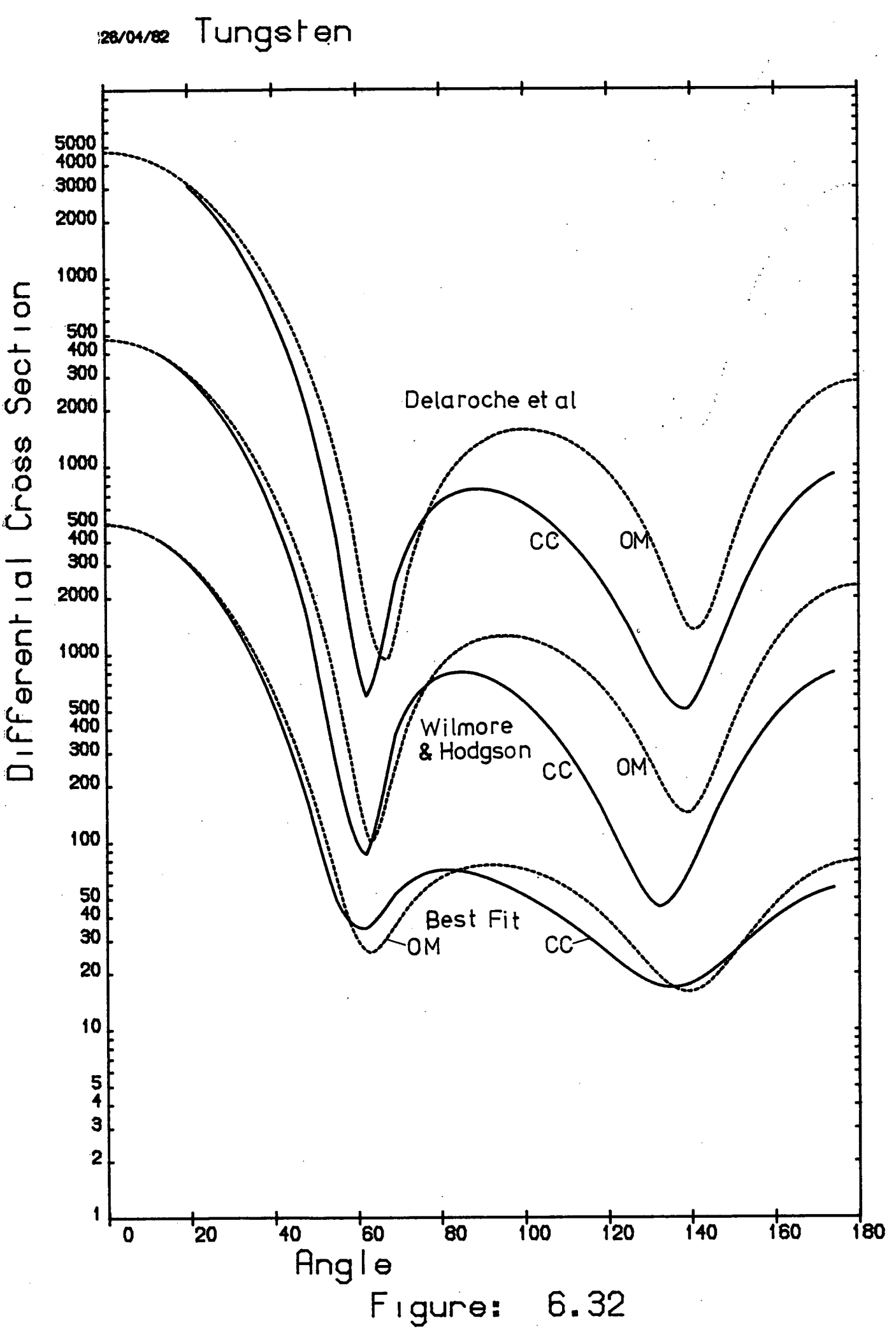
26/04/82 Tungsten
Differential Cross Section
Angle
Delaroche et al
CC
OM
Wilmore
& Hodgson
CC
OM
Best Fit
OM
CC
5000
4000
3000
2000
1000
500
400
300
2000
1000
500
400
300
2000
1000
500
400
300
200
100
50
40
30
20
10
5
4
3
2
1
0
20
40
60
80
100
120
140
160
180

Figure: 6.32

reasonably accurate. Figure 6.30 shows the considerable effects of coupling on analysing power calculations, 6.31 compares the C.C calculations on differential cross sections at 3.0MeV with the present data, and 6.32 the effects of coupling on the calculated differential cross sections which again are large. CC calculations have resulted in significant improvements in fits to both the differential cross section and analysing power for the potentials of Delaroche et al and Wilmore and Hodgson, although they are still by no means good. The neglect of coupling where this is important is known [16,109] to effect optimised OP parameters strongly. It is therefore not surprising that there is not a corresponding improvement in fit using the "Best Fit" potential.

For Uranium the deformation parameters used by Guenther et al were taken.

$$B_2 = 0.216 \ , \ B_4 = 0.064$$

The potentials of Guenther et al and Wilmore and Hodgson as well as the Best Fit potential were used. Analysing power fits (figure 6.33) are improved, less so for the Best Fit potential, but are still not good, and coupling can be seen (figure 6.34) to have a considerable effect on the calculation. Apart from the best fit potential, coupling improves the differential cross section fits (figure 6.35), especially using the potential of Guenther et al, and influences the cross section considerably (figure 6.36) at angles greater than 60 degrees. The differential cross section data of Beghian et al is included in figure 6.35 for comparison. It is unfortunate that they did not cover a fuller angular range which might give more indication as to the quality of their data. However it lies reasonably close to the calculated curve using the potential of Guenther et al which was formulated with the intention of fitting Uranium cross sections, and since they used the time of flight technique separating neutrons scattering from the 0.045MeV 1st excited state their data ought to be more reliable.

27/04/82 Uranium

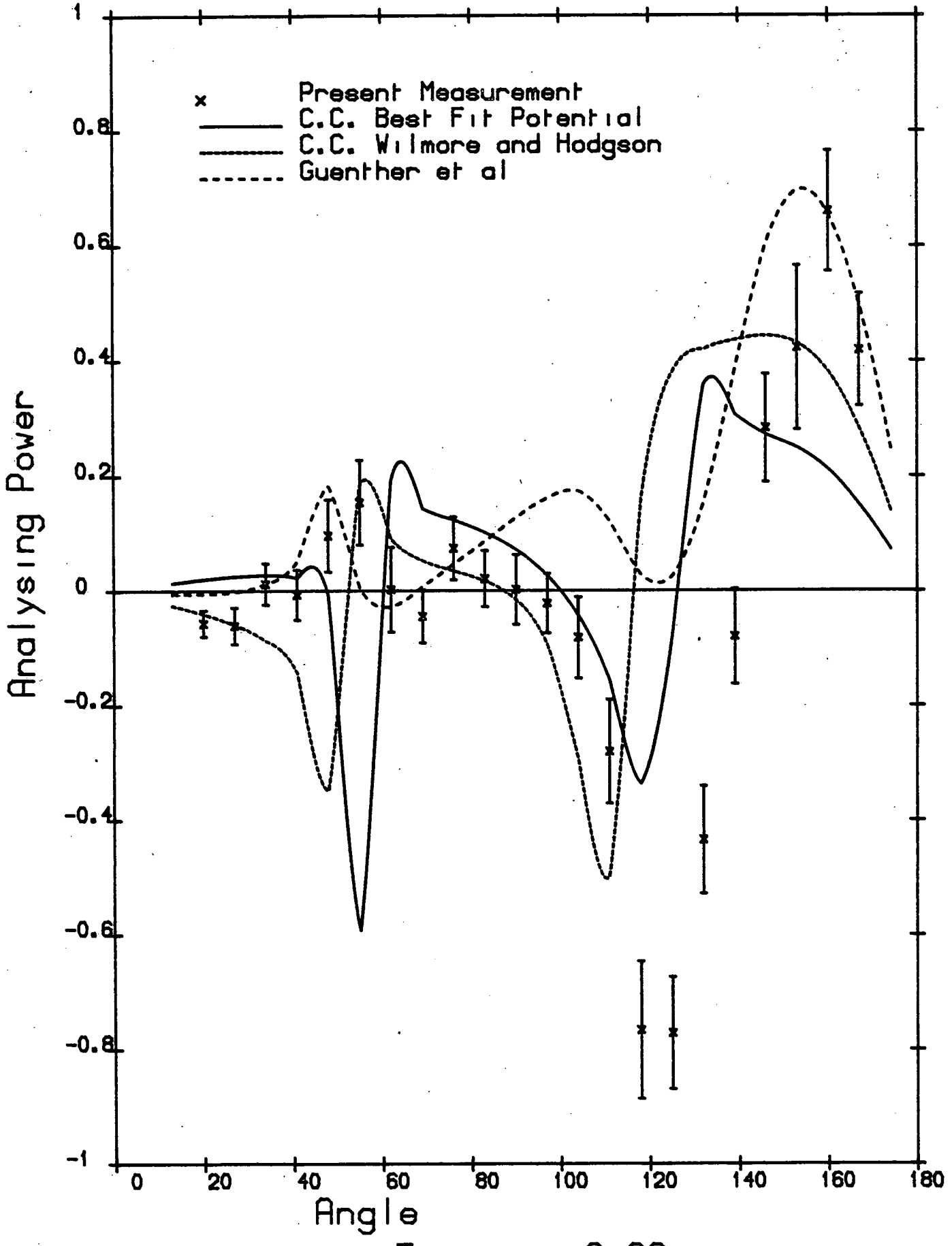

Figure: 6.33

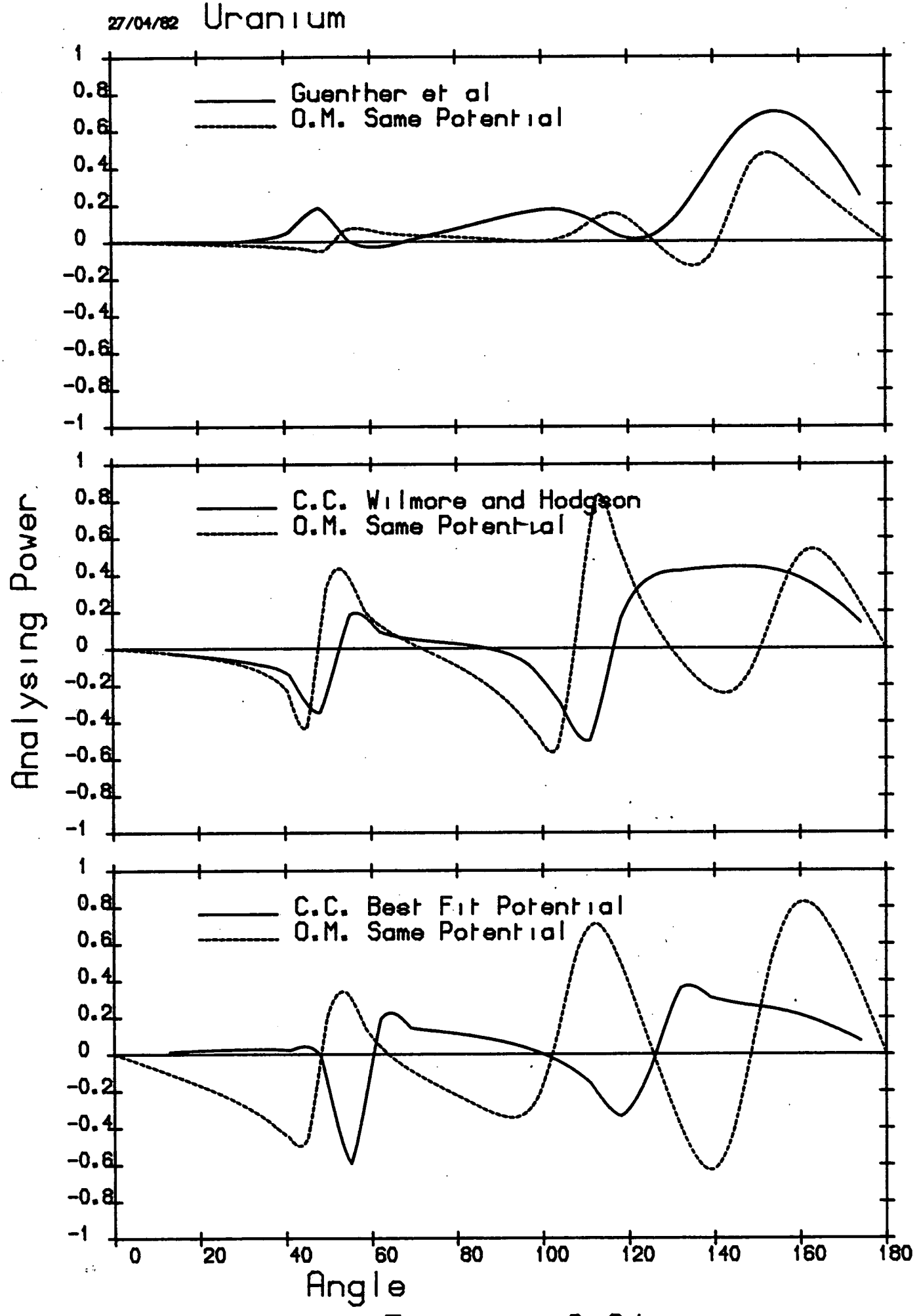
27/04/82 Uranium
Guenther et al
O.M. Same Potential
C.C. Wilmore and Hodgson
O.M. Same Potential
C.C. Best Fit Potential
O.M. Same Potential
Analysing Power
Angle
1
0.8
0.6
0.4
0.2
0
-0.2
-0.4
-0.6
-0.8
-1
0
20
40
60
80
100
120
140
160
180

Figure: 6.34

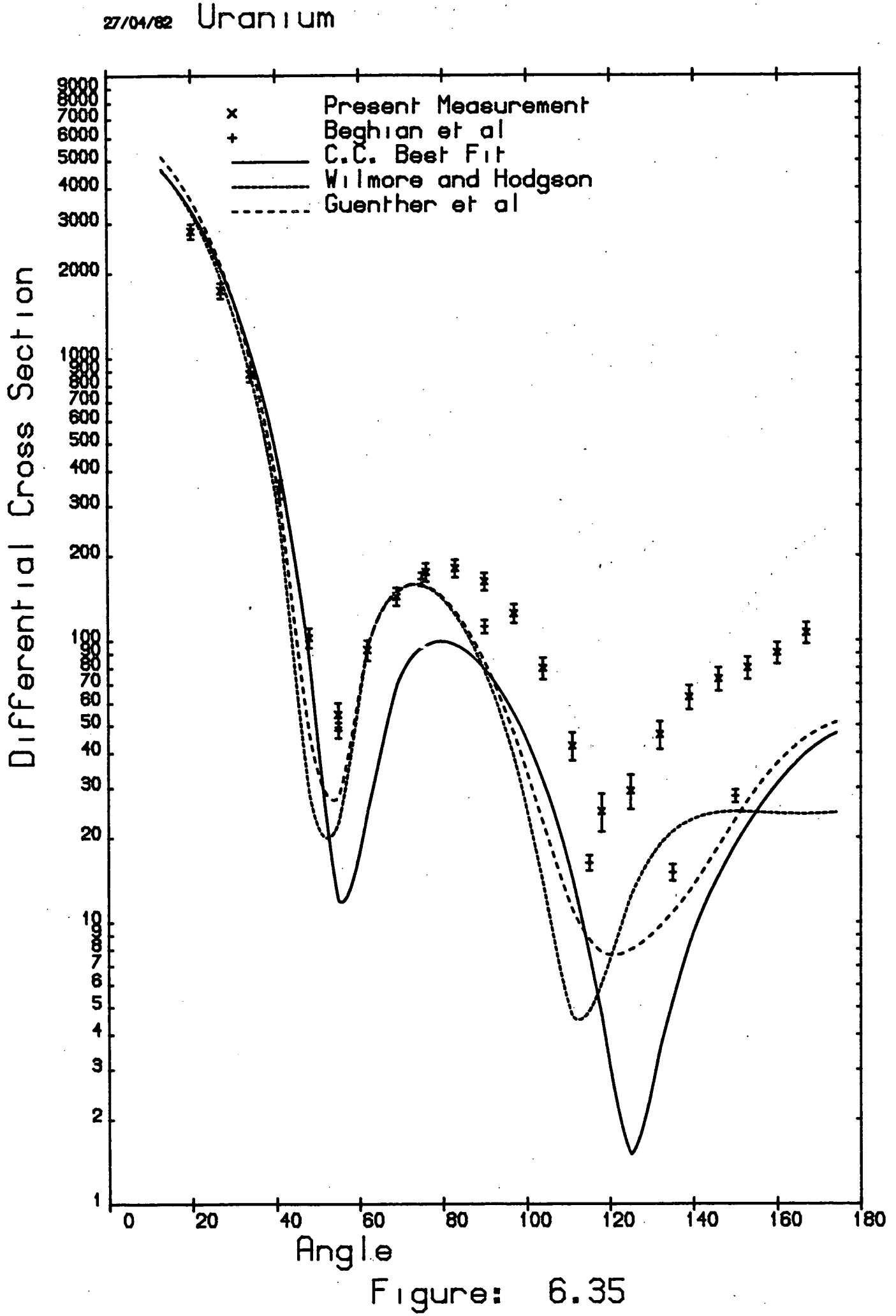
27/04/82 Uranium
Present Measurement
Beghian et al
C.C. Best Fit
Wilmore and Hodgson
Guenther et al
Differential Cross Section
Angle
0
20
40
60
80
100
120
140
160
180

Figure: 6.35

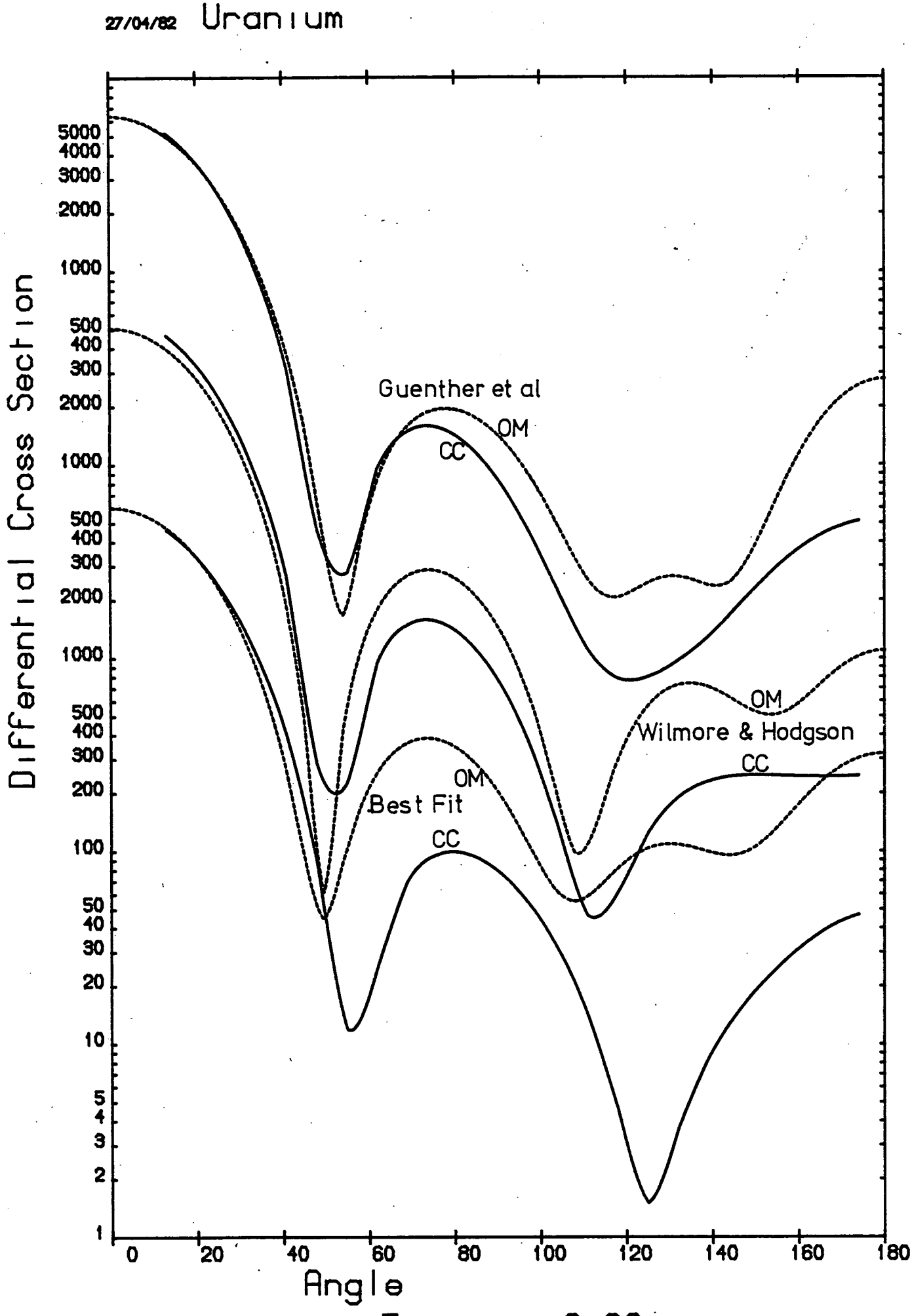
27/04/82 Uranium
Differential Cross Section
5000
4000
3000
2000
1000
500
400
300
2000
1000
500
400
300
2000
1000
500
400
300
200
100
50
40
30
20
10
5
4
3
2
1
0
20
40
60
80
100
120
140
160
180
Angle
Guenther et al
OM
CC
OM
Wilmore & Hodgson
CC
OM
Best Fit
CC

Figure: 6.36

Possible causes of the discrepency are neglection of the effects of inelastic neutrons, scattering from excited states above 0.148MeV, on the experimental data and insufficient allowance for the effects of neutron induced fission.

For lead the dynamical deformation parameters recommended by Fu and Perey were taken.

^{206}Pb: B_2= 0.037 (Couples ground 0^+ and 1st excited 2^+,0.803MeV states)

^{207}Pb: B_3= 0.072 (Couples ground $1/2^+$ and $5/2^+$,2.624MeV states)

^{208}Pb: B_3= 0.120(Couples ground 0^+ and 1st excited, 3^-,2.615MeV states)

The potentials of Fu and Perey, Wilmore and Hodgson and the Best Fit potential were tried. Contrary to the case with permanently deformed nuclei, no improvement in fit to the present data is observed when coupling is introduced. Analysing power fits (figure 6.37), although marginally better using the potential of Fu and Perey, are significantly worse with the other two potentials. The effect of introducing coupling (figure 6.38) is to roughly halve the magnitude of the calculated analysing power, while not changing the shape very much. The quality of fit to differential cross sections (6.39) is altered very little, and this is borne out by the close correspondence (figure 6.40) between spherical and CC calculations.

6.5 Conclusions

This project was started with the aim of improving the accuracy of analysing power measurements and the reliability of differential cross section measurements, compared with those made with previous neutron polarimeters used in the Edinburgh Neutron Physics Laboratory. To a

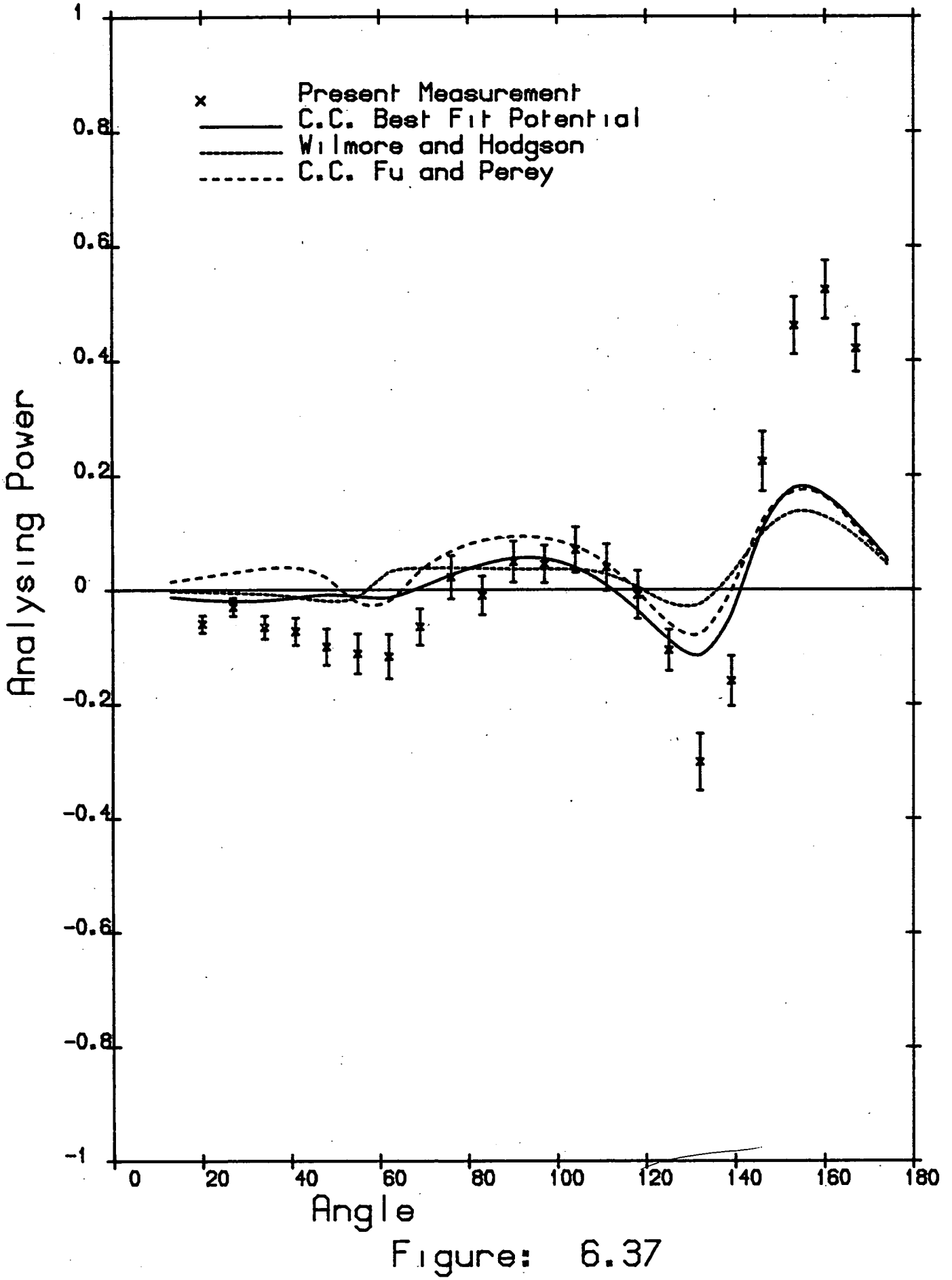
27/04/82 Lead
Present Measurement
C.C. Best Fit Potential
Wilmore and Hodgson
C.C. Fu and Perey
Analysing Power
Angle
1
0.8
0.6
0.4
0.2
0
-0.2
-0.4
-0.6
-0.8
-1
0
20
40
60
80
100
120
140
160
180

Figure: 6.37

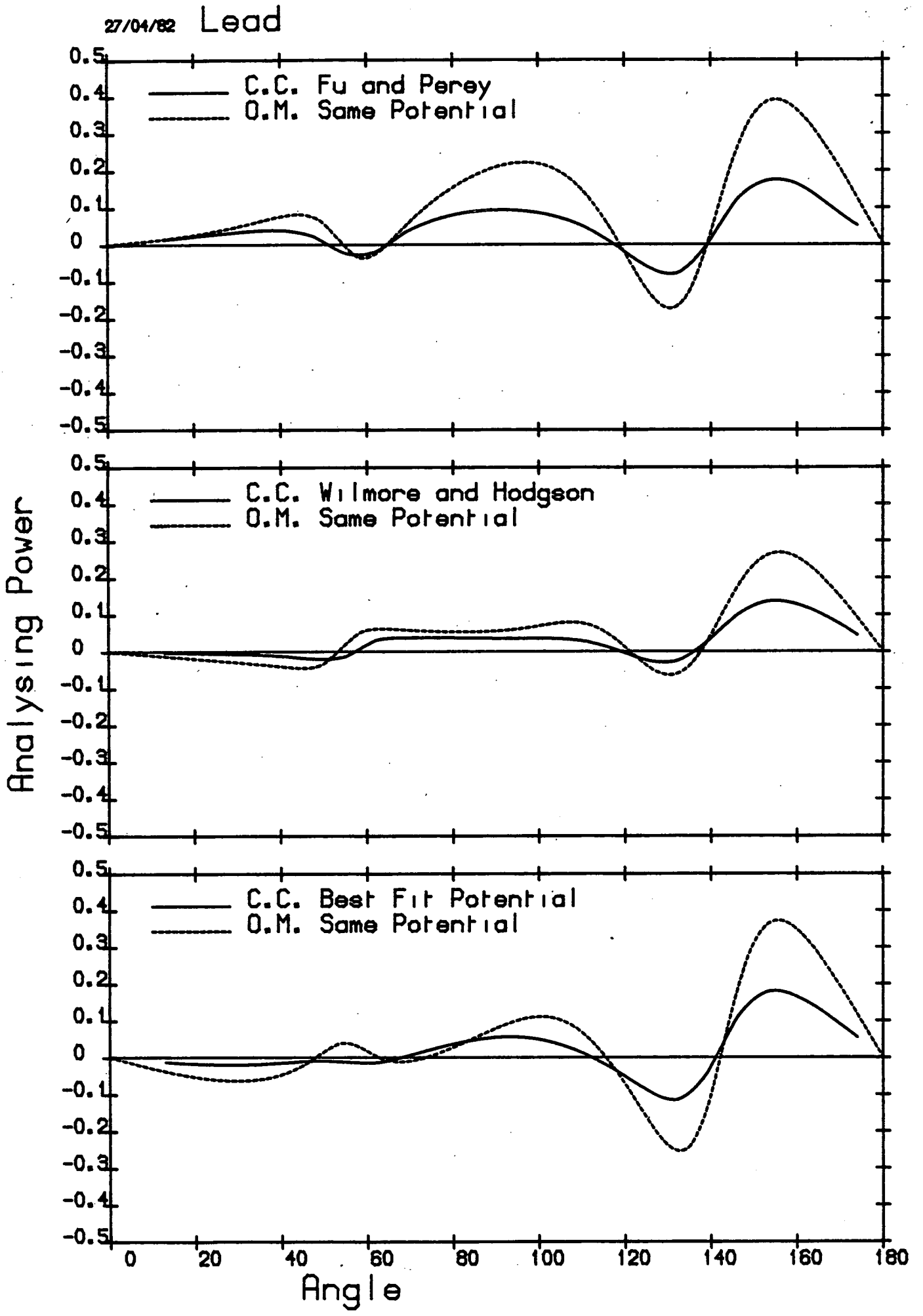
27/04/82 Lead
C.C. Fu and Perey
O.M. Same Potential
C.C. Wilmore and Hodgson
O.M. Same Potential
C.C. Best Fit Potential
O.M. Same Potential
Analysing Power
Angle
0.5
0.4
0.3
0.2
0.1
0
-0.1
-0.2
-0.3
-0.4
-0.5
0
20
40
60
80
100
120
140
160
180

Figure: 6.38

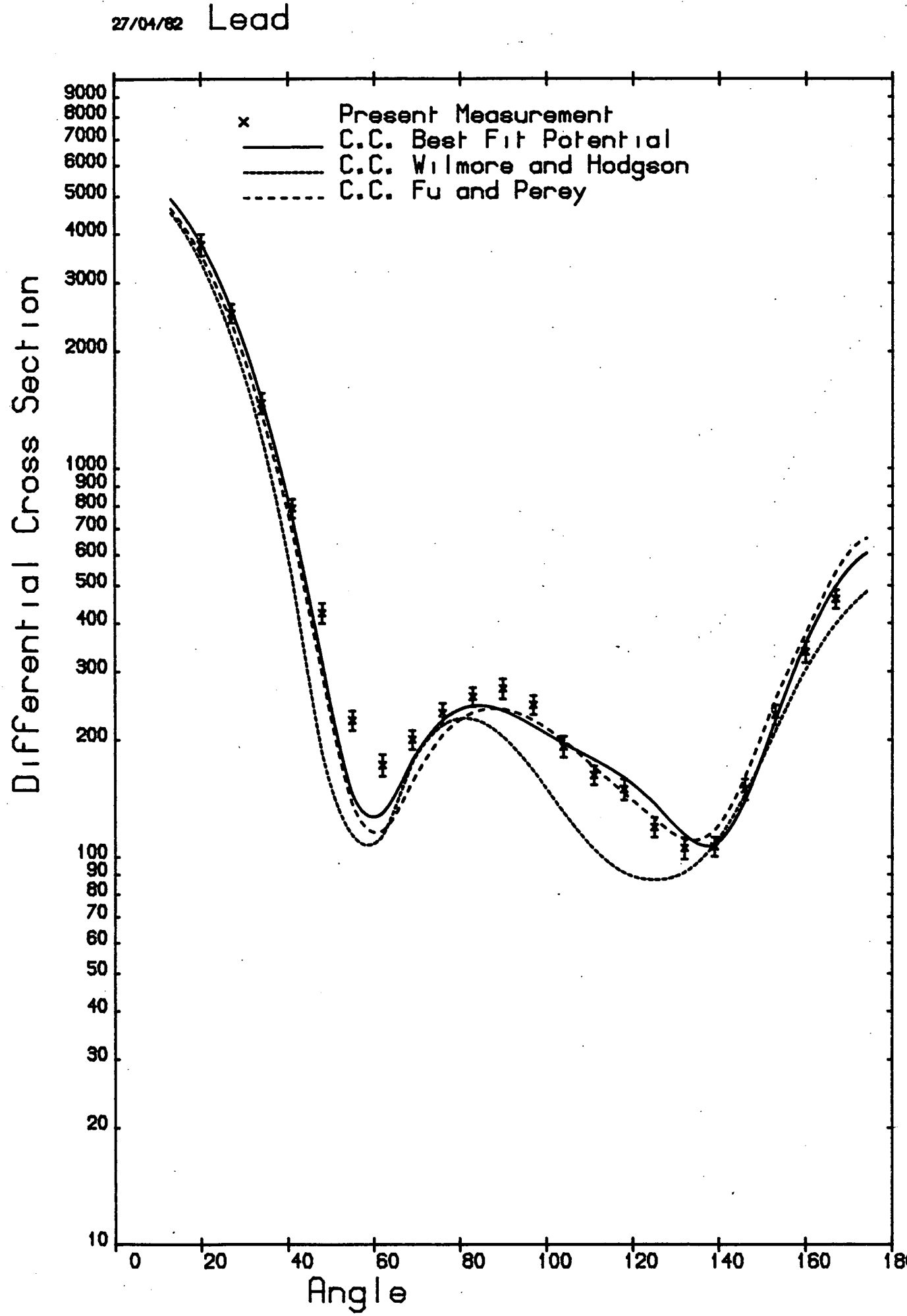
27/04/82 Lead
Present Measurement
C.C. Best Fit Potential
C.C. Wilmore and Hodgson
C.C. Fu and Perey
Differential Cross Section
9000
8000
7000
6000
5000
4000
3000
2000
1000
900
800
700
600
500
400
300
200
100
90
80
70
60
50
40
30
20
10
0
20
40
60
80
100
120
140
160
180
Angle

Figure: 6.39

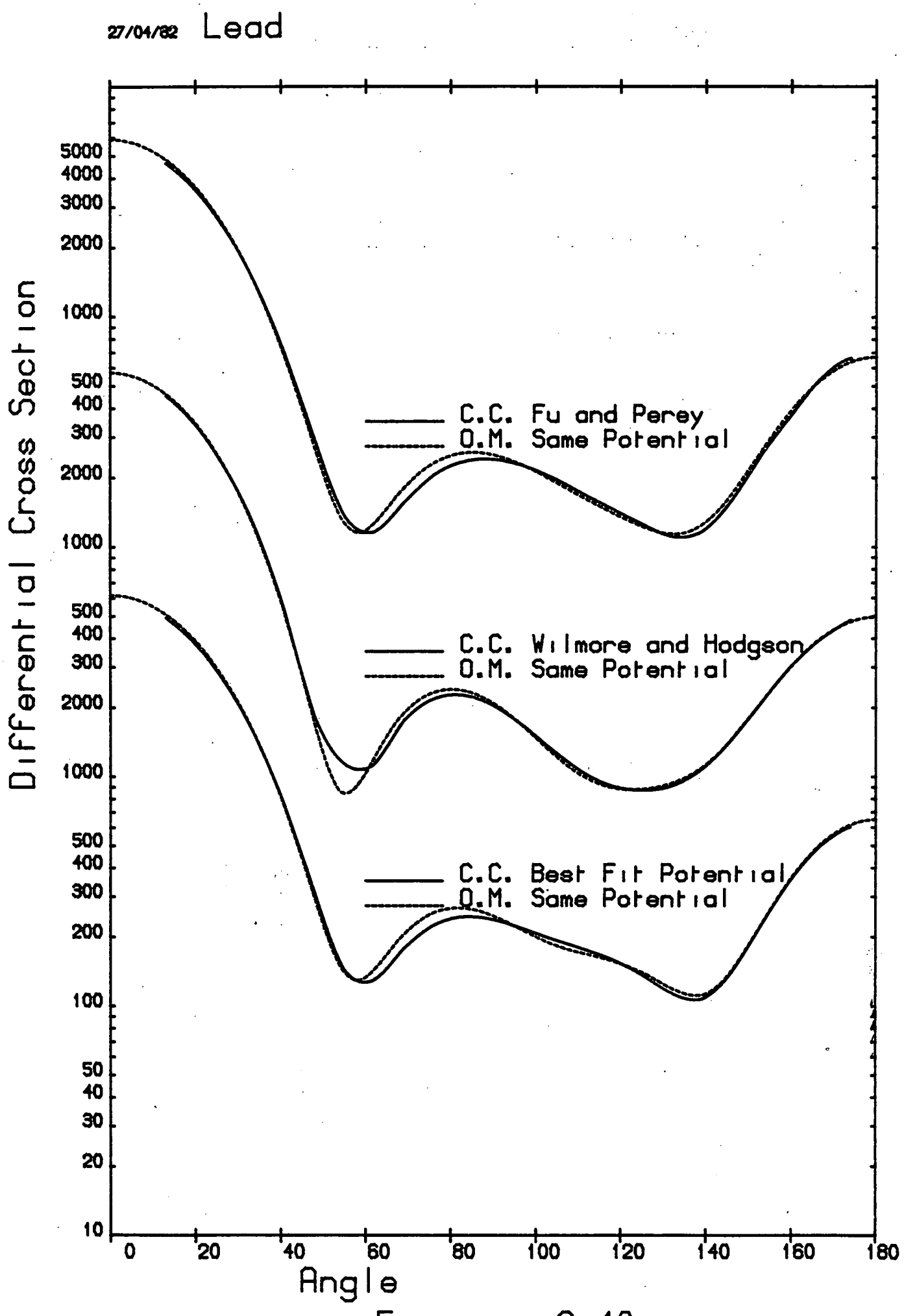
27/04/82 Lead
Differential Cross Section
5000
4000
3000
2000
1000
500
400
300
2000
1000
500
400
300
2000
1000
500
400
300
200
100
50
40
30
20
10
C.C. Fu and Perey
O.M. Same Potential
C.C. Wilmore and Hodgson
O.M. Same Potential
C.C. Best Fit Potential
O.M. Same Potential
0
20
40
60
80
100
120
140
160
180
Angle

Figure: 6.40

large extent this has been achieved. At backward angles the accuracy is improved by factors of two up to five . Although other measurements made around 3.0MeV may have comparable accuracy at some angles no published data covers as large an angular range with as many angles measured. Measurement at 7 degree intervals has greatly improved the definition of analysing power distributions especially at backward angles were there are sharp swings from negative to positive polarisation. Improvements in detection efficiency intercalibration have resulted in cross sections which show a smooth angular dependence and exibit improved agreement , and in the case of Bismuth very good agreement, with previously measured cross sections where these are of good accuracy, made using the time of flight method. Where no time of flight data exists the present data is thought to be the most reliable.

Simultaneous fitting of analysing powers and differential cross sections over the angular range 20-167 degrees has provided a very exacting test of the OM. This was not expected to provide especially good fits for the permanently deformed nuclei of tungsten and uranium. However discrepencies also exist between OM calculations and measurements for the nuclei usually assumed spherical. - CC calculations with some of the potentials used in the OM calculations, and previously determined nuclear deformation parameters have improved the quality of fit for rotational nuclei, although the fit is still not good. Calculations made assuming coupling between the ground and 1st collective(vibrational) states of the lead isotopes show no improvement in fit compared with spherical OM calculations. The CC calculations were by no means exhaustive in that a complex form factor was not used, that is V_{couple} was assumed real, and no attempt was made to vary the deformation parameters. The consideration of a complex V_{couple} may remove some of the discrepencies, but the effect of this is likely to be less than that of the effect of initially considering the nucleus

deformed at all. Variation of the deformation parameters will certainly effect the calculated cross sections and analysing powers. However it is difficult to envisage parameters used apparently successfuly in a cross section analysis not being applicable to analysing powers. Another possible cause of discrepencies may be inadaquacy of the phenomenological OP itself. In a series of papers Brieva and Rook [110,111,112] have derived a nucleon nucleus potential from the known force between two nucleons and compared the results of calculations using this potential with neutron and proton scattering data on ^{40}Ca and ^{208}Pb at energies above 7 MeV. Using their potential they find improved agreement with measurements, compared with phenomenological potentials. Unfortunately their calculations produce no convenient analytical form for the potential. The results of their calculations on the radial dependence of the various components of the potential show a more complicated shape than given by the corresponding phenomenological components. A similar calculation at 3 MeV for ^{208}Pb might provide an explanation for the discrepancies between model calculations and experimental data observed here.

References

1: R.E.Le Levier and D.S.Saxon, Phys.Rev.**87**(1952),40

2: H.Feshbach, C.E.Porter and V.F.Weisskopf, Phys.Rev.**96**(1954),448

3: Proc.International Symposium on Polarisation Phenomena of Nucleons (Basel 1960), Suppl. Helv.Phys.Acta **6**(1961)

4: H.H.Barschall, Phys.Rev.**86**(1952),431

5: R.K.Adair, S.E.Darden and R.E.Fiddo, Phys.Rev.**96**(1954),503

6: G.V.Gorlov, N.S.Lebedeva and V.M.Morozov, Yad.Fiz.**5**(1967),910
Trans. Sov.J.Phys.**6**(1968),663

7: A.T.G.Ferguson, R.E.White and D.Wilmore, Nucl.Phys.**76**(1966),369

8: F.G.Perey and B.Buck, Nucl.Phys.**32**(1962),353

9: R.L.Becker, W.G.Guindon and G.J.Smith, Nucl.Phys.**89**(1966),154

10: A.S.Mahajan, Nucl.Phys.**A95**(1967),193

11: L.Rosen, J.G.Beery, A.S.Goldhaber and E.H.Auerbach, Ann.Phys.**34**(1965),96

12: D.Ellgehausen, E.Baumgartner, R.Gleyvod, P.Huber, A.Stricker and K.Wiedemann, Helv.Phys.Acta **42**(1969),252

13: K.Wiedemann, E.Baumgartner, D.Ellgehausen, R.Gleyvod and P.Huber, Helv.Phys.Acta **42**(1969),252

14: B.Holmqvist, Ark.Phys**38**(1968),403

15: M.V.Pasechnik, I.A.Korzh, I.E.Kashuba, V.M.Mishchenko, N.M.Pravdivy and I.E.Sanzhur, Yad.Fiz.**11**(1970),533
Trans. Sov.J.Phys.**11**(1970),533

16: E.Zijp and C.C.Jonker, Nucl.Phys.**A222**(1974),93

17: A.H.Hussein, J.M.Cameron, S.T.Lam, G.C.Neilson and J.Soukup, Phys.Rev.**C15**(1977),233

18: F.D.Becchetti and G.W.Greenlees, Phys.Rev.**182**(1969),1190

19: J.Schwinger, Phys.Rev.**73**(1948),407

20: E.Ramstrom and P.A.Goransson, Nucl.Phys.**A284**(1977),461

References Continued

21: R.B.Galloway and A.Waheed, Nucl.Phys.A318 (1979),173

22: P.T.Guenther, D.G.Havel, A.Smith, Technical Notes
Nucl.Sci.and Eng.65(1978),174

23: A.Smith, P.Guenther, P.Moldauer and J.Whalen,
Nucl.Phys.A307(1978),224

24: A.Smith, Nucl.Phys.A332(1979),297

25: A.Smith and P.Guenther, Nucl.Sci.and Eng.73(1980),186

26: A.B.Smith, P.Guenther and J.Whalen, Nucl.Sci.and Eng.75(1980),69

27: L.E.Beghian, G.H.R.Kegel, T.V.Marcella, B.K.Barnes, G.P.Couchell,
J.J.Egan, A.Mittler, D.J.Pullen and W.A.Schier,
Nucl.Sci and Eng.69(1979),191

28: A.Begum and R.B.Galloway, J.Phys.G 7(1981),535

29: C.Y.Fu and F.G.Perey,
Atomic Data and Nuclear Data Tables 16(1975),409

30: S.Tanaka, Y.Tomita, K.Ideno and S.Kikuchi, Nucl.Phys.A179(1972),513

31: W.Hauser and H.Feshbach, Phys.Rev.87(1952),366

32: P.A.Moldauer, Phys.Rev.135B(1964),642

33: T.Tamura, Rev.Mod.Phys.37(1965),241

34: R.B.Galloway and A.Waheed, Nucl.Inst.and Meth.128(1975),515

35: H.Davie and R.B.Galloway, Nucl.Inst.and Meth.92(1971),547

36: H.Davie, PhD Thesis, University of Edinburgh 1972

37: M.L.Roush, M.A.Wilson and W.F.Hornyak,
Nucl.Inst.and Meth.31(1964),112

38: A.Begum, PhD Thesis, University of Edinburgh 1979

39: F.K.McNeil-Watson, Nucl.Inst.and Meth.137(1976),193

40: Digital Equipment Corporation, Floating Point Arithmetic Software.

41: K.Masood Ali, R.B.Galloway and D.G.Vass,
Nucl.Instr. and Meth. 92(1971),553

References Continued

42: J.H.Ormrod, Nucl.Instr.and Meth. 95(1971)

43: D.C.Stantry and R.D.Werner, Nucl.Instr.and Meth. 188(1981),211

44: W.Whalen, Handbuch der Fysik 34(1958),431

45: R.B.Galloway, Nucl.Inst.and Meth.172(1980),431

46: H.Faissner, F.Ferrero, A.Ghani and M.Reinharz,
Nucl.Inst.and Meth.20(1963),289

47: P.Kuijper, C.J.Tiesinga, C.C.Jonker, Nucl.Inst.and Meth42(1966),56

48: R.De Leo, G.D'Erasmo, A Pantaleo and G.Russo,
Nucl.Inst.and Meth.119(1974),559

49: R.De Leo, G.D'Erasmo and A.Pantaleo,
Nucl.Inst.and Meth.129(1975),501

50: G.W.Clark, IEEE Trans.Nucl.Sci.NS7(1960),164

51: E.D.Cashwell and C.J.A.Everette, A Practical Manual on the
Monte Carlo Random Walk Method, Pergammon Press, New York 1959

52: A.Horsely, Nuclear DataA2(1966),243

53: C.Y.Fu and F.G.Perey,
Atomic Data and Nuclear Data Tables 22(1978),249

54: R.Madey, F.M.Waterman, A.R.Baldwin, J.Knudson, J.D.Carlson and
J.Rapaport, Nucl.Inst.and Meth151(1978),445

55: R.A.Cecil, A.B.Anderson, R.Madey, Nucl.Inst.and Meth.161(1979),439

56: J.Bloch and C.C.Jonker, Physica 18(1952),809

57: S.A.Cox, Nucl.Inst.and Meth.56(1967),245

58: C.A.Engelbrecht, Nucl.Inst.and Meth.80(1970),187

59: C.A.Engelbrecht, Nucl.Inst.and Meth.93(1971),103

60: B.Holmqvist, B.Gustavson, T.Wiedling, Ark.Fys.34(1967),481

61: O.Aspelund and B.Gustavson, Nucl.Inst.and Meth.57(1967),197

62: W.E.Kinney, Nucl.Inst.and Meth.83(1970),14

63: T.G.Miller and F.P.Gibson, Nucl.Inst.and Meth.80(1970),325

64: J.B.Parker, J.H.Towle, D.Sams, W.B.Gilboy, A.D.Purnell and H.J.Stevens, Nucl.Inst.and Meth.30(1964),77

65: G.M.Stinson, S.M.Tang and J.T.Sample, Nucl.Inst.and Meth.62(1968),13

66: D.E.Velkley, J.D.Brandenberger, D.W.Glasgow and H.T.McEllistrem, Nucl.Inst.and Meth.129(1975),231

67: H.Liskien and A.Paulsen, Nucl.Data Tables 11(1973),587

68: J.P.Delaroche, G.Haouat, J.Lachkar, Y.Patin, J.Sigaud, J.Chardine, Phys.Rev.C23(1981),136

69: R.P.Gardner and K.Verghese, Nucl.Instr.and Meth.93(971),163

70: R.L.Craun and L.Smith, Nucl.Instr.and Meth.80(1970),239

71: H.J.Boersma, C.C.Jonker, J.E.Nigenhuis, P.J.van Hall, Nucl.Phys.46(1963),660

72: A.F.Behof, T.H.May, W.I.McGarry, Nucl.Phys.A108(1968),250

73: P.Roding and H.Scholerman, Nucl.Phys.A125(1969),585

74: H.Davie and R.B.Galloway, Nucl.Instr.and Meth.108(1973),581

75: R.B.Galloway and R.Martinez Lugo, Nucl.Instr.and Meth.158(1979),153

76: R.L.Walter, Polarisation Phenomena in Nuclear Reactions. Ed. H.H.Barschall and W.Haeberli (Univ.Wisconsin Press, Madison 1971), 317

77: D.G.Foster and D.W.Glasgow, Phys.Rev.C3(1971),576

78: M.R.Schmorak, Nucl.Data Sheets 14(1975),559

79: A.Artna-Cohen, Nucl.Data Sheets 16(1975),267

80: M.J.Martin and P.H.Stelson, Nucl.Data Sheets 21(1977),1

81: M.R.Schmorak, Nucl.Data Sheets 13(1974), 267

82: K.Tsukada, S.Tanaka, Y.Tomita, M.Maruyama, Nucl.Phys.A125(1969),641

83: B.Harmatz, Nucl.Data Sheets 21(1977),377

84: J.Halperin, Nucl.Data Sheets 24(1978),57

85: M.R.Schmorak, Nucl.Data Sheets 26(1979),81

86: M.R.Schmorak, Nucl.Data Sheets 25(1978),13

87: M.R.Schmorak, Nucl.Data Sheets 25(1978),675

88: M.R.Schmorak, Nucl.Data Sheets 27(1979),581

89: P.A.Moldauer, Nucl.Phys.47(1963),65

90: M.R.Schmorak, Nucl.Data Sheets 24(1978),117

91: M.R.Schmorak, Nucl.Data Sheets 23(1978),287

92: E.J.Feicht and H.Gobel, Z.Physik 245(1971),13

93: N.Ahmed, D.R.Gill, W.J.McDonald, G.C.Neilson and W.K.Davison, Phys.Rev.C11(1975),869

94: C.Y.Fu and F.G.Perey, Atomic Data and Nuclear Data Tables 16(1975),411

95: L.Cranberg, T.A.Oliphant, J.Levin and C.D.Zafiratos Phys.Rev.159(1967), 969

96: H.Kidwai and J.R.Rook, Nucl.Phys.A169(1971),417

97: M.J.Martin, Nucl.Data Sheets 22(1977),545

98: Y.A.Ellis, Nucl.Data Sheets 21(1977),549

99: R.Batchelor, W.B.GIlboy and J.H.Towle, Nucl.Phys. 65(1965),236

100: W.W.Osterhage, S.J.Hall, J.D.Kellie and G.I.Crawford, J.Phys.G4(1978),587

101: P.E.Hodgson, The Optical Model of Elastic Scattering (Clarendon Press, Oxford 1963)

102: P.E.Hodgson, Nuclear Reactions and Nuclear Structure (Clarendon Press, Oxford 1971)

103: P.A.Moldauer, Phys.Rev.C11(1975),426

104: H.Hofmann, J.Richert, J.Tepel and H.Weidenmuller, Ann.Phys.90(1975),403

105: D.Wilmore and P.E.Hodgson, Nucl.Phys.55(1964),673

106: W.R.Smith, Comp.Phys.Comm.1(1969),106

107: E.Sheldon, S.Mathur and D.Donati, Comp.Phys.Comm,2(1971),272

108: T.Tamura, Computer Program Jupitor-1 for Coupled Channel Calculations ,ORNL-4152 Oak Ridge National Laboratory 1967

109: F.G.Perey, Phys.Rev.131(1963),745

110: F.A.Brieva and J.R.Rook, Nucl.Phys.A291(1977),317

111: F.A.Brieva and J.R.Rook, Nucl.Phys.A297(1978),206

112: F.A.Brieva and J.R.Rook, Nucl.Phys.A307(1978),493

Acknowledgments

I would like to thank Dr.R.B.Galloway, who initiated this project and acted as my supervisor throughout its duration, for his invaluable support and advice. The many discussions which we have had on the project have proved indispensible to bringing the neutron polarimeter to an operational state and results to fruition. I would also like to thank Dr.D.G.Vass for his help and encouragement.

On technical matters the assistance of Mr H.J.Napier and Mr.G.Turnbull is much appreciated. Mr.Napier has tended the Van de Graaff accelerator often outside normal working hours and Mr.Turnbull has built many of the electronic units used in the experiment.

I would like to express my gratitude to the Science and Engineering Research Council who supported me financially during the first two years of the project.

Finally, but certainly not least, I would like to thank my family, especially my wife Janette, for stoically enduring the constant abnormal working hours, and occasional moods of despair when the Fates seemed to have turned against me. She has had to suffer many lonely evenings and in spite of this has remained ever cheerfull and a source of constant encouragement. Without her support my starting and completing this work would not have been possible.

John R.M. Annand.

April 1982